

## **Ablative heat shield design for space shuttle**



1. Report No. NASA CR-132282		2. Government Accession No.		3. Recipient's Catalog No.	
4. Title and Subtitle Ablative Heat Shield Design for Space Shuttle				5. Report Date	
				6. Performing Organization Code	
7. Author(s) R. W. Seiferth				8. Performing Organization Report No. MCR-73-147	
9. Performing Organization Name and Address Martin Marietta Corporation Denver Division Denver, Colorado 80201				10. Work Unit No.	
				11. Contract or Grant No. NAS1-11592	
12. Sponsoring Agency Name and Address National Aeronautics and Space Administration Washington D.C., 20546				13. Type of Report and Period Covered Final May 1972 - August 1973	
				14. Sponsoring Agency Code	
15. Supplementary Notes					
16. Abstract  Ablator heat shield configuration optimization studies were conducted for the Orbiter. Ablator and RSI trajectories for design studies were shaped to take advantage of the low conductance of ceramic RSI and high temperature capability of ablators. Comparative weights were established for the RSI system and for direct bond and mechanically attached ablator systems. Ablator system costs were determined for fabrication, installation and refurbishment. Cost penalties were assigned for payload weight penalties, if any. The direct bond ablator is lowest in weight and cost. A mechanically attached ablator using a magnesium subpanel is highly competitive for both weight and cost.					
17. Key Words (Suggested by Author(s)) Space Shuttle Heat Shield Ablators Design Criteria Environmental Testing Coatings Cost Analyses Trajectory Shaping Reusable Surface Insulation				18. Distribution Statement  Unclassified - Unlimited	
19. Security Classif. (of this report) Unclassified		20. Security Classif. (of this page) Unclassified		21. No. of Pages 254	22. Price*

\* For sale by the National Technical Information Service, Springfield, Virginia 22151



## FOREWORD

This report was prepared by Martin Marietta Corporation, Denver Division, Denver, Colorado, under Contract NAS1-11592, "Ablative Heat Shield Design for Space Shuttle." The contract was administered under the direction of Mr. Claud M. Pittman, Technical Representative of the NASA Langley Research Center Contracting Officer.

The program was performed by members of the Ablative Systems Section, the Advanced Structures and Materials Department, the Mechanical Design Engineering Department and the Systems Analysis Department. The program manager for Martin Marietta from the start of the contract on May 17, 1972 to September 5, 1972 was Mr. Daniel V. Sallis; Mr. Rolf W. Seiferth was program manager from September 5, 1972 through August 31, 1973.

This final report covers the contract period from May 17, 1972 through August 31, 1973.

Many persons contributed during the performance of the program and in the preparation of this report.

### Langley Research Center - NASA

Claud M. Pittman, LRC Technical Representative

### Martin Marietta Aerospace

D. V. Sallis, Program Manager through September 5, 1972

H. H. Chandler, Technical Director through September 5, 1972

W. R. Woodis, Trajectory Analysis

D. A. Schmitt, Aerothermal Analysis

W. D. Schwerin, Aerothermal Analysis

R. Stevenson, Aerothermal Analysis

D. G. Herbener, Thermal Analysis

S. C. Copey, Thermal Analysis

E. T. Haire, Design Criteria  
G. F. Molby, Stress Analysis  
T. L. Hibbard, Mechanical Design  
A. P. Lambatos, Weights Analysis  
J. M. Toth, Jr., Design Verification  
H. L. Draper, Design Verification  
J. W. Maccalous, Design Verification  
R. V. Kromrey, Design Verification  
G. T. Kelly, Cost Analysis  
W. L. Brown, Report Illustrator  
C. F. Cancalosi, Schedule Coordination

## CONTENTS

	Page
Foreword . . . . .	ii
Contents . . . . .	iv
Summary . . . . .	1
I. INTRODUCTION . . . . .	2
A. Task 1 - Design Criteria . . . . .	3
B. Task 2 - Flight Environment . . . . .	3
C. Task 3 - Heat Shield Designs . . . . .	3
D. Task 4 - Design Verification . . . . .	3
E. Task 5 - Weight and Cost Analysis . . . . .	3
II. DESIGN CRITERIA . . . . .	4
A. Scope . . . . .	4
B. Applicable Documents . . . . .	4
C. Definitions . . . . .	5
D. Basic Requirements . . . . .	5
E. System Definition . . . . .	14
F. Vehicle Description . . . . .	20
G. Environments . . . . .	21
H. Input Variable Uncertainties and Design Factors . . . . .	31
I. Interface Compatibility . . . . .	32
J. Quality . . . . .	33
K. Maintainability . . . . .	33
III. FLIGHT ENVIRONMENT . . . . .	34
A. Trajectory Analysis . . . . .	34
B. Aerothermal Analysis . . . . .	57
IV. HEAT SHIELD DESIGNS . . . . .	73
A. Design Description . . . . .	76
B. Subpanel Selections . . . . .	88
C. Stress Analysis . . . . .	90
D. Thermal Analysis . . . . .	93
E. TPS Weigh-Ins . . . . .	110
V. DESIGN VERIFICATION . . . . .	122
A. Open-Gap Panel Test . . . . .	124
B. Gap-Sealer Material Resiliency Tests . . . . .	135
C. Sealed-Gap Panel Test . . . . .	139
D. General Summary . . . . .	148

VI.	WEIGHT AND COST ANALYSES . . . . .	149
	A. Payload Weight Penalty Costs . . . . .	149
	B. Operational Costs, TPS . . . . .	154
	C. Reliability Costs . . . . .	154
	D. Total Program Costs for the Total TPS . . . . .	157
	E. Program Costs and TPS Weights by Temperature Regions . . . . .	157
	F. Leading Edge and Nose Cap Costs and Weights . . . . .	168
VII.	CONCLUSIONS AND RECOMMENDATIONS . . . . .	170
	A. Conclusions . . . . .	170
	B. Recommendations . . . . .	171
	APPENDIXES	
	A. Trajectory Analysis . . . . .	173
	B. Aerothermal Analysis . . . . .	181
	C. Stress Analysis . . . . .	195
	D. Thermal Analysis . . . . .	203
	E. Verification Testing . . . . .	220
	REFERENCES . . . . .	252
		thru
		254

Figure

1	Properties of Ablator Core Use in this Study . . .	10
2	Thermal Properties of SLA-561V Ablator . . . . .	11
3	Thermal Properties of ESA 3560HF Ablator . . . . .	11
4	Thermal Properties of ESA 5500M3 Ablator . . . . .	12
5	LI-1500 Thermal Properties . . . . .	12
6	Thermal-Mechanical Properties of SLA-561 Ablator . . . . .	13
7	Overall Acoustic Environments . . . . .	17
8	Local Acoustic Environments . . . . .	17
9	Typical Orbiter Effective Aluminum Heat Sink Mass . . . . .	20
10	Aerodynamic Pressure Distributions, Outer Surface Envelope . . . . .	30
11	Trajectory Shaping Philosophy . . . . .	35
12	Baseline Trajectory, Altitude . . . . .	39
13	Baseline Trajectory, Acceleration and Heating Rates . . . . .	39
14	Altitude and Heating Rate for 185 km (100 n. m.), 55° Trajectory . . . . .	40
15	Acceleration and Heating Rate for 185 km (100 n. mi.), 55° Trajectory . . . . .	40
16	Altitude for 930 km (500 n. mi.), 55° Trajectory . . . . .	41
17	Acceleration and Heating Rate for 930 km (500 n. mi.), 55° Trajectory . . . . .	41
18	Effect of $\gamma_{I_0}$ on Entry Time to 91.4 km (300 000 ft) . . . . .	43
19	Effect of $\gamma_{I_0}$ on Entry Time of Interval between 91.4 km (300 000 ft) and $\dot{q}_{\max} = 300 \text{ kW/m}^2$ (26.0 Btu/ft <sup>2</sup> -sec) . . . . .	43
20	Total Integral of $\dot{q} \Delta T$ $\dot{q}_{\max} = 300 \text{ kW/m}^2$ (26 Btu/ ft <sup>2</sup> -sec) as a Function of $\gamma_{I_0}$ . . . . .	44
21	Change in Deorbit Propellant Caused by Different $\gamma_{I_0}$ Degrees . . . . .	44
22	Effect of Initial Bank Angle on Vehicle Heating at $\dot{q}_{\max} = 300 \text{ kW/m}^2$ (26 Btu/ft <sup>2</sup> -sec) . . . . .	46
23	Inertial Crossrange as a Function of Initial Bank Angle at $\dot{q}_{\max} = 300 \text{ kW/m}^2$ (26 Btu/ft <sup>2</sup> - sec) . . . . .	46

24	Time Required for Vehicle to Attain Maximum Heating versus Initial Bank Angle . . . . .	47
25	Total Reentry Time Required to Reach Crossrange . . . . .	48
26	Total Reentry Heat Required by Crossrange . . . . .	48
27	Altitude for 185-km (100 n. mi.) Polar Orbit Trajectory, Unlimited $\dot{q}$ . . . . .	50
28	Acceleration and Heating Rate for 185-km (100 n. mi.) Polar Orbit Trajectory, Unlimited $\dot{q}$ . . . . .	51
29	Altitude for 185-km (100 n. mi.) Polar Orbit Trajectory, $\dot{q}_{\max} = 12.8$ . . . . .	51
30	Acceleration and Heating Rate for 185-km (100 n. mi.) Polar Orbit Trajectory, $\dot{q}_{\max} = 12.8$ . . . . .	52
31	Total Heat versus Peak Heating Rate . . . . .	52
32	Ascent Heating Rate Distribution . . . . .	59
33	Entry Heating Rates, Ablator Trajectory . . . . .	60
34	Entry Heating Rates, RSI Trajectory . . . . .	61
35	Ascent Heating Rate History at the Body Lower Centerline Reference Location . . . . .	62
36	Entry Heating Rate Histories at the Body Lower Centerline Reference Location . . . . .	62
37	Ascent Heating Rate Distribution around Nose Cap (Windward and Leeward) . . . . .	64
38	Entry Heating Rate Distribution around Nose Cap for Ablator Trajectory . . . . .	64
39	Entry Heating Rate Distribution around Nose Cap for Reusable TPS Trajectory . . . . .	65
40	Ascent Heating Rate Distribution around Wing Leading Edge (Windward and Leeward) . . . . .	65
41	Entry Heating Distribution around Wing Leading Edge for Ablator Trajectory . . . . .	66
42	Entry Heating Distribution around Wing Leading Edge for Reusable TPS Trajectory . . . . .	66
43	Orbiter/External Tank Shock Interference Heating on Orbiter Lower Surface During Ascent . . . . .	67
44	Ascent Local Static Pressure History . . . . .	68
45	Entry Local Static Pressure Histories at Stagnation Regions . . . . .	69
46	Entry Local Static Pressure Histories along Body Lower Centerline . . . . .	70
47	Entry Local Static Pressure History at Leeward and Side Locations . . . . .	71
48	Locations of Investigation Points . . . . .	75
49	Attachment Configurations . . . . .	75
50	Ablator Design, Fuselage Side . . . . .	78

51	Mechanical Fastener . . . . .	80
52	Ablator Design, Fuselage Top, $F\dot{q} = 0.033$ , Direct Bond . . . . .	81
53	Ablator Design, Reference Point, Standoff Panel . . . . .	83
54	Ablator Design, Fuselage Bottom Centerline, $F\dot{q} = 2$ . . . . .	84
55	TPS Design, Fin Leading Edge . . . . .	86
56	TPS Design, Wing Leading Edge . . . . .	87
57	TPS Design, Fuselage Nose Cap . . . . .	89
58	SLA-561 Ablator Requirements, Direct Bond to the Orbiter Structure . . . . .	94
59	SLA-561 Ablator Requirements, Aluminum Subpanel Mechanically Attached Directly to the Orbiter Structure . . . . .	95
60	SLA-561 Ablator Requirements, Lockalloy Subpanel Mechanically Attached Directly to the Orbiter Structure . . . . .	95
61	SLA-561 Ablator Requirements, Magnesium Subpanel Mechanically Attached Directly to the Orbiter Structure . . . . .	96
62	SLA-561 Ablator Requirements, Aluminum Honeycomb Subpanel Mechanically Attached Directly to the Orbiter Structure . . . . .	96
63	SLA-561 Ablator Requirements, Magnesium Honeycomb Subpanel Mechanically Attached Directly to the Orbiter Structure . . . . .	97
64	SLA-561 Ablator Requirements, Graphite/Polyimide Honeycomb Subpanel Mechanically Attached Directly to the Orbiter Structure . . . . .	97
65	SLA-561 Ablator Design Chart . . . . .	98
66	SLA-561 Requirement versus $Q/Q_{ref}$ versus Heat Capacity of Backup Structure for Direct Attach Subpanels . . . . .	98
67	SLA-561 Ablator Requirements, Aluminum Honeycomb Subpanel Mechanically Attached through Standoff Fittings to the Orbiter Structure . . . . .	100
68	SLA-561 Ablator Requirements, Graphite/Polyimide Honeycomb Subpanel Mechanically Attached through Standoff Fittings to the Orbiter Structure . . . . .	100
69	RSI LI-1500 Requirements, Direct Bond to the Orbiter Structure . . . . .	101
70	Lambda Distributions at Top Fuselage, Reusable TPS Trajectory . . . . .	102
71	RSI Trajectory, Lee Surface SLA-561 Ablator Reuse Assessment . . . . .	102

72	Reference Point Heating versus Ablator Trajectory Time . . . . .	103
73	Reference Point Heating versus RSI Trajectory Time . . . . .	103
74	Nose Cap Ablator Thickness for Ablator Trajectory, R = 91.4 cm (36 in.) . . . . .	105
75	Ablator Trajectory Nose Cap Design . . . . .	105
76	Nose Cap Ablator Thickness for RSI Trajectory, R = 91.4 cm (36 in.) . . . . .	106
77	RSI Trajectory Nose Cap Design . . . . .	106
78	Wing Leading Edge Ablator Thickness for Ablator Trajectory, R = 15.25 cm (6 in.) . . . . .	107
79	Ablator Trajectory Wing Leading Edge Design . . . . .	107
80	Ablator Thickness for RSI Trajectory Wing Leading Edge, R = 15.25 cm (6 in.) . . . . .	108
81	RSI Trajectory Wing Leading Edge Design . . . . .	108
82	Ablator Thickness for Ablator Trajectory Fin Leading Edge . . . . .	109
83	Ablator Thickness for RSI Trajectory Fin Leading Edge . . . . .	109
84	RSI Thickness versus Weight . . . . .	118
85	TPS Attachment Configuration Weight versus Fastener Spacing . . . . .	118
86	Composite Test Panel Configuration . . . . .	123
87	Subpanel Attachment . . . . .	123
88	Open-Gap Test Panel . . . . .	125
89	X-Ray of Gap Closure Pins . . . . .	128
90	Radiant-Heat Test Facility (Ablator Panel) . . . . .	128
91	SLA-561 Reference Point Heating (Descent) . . . . .	129
92	Strain Gage Data (S/G 1, 3, 5, and 7) . . . . .	131
93	Strain Gage Data (S/G 2, 4, 6, and 8) . . . . .	131
94	Posttest Condition of Gap Area (Open-Gap Panel) . . . . .	133
95	Cross Section of Tested Subpanel (Open-Gap Panel) . . . . .	134
96	Test Fixture, Gap Sealer Material . . . . .	136
97	Blanket Material Specimens . . . . .	137
98	Fiberfrax Rope Specimen . . . . .	137
99	Sealed-Gap Test Panel . . . . .	140
100	Sealed-Gap Panel, Pretest Appearance . . . . .	143
101	SLA-561 Reference Point Heating (Ascent) . . . . .	143
102	Temperature Uniformity and Gap Temperature Comparison, Back of 0.254-cm (0.10 in.) Primary Structure Sheet . . . . .	144
103	Strain Gage Data (S/G 1, 2, 3, and 4) . . . . .	146
104	Strain Gage Data (S/G 5, 6, 7, and 8) . . . . .	146
105	Maximum Temperatures at Strain Gages, Gages between Ablator and 0.102-cm (0.040 in.) Sheet . . . . .	147

106	Sealed-Gap Panel Posttest Appearance . . . . .	147
107	Orbiter TPS Weight vs. $F\dot{q}$ . . . . .	163
108	Heat Load vs. Area . . . . .	164
109	Orbiter General Panel Location and Quantity . .	165
110	TPS Program Cost and Weight for Given Temperatures and Above . . . . .	166
111	GAC Orbiter Drag Coefficients . . . . .	175
112	GAC Orbiter Lift Coefficients . . . . .	176
113	GAC Orbiter Angle of Attack . . . . .	177
114	Design Chart, SLA-561 Direct Bond Orbiter Entries . . . . .	178
115	Entry Heating Rate Histories on the Forward Portion of the Body Lower Centerline for Ablator Trajectory . . . . .	182
116	Entry Heating Rate Histories on the Forward Portion of the Body Lower Centerline for the Reusable TPS Trajectory . . . . .	183
117	Entry Heating Rate Histories on Bottom of Wing (Midspan Location) for Ablator Trajectory . . .	183
118	Entry Heating Rate Histories on Bottom of Wing (Midspan Location) for Reusable TPS Trajectory .	184
119	Ascent Local Dynamic Pressure History . . . . .	185
120	Ascent Local Mach Number History at Body Lower Centerline Reference Location and at Stagnation Line of Wing Leading Edge . . . . .	186
121	Ascent Local Mach Number History at Forward Centerline and at Leeward and Side Locations . .	186
122	Ascent Shear Stress History at Body Lower Centerline Reference Location and at Stagnation Line of Wing Leading Edge . . . . .	187
123	Ascent Shear Stress History at Forward Lower Centerline and at Leeward and Side Locations . .	187
124	Entry Local Dynamic Pressure History at Body Lower Centerline Reference Location . . . . .	188
125	Entry Local Dynamic Pressure History at Stagnation Line of Wing Leading Edge (Midspan Location) . . . . .	188
126	Entry Local Dynamic Pressure History at the Forward Lower Centerline Location . . . . .	189
127	Entry Local Dynamic Pressure History at Leeward and Side Locations . . . . .	189
128	Entry Local Mach Number History at Body Lower Centerline Reference Location . . . . .	190
129	Entry Local Mach Number History at Stagnation Line of Wing Leading Edge (Midspan Location) . .	190
130	Entry Local Mach Number History at the Forward Lower Centerline Location . . . . .	191

131	Entry Local Mach Number History at Leeward and Side Locations . . . . .	191
132	Entry Shear Stress History at Body Lower Centerline Reference Location . . . . .	192
133	Entry Shear Stress History at Stagnation Line of Wing Leading Edge (Midspan Location) . . . . .	192
134	Entry Shear Stress History at the Forward Lower Centerline Location . . . . .	193
135	Entry Shear Stress History at Leeward and Side Locations . . . . .	193
136	Fuselage Nose Cap Geometry . . . . .	201
137	Heat Transfer through Sandwich Structure, Triangular Pulse . . . . .	204
138	Heat Transfer through Sandwich Structure, Ramp Pulse . . . . .	205
139	Heat Transfer across Subpanel, Primary Structure Interface, $\epsilon = 0.9$ . . . . .	207
140	Heat Transfer across Subpanel, Primary Structure Interface, $\epsilon = 0.2$ . . . . .	208
141	Heat Transfer across Subpanel, Primary Structure Interface (Fastener Conduction Included) . . . . .	210
142	Coating Requirements in Acreage Areas . . . . .	212
143	Ascent and Orbit Heating Surface and Structural Temperatures, $F\dot{q} = 1.0$ . . . . .	213
144	Ascent and Orbit Heating Surface and Structural Temperatures, $F\dot{q} = 4.0$ . . . . .	213
145	Thermal Control Coating Requirements in Nose Cap and Leading Edge Areas . . . . .	214
146	Nose Stagnation Point Ascent and Orbit Heating Surface and Structural Temperatures . . . . .	215
147	Weight of TPS in Nose Cap Area . . . . .	217
148	Backup Structure Heat Capacity vs. Ablator Requirement . . . . .	219
149	Test Panel . . . . .	221
150	Surface Thermocouple Measurements . . . . .	223
151	Thermocouple Measurements (T/C 1, 2, 3, and 4) . . . . .	224
152	Thermocouple Measurements (T/C 1, 2, 5, and 6) . . . . .	225
153	Thermocouple Measurements (T/C 3, 4, 7, and 8) . . . . .	226
154	Thermocouple Measurements (T/C 5, 6, 7, and 8) . . . . .	227
155	Thermocouple Measurements (T/C 9 and 10) . . . . .	228
156	Thermocouple Measurements (T/C 12, 13, and 14) . . . . .	229
157	Thermocouple Measurements (T/C 15, 16, 17, and 18) . . . . .	230
158	Thermocouple Measurements (T/C 19, 20, 21, and 22) . . . . .	231
159	Thermocouple Measurements (T/C 24, 25, 27, and 28) . . . . .	232

160	Thermocouple Measurements (T/C 25, 28, 32, and 33) . . . . .	233
161	Thermocouple Measurements (T/C 35 through 41) .	234
162	Thermocouple Measurements (T/C 1, 3, 4, and 10) . . . . .	238
163	Thermocouple Measurements (T/C 5, 6, 7, and 8) .	239
164	Thermocouple Measurements (T/C 8, 9, 37, and 38) . . . . .	240
165	Thermocouple Measurements (T/C 12, 14, 21, and 23) . . . . .	241
166	Thermocouple Measurements (T/C 15, 16, 17, and 18) . . . . .	242
167	Thermocouple Measurements (T/C 30, 31, 12, and 40) . . . . .	243
168	Thermocouple Measurements (T/C 12, 31, and 40) .	244
169	Thermocouple Measurements (T/C 13, 19, 20, and 22) . . . . .	245
170	Thermocouple Measurements (T/C 23, 28, 29, and 30) . . . . .	246
171	Thermocouple Measurements (T/C 24, 25, 26, and 27) . . . . .	247
172	Thermocouple Measurements (T/C 28, 29, 29A, and 30) . . . . .	248
173	Thermocouple Measurements (T/C 31, 38, and 40) .	249
174	Thermocouple Measurements (T/C 32, 33, and 41) . . . . .	250
175	Thermocouple Measurements (T/C 34, 35, 36, and 37) . . . . .	251

Table

1	Design Factors on Heating Rates . . . . .	8
2	List of Materials . . . . .	9
3	Ablator Application . . . . .	15
4	Viking Flexure Tests . . . . .	19
5	Modification of the Nondimensional Panel Flutter Parameter . . . . .	25
6	Equivalent Static Loads for Acoustic Pressures . . . . .	26
7	Typical Maximum Local Static Pressures During Entry Heating . . . . .	27
8	Design Limit Pressures for Standoff Heat Shield Panels . . . . .	29
9	Safety Factors on Loads and Pressures . . . . .	31
10	Summary of Entry Trajectories . . . . .	38
11	Maximum and Minimum Heating Rate Trajectories . . . . .	49
12	Dispersion Summary . . . . .	53
13	TPS Materials used in Baseline Designs . . . . .	73
14	TPS Configurations and Materials . . . . .	77
15	Selection of Subpanels for Tradeoff Studies . . . . .	90
16	Design Loading Conditions . . . . .	91
17	Subpanel Gages Required for Direct Attachment Application . . . . .	92
18	Design Locations and Heating Loads . . . . .	94
19	Orbiter TPS Weight, Ablator Trajectory, SLA-561 Direct Bond . . . . .	111
20	Orbiter TPS Weight, Reusable TPS Trajectory, LI-1500 . . . . .	113
21	Orbiter TPS Weight, Ablator Trajectory, 0.079 cm (0.031 in.) Aluminum Plate Subpanel Direct Attachment, Fastening Spacing 12.7 cm (5 in.) . . . . .	115
22	Aluminum (2024-T81) Plate, Direct Attached . . . . .	119
23	Magnesium (HM-21A) Plate, Direct Attached . . . . .	119
24	Lockalloy Plate, Direct Attached . . . . .	119
25	Aluminum Honeycomb, Direct Attached . . . . .	119
26	Magnesium Honeycomb, Direct Attached . . . . .	120
27	Graphite Polyimide Honeycomb, Direct Attached . . . . .	120
28	Aluminum Honeycomb, Standoff . . . . .	120
29	Graphite Polyimide Honeycomb, Standoff . . . . .	120
30	Switch Data for Gap Movement . . . . .	132
31	Gap Temperature Comparison . . . . .	133
32	Stud-Bolt Counterbore Heating Comparison, Open- Gap Panel . . . . .	134
33	Gap Sealer Resiliency Testing . . . . .	138
34	Stud-Bolt Counterbore Heating Comparison, Sealed-Gap Panel, Descent Heating . . . . .	145

35	Verification Test Program . . . . .	148
36	Payload Weight in First 151 Flights . . . . .	149
37	Sample Calculation, Weight Penalty Cost, 1981 Model . . . . .	151
38	Payload Weight Penalty Costs . . . . .	153
39	Operational Costs for 151 Flights (\$K) . . . . .	155
40	Reliability Costs for 151 Flights (\$K) . . . . .	156
41	Weight and Cost Summary, 12.7-cm (5 in.) Fastener Spacing . . . . .	158
42	Weight and Cost Summary, 25.4-cm (10 in.) Fastener Spacing . . . . .	159
43	Weight and Cost Summary, 38.1-cm (15 in.) Fastener Spacing . . . . .	160
44	Weight and Cost Summary, 50.8-cm (20 in.) Fastener Spacing . . . . .	161
45	Ablator Material Costs . . . . .	167
46	Nose Cap and Leading Edge TPS Areas and Weights . . . . .	169
47	Nose Cap and Leading Edge Costs . . . . .	169
48	Heating Rate Distribution and Areas . . . . .	179
49	Applied Loadings . . . . .	195
50	Allowable Loadings . . . . .	196
51	Airload Bending Moment and Minimum Thickness . .	198
52	Plate Thickness Required for $MAS \geq$ Airload Moment . . . . .	198
53	Summary of Plate t to Meet Deflection and MAS .	198
54	Subpanel Gages . . . . .	200
55	Material Properties . . . . .	202
56	Nose Cap Configurations . . . . .	202



# ABLATIVE HEAT SHIELD DESIGN FOR SPACE SHUTTLE

## FINAL REPORT

By Rolf W. Seiferth  
Martin Marietta Corporation

### SUMMARY

State-of-the-art ablative materials were used to design a thermal protection system (TPS) for the Space Shuttle Orbiter. An "ablator trajectory" was developed within the bounds of 2.5 g acceleration and 300 kW/m<sup>2</sup> (26 Btu/ft<sup>2</sup>-sec) heating rate at the reference point 15.24 m (50 ft) aft of the fuselage nose on the bottom centerline. An "RSI trajectory" was also developed for design comparison purposes. This trajectory was shaped to minimize heating rate within the limits of skipout during reentry. Heating rates and total heats were developed for the total Orbiter. Ablative heat shield designs were derived for numerous locations on the Orbiter using direct bond and mechanically attached concepts. A reusable surface insulation (RSI) TPS was also developed for weight comparison purposes. Radiant heat tests were conducted on mechanically attached ablator specimens to verify design concepts.

A cost analysis was prepared for the various heat shield concepts. Weight was considered as a cost factor by determining a cost per pound to orbit using the "Preliminary Traffic Model for the Space Shuttle," published by NASA-MSFC (ref. 1). Ablator TPS operation was assumed for the first five years of Shuttle service. Cost data were derived for the operational phase and for reliability, which was treated as a quality assurance item. The sum of the weight costs, operational costs, and reliability costs was used to rate the various heat shield concepts and select this optimum ablator configuration.

The direct bond ablator system had the lowest weight and program cost of all the systems examined. Mechanically attached plates with ablator bonded to them are very competitive for both weight and cost.

## I. INTRODUCTION

Ablators are a well-established system of thermal protection, having been used on such vehicles as Apollo, Gemini, Viking Spacecraft, X-15, Titan, PRIME, and others. The need for refurbishment following each thermal usage is a serious drawback of this thermal protection system and has led NASA and industry into the development of reusable surface insulation (RSI) ceramics. This system of thermal protection has been baselined for use on the Shuttle Orbiter.

Much work is necessary to flight-qualify the RSI for Space Shuttle application and, to quote E. S. Love from the Tenth Von Karman Lecture (ref. 2), "Ablators offer a confident fall-back solution (temporary) for both leading edges and large surface areas, should development of the baseline approaches lag."

In the past, ablator systems have been bonded directly onto the structures they are designed to protect. While this approach is both low in weight and cost effective, it has the serious drawback for the Shuttle Orbiter of taking up critical turnaround time for refurbishment between flights, and during refurbishment creates a considerable problem of debris and dust control.

The purpose of this program is to prepare Shuttle Orbiter TPS design concepts using available state-of-the-art ablators and meeting the unique requirements of the Shuttle Orbiter. An end objective of the program was to obtain weight and cost sensitivities based on detailed, verified heat shield designs. Direct bond ablator and RSI designs were prepared for weight comparison purposes. A key part of the effort dealt with methods of mechanically attaching prepared ablator panels onto the Orbiter. Radiant heat tests were conducted to verify the design concepts, and weight and cost analyses were prepared for comparison with the direct bond approach.

The program was divided into five tasks:

- Task 1 - Design Criteria;
- Task 2 - Flight Environment;
- Task 3 - Heat Shield Designs;
- Task 4 - Design Verification;
- Task 5 - Weight and Cost Analysis.

#### A. Task 1 - Design Criteria

Criteria were prepared to develop the design trajectories, thermal loadings, structural and thermal factors of safety, backface temperature limits, and ablator-subpanel design.

#### B. Task 2 - Flight Environment

Trajectories were established for ablator designs and RSI design. Thermal loadings for these trajectories were detailed for the entire Orbiter surface.

#### C. Task 3 - Heat Shield Designs

Heat shield designs were prepared for numerous specified locations on the Orbiter. Direct bond and mechanically attached TPS designs were prepared. Both direct mechanically attached and standoff concepts were evaluated. Subpanel materials and attachment spacing was varied to determine the best choice.

#### D. Task 4 - Design Verification

A test program was conducted to verify important facets of the heat shield design. The open gap and the sealed gap concepts were tested, gap sealers were tested, and the mechanically attached configuration was verified.

#### E. Task 5 - Weight and Cost Analysis

A weight and cost analysis was performed for competitive ablator systems. Data are presented showing ablator TPS weights and program costs in the specified thermal zones. Payload weight penalty determinations were made using the Shuttle payload model developed by MSFC, "Preliminary Traffic Model for Space Shuttle" (ref. 1).

## II. DESIGN CRITERIA

### A. Scope

The design criteria used in the development of an ablator thermal protection system are presented here. The criteria, whenever possible, are based on the Orbiter vehicle of the Space Shuttle Program. The total environment was considered in determining the design criteria.

### B. Applicable Documents

The following documents form a part of this criteria document to the extent specified herein.

#### 1. National Aeronautics and Space Administration (NASA).-

NASA TMX-43865, *Space Environment Criteria for the NASA Space Station Program*, Second Edition, August 20, 1970.

NASA TMX-53957, *Space Environment Criteria Guidelines for Use in Space Vehicle Development*, 1969 Revision, Second Edition, August 26, 1970.

NASA TMX-64589, *Terrestrial Environment (Climatic) Criteria Guidelines for Use in Space Vehicle Development*, 1971 Revision, May 10, 1971.

NASA SP-8057, *Structural Design Criteria Application to the Space Shuttle*.

Space Shuttle Program RFP No. 9-BC421-67-2-40P.

#### 2. Military.-

MIL-B-5087B, *Bonding, Electrical and Lightning Protection for Aerospace Systems*.

MIL-STD-810B, *Environmental Test Methods*.

#### 3. Martin Marietta Corporation.-

M-67-45, *Test Methods and Controls*.

MMC-SSO-0202, *General Test Plan*.

#### 4. Grumman Aerospace Corporation.-

B61CSZ003, Structural/Environmental Design Criteria,  
General Specification for Space Shuttle Orbiter, Phase  
C-D Proposal.

##### C. Definitions

Terms used within this document are defined by NASA's Shuttle design criteria document (ref. 3). In addition, the following terms are specific for this report:

Limit temperature is the maximum structural temperature (consistent with acceptable reliability) resulting from performing the missions (including dispersed trajectories) being considered. Thus, there is no ultimate temperature.

Limit thermal stress or strain is the maximum stress or strain (consistent with acceptable reliability) arising from limit temperature distributions and associated differential thermal expansion between TPS components and supporting substructure. (There is no ultimate thermal stress or strain.) Limit thermal stress or strain conditions may not correspond to limit temperature conditions because they are associated with transient rather than steady-state heating.

Nominal temperature is the structural temperature resulting from the accomplishment of a nominal trajectory.

##### D. Basic Requirements

1. Thermal protection.- The thermal protection system will protect the primary airframe, the crew and passengers, the payload, and the vehicle subsystems from aerodynamic heating during ascent and entry and from convective and radiative heating from the engine exhaust.

An ablative-type TPS will be used initially. The impact of incorporating reusable systems later will be identified. Surface contour changes, particularly of critical aerodynamic surfaces; attachment provisions; and refurbishment and panel sizes will be evaluated. The required thicknesses of the ablative and reusable heat shield panels will not be exactly the same. The optimum panel sizes and configurations of the ablative and reusable panels for replacement and refurbishment may differ in some respects. These differences will be evaluated in terms of delta weights and costs.

Selection of design trajectory/or trajectories will result in a TPS capable of safe vehicle flight within an operational envelope that includes all mission and abort requirements, trajectory excursions, and atmospheric deviations.

Ablator material properties (thermal and mechanical) will be nominal values. The statistical uncertainty and reuse degradation effects associated with the fabricated and installed panel will be accounted for by a 10 percent increase in the ablator thickness required for design aerodynamic heating. Minimum thickness will be 0.64 cm (0.25-in.).

Thermal control coating will be applied to the external (exposed) surfaces of the ablative heat shielding as required for the following purposes:

- 1) To control TPS and substructural temperatures at the start of entry, consistent with optimum heat shield design;
- 2) To protect the ablator against damaging natural and induced environments throughout the mission cycle.

The hazards prevailing during prelaunch, launch, ascent, exit, and orbit to start of entry will not impair the capability of the coating to perform its functions.

The test data available characterizing the properties of installed panels are not sufficient to establish minimum guaranteed values for design. The percentage reduction is not included as a safety factor or design factor because it adjusts the allowable capability of the heat shield and does not relate to environmental exposures. The safety factors listed are applied to loads and pressures. Variations and uncertainties in aerodynamic heating rates are accounted for by design factors applied to nominal heating rates. The 10 percent increase in ablator thickness is based on previous experience with panel and materials testing associated with the PRIME and Shuttle insulating heat shieldings. An ablator thickness of 0.64 cm (0.25 in.) is considered the minimum that can be fabricated into a reliable heat shield accounting for geometric tolerances and environmental and heat shield property dispersions.

2. Space Shuttle reference missions.- The Space Shuttle system will be designed to accomplish a wide variety of missions. The reference missions for the Space Shuttle system are described

below and shall be used in conjunction with the other requirements specified herein to design the TPS. For performance comparisons, Missions 1 and 2 will be launched from Kennedy Space Center into a 93 by 185 km (50 by 100 n. mi.) insertion orbit and Mission 3 will be launched into the same insertion orbit from the Western Test Range. The mission on-orbit translational delta V capability (in excess of that required to achieve the insertion orbit and that required for on-orbit and entry attitude control) is stated for each mission and includes on-orbit delta V reserves. The Reaction Control System (RCS) translational delta V required for each mission is used to accomplish all rendezvous maneuvers after terminal phase initiation.

Mission 1: This mission is a payload delivery mission to a 185 km (100 n. mi.) circular orbit. The mission will be launched due east and requires a payload capability of 29 000 kg (65 000 lb) with the Orbiter vehicle air-breathing engines removed. The purpose of this mission will be assumed to be placement and/or retrieval of a satellite. The Orbiter vehicle on-orbit translation delta V requirement is 290 m/s (950 ft/s) from the Orbital Maneuver Subsystem (OMS) and 37 m/s (120 ft/s) from the RCS.

Mission 2: This is a resupply mission to an orbital element in a 500 km (270 n. mi.) circular orbit at 55° inclination. The rendezvous is accomplished using a 17 orbit coelliptic rendezvous sequence (sequence is for reference only). The payload requirement is assumed to be 11 000 kg (25 000 lb). The Orbiter vehicle on orbit translation delta V requirement is 430 m/s (1400 ft/s) from the OMS and 37 m/s (120 ft/s) from the RCS.

Mission 3: This mission is a payload delivery or mission to a 185 km (100 n. mi.) circular polar orbit and return to launch site in a single revolution. The payload is 18 000 kg (40 000 lb) with Orbiter vehicle air-breathing engines removed. The Orbiter vehicle on-orbit translation delta V requirement is 150 m/s (500 ft/s) from the OMS and 46 m/s (150 ft/s) from the RCS.

3. Crossrange capability.- The Orbiter vehicle will have the aerodynamic crossrange capability to return to the launch site at the end of one revolution for all inclinations within the Shuttle System capability. Crossrange is to be achieved during entry, which is defined as beginning at 120-km (400 000 ft) altitude and ending at 15-km (50 000 ft) altitude. Crossrange and reentry payload weights for each mission will be defined. Adequate provisions will be made for downrange maneuvering capability and for the effects of entry guidance and deorbit and entry dispersions,

including navigation, aerodynamic, atmospheric, and weight uncertainties. These provisions are in the form of limit design factors (table 1) applied to nominal heating. The entry path angle will be held above the minimum  $-0.89^\circ$  necessary to maintain downrange dispersions within required limits for a lift vector down for the 185.5 km (100 n. mi.) orbits, both polar and  $55^\circ$  inclination.

TABLE 1.- DESIGN FACTORS ON HEATING RATES

Vehicle surface location	Design factor (limit/ nominal)
Lower surface forward centerline (windward)	1.15
Lower surface aft centerline (windward)	1.25
Upper surfaces (leeward)	1.50
Wing bottom	1.25
Leading edges	1.15

The crossrange will be 2040 km (1100 n. mi.) for 185.2 km (100 n. mi.) polar orbit once around; 1481.6 km (800 n. mi.) for the 185.2 km (100 n. mi.)  $55^\circ$  inclination; and greater than 926.0 km (500 n. mi.) for the 926.0 km (500 n. mi.)  $55^\circ$  inclination direct abort.

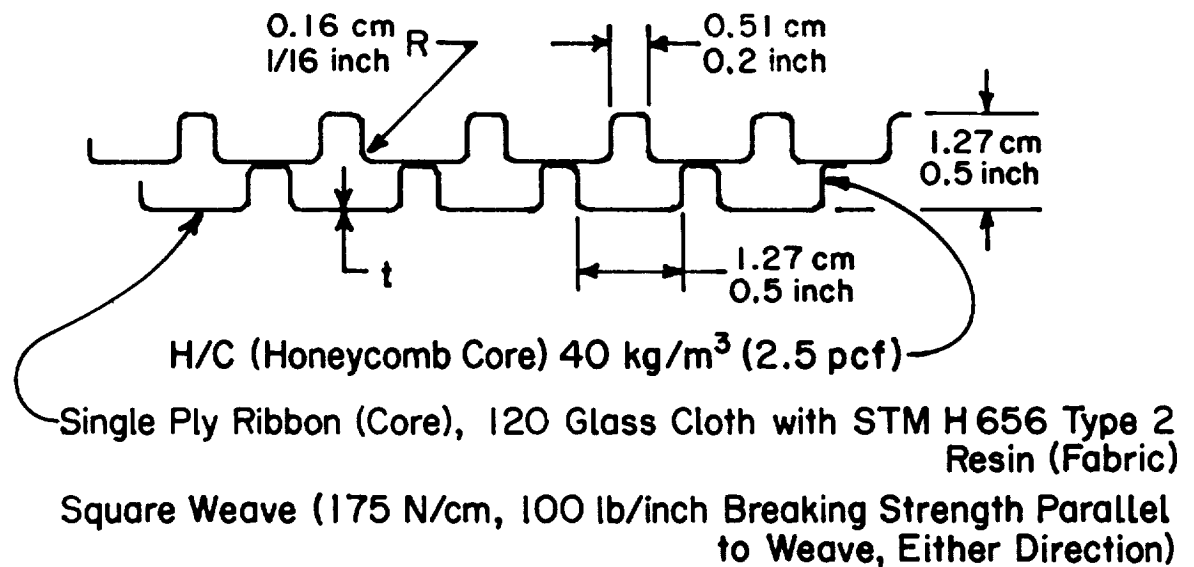
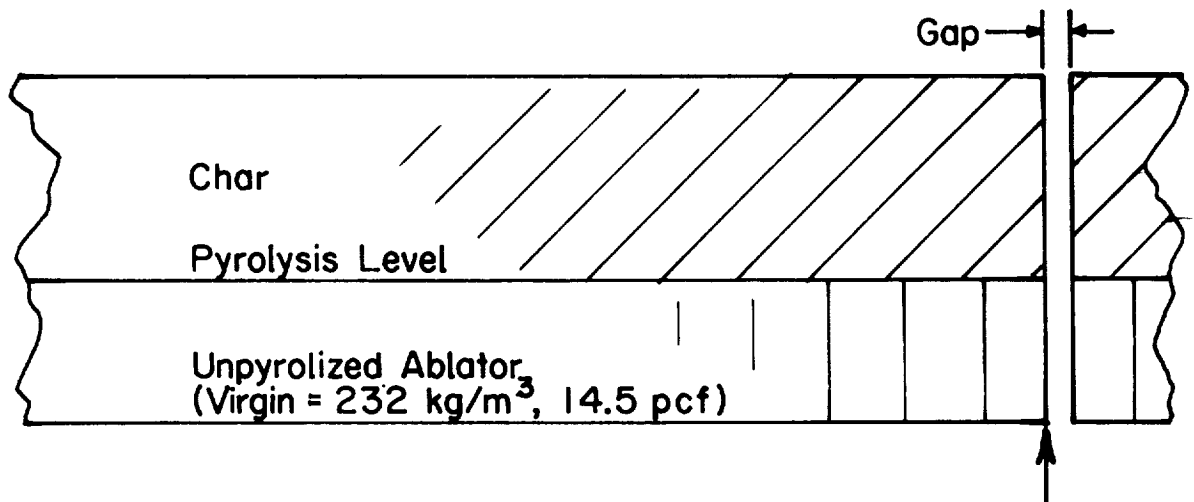
The entry payload will be 1810 kg (40 000 lb) and the entry weight, 9280 kg (205 000 lb).  $W/C_L S$  is  $500 \text{ N/m}^2$  ( $104 \text{ lb/ft}^2$ ).

4. Abort.- Fail-safe deorbit and direct reentry abort capability will be provided from a 926 km (500 n. mi.) circular orbit.

5. Material Properties.- Thermal and mechanical properties for design of structure, subpanels, and joints in their design environments are presented or referenced (table 2). Material properties not presented shall be obtained from the respective reference, table 2, or other approved source.

TABLE 2.- LIST OF MATERIALS

Material	Density		Property reference
	lb/ft <sup>3</sup>	kg/m <sup>3</sup>	
Subpanel Plate: 2024-T81 Al HM-21A magnesium Lockalloy	110.0 130.0	1770.0 2070.0	Ref. 4 Ref. 4 Ref. 5
Subpanel sandwich faces: 2040-T81 Al sheet HM-21A magnesium sheet Graphite polyimide	95.0	1520.0	Ref. 4 Ref. 4 In-house
Subpanel sandwich cores: 5053-H39 Al foil H/C - 0.32 cm (1/8 in.) cell Hexcell HRH 327 glass reinforced - 0.48 cm (3/16 in.) cell	3.1 3.0	49.6 48.0	Ref. 6 Ref. 7
Plastic H/C Face to core adhesive: Epoxy 0.34 kg/m <sup>2</sup> (0.07 psf)			HT-424 epoxy phenolic temperature range 172 to 533°K, (-150 to 500°F)
Ablator to subpanel bond: GX6300-0.067 cm (0.030 in.) thick, 1.47 kg/m <sup>2</sup> (0.235 lb/ft <sup>2</sup> )	94.0	1510.0	
Ablator surface coating DC93-044, 0.127 cm (0.050 in.) thick, 0.864 kg/m <sup>2</sup> (0.177 lb/ft <sup>2</sup> )	42.5	682.0	Ref. 8
Panel edge Corfil 615	40.5	650.0	Ref. 9
Ablators: SLA-561 [two dimensional ESA 3560 HF bending core ESA 5500M3 figure 1]	14.5 30.0 58.1	233.0 482.0 934.0	Figs. 2 and 6 Fig. 3 Fig. 4
Reusable surface insulation: LI-1500	15.0	241.0	Fig. 5



**Core Only**

**Compressive Strength of Fabricated Core (No Ablative Material)**

$F_c$  (Ult) = 414 kN/m<sup>2</sup> (60 psi) Minimum

690 kN/m<sup>2</sup> (100 psi) Average

276 Running meters of Core per Square meter

(7 Running inches of Core per Square inch)-

$$\therefore P_c/m = \frac{414}{276} = 1.5 \text{ kN/m Minimum Strength}$$

$$(P_c/\text{inch} = \frac{60}{7} = 8.6 \text{ lb/inch Minimum Strength})$$

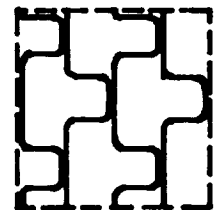


Figure 1.- Properties of Ablator Core Use in this Study

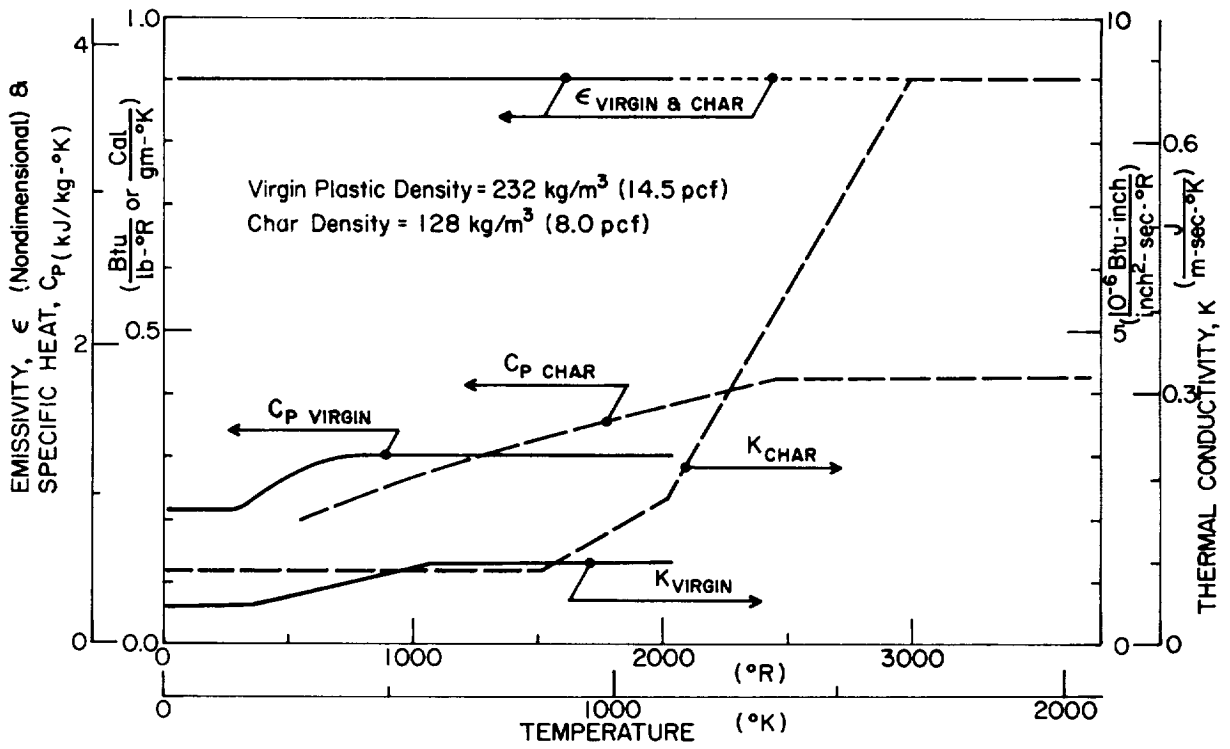


Figure 2.- Thermal Properties of SLA-561 Ablator

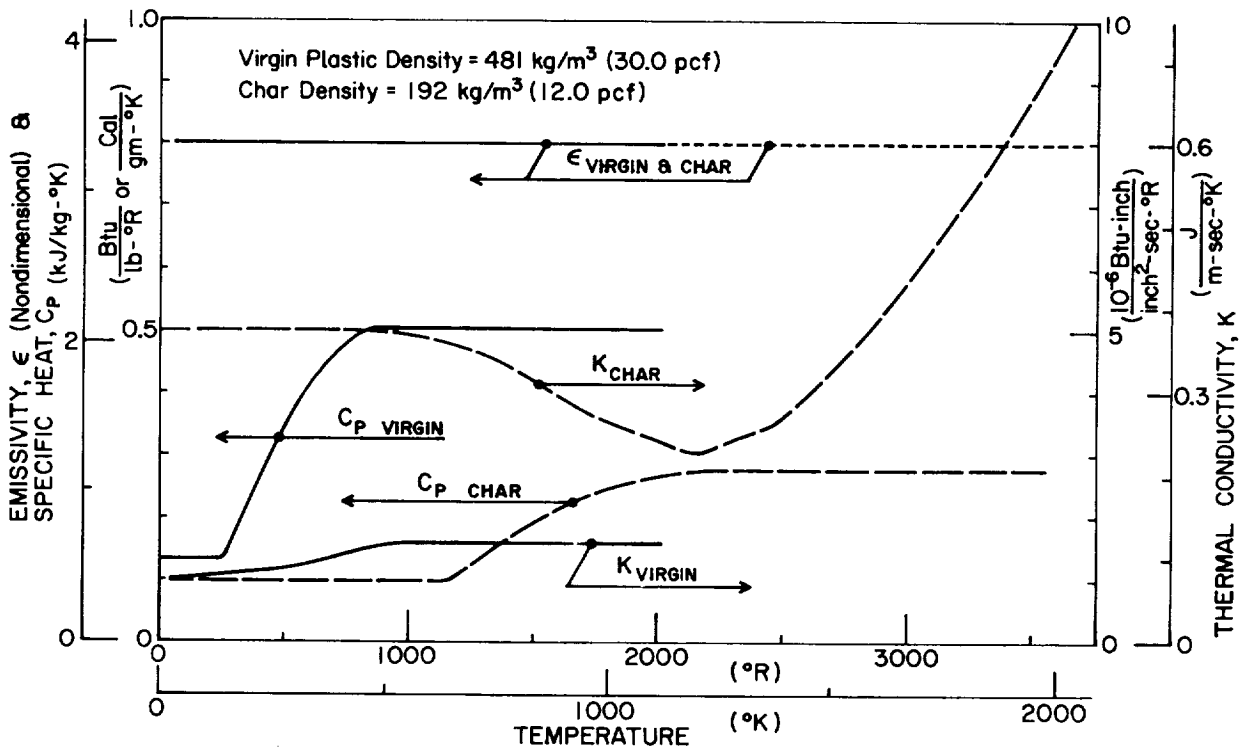


Figure 3.- Thermal Properties of ESA 3560HF Ablator

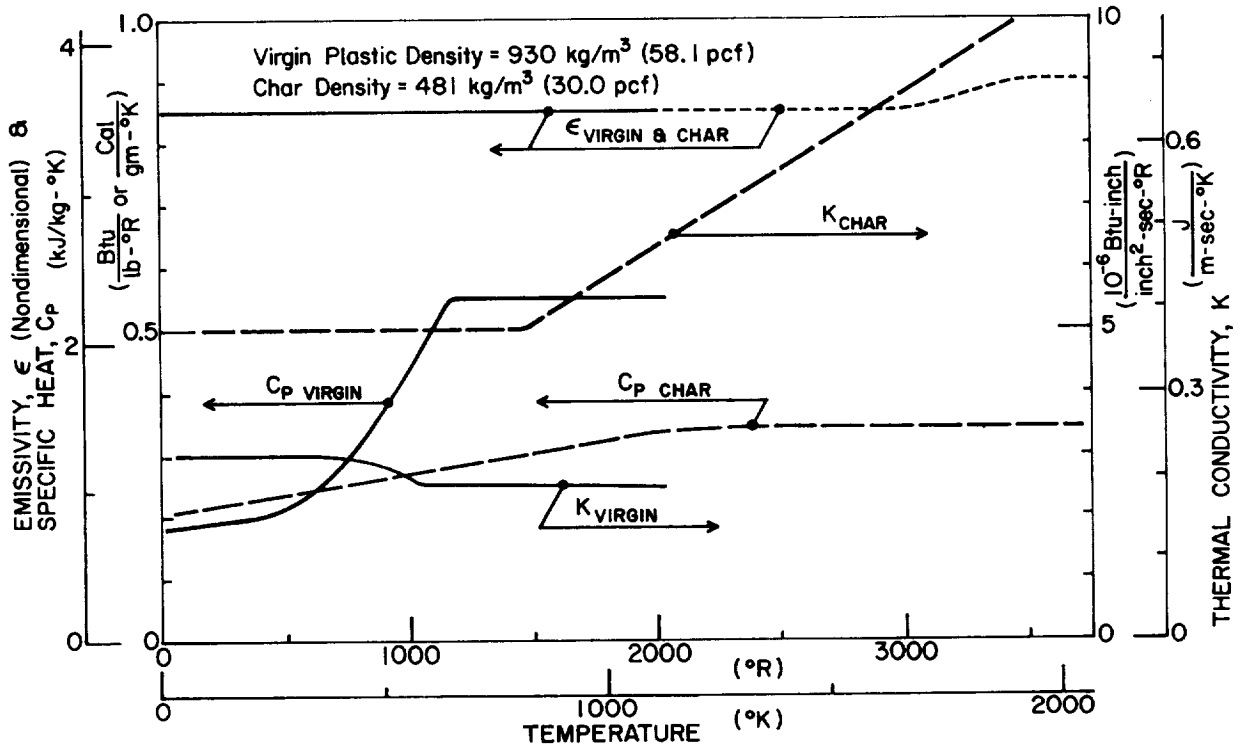


Figure 4.- Thermal Properties of ESA 5500M3 Ablator

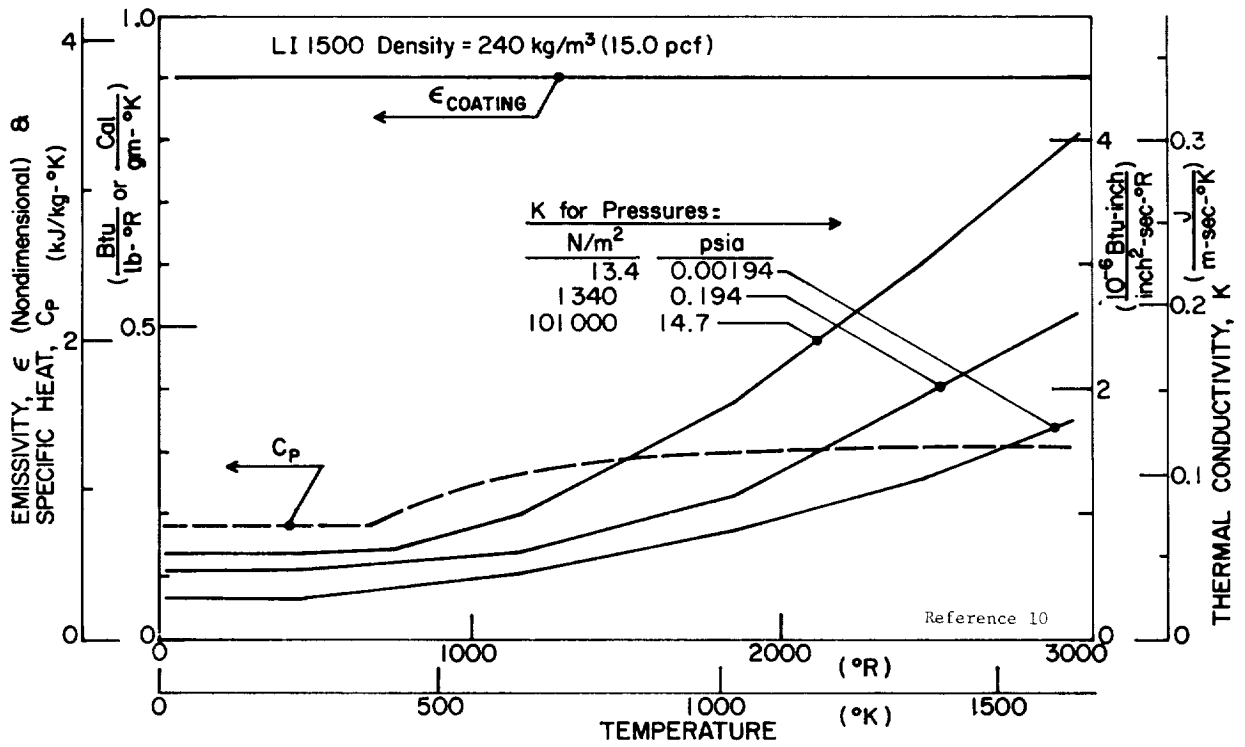


Figure 5.- LI-1500 Thermal Properties

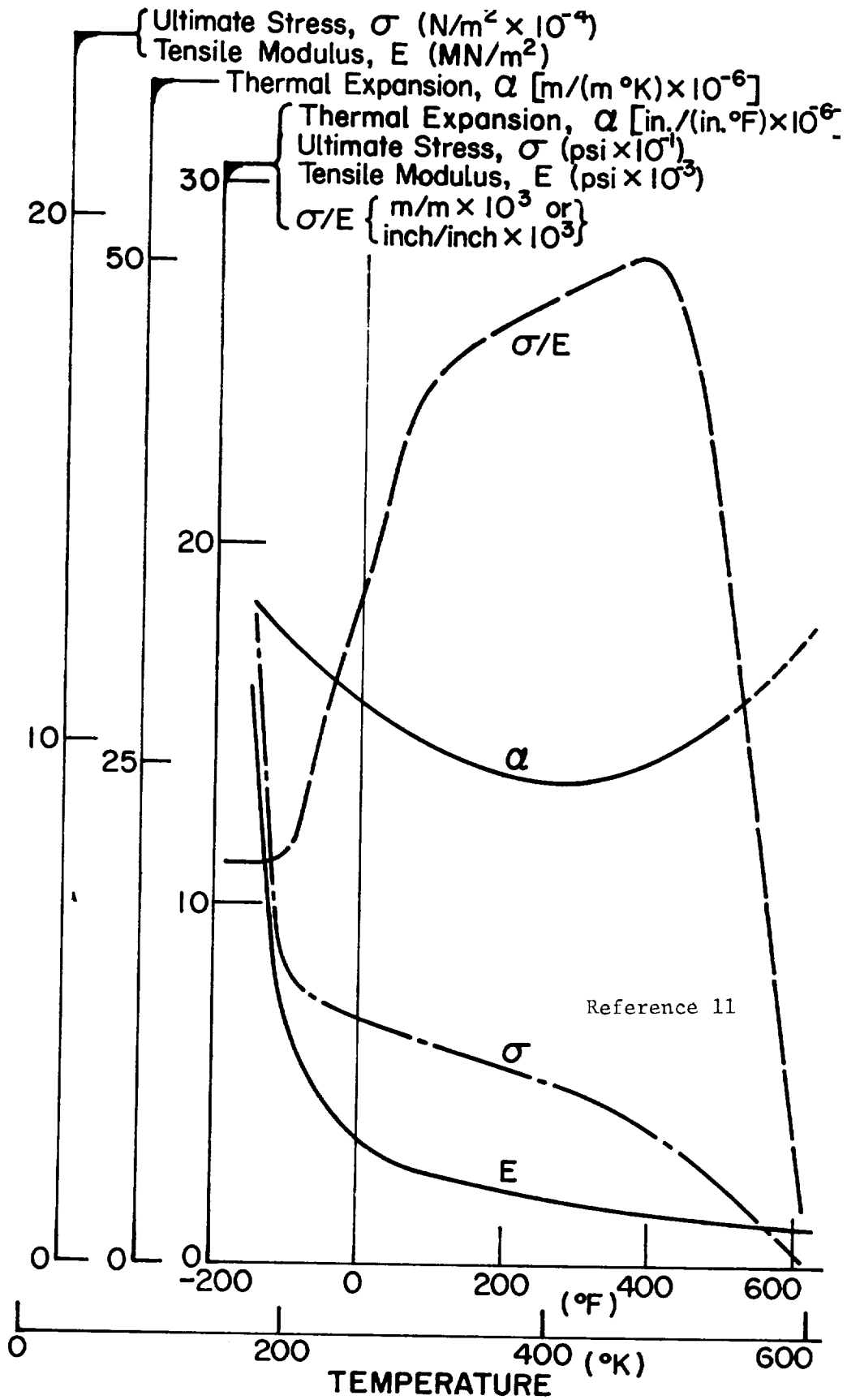


Figure 6.- Thermal-Mechanical Properties of SLA-561 Ablator

6. Aerothermal environment.- The heating rates used in the trajectory studies shall be cold wall rates based on a 311°K (100°F) wall temperature. They shall be predicted using the methods recommended by the Thermal Panel of the Aerothermodynamics Working Group. Specifically, local flow properties will be determined from conical shock relations assuming the surface at the reference point location is an equivalent cone whose half angle is equal to the local body slope plus the angle of attack. Laminar heating rates should be predicted using Eckert's laminar reference relation and turbulent values should be based on Spanding and Chi's skin friction correlation using Colburn's Reynolds analogy factor. Cross flow effects will be included for the entry heating calculations. Boundary layer transition is to be predicted using the correlation parameter of the local Reynolds number based on momentum thickness divided by the local Mach number and the local unit Reynolds number raised to the 0.2 power. Transition onset will be taken to occur when this parameter reaches a value of 10. Fully turbulent flow should be assumed to occur at a location twice the length of the transition onset length. Heating in the transition zone will be computed using a linear variation between the heating levels at the transition onset and fully turbulent points.

#### E. System Definition

1. Thermal protection system (TPS).- The TPS will be an ablator. The ablator will be attached to the primary structure of the vehicle by: (1) direct bonding; (2) direct mechanical attachments with no standoff; or (3) direct mechanical attachments with standoff space between heat shield and primary structure. Mechanically attached heat shielding will consist of a subpanel or backface sheet to which the ablator is direct bonded. Consideration will be given to the observations made in reference 12, a study of the effects and criticality of fabrication-induced flaws.

The following charring ablators will be used within the heating rate ranges indicated in table 3 for single use: SLA-561 for the acreage, and ESA 3560 and ESA 5500 for leading edges and other surface areas where the heating is too severe for SLA-561.

TABLE 3.- ABLATOR APPLICATION

Charring Ablator	Heating Rate Ranges	
	kW/m <sup>2</sup>	Btu/ft <sup>2</sup> -s
SLA-561	0 to 60	0 to 682
ESA 3560	60 to 90	682 to 1023
ESA 5500	90 to 150	1023 to 1700

The ablators will be reusable for an unlimited number of missions in locations where radiation equilibrium temperatures are under 70°K (800°F). Reusable ablators will be direct-bonded to the primary structure.

2. Failure mechanisms.- Failure mechanisms that will be accounted for by analysis and/or tests are as follows:

- 1) Excessive induced strains in TPS due to thermal stresses caused by differential expansion between TPS materials and substructure (TPS in charred and uncharred condition).
- 2) Excessive induced strains in TPS components due to TPS thermal gradients considering attachment to substructure (TPS in charred and uncharred condition).
- 3) Excessive induced strains due to primary structure (or subpanel) straining and/or surface contour changes (TPS in charred or uncharred condition).
- 4) Combination of 1), 2), and 3) above.
- 5) Failure of bond or mechanical attachment between TPS components and substructure due to inadequate venting capability or inadequate strength.
- 6) Excessive temperature of primary structure including effects of gaps, venting provisions, and inflow of hot gas.

The ablator may fail due to imposed deformations exceeding the ablator capability to deform. These deformations may result from differential thermal expansions and contractions with respect to the substructure. They can also be caused by deformation of the supporting structure due to overall loads imposed on

the vehicle or by the application of local pressure causing deflection of the subpanel or supporting primary structure. Deformations occurring during flyback are particularly important because of the decreased deformation capability of the charred ablator material and the detrimental effects of erosion of the vehicle.

3. Service life.- The TPS will not fail during one mission of service life. To assure this life capability, time-dependent failure mechanisms (fatigue and cumulative deformation of subpanel) will be designed for exposure times four times those expected during any one mission. The exposures considered will be acoustics (for fatigue) and static pressure at elevated temperature (for cumulative deformation of subpanel). Degradation of mechanical properties of supporting subpanel structures will be taken into account.

Experience has shown that there is great scatter of life (fatigue, crack, property degradation) among nominally identical structural specimens. The factor of 4 has become common practice during the past ten years.

Fatigue: The TPS will be designed for acoustic decibel levels (figs. 7 and 8) for the specified time periods to assure adequate fatigue life. Predominant acoustic environments are associated with main engine noise at ignition and liftoff, boundary layer turbulence during ascent in the transonic and max q regions, entry hypersonic and supersonic flight, and ABES operation. Predominant vibration environments are associated with main engine characteristics at ignition and liftoff, aerodynamic and main engine characteristics during ascent, OMS and RCS operation in space (negligible significance), aerodynamic characteristics during entry, and ABES operation during atmospheric flight. The acoustic exposures presented in figures 7 and 8 are assumed adequate for the objectives of this study.

Strength analysis: The ablator material will be included in the strength analysis only in the way it may affect lateral panel stiffness and vibrational damping. The ablation material will not be considered load carrying, but shall be included in thermal and mechanical deflection analysis to determine the strain in the ablation material. The subpanel will be capable of carrying design loads without the ablator, and without exceeding the following surface waviness deflection criteria:

$$H = 0.0125L \text{ Limit}$$

where  $L$  = panel (wave) length, and  $H$  = maximum deflection (wave height).

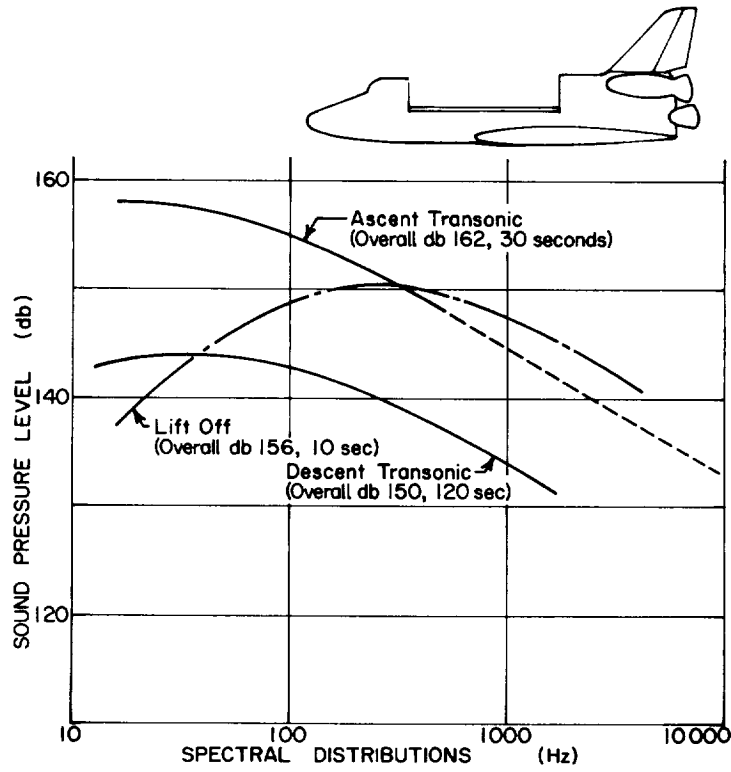


Figure 7.- Overall Acoustic Environments  
Hypersonic Flight, Descent Phase, M=4.0

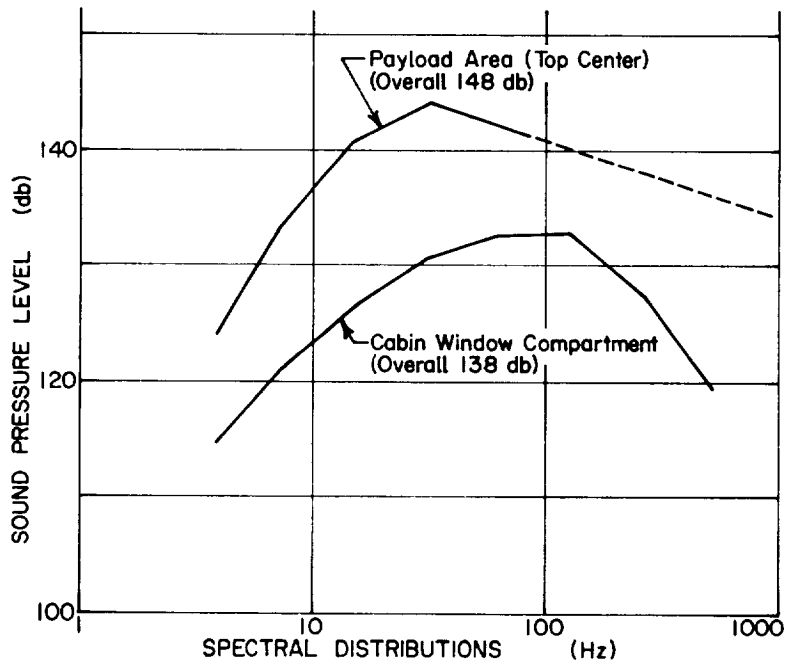


Figure 8.- Local Acoustic Environments

Some subpanels are expected to be of very low stiffness and would result in unacceptable waviness of the surface unless limited by a deflection criteria. The criterion proposed is considered a practical limit to avoid significant increases in aerodynamic heating.

Heat shield temperature at initiation of deorbit: The thermal analyses will consider a range of heat shield temperatures at initiation of deorbit from 172 to 311°K (-150 to 100°F). These temperatures will be assumed constant through the heat shield thickness and adjacent primary structure.

The lower temperature is considered the lowest expected as a result of exposure during ascent and on orbit for most of the vehicle surface. It has been demonstrated that the upper limit can be achieved by use of thermal control coating.

Ablator bondline: Ablator bondline temperature will be restricted to 533°K (500°F) maximum. This is considered the top temperature limit for a silicone adhesive (ref. 13).

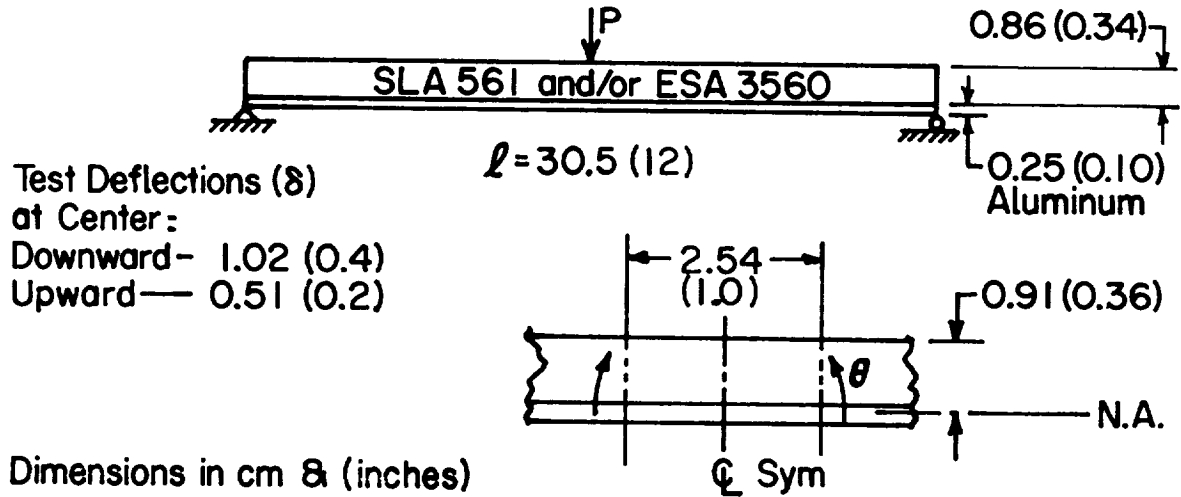
Ablator strain: Maximum strain in the ablator resulting from both mechanical and thermal loading will be 1% for virgin material. For charring and charred material, maximum tension strain will be 0.6%, maximum compression strain will be 1%.

Flexure tests conducted by Martin Marietta's Denver Division during the charring process under the plasma arc have demonstrated that the material has at least the strain capabilities stated above. Table 4 has the details of these tests.

Ablator cracking: Design limit loads or strains will not propagate cracks in the ablator, virgin or charred.

Gap size limitation: The maximum gap between adjacent panels at entry, due to differential thermal expansions or contractions superimposed on manufacturing tolerances, will be controlled to close before the surface temperature reaches 450°K (350°F). Thermal stress restraint to thermal expansion will be taken into account.

TABLE 4.- VIKING FLEXURE TESTS



Panel was 20 cm (8 in.) wide  
(Reference 14)

Strain ( $\epsilon$ )

$$\epsilon = \frac{My(1-\mu^2)}{EI}, M = \frac{Pl}{4}, \delta = \frac{Pl^3(1-\mu^2)}{48EI}$$

$$\epsilon = \frac{12\bar{y} \delta}{l^2}$$

Compressive Strain  $\epsilon_c$

$$\epsilon_c = \frac{12(0.91)(1.02)}{(30.5)^2} = 0.012 \text{ cm/cm (0.012 in./in.) } \underline{\text{No Failure}}$$

Tensile Strain  $\epsilon_T$

$$\epsilon_T = \frac{12(0.91)(0.51)}{(30.5)^2} = 0.006 \text{ cm/cm (0.006 in./in.) } \underline{\text{No Failure}}$$

Char flexure during test heating pulse:

Compressive Strain  $\epsilon_c$  ( $\dot{q} = \text{kW/m}^2 \text{ (Btu/ft}^2\text{-s)}$ )

0 - 30 s  $\dot{q} = 284 \text{ (25)}$   $\epsilon_c = 0 \text{ to } .012 \text{ to } 0$

30 - 70 s  $= 170 \text{ (15)}$   $\epsilon_c = 0 \text{ to } .006 \text{ to } 0$

70 - 110 s  $= 71 \text{ (6.3)}$

Total 110 s

Tensile Strain

0 - 30 s  $\dot{q} = 284 \text{ (25)}$   $\epsilon_t = 0 \text{ to } .006 \text{ to } 0$

30 - 70 s  $= 170 \text{ (15)}$   $\epsilon_t = 0 \text{ to } .003 \text{ to } 0$

70 - 110 s  $= 71 \text{ (6.3)}$

### F. Vehicle Description

The basic vehicle for this study will be the Grumman-proposed Orbiter as submitted in their technical proposal for Phase C/D contract. The Orbiter structural skin will be assumed not to buckle with respect to the interface between heat shield and aluminum substructure. Smearred thickness distributions of the aluminum substructural shell are presented in figure 9. These thicknesses will be used for thermal analyses of this study.

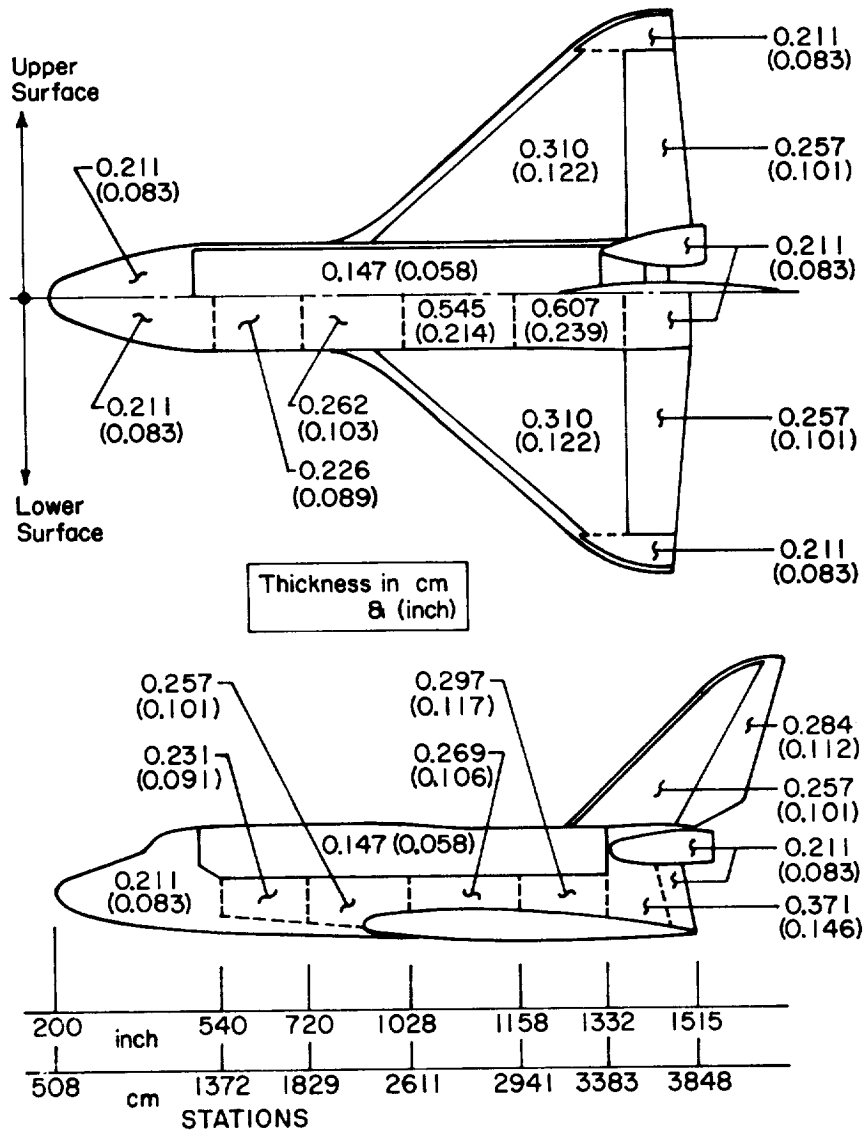


Figure 9.- Typical Orbiter Effective Aluminum Heat Sink Mass

## G. Environments

1. Natural environments.- The TPS, attached to the Orbiter, will be capable of meeting the following requirements (per indicated sections of ref. 15):

- 1) Sand and dust, Sec. 6.2;
- 2) Ozone, Sec. 12.2;
- 3) Humidity, Sec. 3.2;
- 4) Precipitation, Sec. IV;
- 5) Solar Radiation, Sec. II;
- 6) Winds;
- 7) Noncritical sensitivity to on-board fluids;
- 8) Flutter.

Flutter criteria apply to the design of mechanically attached standoff heat shield panels only and will be discussed in detail here. Panels directly attached to the primary structure with no standoff space will be designed to respond to vibratory excitations in combination with the primary structure. The stiffness required to prevent flutter will be a primary criterion for the design of standoff panels. The criteria will take into account the following parameters for each selected surface location on the vehicle:

- |                            |                             |
|----------------------------|-----------------------------|
| - Dynamic pressure         | - Support conditions        |
| - Mach number              | - Curvature                 |
| - Angle of attack          | - Differential temperatures |
| - Panel length/width ratio | - Differential pressures    |
| - Flow angularity          | - Cavity effect             |

Each heat shield panel will be free of destructive flutter at all dynamic pressures up to 1.5 times the maximum local dynamic pressure expected to be encountered at any Mach number within the normal operating envelope and during aborts from the normal operating conditions (ref. 15).

The criteria will be based on the widely used nondimensional panel flutter parameter =  $(\beta E/q)^{1/3} t/\ell$ , modified and corrected according to reference 17.

For preliminary designs involved in the trade studies, two flight conditions (ascent and descent) will be checked under maximum free stream conditions of the dynamic pressure/mach number parameter. Designs found critical by this check will be further analyzed by taking into account local dynamic pressure and local Mach number with the associated local static pressure differential and other corrections stated herein. The panel thickness (t) used in the flutter parameter will be replaced by its equivalent in terms of bending stiffness ( $t = \sqrt[3]{12I}$ ) so that all subpanel requirements will be in common terms.

The resulting expressions for the preliminary check are as follows:

Ascent

Calculate:  $1.5 q/f(m)_{\max}$ .

then  $C_a = E t_B/\ell^3$  from figure 3 of reference 17

and I required =  $\frac{C_a \ell^3}{12E}$

Descent

Similarly, I required =  $\frac{C_d \ell^3}{12E}$

Support conditions and cavity effect will be taken into account by this preliminary check.

The reason for the abbreviated preliminary check is to reduce the time and effort involved. The justification is the expectation that the procedure is conservative for the anticipated designs. Further, more detailed analysis of critical panels is required to minimize the weight penalty due to overly conservative criteria as well as to assure adequate flutter resistance. Also the trade studies can continue while a complete survey of local dynamic pressure/Mach number conditions over the entire flight path is being completed.

The need to consider support conditions is that figure 4 of reference 17 is based on fixed edges and both bending and in-plane (axial) stresses can be avoided by using floating attachments that accommodate differential movement between subpanel and primary structure. Such movements will result from differential thermal and/or load-induced strains.

Cavity effect must be included in the preliminary check because maintaining ambient pressure behind the panel within a specified venting lag is a criteria requirements.

The anticipated panels are square, symmetrically supported so that flow angularity and length/width ratio will not be significant variables.

Literature searches indicate that the maximum free stream condition value of the dynamic pressure/Mach number parameter is not critical for flutter during descent for the standoff panels being considered. During ascent some panels have been found slightly flutter-critical under the maximum free stream condition (dynamic pressure 33 500 N/m<sup>2</sup> (701 psf), Mach 1.155). The required panel stiffness (EI) for this condition is as follows:

$$EI_{\text{required}} = 14.0 (1 - \nu^2) \ell^3$$

where:  $\ell$  = panel length (square panel),  $\nu$  = Poisson's ratio; E = modulus of elasticity, and I = moment of inertia. This criterion is corrected for simple supports. Cavity effect will be negligible with the larger gaps between panels now considered feasible.

The free stream criterion is believed conservative for the standoff panels now being designed for the bottom centerline reference location because of the high pressure induced by the interference flow during ascent. The local dynamic pressure/Mach number parameter is being determined for this location. An additional correction for supports is being considered to take into account the difference between the actual square array of posts and the conventional simple edge supports assumed in the present criterion.

Final flutter criteria for the design of ablator heat shield panels and standoff supports: The practical experience on which most of the existing panel flutter criteria is based has been with aluminum alloy structures, consisting of sheet attached to

stringers and frames. The response of sheet panels to dynamic pressure fluctuations was strongly limited by the induced membrane tension in the sheet. The energy absorbed by bending was relatively very small. The ablator heat shield panels being considered must be designed to avoid axial stressing because of the severe thermal stresses that would otherwise be induced. These "floating" panels must absorb the energy by bending.

The basic flutter criteria of figure 3 in reference 17 has been modified here on the assumption that it is applicable to well designed conventional structures consisting of aluminum alloy sheet, stringers, and frames. The modification attempts to account for the differences on the basis that susceptibility to flutter is a function of panel deflection and panel length with respect to bending. Also, a correction is included to account for the elimination of membrane stressing. Because of the complexity of the input response phenomena, each particular panel/support configuration selected for possible service application will require testing in the final installation to verify the response characteristics. The modified criteria are presented in table 5 using the local dynamic pressures and Mach number of reference 18.

2. Meteoroid.- The TPS will be designed for at least a 0.95 probability of no puncture during the maximum total time in orbit using the meteoroid model defined in Section 2.5.1 of reference 19.

3. Acoustics.- Typical overall sound pressure levels and spectral frequency distributions for specified surface locations are presented in figures 7 and 8. The overall decibel levels and frequency spectra will be varied as appropriate for other surface locations of interest.

Liftoff and ascent transonic acoustics are most critical for subpanels and attachments. Entry (hypersonic) acoustics are applied during the aeroheating flight phase; the outer surface of the heated ablator will not be adversely affected. Descent transonic acoustics are applied to the cooled charred surface of the ablator.

4. Pressures.- The heat shield subpanels and supporting attachments will be designed to withstand the static pressure differentials imposed upon them during mission flights. These differential pressures are both positive (externally applied) and negative (internally applied) between the primary structural shell and the heat shield.

TABLE 5.- MODIFICATION OF THE NONDIMENSIONAL PANEL FLUTTER PARAMETER

Location on vehicle surface, sta m (in.)	q <sub>L</sub> (max)		M <sub>L</sub>	f(M <sub>L</sub> )	C	
	N/(cm) <sup>2</sup>	lb/in. <sup>2</sup>			N/cm	lb/in.
Ascent (subpanel at room temperature)						
Lower centerline						
Sta 10.16 (400)	3.37	4.89	1.10	0.48	18.4	10.5
Sta 20.32 (800)	3.34	4.85	1.22	0.49	17.9	10.2
Upper centerline						
Sta 27.94 (1100)	3.40	4.92	1.16	0.48	18.4	10.5
Fuselage side						
Sta 15.24 (600), W.L. 12.70 (500)	3.66	5.30	1.30	0.51	18.8	10.7
Descent (subpanel at elevated temperature)						
Lower centerline						
Sta 10.16 (400)	0.62	0.90	0.56	0.48	3.33	1.9
Sta 20.32 (800)	0.66	0.96	0.60	0.48	3.68	2.1
Upper centerline						
Sta 27.94 (1100)	0.73	1.05	0.62	0.48	3.86	2.2
Fuselage side						
Sta 15.24 (600) W.L. 12.70 (500)	0.72	1.04	0.62	0.48	3.86	2.2

Note: This modification is necessary to make it applicable to a square ablator heat shield panel floating on four corner posts.

$$I(\text{required}) = \frac{C_s t_B^3}{12} = \frac{C_s t_B^3}{12} \left( \frac{1.5q_L}{f(M_L)} \right) \left( \frac{\ell^3}{E} \right)$$

$$\text{define: } C = \frac{C_s t_B^3}{12} \frac{1.5q_L}{f(M_L)}$$

$$\text{and: } C_s = C_d C_b C_L = 163 \text{ (nondimensional)}$$

since: C<sub>d</sub> = modification for elimination of membrane stress (involving riveted, held and fixed edges to prevent rotation and vertical translation) ref. 20

C<sub>b</sub> = modification from a condition of fixed edges to one of four sides elastically supported with four-corner support, ref. 21

C<sub>L</sub> = modification for bending support across diagonals to an effective length,  $\ell_e^4 = \ell^4 (\sqrt{2})^4$

For heat shield panels mechanically attached to the primary structure with multiple fasteners and no intervening standoff space, the design limit negative pressure shall be 3447 N/m<sup>2</sup> (0.4 psi) during ascent at room temperature, and 2068 N/m<sup>2</sup> (0.3 psi) during ascent at 450°K (350°F). Positive pressures will be transmitted directly to the primary structure so they will not affect the design of the heat shield subpanel or attachments.

For heat shield panels mechanically attached to primary structure with intervening standoff rails or posts, the design limit pressures will be derived as follows for each specified surface location: outer surface pressure minus ambient pressure increased numerically by acoustic pressure as listed in table 6.

During entry the internal pressure will be assumed zero and the heat shield will be designed for the externally applied aerodynamic pressure. Positive pressures will be those associated with the aerodynamic heating analysis for windward surfaces. For leeward surfaces, nominal positive pressures will be applied. Typical entry pressures are listed in table 7 for the different surface locations of the vehicle.

TABLE 6.- EQUIVALENT STATIC LOADS FOR ACOUSTIC PRESSURES

Condition	kN/m <sup>2</sup> *	psi*
Maximum q or $\beta$	6.2	0.9
End boost	None	None
Orbit ignition	None	None
Entry and descent	5.5	0.8
2½ g pullout	None	None
Landing	None	None
Liftoff (X/L = 0.00 to 0.30)	9.7 overpressure	1.4 overpressure
(X/L = 0.30 to 0.70)	11.0 overpressure	1.6 overpressure
(X/L = 0.70 to 0.90)	15.9 overpressure	2.3 overpressure
(X/L = 0.90 to 1.00)	22.1 overpressure	3.2 overpressure

\*3.3 RMS Values (Max)

TABLE 7.- TYPICAL MAXIMUM LOCAL STATIC PRESSURES DURING ENTRY HEATING

Vehicle surface location	Optimum ablator trajectory		Reusable TPS trajectory	
	kN/m <sup>2</sup>	psi	kN/m <sup>2</sup>	psi
Fuselage				
Forward centerline	6.9	1.00	6.5	0.95
Aft centerline	5.5	0.80	5.2	0.75
All upper surfaces	1.4	0.20	1.4	0.20
Wing bottom	5.5	0.80	5.2	0.75
Leading edges	11.0	1.60	9.7	1.40
Nose cap	19.3	2.80	16.5	2.40

During transonic and subsonic flyback, both positive and negative pressure differentials will be considered in the heat shield design. These design pressures will be derived from aerodynamic flow analysis and consideration of heat shield venting characteristics. Aerodynamic shear forces on the charred ablator surfaces will be taken into account.

Standoff panel pressure sources: Standoff heat shield panels are much more vulnerable to pressures than panels attached to the primary structure with no intervening space. The following two paragraphs explain why this is true.

The volume of air behind the standoff heat shield is so large that practical venting capability cannot relieve the differential pressures resulting from rapid fluctuations of external pressure. The very small volume of air pressure behind directly attached panels with no standoff can be relieved by practical heat shield venting capability. Also, substantial pressure relief will result from volume increases due to panel deflections. This volume is significant when compared to the initial, installed volume of space attributable to inherent waviness in the panel and/or the structural surfaces. Negative pressures due to any leakage of internal pressure from the vehicle compartments will be negligible for mechanically-attached panels because the leakage rates are well within practical venting capabilities.

Standoff heat shield panels are susceptible to aeroelastic instability in the form of flutter and dynamic response to acoustic loading because they are capable of reversible elastic deflections. Heat shield panels without standoff will be designed to respond in combination with the primary structure, and the attachment loading is determined accordingly. The attachment loading is the inertia force required to make the heat shield panel and the primary structure respond as a unit. This force has been estimated to be from 15 to 20 g (typical), with a  $3\sigma$  value of 50 g. For the typical panel weighing about  $71.8 \text{ N/m}^2$  ( $1.5 \text{ lb/ft}^2$ ), 50 g is equivalent to a negative pressure of  $3.5 \text{ kN/m}^2$  (0.5 psi). During descent the vibratory exposures are significantly less severe than during liftoff and ascent. So  $2.1 \text{ kN/m}^2$  (0.3 psi) is estimated to be a reasonable design limit. For the reasons discussed above, no venting lag need be superimposed on these inertia forces.

Standoff panel design pressures: The design limit pressures for standoff heat shield panels presented in table 8 include ascent and descent. Pressures associated with entry heating are not critical for subpanel design because the subpanels do not reach maximum temperature until much higher pressures are imposed at the lower altitudes. Both ascent and descent conditions must be considered because either may be critical. The higher ascent pressures coupled with room temperature strength properties must be compared to the lower descent pressures coupled with reduced strength properties at maximum temperature.

The ascent pressures for the specified fuselage locations were derived from Ames Pressure Test Number 608, references 22 and 23. The derivation included two maximum  $q\alpha$  conditions and one maximum  $q\beta$  condition. The envelope of these conditions for the top and bottom centerlines of the fuselage surface is plotted in figure 10. Leading edge steady-state pressures were assumed to be 0.8 of the free stream dynamic pressure at maximum  $q$ . Equivalent acoustic panel pressures at liftoff are based on data presented in references 24 and 25.

The descent pressures are considered practical minimums. Because of the relatively low free stream dynamic pressure [ $6.0 \text{ kN/m}^2$  (125 psf) maximum at Mach 0.834 as compared to ascent maximum of  $35.4 \text{ kN/m}^2$  (739 psf) at Mach 0.86], coupled with a low angle of attack (less than  $10^\circ$ ), the aerodynamic steady-state pressures are generally less than  $7.0 \text{ kN/m}^2$  ( $1 \text{ lb/in.}^2$ ) on the fuselage. A numerical minimum pressure of  $3.5 \text{ kN/m}^2$  ( $0.5 \text{ lb/in.}^2$ ) has been somewhat arbitrarily established.

TABLE 8.- DESIGN LIMIT PRESSURES FOR STANDOFF HEAT SHIELD PANELS

Surface Location	Ascent at room temperature						Descent at elevated temperature					
	$\Delta P \pm$ acoustic	Positive		Negative		$\Delta P \pm$ acoustic	Positive		Negative			
		(a)	kN/m <sup>2</sup>	psi	kN/m <sup>2</sup>		psi	kN/m <sup>2</sup>	psi	kN/m <sup>2</sup>	psi	
Fuselage lower centerline Sta 400	+ 3.1+0.9	BF	27.6	4.0		$\Delta P \pm 0.8$	13.8	2.0				
-	1.1+0.9	BF			17.2	$\Delta P \pm 0.8$			13.8	2.0		
Sta 800	+ 2.1+0.9	BF	20.7	3.0		$\Delta P \pm 0.8$	13.8	2.0				
-	Acoustics	LO			17.2	$\Delta P \pm 0.8$			13.8	2.0		
Fuselage upper centerline Sta 1100	+ 1.1+0.9	BF	13.8	2.0		$\Delta P \pm 0.8$	13.8	2.0				
-	$\Delta P \pm 0.9$	BF			17.2	$\Delta P \pm 0.8$			13.8	2.0		
Fuselage side Sta 600, WL 500	+ 1.1+0.9	BF	13.8	2.0		$\Delta P \pm 0.8$	13.8	2.0				
-	2.6+0.9	BF			27.6	$\Delta P \pm 0.8$			13.8	2.0		
Leading edge wing BL 314 Sta 1000	+ 3.5+2.5	BF	41.4	6.0		$\Delta P \pm 0.8$	17.2	2.5				
-	3.5+2.5	BF			44.8	$\Delta P \pm 0.8$			13.8	2.0		
Tail, WL 740 Sta 1395	+ 3.5+1.4	BF	41.4	6.0		$\Delta P \pm 0.8$	17.2	2.5				
-	0.0+3.5	LO			44.1	$\Delta P \pm 0.8$			13.8	2.0		

<sup>a</sup> BF indicates a maximum q condition (boost flight); LO indicates liftoff 3.3 g equivalent acoustic pressure;  $\pm 13.8$  kN/m<sup>2</sup> (2.0 psi) is considered a practical minimum;  $\Delta P > 6.9$  kN/m<sup>2</sup> (1.0 psi) (numerically) for ascent and 3.4 kN/m<sup>2</sup> (0.5 psi) for descent.

478 Ascent Configuration Orbiter Fuselage

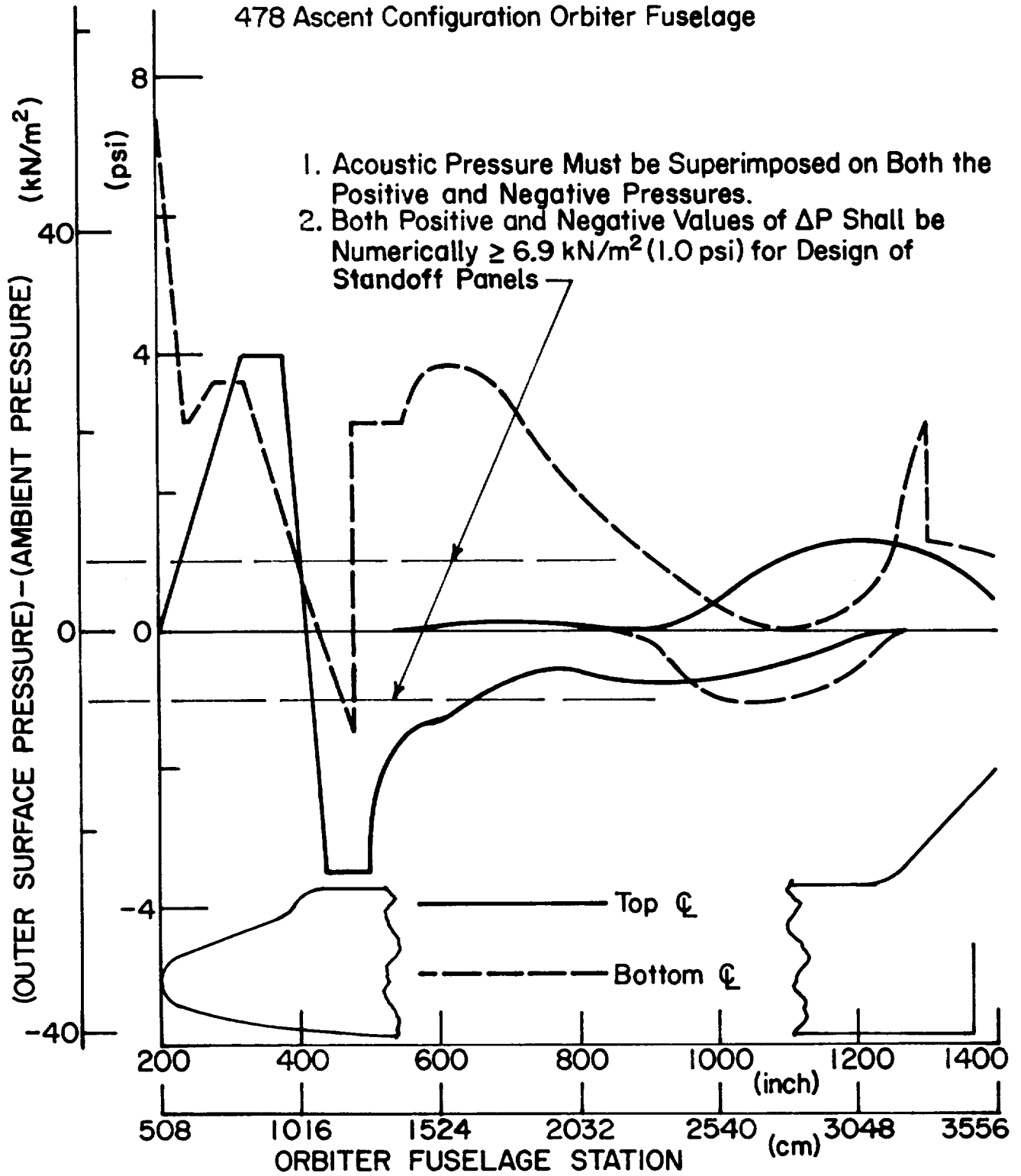


Figure 10.- Aerodynamic Pressure Distributions, Outer Surface Envelope

## H. Input Variable Uncertainties and Design Factors

Factors of safety for areas of design which are not amenable to contemporary prediction methods shall be estimated in a rational manner. Design factors for predictable regions will be lower than those above. Both shall be applied to nominal heating rates to produce limit heating rates.

Derivation of limit aerodynamic heating rates and pressures will differentiate with respect to vehicle surface (windward, leeward, body, aerodynamic surfaces, movable surfaces, covers, and leading edges). Minimum limit values will account for all dispersions and uncertainties associated with the particular application.

1. Safety factors and design factors.- Safety factors on loads and pressures are presented in table 9. The safety factor for prelaunch through deorbit is based on engineering practice developed for boosters and spacecraft. The safety factor for entry and atmospheric flight is that commonly used in the design of aircraft.

2. Input variable uncertainties.- Statistical methods will be used to establish TPS integrity. The results of previous statistical studies are expressed in terms of design limit factors for different surface locations.

3. Combined loads.- The mechanical external, thermally induced, and internal pressure limit loads will be combined to determine the combined limit load. The combined limit load will be equal to or greater than the sum of the nominal loads plus three combined standard deviations. The combined standard deviation will be derived by combining the standard deviations of the respective loads (external, thermal, pressure) on the basis of the root sum squaring principle. The combined ultimate load will be equal to the combined limit load multiplied by the ultimate safety factor.

TABLE 9.- SAFETY FACTORS ON LOADS AND PRESSURES

Flight phase	Safety factor (ultimate/limit)
Prelaunch through deorbit	1.4
Entry and atmospheric flight	1.5

## I. Interface Compatibility

1. Provision for thermal expansion.- TPS installations will be physically and functionally compatible with the structural surface and with the aerodynamic boundary layer. Differential thermal expansion effects will be adequately taken into account. Provisions for sealing to avoid high enthalpy gas flow will be made, when necessary. The interfaces will be designed to withstand aerodynamic, acoustic, vibration, and shock loadings under all expected operating environments. The structure interface will be designed so that panel flutter is prevented. The evaluation will consider structural panel size and edge supports. The method of attachment of TPS to structure (bonding, mechanical means, or combination) will be compatible with interface conditions.

Control of gaps between adjacent ablator panels: Gaps (including tolerances) between adjacent ablator panels, when installed on the vehicle, will be designed to be compatible with the following requirements: (1) venting during ascent; (2) limitation of hot gas flow to primary structure during aerodynamic heating; (3) venting during descent through subsonic flight; and (4) Gap sealant material to assure retention of limited resiliancy sealants. During ascent, the need to design the subpanel for vent-lag internal pressure buildup is dependent on the width of the gap. Sufficient gap to permit full venting would result in a lighter subpanel.

2. Substructure compatibility.- The compatibility requirements of the substructure will be the physical, mechanical, and thermal properties of the structural material, surface contour, axial and bending strains induced by external loads and/or differential thermal expansion.

3. TPS compatibility.- The compatibility requirements of the TPS will be the physical, mechanical, and thermal properties required to sustain the forces, induced strains, and environments throughout all mission life phases and limit the substructure temperature to 450°K (350°F) maximum.

4. Thermal compatibility.- Thermal design will protect against the effects of (1) orbital fluxes; (2) ascent and entry heating; and (3) interference heating effects.

#### J. Quality

Inspection and certification requirements as they effect heat shield costs will be determined.

#### K. Maintainability

The number of different size TPS panels will be minimized. Access to and arrangement of TPS panels will be considered to allow for an easy and timely inspection and repair or replacement. TPS panel design will consider all features that will minimize maintenance manhours expended for removal and replacement of damaged areas. Finally, the replacement procedure will be consistent with the required (160 hour, 114 day) turnaround time with respect to adequate inspection, repair, and proper insulation.

## III. FLIGHT ENVIRONMENT

### A. Trajectory Analysis

1. Introduction.- Several trajectory trade studies were performed to provide the design criteria for an ablative heat shield. The results of the Phase B Shuttle studies, the Martin Marietta-Grumman proposal studies, MMC past experience, and available NASA data were reviewed for applicability to the ablative heat shield design criteria.

Entry trajectories were shaped to take advantage of the ablative heat shield concept, whereas previous studies shaped trajectories for a Reusable Surface Insulation (RSI). The methodology of this analysis is presented in Appendix A.

The vehicle configuration for these studies was the Grumman Corporation Configuration 619. The total entry weight was 93 000 kg (205 000 lb) including a payload weight of 18 000 kg (40 000 lb). The resulting hypersonic glide parameter ( $W/C_{L,S}$ ) was 4980 N/m<sup>2</sup> (104 psf). The aerodynamic coefficients and trim capabilities corresponding to a forward center of gravity condition were used.

Three basic missions were evaluated to define the worst case design environment. These missions are:

- 1) 2040 km (1100 n. mi.) crossrange from a 185 km (100 n. mi.) polar orbit;
- 2) 1480 km (800 n. mi.) crossrange from a 185 km (100 n. mi.), 55° inclination orbit;
- 3) 1480 km (800 n. mi.) crossrange from a 930 km (500 n. mi.), 55° inclination orbit.

2. Trajectory shaping approach.- The trajectory shaping approach was to tailor the heating rate history to take advantage of the ablative heat shield characteristics. The characteristics of the ablative heat shield are such that it can withstand a relatively high heat rate for a short period of time. The magnitude of the maximum allowable heat rate depends on the material selected for use. The entry trajectory shaping approach was to attain a prescribed heating rate as early as possible upon entry into the atmosphere and follow that limit until the acceleration limit was reached. At this time, the acceleration limit was followed.

until it was necessary to deviate from the limit to achieve the desired crossrange. In this manner, the heat rate-versus-time profiles approximated square wave forms. This technique provides the minimum total heat and entry time that can be achieved for a given set of heating rate and acceleration limits. Figure 11 shows the various trajectory segments in the altitude-velocity space.

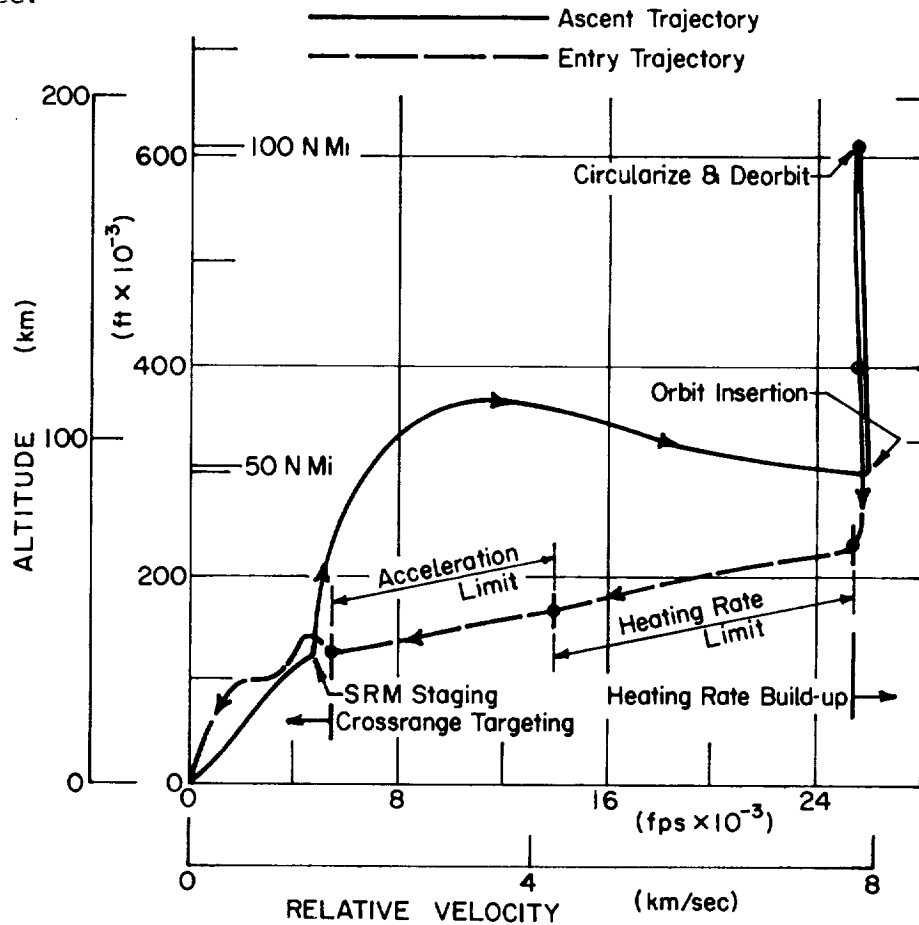


Figure 11.- Trajectory Shaping Philosophy

The angle of attack was held constant at  $30^\circ$  from the start of entry until Mach 5, at which time a transition was made to the angle of attack that yields the maximum lift-to-drag ratio. Bank angle modulation was used to produce the desired trajectory profile in terms of heating rate and acceleration limits and also to achieve the required cross range. The constant angle of attack during the high heating rate and acceleration portion of the trajectory simplifies the vehicle design requirements in terms of heat shield and aerodynamic trim capability in the high Mach number region.

3. Results of trajectory trade studies.- Several trajectory trade studies were conducted to determine the optimum design conditions for the ablative heat shield. These studies were:

- 1) Deorbit propellant plus heat shield weight trajectory optimization;
- 2) Low density class ablator trajectory optimization;
- 3) Minimum total heat with only a g-constraint trajectory optimization;
- 4) Minimum heating rate, nominal mission trajectory optimization, with design trajectory total heat constraint.

The results of the trajectory trade studies are summarized as follows:

- 1) The 185-km (100 n. mi.) polar orbit with 2040-km (1100 n. mi.) crossrange is the critical mission in terms of total heat;
- 2) The heat shield weight plus the deorbit propellant weight is minimized at the smallest entry flight path angle magnitude;
- 3) The entry time and total heat are both minimized by inverted entry;
- 4) Bank angle modulation to follow the heating rate and acceleration limits minimizes entry time and total heat;
- 5) The minimum peak heating rate is  $145 \text{ kW/m}^2$  ( $12.8 \text{ Btu/ft}^2\text{-s}$ ) for this configuration.

**Mission selection:** The relevant mission constraints were reviewed in terms of orbit altitude and crossrange. Three missions were selected to define the heat shield design criteria. These missions are listed on page 34.

Mission 1 is for a once-around mission in which the vehicle ascends into a 185-km (100 n. mi.) circular polar orbit and performs a deorbit maneuver that results in the vehicle returning to the launch site on the first pass. This mission imposes the largest crossrange requirement, 2040 km (1100 n. mi.).

Missions 2 and 3 represent entry orbits for normal mission termination. Mission 2 is a 185-km (100 n. mi.) altitude circular orbit targeted to a crossrange of 1480 km (800 n. mi.), which is the crossrange required for a first pass return for a 55° inclination orbit. Mission 3 is a high-altitude orbit, which represents direct entry from a high-energy orbital mission. Note that a crossrange of less than 1480 km (800 n. mi.) does not impose any greater total heat input than does the 1480 km (800 n. mi.) crossrange condition. As a result, any mission that did not require the full 1480 km (800 n. mi.) crossrange would be achievable with no design impact.

Entry trajectories for all three missions were shaped to the following parameter upper bounds: 2.5 g acceleration 300 kW/m<sup>2</sup> (26 Btu/ft<sup>2</sup>-s), bottom centerline heating rate at the reference point, and 250 N/m<sup>2</sup> (5 lb/ft<sup>2</sup>) shear force. The trajectory that produced the most severe heating under these conditions was selected as the baseline trajectory.

The results of the above three entry trajectories are summarized in table 10 and figures 12 through 17.

Entry from a 185-km (100 n. mi.) orbit at 55° inclination results in a considerably lower total heat and entry time than a comparable polar entry, as seen in figures 12 through 15. This fact results from the lower relative velocity at entry due to the effect of the earth's rotation and the reduced crossrange requirement.

Entering from a 930-km (500 n. mi.) orbit requires a higher entry flight path angle to avoid skip-out. This condition also requires more deorbit  $\Delta V$ , and therefore considerably more deorbit propellant. Figures 16 and 17 present the results of this trajectory.

The combined effects of the earth's rotation and the smaller crossrange requirement for the 55° inclination result in a less severe entry environment than the polar entry from 185 km (100 n. mi.). Therefore, the polar mission has been selected as the baseline for the heat shield design.

The altitude versus velocity profile and the heating rate and g-level time histories are shown in figures 12 and 13 for the baseline trajectory.

TABLE 10.- SUMMARY OF ENTRY TRAJECTORIES

	Mission 1	Mission 2	Mission 3
Orbit conditions			
Inclination, deg	90	55	55
Altitude, km (n. mi.)	185 (100)	185 (100)	930 (500)
Entry conditions			
Altitude, km (1000 ft)	121.9 (400)	121.9 (400)	121.9 (400)
Flight path angle (relative), deg	-0.893	-0.879	-1.971
Flight path angle (inertial), deg	-0.893	-0.850	-1.907
Velocity (relative), m/s (ft/s)	7830 (25 718)	7540 (24 761)	7780 (25 533)
Velocity (inertial), m/s (ft/s)	7830 (25 718)	7800 (25 620)	8040 (26 392)
Deorbit			
Propellant weight, kg (lb)	2300 (5055)	2080 (4581)	7400 (16 286)
$\Delta V$ , m/s (ft/s)	74 (243)	67 (220)	232 (762)
Entry summary			
Max heating rate, kW/m <sup>2</sup> (Btu/ft <sup>2</sup> -s)	300 (26.4)	300 (26.4)	300 (26.4)
Max acceleration, g	2.5	2.5	2.5
Crossrange (to 15.24 km; 50 000 ft), km (n. mi.)	2040 (1100)	1480 (800)	1800 (970)
Downrange (15.24 km; 50 000 ft), km (n. mi.)	6500 (3512)	6460 (3496)	5790 (3130)
Total heat, MJ/m <sup>2</sup> (Btu/ft <sup>2</sup> )	216.5 (19 086)	194.9 (17 170)	212 (18 702)
Panel weight, kg (lb)	9240 (20 315)	8390 (18 471)	8190 (18 028)
Time (121.92 to 15.24 km; 400 000 to 50 000 ft), s	1536	1438	1349
Time ( $\dot{q}_{max}$ to 15.24 km or 50 000 ft), s	1139	1003	1069
Time above $\dot{q} = 22.7$ kJ/m <sup>2</sup> (2 Btu/ft <sup>2</sup> ), s	895	855	905

100 N Mi (185 km) Polar Orbit Baseline

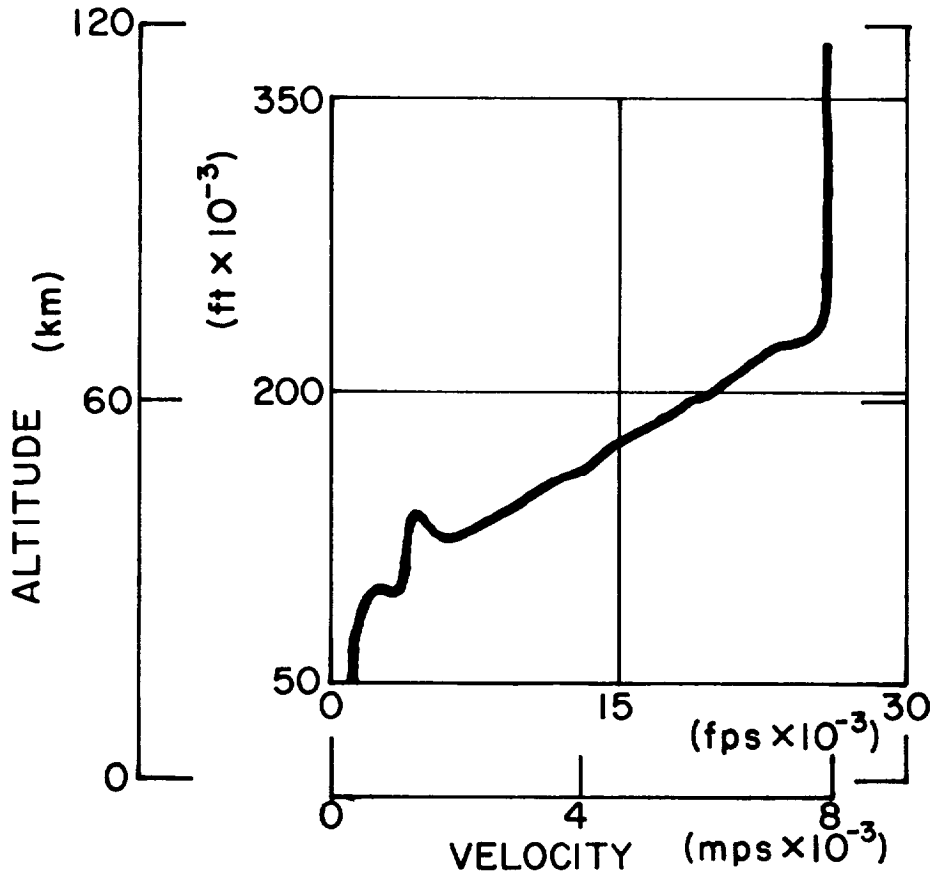


Figure 12.- Baseline Trajectory, Altitude

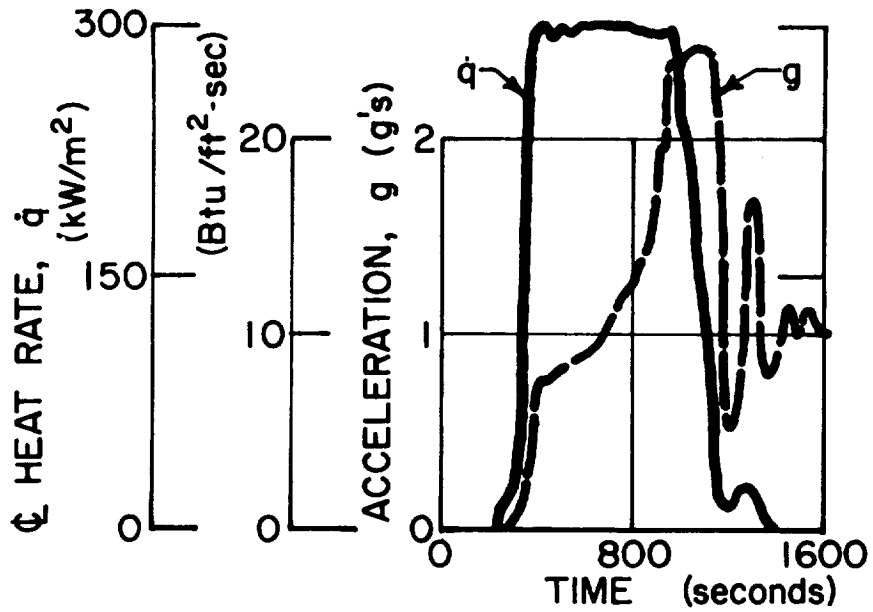


Figure 13.- Baseline Trajectory, Acceleration and Heating Rates

100 N Mi (185 km) Orbit, 55° Inclination

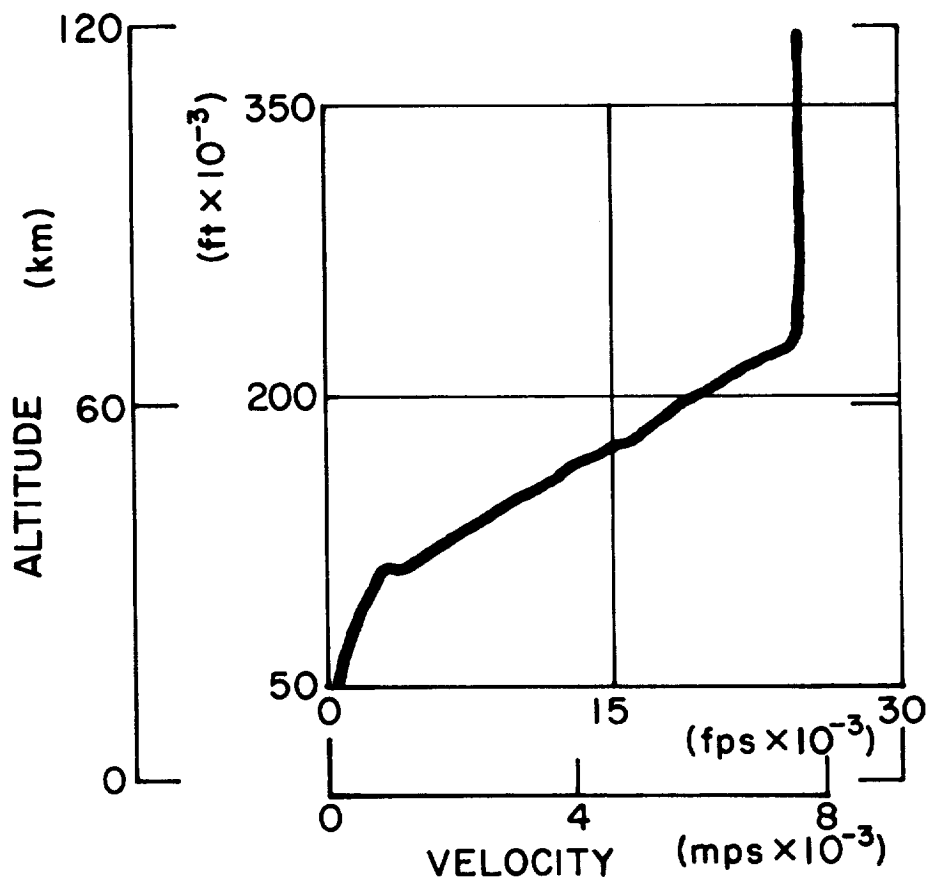


Figure 14.- Altitude for 185 km (100 n. mi.), 55° Trajectory

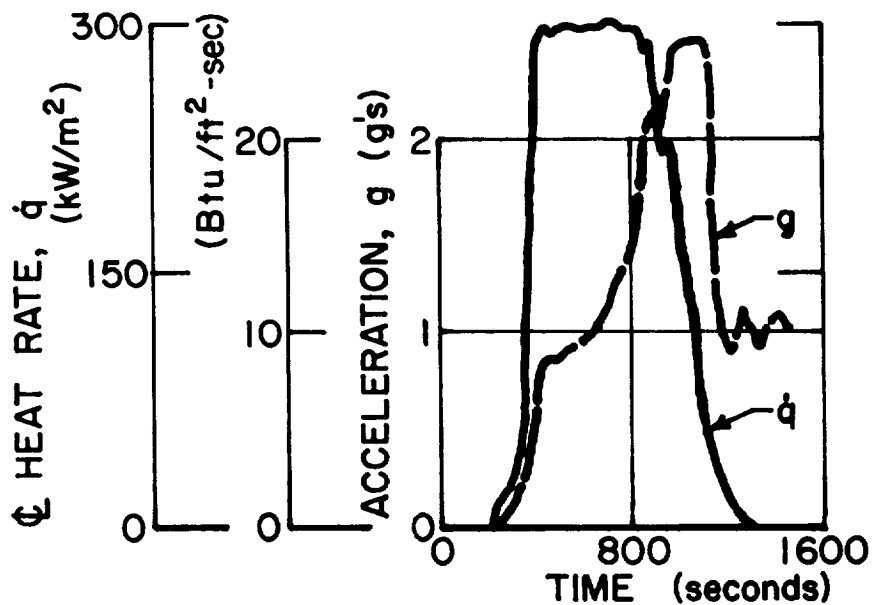


Figure 15.- Acceleration and Heating Rate for 185 km (100 n. mi.), 55° Trajectory

500 N Mi (930 km) Orbit, 55° Inclination

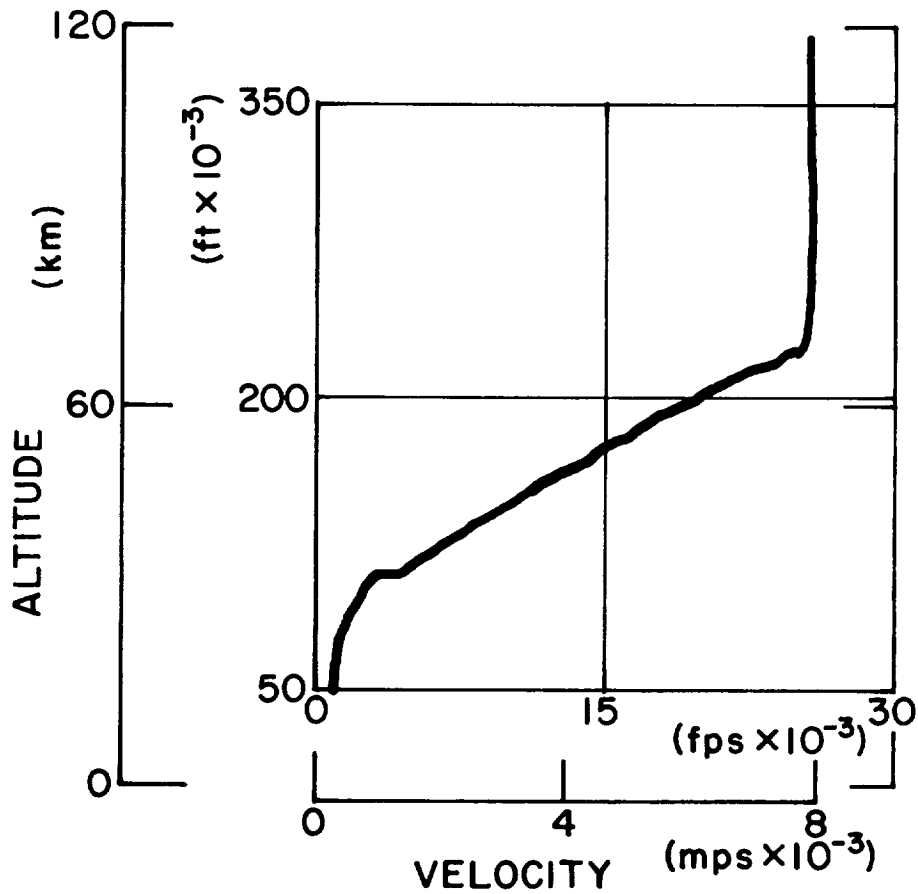


Figure 16.- Altitude for 930 km (500 n. mi.), 55° Trajectory

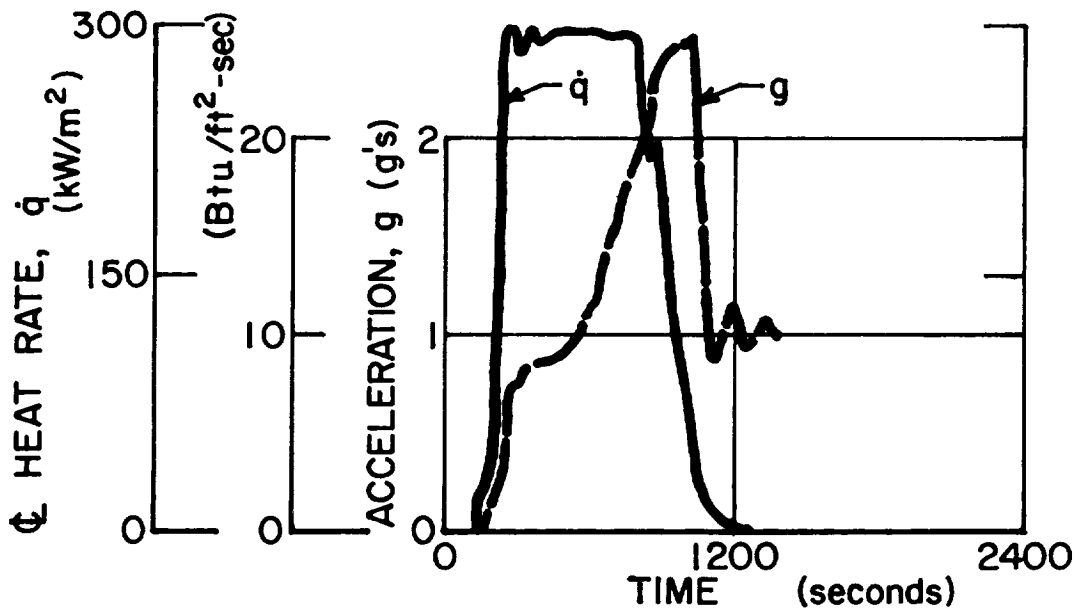


Figure 17.- Acceleration and Heating Rate for 930 km (500 n. mi.), 55° Trajectory

Entry flight path angle selection: The results of this study indicate that the entry conditions at the minimum allowable path angle produce the lightest total system weight in terms of deorbit propellant weight plus heat shield weight. This same conclusion was reached in previous studies at Mattin Marietta and NASA/LRC (ref. 26). The entry path angle should be selected as the minimum value allowed by the skip-out limit. The skip-out limit for this vehicle entering inverted (bank angle of  $180^\circ$ ) from a 185-km (100 n. mi.) polar orbit is approximately  $-0.55^\circ$ . Applying three-sigma guidance errors plus atmospheric and vehicle dispersions of  $\pm 0.34^\circ$  to the entry path angle results in a nominal value of  $-0.89^\circ$ . This value of path angle has been selected for the base-line trajectory.

The heat rate for the trajectories in this study was limited to  $300 \text{ kW/m}^2$  ( $26 \text{ Btu/ft}^2\text{-s}$ ) at the reference point. After the heat rate limit is reached, the trajectories follow the same altitude-versus-velocity profile until deviating from the acceleration limit to achieve the required crossrange. Thus, the only effects that the entry conditions have on the heat shield weight result from: (1) the time to reach the peak heating rate; and (2) the total heat accumulated up to this time. Figure 18 shows that the time required to reduce the altitude from 121.9 km (400 000 ft) to 91.4 km (300 000 ft) (initial heat rate calculation) increases rapidly as the magnitude of the entry path angle is reduced. Figure 19 shows that the time interval between the start of the heating rate calculations 91.4 km (300 000 ft) and the heat rate limit of  $300 \text{ kW/m}^2$  ( $26 \text{ Btu/ft}^2\text{-s}$ ) also increases rapidly as entry path angle decreases. The total heat input at the time the heat rate reaches  $300 \text{ kW/m}^2$  ( $\text{Btu/ft}^2\text{-s}$ ) is presented in figure 20. The change in deorbit propellant weight is shown in figure 21. Figures 18 and 21 show that increasing the entry path angle from  $-0.55^\circ$  to  $-1.1^\circ$  would reduce the entry time after the onset of significant heating by 68 s and the total heat input by  $2.8 \text{ MJ/m}^2$  ( $250 \text{ Btu/ft}^2$ ). However, an increase in deorbit propellant of nearly 1370 kg (3000 lb) would be required to change the entry angle by that amount.

Initial bank angle selection: The initial value of bank angle at the start of entry was studied to determine the value that would allow the smallest entry angle magnitude without skip-out and still provide the required crossrange.

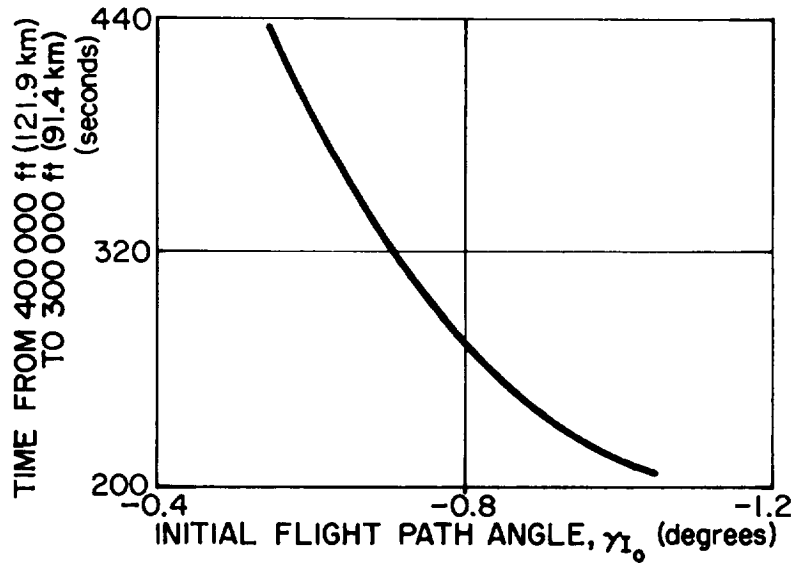


Figure 18.- Effect of  $\gamma_{I_0}$  on Entry Time to 91.4 km (300 000 ft)

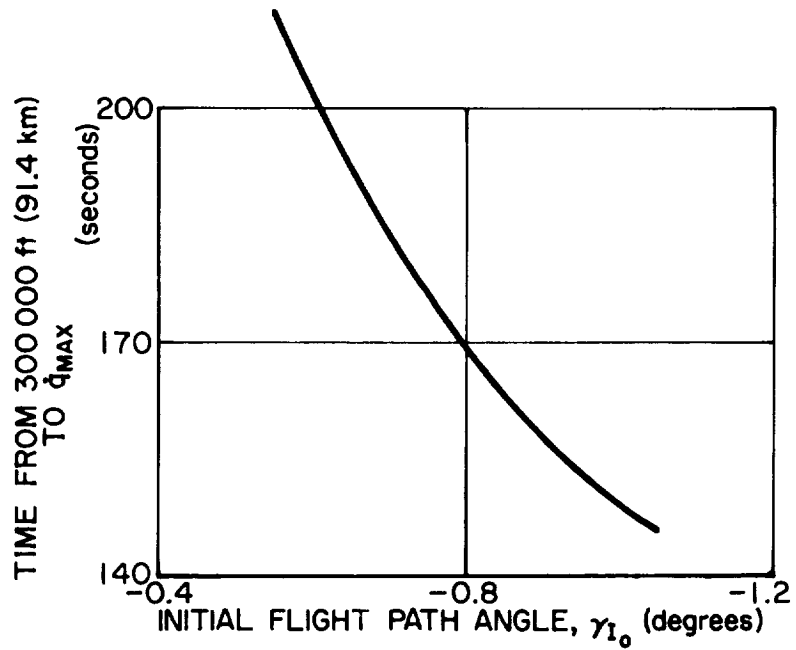


Figure 19.- Effect of  $\gamma_{I_0}$  on Entry Time of Interval between 91.4 km (300 000 ft) and  $\dot{q}_{max.} = 300 \text{ kW/m}^2$  (Btu/ft<sup>2</sup>-sec)

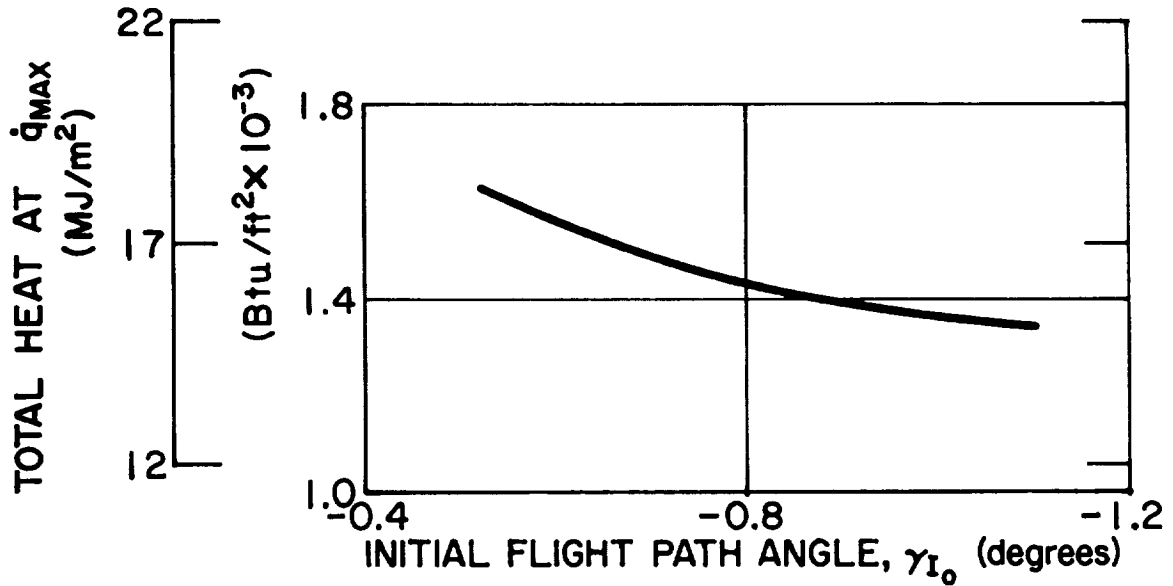


Figure 20.- Total Integral of  $\dot{q} \Delta T \dot{q}_{max.} = 300 \text{ kW/m}^2$   
 (26 Btu/ft<sup>2</sup>-sec) as a Function of  $\gamma_{I_0}$

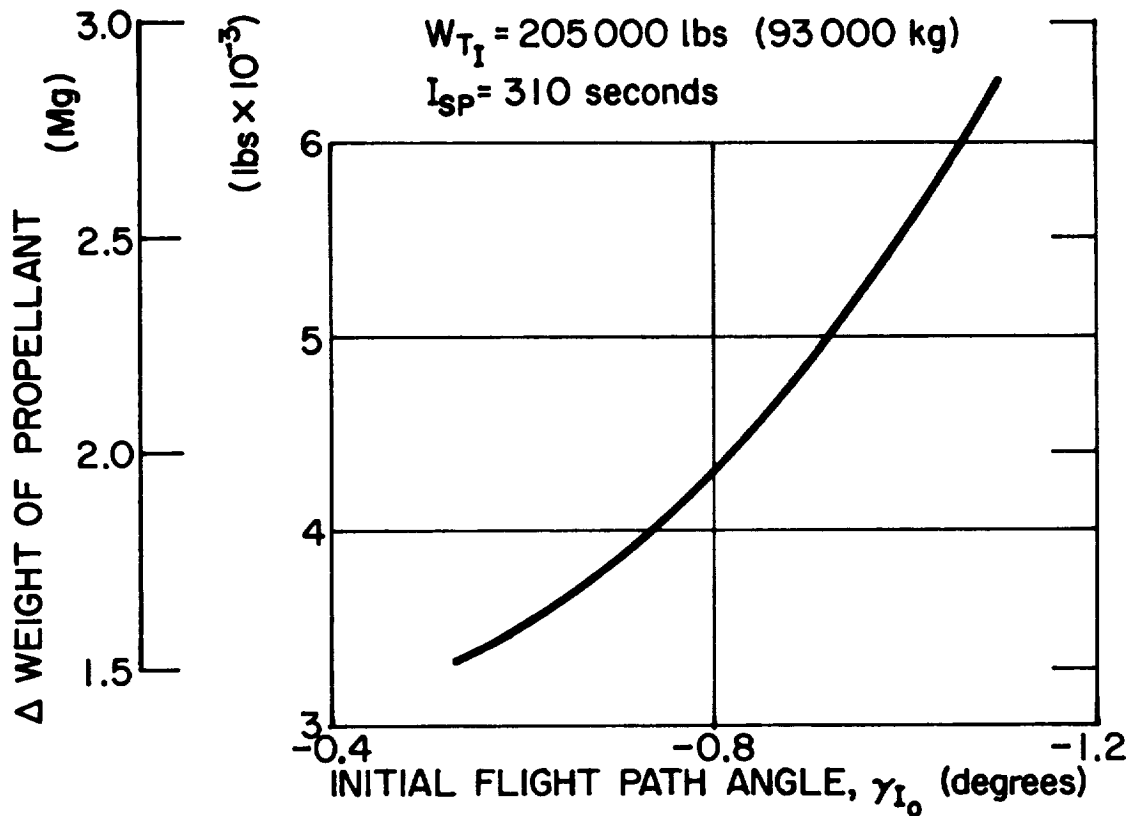


Figure 21.- Change in Deorbit Propellant Caused by  
 Different  $\gamma_{I_0}$  Degrees

Figures 22 through 24 show the effect of the initial bank angle on conditions at the time the heating rate maximum  $\dot{q}_{\max}$  of  $300 \text{ kW/m}^2$  ( $26 \text{ Btu/ft}^2\text{-sec}$ ) is reached. Once this rate is attained, the trajectory produces a constant heating rate until  $2.5 \text{ g}$  is reached. This acceleration limit is maintained as long as possible to minimize reentry time by modulating bank angle. At the latest time possible, the trajectory stops controlling the acceleration limit and optimizes the bank angle history to achieve the required crossrange. Once the desired heating rate value is reached, the trajectories will be identical in the altitude velocity space until they deviate from the acceleration limit to achieve the proper crossrange at  $15.2\text{-km}$  ( $50 \text{ 000 ft}$ ) altitude. The differences in total heat, entry time, and panel weight between the different initial bank angles result from: (1) variations of time, heading, and cross range before the heating rate limit is reached; and (2) the time (or altitude) at which the acceleration limit must be left to achieve the required crossrange. Since an initial bank angle of  $90^\circ$  provides more crossrange and heading change at the point when the heating rate limit is reached, these trajectories can follow the acceleration limit to a lower altitude and still obtain the required crossrange.

Figures 22 and 23 show the effect of the initial bank angle on heading angle and crossrange at  $\dot{q}_{\max}$ . The slopes of the curves become increasingly steep as they approach an initial bank angle of  $90^\circ$ , showing the better crossrange advantage for this angle. However, figure 24 shows that the entry time also increases rapidly as the initial bank angle approaches  $90^\circ$ . Time is considered from  $91.4 \text{ km}$  ( $300 \text{ 000 ft}$  since heating rate is insignificant above this altitude). Comparing the two bank angle extremes ( $90^\circ$  and  $180^\circ$ ), the combined effects of time, heading angle, and crossrange at  $\dot{q}_{\max}$  on the reentry time and crossrange become apparent.

Figure 25 shows that inverted entry will achieve the required crossrange in about  $20 \text{ s}$  less time than a  $90^\circ$  initial bank angle. Figure 26 shows that an initial bank angle of  $180^\circ$  results in a reduction of over  $3.4 \text{ MJ/m}^2$  ( $300 \text{ Btu/ft}^2$ ) in total heat at  $2040 \text{ km}$  ( $1100 \text{ n. mi.}$ ) crossrange.

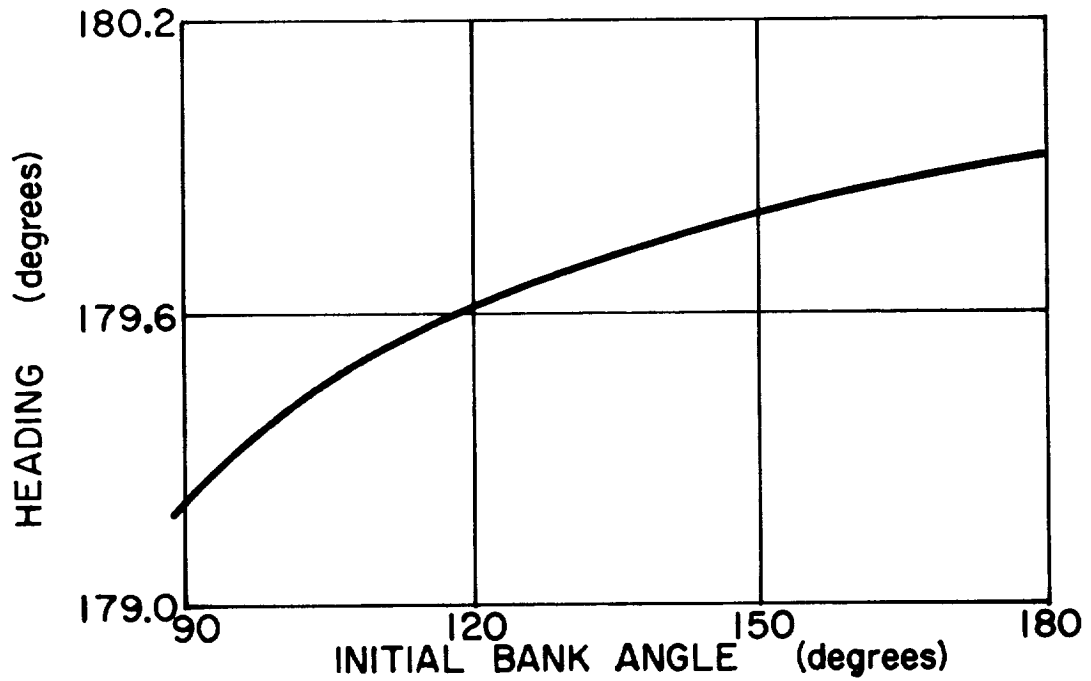


Figure 22.- Effect of Initial Bank Angle on Vehicle Heating at  $\dot{q}_{\max.} = 300 \text{ kW/m}^2$  (26 Btu/ft<sup>2</sup>-sec)

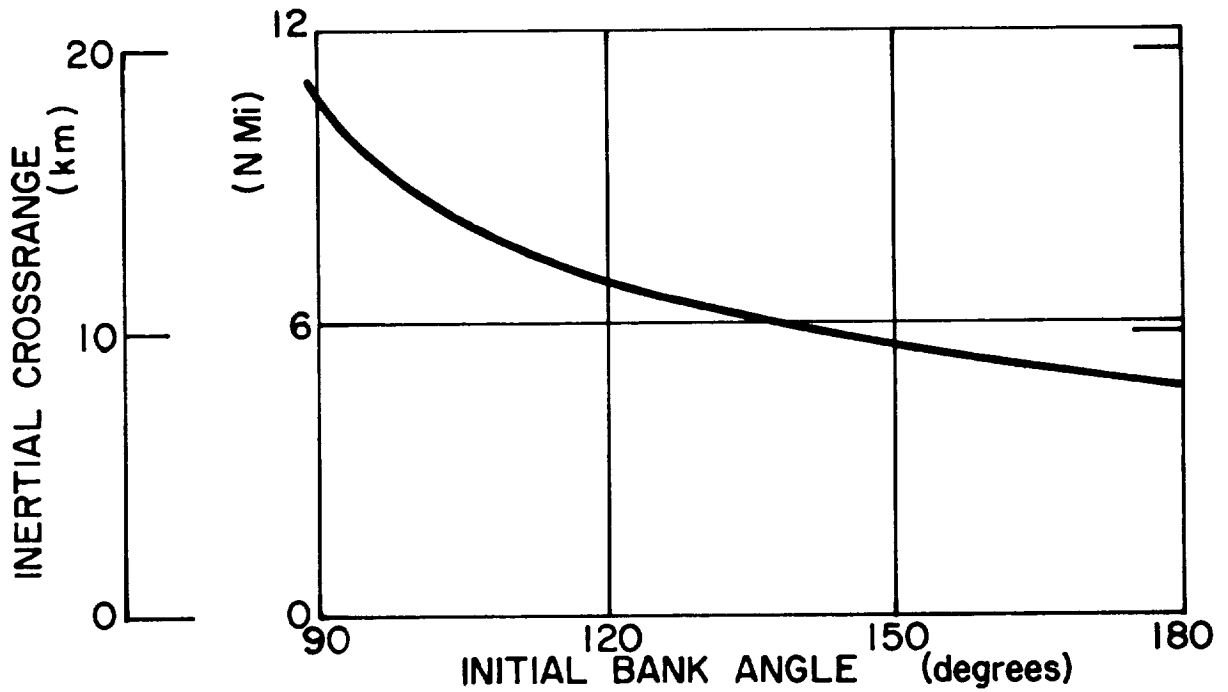


Figure 23.- Inertial Crossrange as a Function of Initial Bank Angle at  $\dot{q}_{\max.} = 300 \text{ kW/m}^2$  (26 Btu/ft<sup>2</sup>-sec)

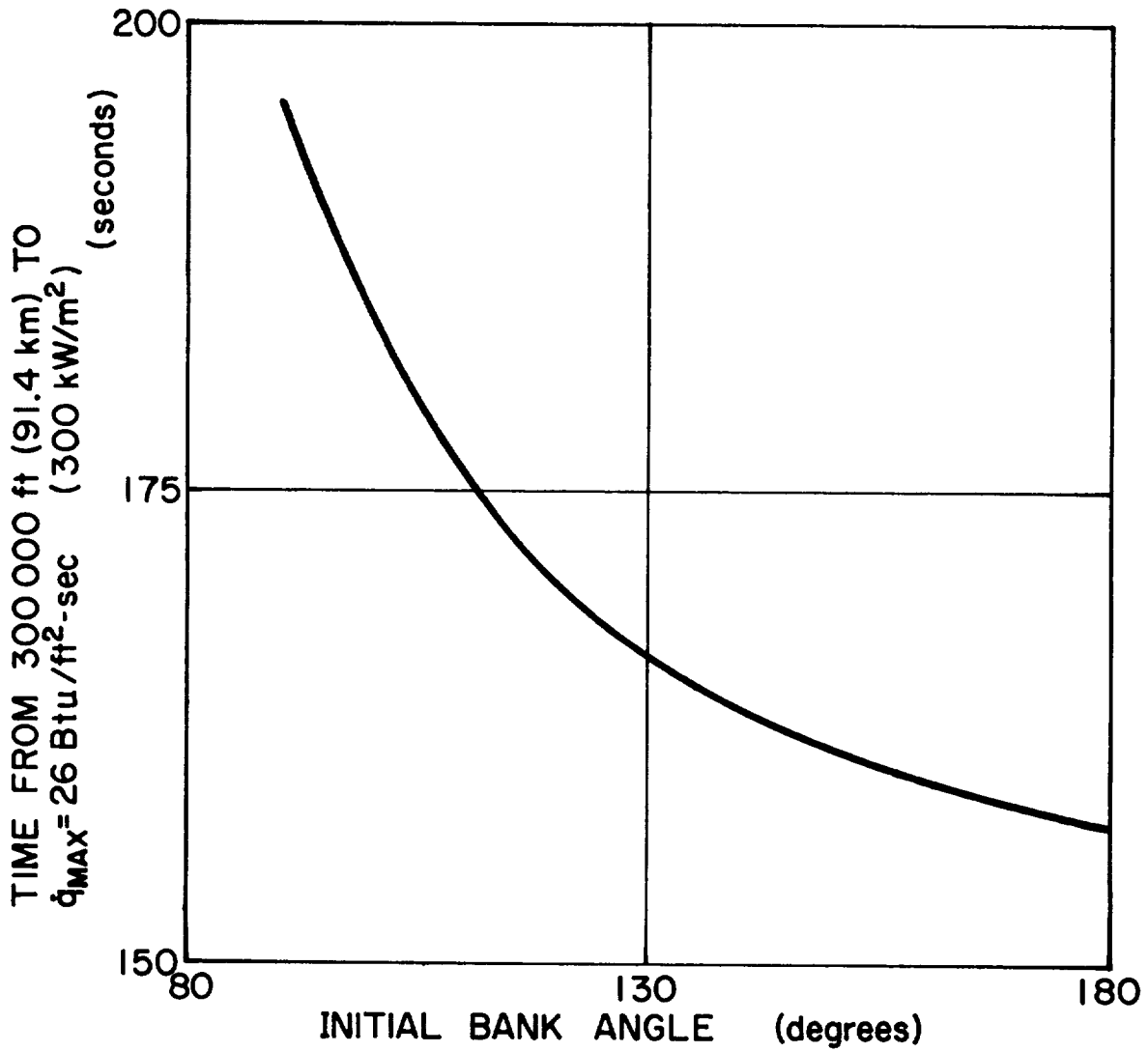


Figure 24.- Time Required for Vehicle to Attain Maximum Heating versus Initial Bank Angle

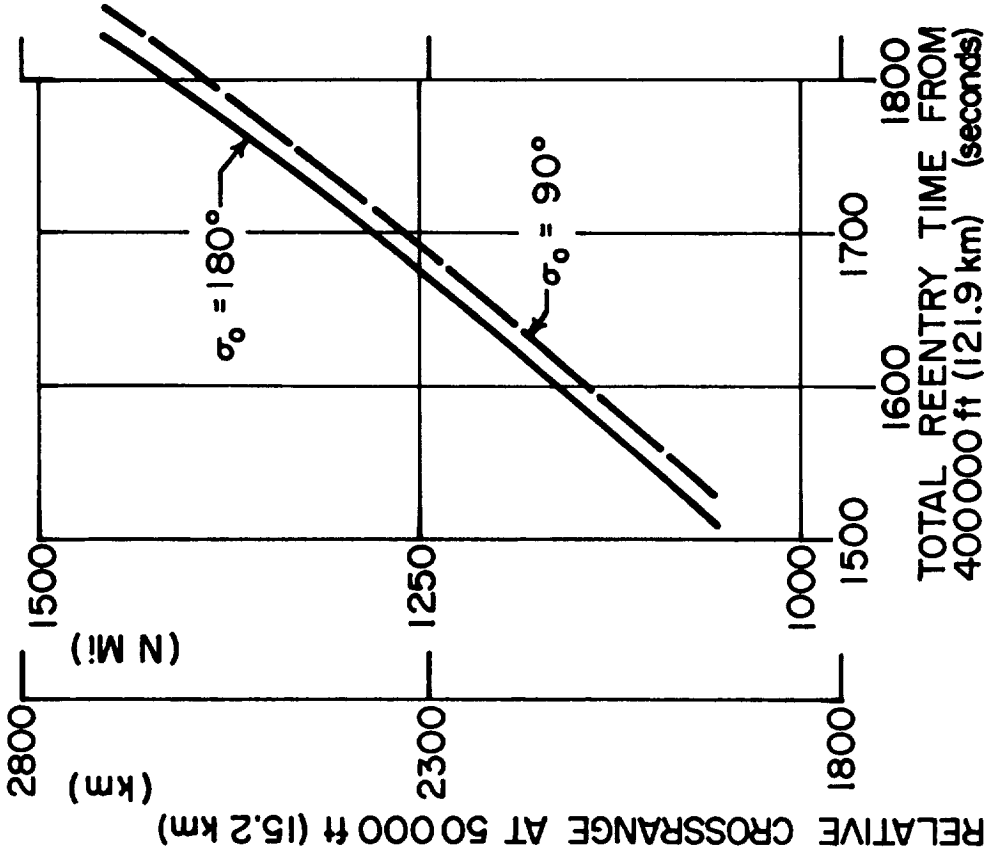


Figure 25.- Total Reentry Time Required to Reach Crossrange

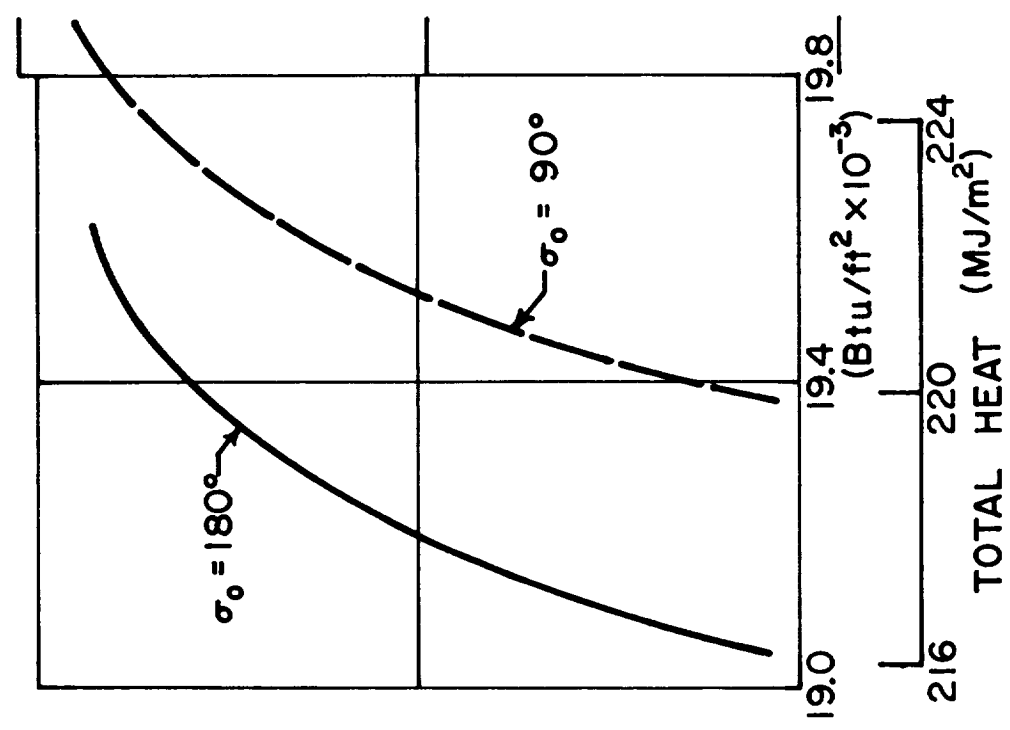


Figure 26.- Total Reentry Heat Required by Crossrange

Entry parameter trade studies: To assess the effects of the heating rate and acceleration limits on the total heat and entry time, trajectories were generated for two conditions: (1) the heating rate limit was removed and only the acceleration limit of 2.5 g was imposed; and (2) the heating rate limit was reduced to the minimum value that could be maintained without skip-out.

Table 11 summarizes the results of the two trajectories described above. The peak heating rate increases to 802 kW/m<sup>2</sup> (70.7 Btu/ft<sup>2</sup>-s), but the total integrated heat, the entry time, and the downrange are reduced for the maximum heating rate trajectory. The minimum heating rate trajectory results in a peak heating rate of 145 kW/m<sup>2</sup> (12.8 Btu/ft<sup>2</sup>-s), the down range is increased to 12 460 km (6732 n. mi.), the total heat input increased to 233.5 MJ/m<sup>2</sup> (20 595 Btu/ft<sup>2</sup>), and the entry time increased to 2351 s.

TABLE 11.- MAXIMUM AND MINIMUM HEATING RATE TRAJECTORIES

Primary factors	Maximum heating rate	Minimum heating rate
	No $\dot{q}$ limit Acceleration limit = 2.5 g	No skip-out
Orbit		
Inclination, deg	90	90
Altitude, km (n. mi.)	185 (100)	85 (100)
Entry		
Altitude, km (100 ft)	121.9 (400)	121.9 (400)
Flight path angle (relative) deg	-0.893	-0.893
Flight path angle (inertial) deg	-0.893	-0.893
Velocity (relative) m/s (ft/s)	7830 (25 718)	7830 (25 718)
Velocity (inertial) m/s (ft/s)	7830 (25 718)	7830 (25 718)
Deorbit		
Propellant weight, kg (lb)	2300 (5055)	2300 (5055)
$\Delta V$ , m/s (ft/s)	74 (243)	74 (243)
Entry		
Max heating rate, kW/m <sup>2</sup> (Btu/ft <sup>2</sup> -s)	802 (70.7)	145 (12.8)
Max acceleration, g	2.5	2.5
Crossrange to 15.24 km (50 000 ft), km (n. mi.)	2040 (1100)	2040 (1100)
Downrange to 15.24 km (50 000 ft), km (n. mi.)	5000 (2700)	12 460 (6732)
Total heat, MJ/m <sup>2</sup> (Btu/ft <sup>2</sup> )	201.9 (17 779)	233.5 (20 595)
Heat shield weight, kg (lb)	8450 (18 603)	13 020 (28 641)
Time (121.9 to 15.2 km; 400 000 to 50 000 ft), s	1418	2351
Time ( $\dot{q}_{max}$ to 5.2 km; 50 000 ft), s	1000	1924
Time (Above $\dot{q} = 22.7$ kJ/m <sup>2</sup> ; 2 Btu/ft <sup>2</sup> ), s	820	1780

Figures 27 and 28 present the trajectory profiles for the maximum heating rate trajectory. Figures 29 and 30 present the profiles for the minimum heating rate trajectory.

These trajectories show that increasing the peak heating rate tends to reduce total heat input, entry time, and downrange. Since the TPS panel weight is a function of entry time and total heat, increasing the peak heating rate also reduces TPS weight. Figure 31 shows the relationship between the maximum heating rate and the total heat.

**100 N Mi (185 km) Polar Orbit, No Limit on  $\dot{q}_{MAX}$**

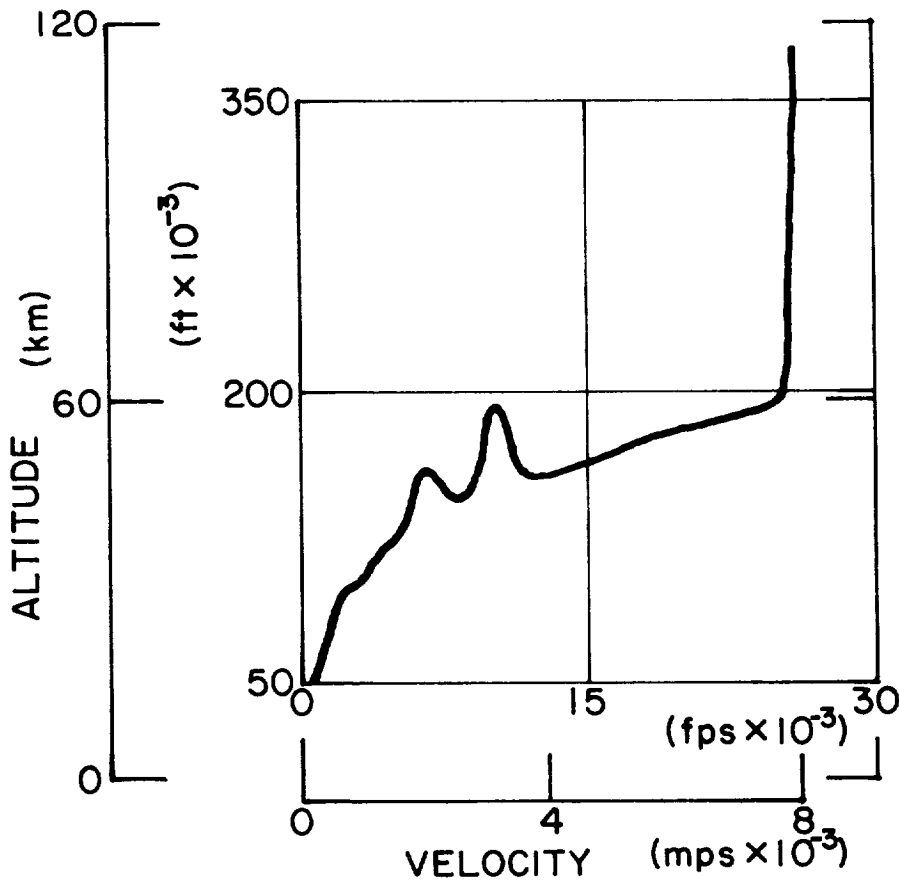


Figure 27.- Altitude for 185-km (100 n. mi.) Polar Orbit Trajectory, Unlimited  $\dot{q}$

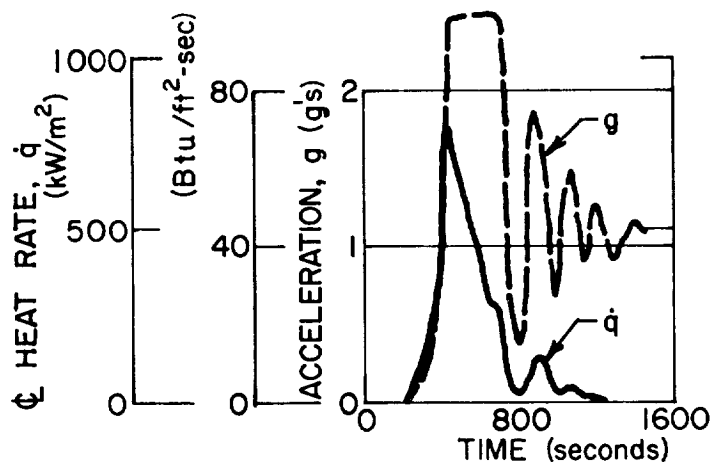


Figure 28.- Acceleration and Heating Rate for 185-km (100 n. mi.) Polar Orbit Trajectory, Unlimited  $\dot{q}$

100 N Mi (185 km) Polar Orbit,  $\dot{q}_{MAX} = 12.8 \text{ BTU/ft}^2\text{-sec}$   
 $= 14.5 \times 10^4 \text{ Watts/m}^2$

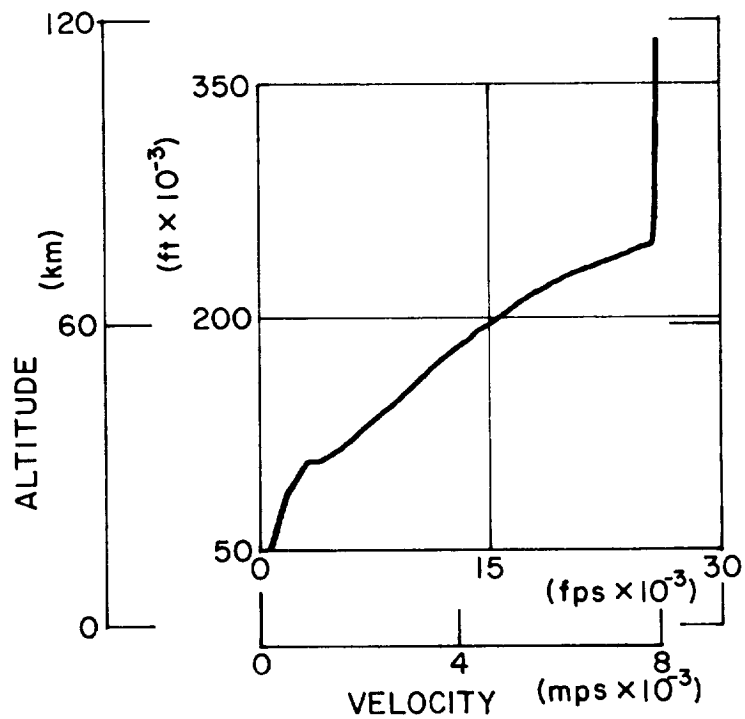


Figure 29.- Altitude for 185-km (100 n. mi.) Polar Orbit Trajectory,  $\dot{q}_{max.} = 12.8$

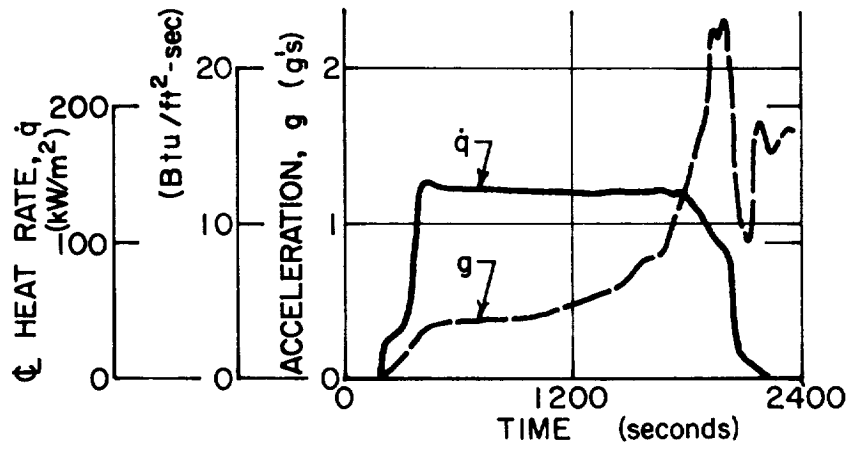


Figure 30.- Acceleration and Heating Rate for 185-km (100 n. mi.) Polar Orbit Trajectory,  $\dot{q}_{\text{max.}} = 12.8$

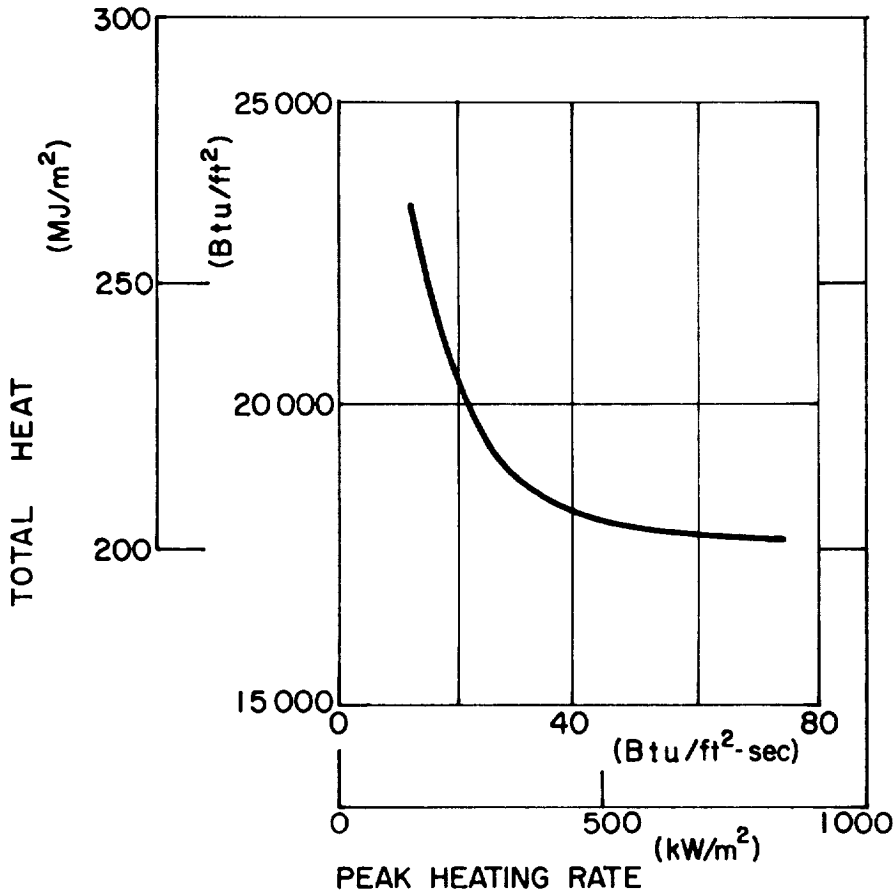


Figure 31.- Total Heat versus Peak Heating Rate

4. Dispersion analysis.- This study was conducted to determine the effect of vehicle and environmental dispersions. The dispersions from the Martin Marietta-Grumman proposal studies were used for this study. The dispersions were scaled in terms of percentage and were applied as safety factors along with other dispersions associated with the heat shield design to obtain the final design values. The results of the Martin Marietta-Grumman proposal studies showed that the three-sigma variation in total heat due to vehicle and environmental dispersions was approximately 15 percent. The major contributors to the total heat are shown in Table 12.

TABLE 12.- DISPERSION SUMMARY

Parameter	Percent total heat dispersion
Atmospheric variations (density and winds)	4
Aerodynamic coefficients (lift and drag)	4
Payload weight	11
Attitude error	7
Entry conditions (velocity, altitude, and path angle)	5
Total (rss)	15

5. Guidance implications.- This study was conducted to recommend a mode of entry guidance that will produce entry profiles which match the heat shield design trajectory. Guidance laws that cause the vehicle to follow paths on the altitude-velocity profile are similar to the scheme used to produce the design trajectories in that feedback of errors and error rates are used to produce commands that null the errors. These techniques are operationally simple and require only a stored nominal trajectory, a look-up scheme for finding nominal values from the storage and an evaluation of the simple algebraic control command equation. Thus the objective of causing the vehicle to fly a desirable altitude-velocity (h-v) profile is easily achieved by classical feedback control methods.

Open-loop downrange control is achieved by adjusting the deorbit point prior to reentry. Minor corrections require closed-loop logic to achieve the desired accuracy. However, since the downrange correction should be minor, angle of attack modulation after leaving the h-v profile should be sufficient to provide good downrange accuracy.

The major design feature for developing guidance logic capable of producing trajectories that are similar to those produced by this study involves a method for determining the point at which a departure from the constant load factor curve must be made to achieve the desired crossrange. Simulation results for the GAC 619 vehicle show that 1670 km (900 n. mi.) of crossrange will be obtained by never leaving the load factor boundary. Crossrange values of less than 1670 km (900 n. mi.) can therefore be achieved by a simple bank angle sign reversal method. This would produce an absolute minimum flight time and total heat value by using very simple guidance calculations. Crossrange targets of greater than 1670 km (900 n. mi.) will require logic to determine when to leave the constant load-factor curve and what commands to issue after that departure.

Ideally, an analytic method for estimating maximum crossrange capability remaining is desirable to establish the point of departure from the constant load factor curve. Unfortunately, no such expression is available for the general case. The flat-earth approximation for heating rate is:

$$\dot{\psi} = \frac{1}{v} \frac{L}{m} \sin \phi$$

where  $\psi$  is heading angle with respect to the downrange,  $v$  is velocity relative to the atmosphere,  $L$  is the lift force,  $m$  is vehicle mass, and  $\phi$  is bank angle. After making an equilibrium glide assumption that lift must balance gravity plus centripetal acceleration, the heading rate equations can be integrated to give

$$\psi = \psi_o - \frac{L}{D} \sin \psi \ln \left( \frac{v}{v_o} \right)$$

where the subscript  $o$  indicates local conditions. The crossrange rate equation (flat earth) is:

$$\dot{\lambda} = v \sin \psi \cos \gamma$$

where  $\ell$  is crossrange distance traveled. Substitution of the  $\psi$  equation into the  $\dot{\ell}$  equation produces an expression that has no analytic integral. However, for guidance purposes, approximations may be made to produce the necessary command equation

$$\dot{\ell} = \frac{d\ell}{dv} \frac{dv}{dt} = \frac{d\ell}{dv} \left( -\frac{D}{m} \right) = v \sin \psi \cos \gamma$$

$$\therefore \frac{d\ell}{dv} \approx \frac{v \sin \psi}{\left( -\frac{D}{m} \right)} \quad \text{for small } \gamma.$$

Since the h-v profile that is being followed is a constant load-factor profile, a constant drag profile can be computed that is compatible with the current trajectory state. Therefore, assuming  $D/m = \text{constant} = C$ :

$$d\ell = \frac{-v}{c} \sin \left[ \psi_o - \frac{L}{D} \sin \phi \ln \left( \frac{v}{v_o} \right) \right] dv$$

This equation, though separable, still cannot be integrated analytically. Therefore, further approximations must be made. If a final velocity at the target is specified, then

$$\psi_f = \psi_o - \frac{L}{D} \sin \phi \ln \left( \frac{v_f}{v_o} \right)$$

An average value of  $\psi$  (averaged over the velocity interval)

$$\psi_{AV} = \frac{1}{2} (\psi_f + \psi_o) = \psi_o - \frac{1}{2} \frac{L}{D} \sin \phi \ln \left( \frac{v_f}{v_o} \right)$$

Using this value in the crossrange equation gives

$$d\ell \approx \frac{v}{c} \sin \psi_{AV} dv$$

$$\therefore \ell_f \approx \ell_o + \frac{v_f^2}{2c} \sin \psi_{AV}$$

Picking a threshold value of  $L/D \sin \phi = (L/D \sin \phi)_T < L/D_{\max}$  to be conservative and provide control margin in the last interval of the trajectory, then the crossrange equation provides an approximate expression for the velocity  $v_o$  at which to leave the h-v profile. Specifically,

$$\ell_f = \ell_o + \frac{v_f^2}{2c} \sin \left[ \psi_o + \frac{1}{2} \left( \frac{L}{D} \sin \phi \right)_T \ln \left( \frac{v_f}{v_o} \right) \right]$$

As the current velocity  $v_o$  decreases, the value of  $\ell_f$  will decrease until reaching the target value. At this time, the guidance philosophy would be altered from the constant load-factor profile to a crossrange targeting mode in which the bank angle commands are generated from the relationship

$$\sin \phi = \frac{\sin^{-1} \left[ \frac{\ell_{f \text{ desired}} - \ell_o}{\frac{v_f^2}{2c}} \right] - \psi_o}{\left[ \frac{1}{2} \ln \left( \frac{v_f}{v_o} \right) \frac{L}{D} \right]}$$

where the value of  $L/D$  is that used in the downrange control channel.

The above development is intended to provide only an example of a guidance approach. It should be regarded as representative of the elementary computations required to produce a closed-loop philosophy that preserves the basic trajectory features produced by open-loop shaping methods in other sections of this study.

**6. Conclusions.**— The trajectory analysis for this study has shown that an ablative heat shield is feasible for the Shuttle Orbiter vehicle. The trajectories for an ablative-type heat shield enter at a higher heating rate and lower total heat than trajectories for a reusable surface insulation. As a result, the downrange distance traveled during entry is considerably shorter for an ablative heat shield trajectory than for a reusable insulation heat shield trajectory at the same crossrange.

It has been shown that an initial bank angle of  $180^\circ$  provides the best reentry trajectory in that the resulting lift vector down orientation allows entry at the smallest possible entry flight path angle without danger of skip-out. The smallest entry path angle produces the minimum system weight in terms of deorbit propellant and heat shield weight.

Trajectories were generated without constraining the heat rate to assess the type of ablator required for the heat shield under these conditions. The resulting peak heating rate would require a higher density material over more of the vehicle than would be required for a lower peak heating rate. As a result, a trajectory that would allow the use of a low density ablator, such as SLA-561, over most of the vehicle was selected as the design condition.

The minimum peak heating rate that could be maintained during entry was also determined for the vehicle configuration being analyzed to evaluate the maximum reuse capability with minimum refurbishment.

## B. Aerothermal Analysis

The aerothermal tasks performed consisted of (1) determining the Orbiter heating rate distribution with particular emphasis on the nose cap and wing leading edge regions; (2) determining localized aerothermal characteristics for numerous specific vehicle locations; and (3) conducting a venting analysis for the stand-off heat shield panels. These tasks were performed for both ascent and entry, with the exception of the total Orbiter ascent heating rate distribution, as discussed below. A brief study was also made of the ascent interference heating effects on the Orbiter. The aerothermal characteristics consisted of the local static and dynamic pressures, local Mach number, and the aerodynamic shear stress. These parameters along with the heat fluxes were used in the design of the heat shield.

1. Orbiter heating rate distributions.- Original Orbiter heating rate distributions were obtained from the GAC/Martin Marietta Phase C shuttle proposal and were normalized to a bottom centerline reference location heating rate. This reference location is a point 15.24 m (50 ft) aft of the nose. However, in the course of determining the heating rate distributions around the nose cap and wing leading edge, it was found that the heating rates for the forward portion of the body and the wing were substantially overpredicted. The distributions of the Phase C proposal were based on the assumption that all points on the body experienced transition at the same time as the reference location. Detailed analysis, however, showed a large variance in the time at which transition occurred at different locations on the body. It was shown that transition at locations near the nose and wing leading edge occurred several hundred seconds after

the time of peak heating (also after transition at the reference location occurred), resulting in lower heating rates than were predicted using the Phase C proposal. Transition onset occurs when

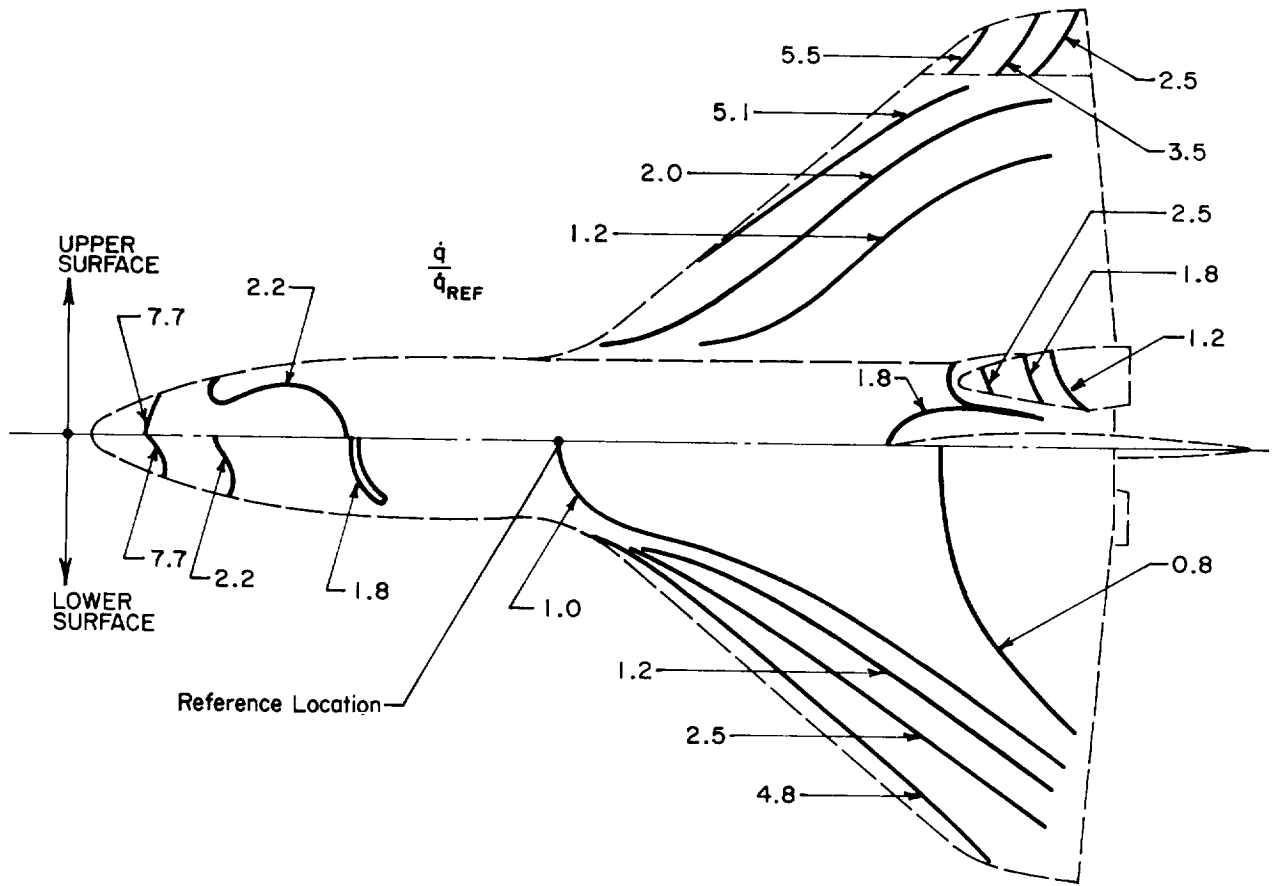
$$\frac{R_{e_{\theta}}}{M_L \left( \frac{R_{e_L}}{X} \right)^{0.2}} = 10$$

where:  $R_{e_{\theta}}$  = local Reynold's number based on momentum thickness,  
 $M_L$  = local Mach number,  
 $R_{e_L} X$  = local unit Reynold's number.

Fully turbulent flow was assumed to occur at a location twice the length of the transition onset length. (Fully turbulent flow occurs at a location twice the distance of the length required to satisfy the above equation.)

The Orbiter heating rate distributions normalized to the reference location heating rate as well as radiation equilibrium temperatures are presented in figures 32, 33, and 34 for the nominal south ascent trajectory, ablator entry trajectory, and the reusable TPS entry trajectory respectively. An altitude-velocity time history for each trajectory is given in Section A of this chapter. The Orbiter ascent heating rate distribution was obtained from Phase C while the entry heating rate distributions have been revised to account for the effect of transition. The ascent heating rates were revised only in the regions of the nose cap, wing leading edge, and interference region as discussed in The following paragraphs.

The methodology used to determine these distributions is discussed fully in appendix B. Large uncertainties in the analytical methods for the upper and side surfaces exist due to the complexity of the flow resulting from the high entry angles of attack. Thus, no further refinements for the regions were warranted and the heating rate distributions remained unchanged from the Phase C data except at the nose cap and wing leading edge regions. The reference point heating rate histories for the various trajectories are shown in figures 35 and 36. The Phase C ascent and entry heating rate distributions were only used to determine the Orbiter weights for the original trajectory trade studies.



NOTE:  
 1. Normalized to Lower Surface Reference Point.

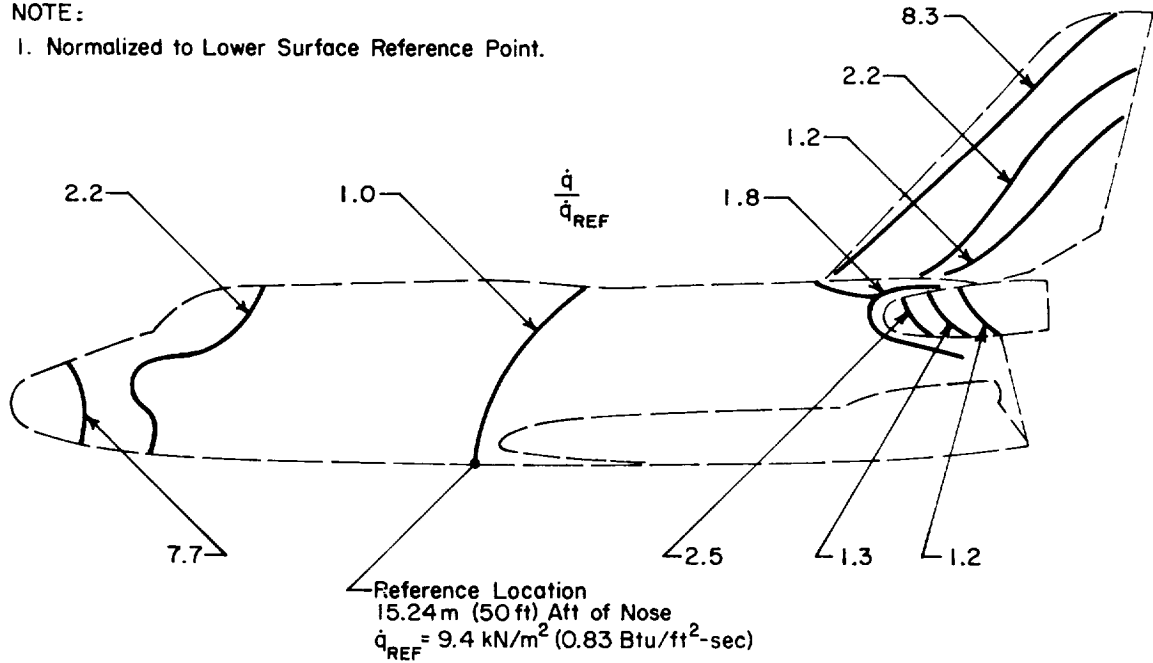
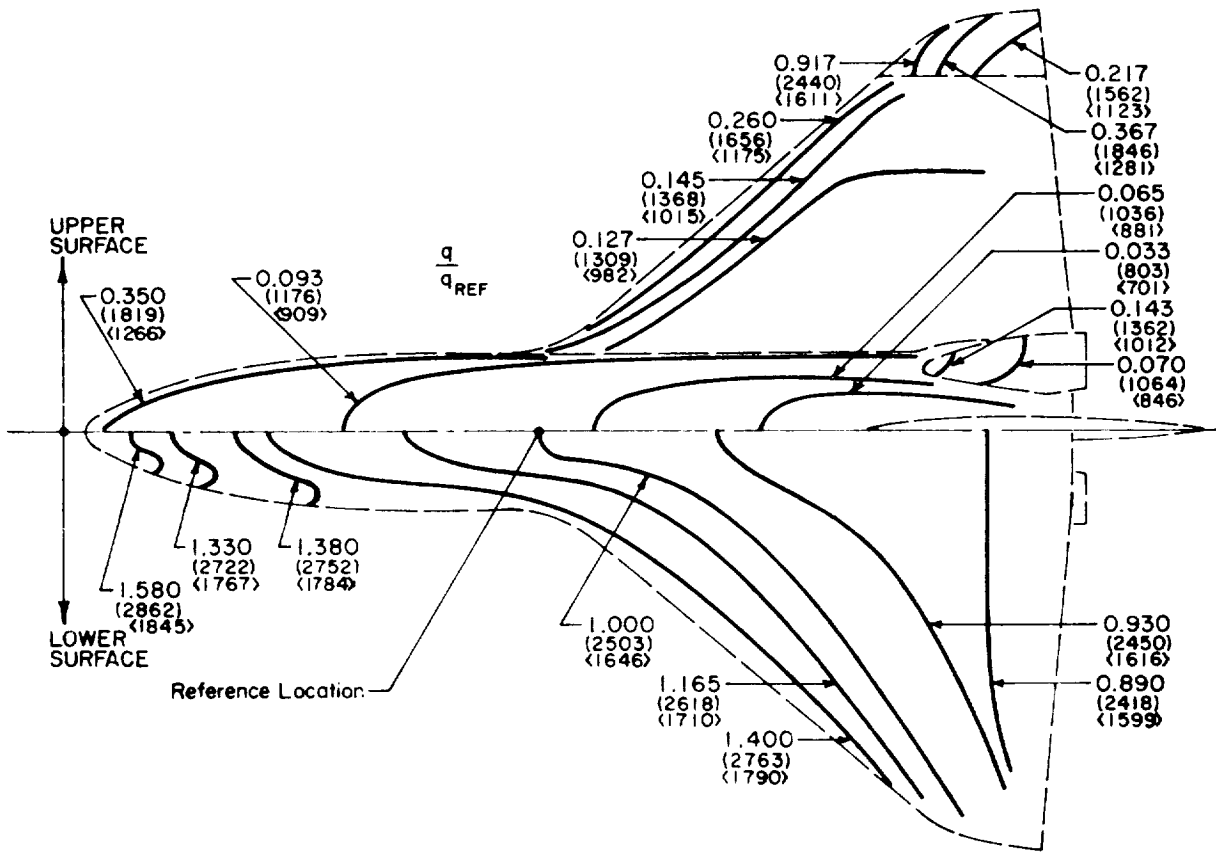


Figure 32.- Ascent Heating Rate Distribution



NOTE:

1.  $\alpha = 30^\circ$
2. Radiation Equilibrium Temp Shown in (°F) (°K)

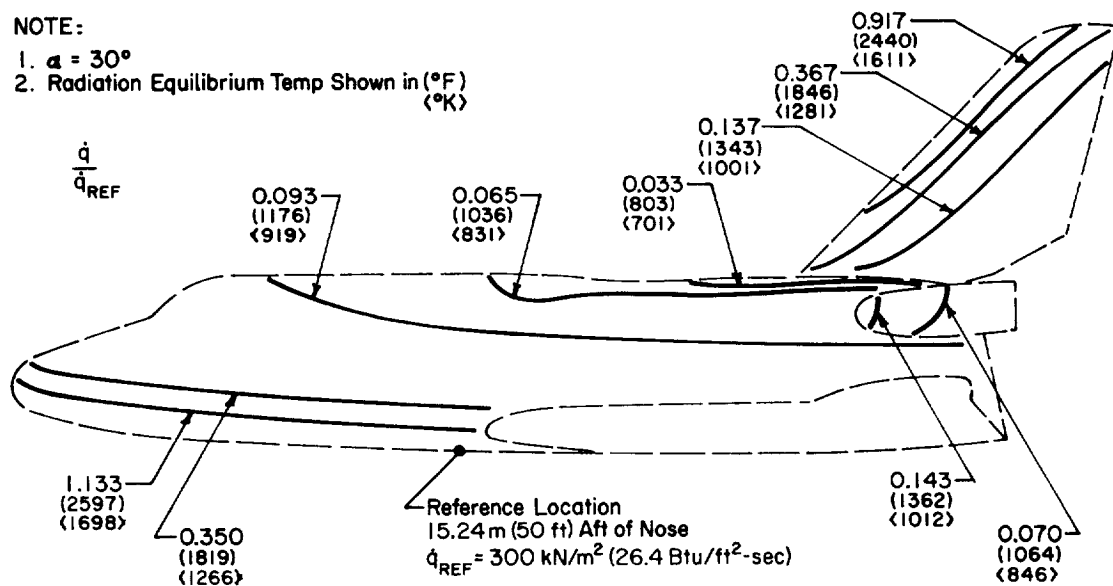
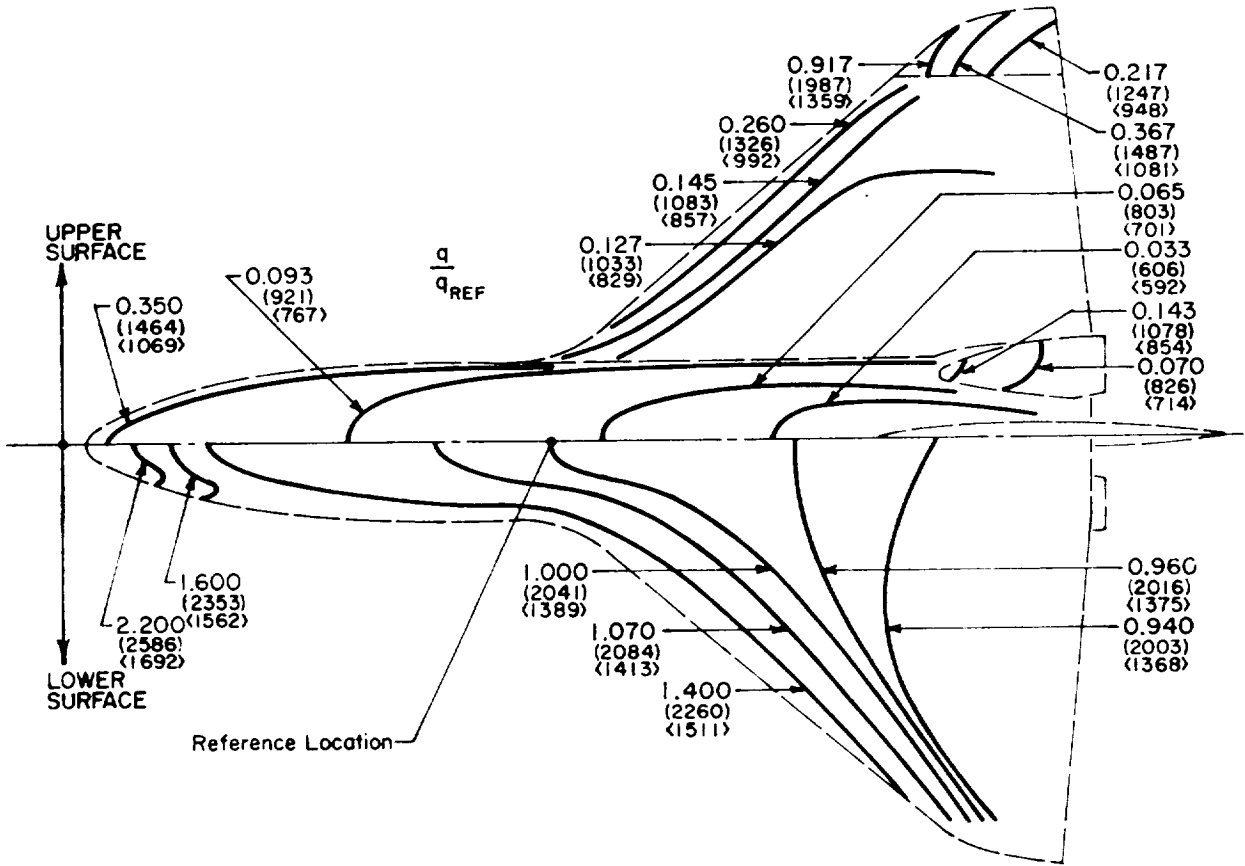


Figure 33.- Entry Heating Rates, Ablator Trajectory



NOTE:

- $\alpha = 30^\circ$
- Radiation Equilibrium Temp Shown in (°F) (°K)

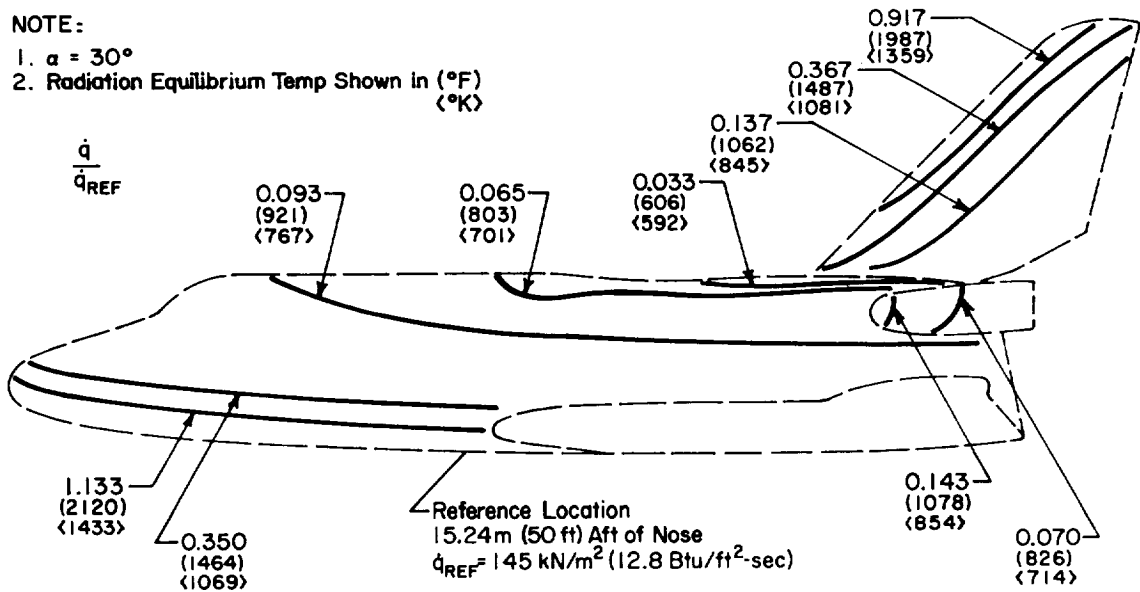


Figure 34.- Entry Heating Rates, RSI Trajectory

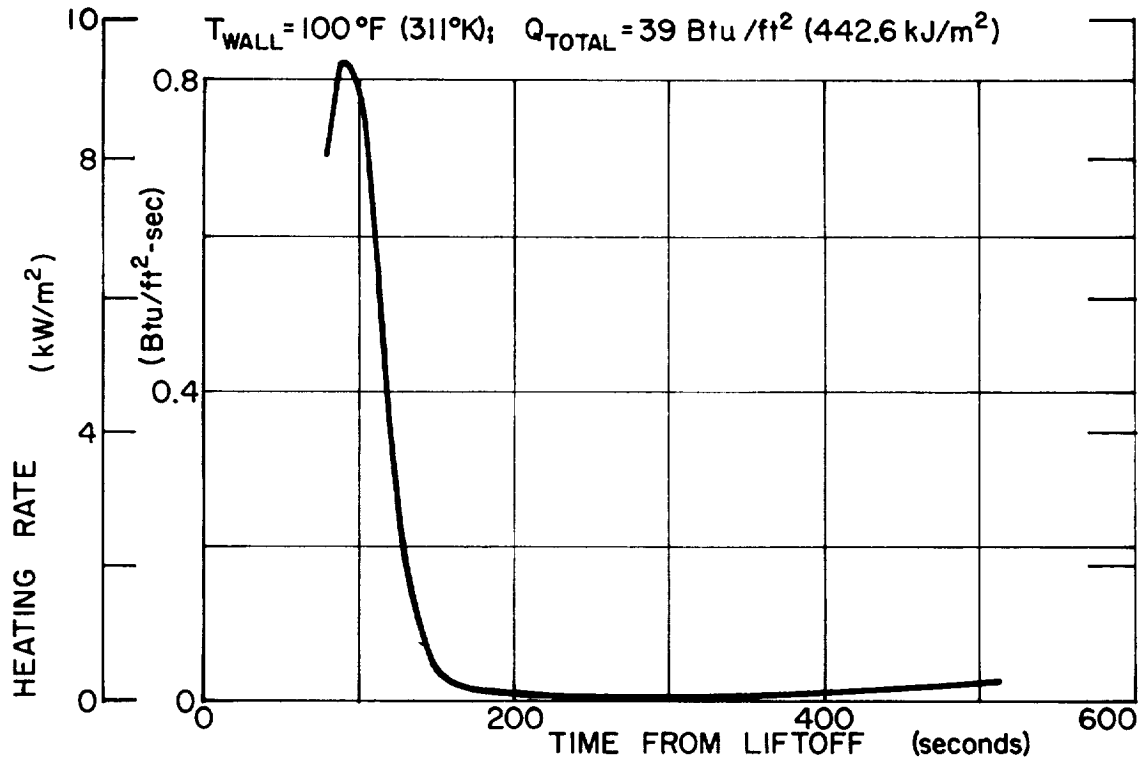


Figure 35.- Ascent Heating Rate History at the Body Lower Centerline Reference Location

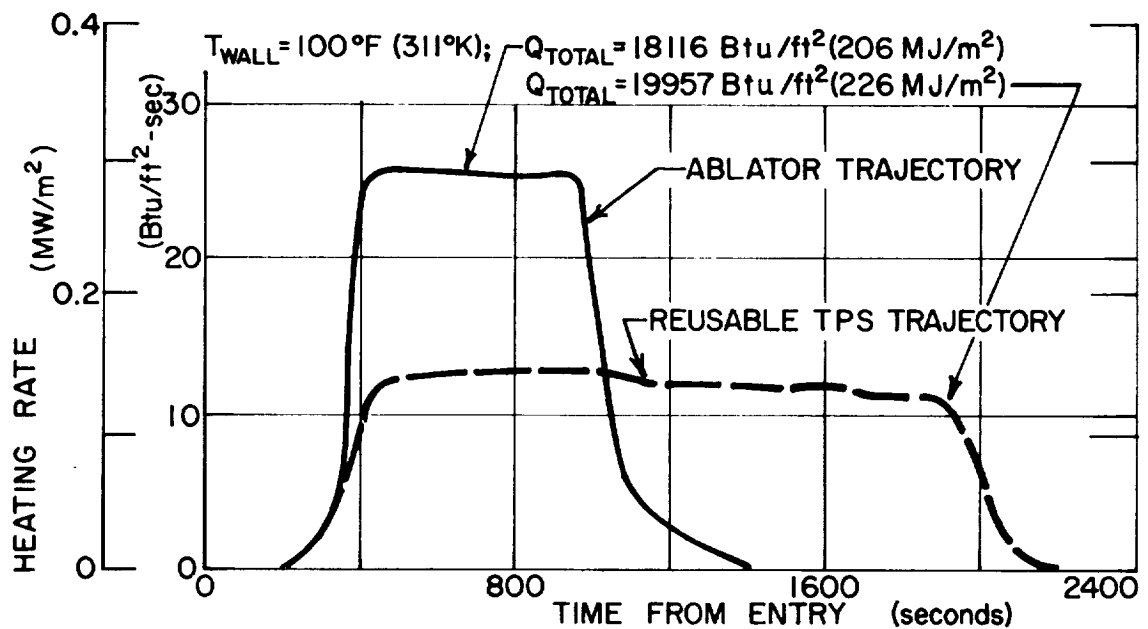


Figure 36.- Entry Heating Rate Histories at the Body Lower Centerline Reference Location

The nose cap heating rate distributions,  $R = 91.44$  cm (36 in.), were calculated for the ascent trajectory and both entry trajectories are presented in figures 37, 38, and 39. The wing leading edge,  $R = 15.24$  cm (6 in.), heating rate distributions are presented in figures 40, 41, and 42. Appendix B discusses the methods used in these analyses.

The vehicle locations at which the previously described aerothermal characteristics were predicted are: (1) stagnation point of the nose; (2) bottom centerline reference location, 15.24 m (50 ft) aft of the nose; (3) wing leading edge stagnation line (mid span); (4) forward lower centerline, 5.09 m (16.7 ft) aft of nose; (5) top centerline (leeward) corresponding to  $F_q = 0.033$ ; and (6) a side cabin area where  $F_q = 0.35$ . Time histories of all the aerothermal characteristics except local static pressure, as well as the procedures used, are presented in appendix B.

Available Phase B Space Shuttle test data were analyzed to determine the ascent interference heating effects on the Orbiter. Mach 10 data indicated that the maximum heating level in the region between the Orbiter and External Tank was 7.5 times the value at the reference point location. This factor would vary with Mach number, but a constant factor of 7.5 was used because it represented an average ascent interference heating factor. The portion of the Orbiter affected by ascent interference heating is shown in figure 43.

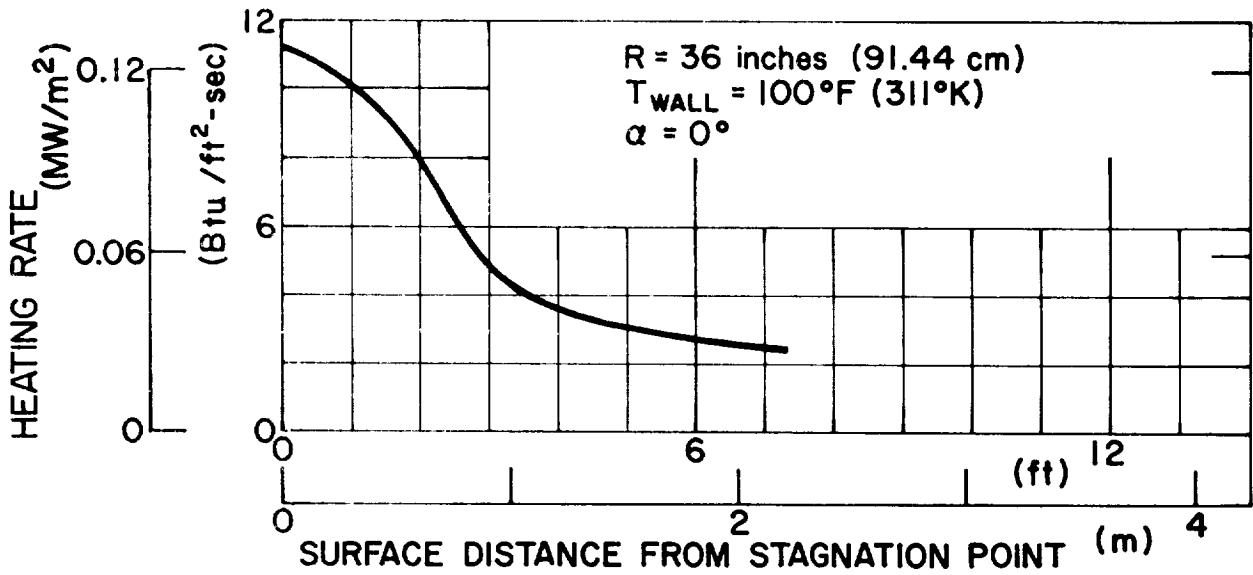


Figure 37.- Ascent Heating Rate Distribution around Nose Cap (Windward and Leeward)

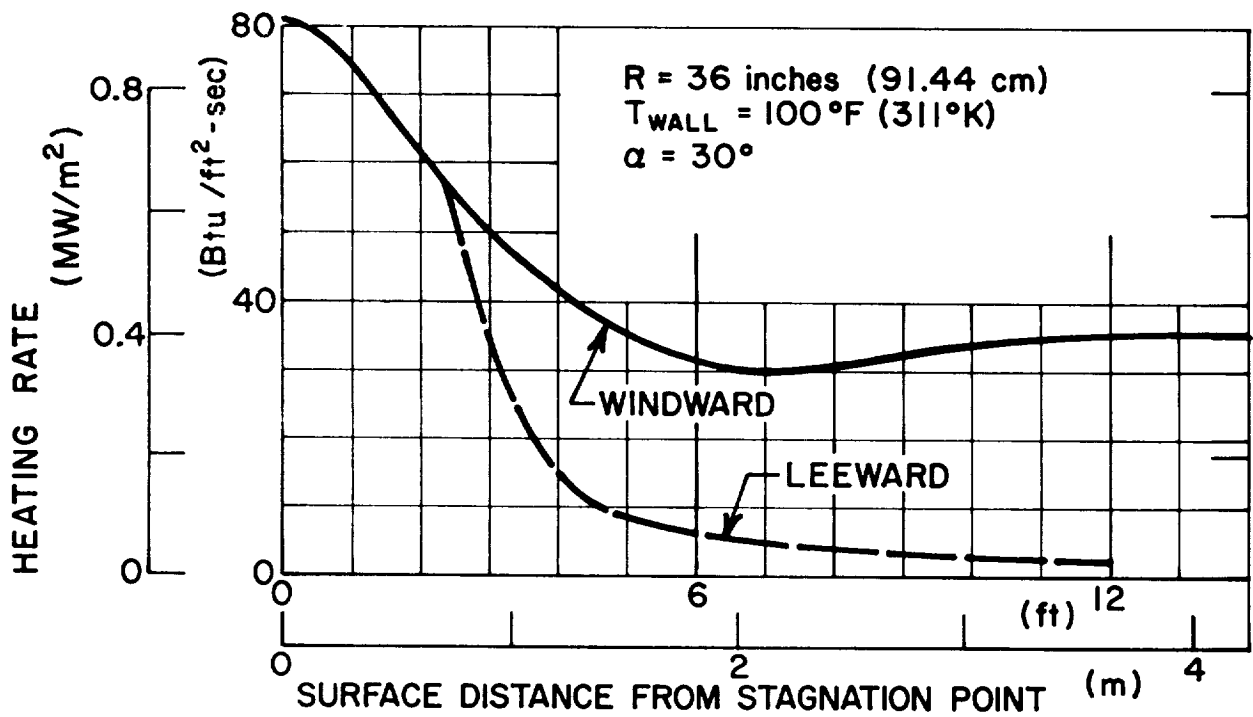


Figure 38.- Entry Heating Rate Distribution around Nose Cap for Ablator Trajectory

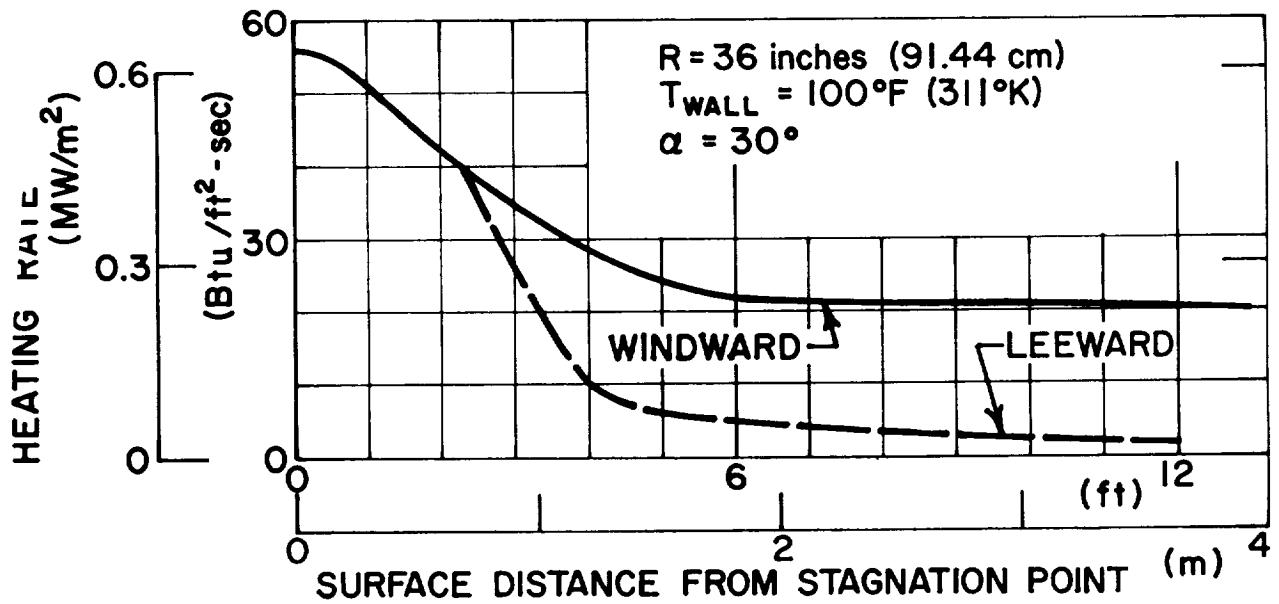


Figure 39.- Entry Heating Rate Distribution around Nose Cap for Reusable TPS Trajectory

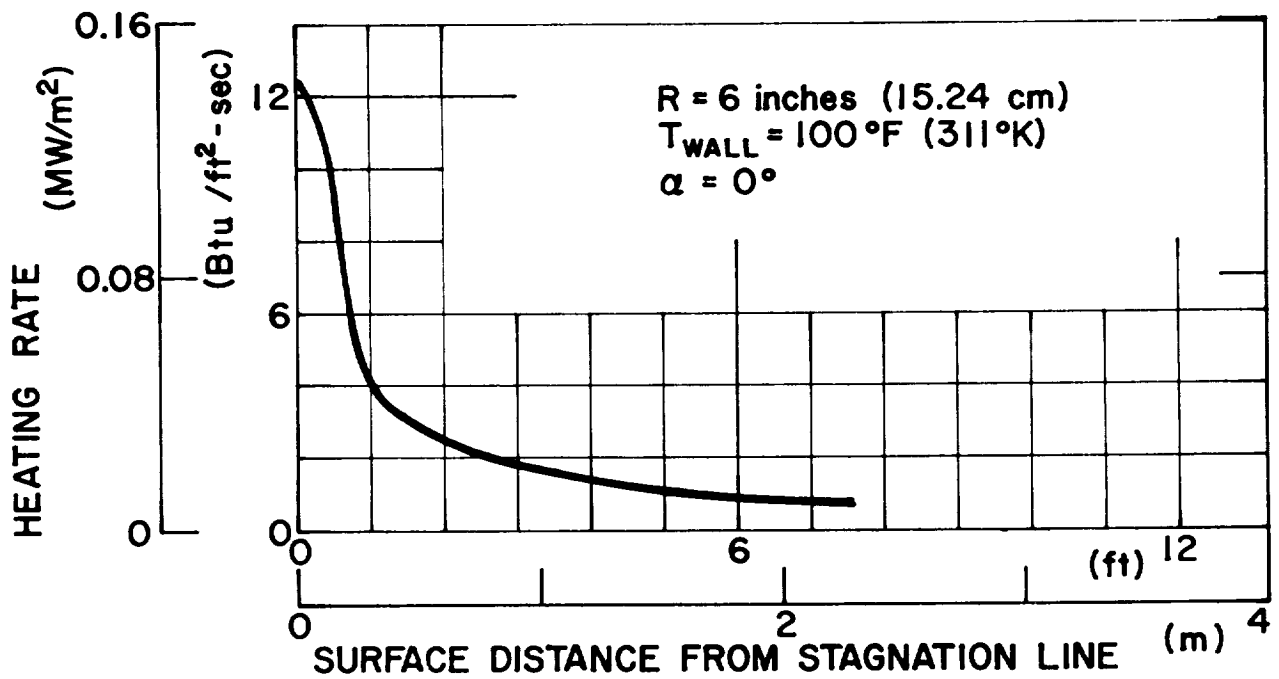


Figure 40.- Ascent Heating Rate Distribution around Wind Leading Edge (Windward and Leeward)

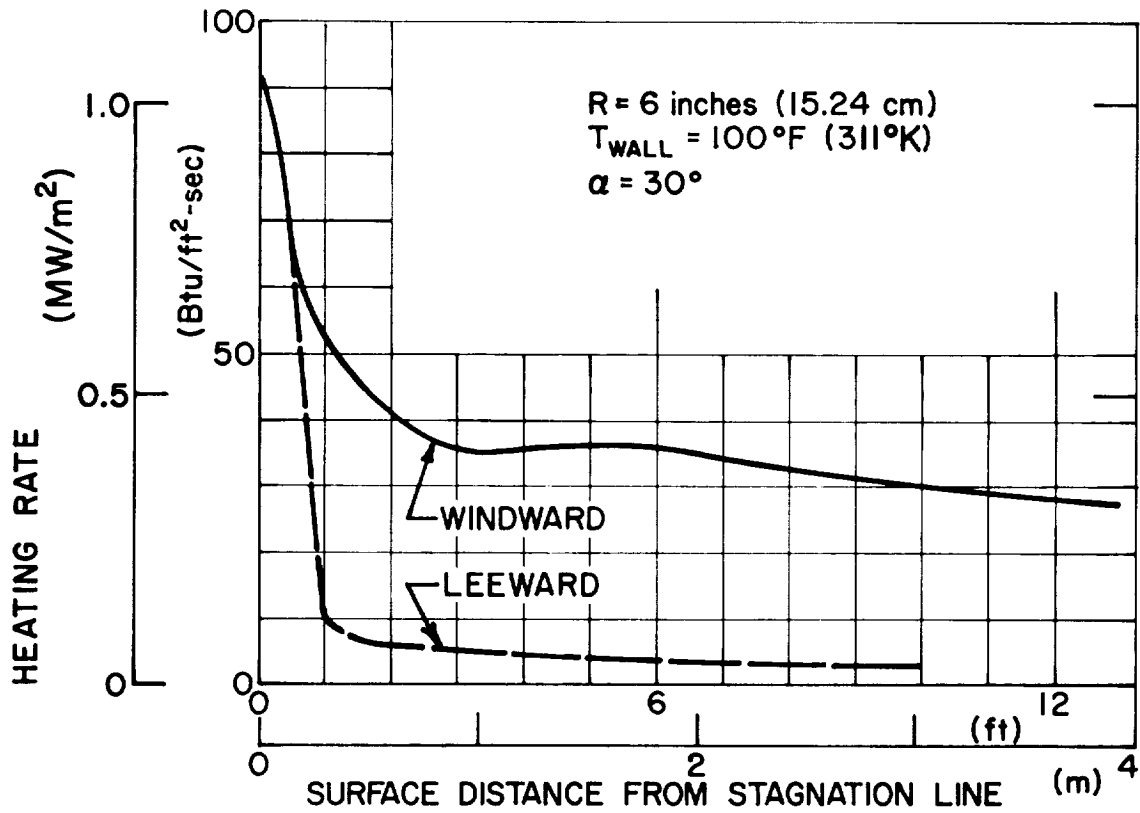


Figure 41.- Entry Heating Distribution around Wind Leading Edge for Ablator Trajectory

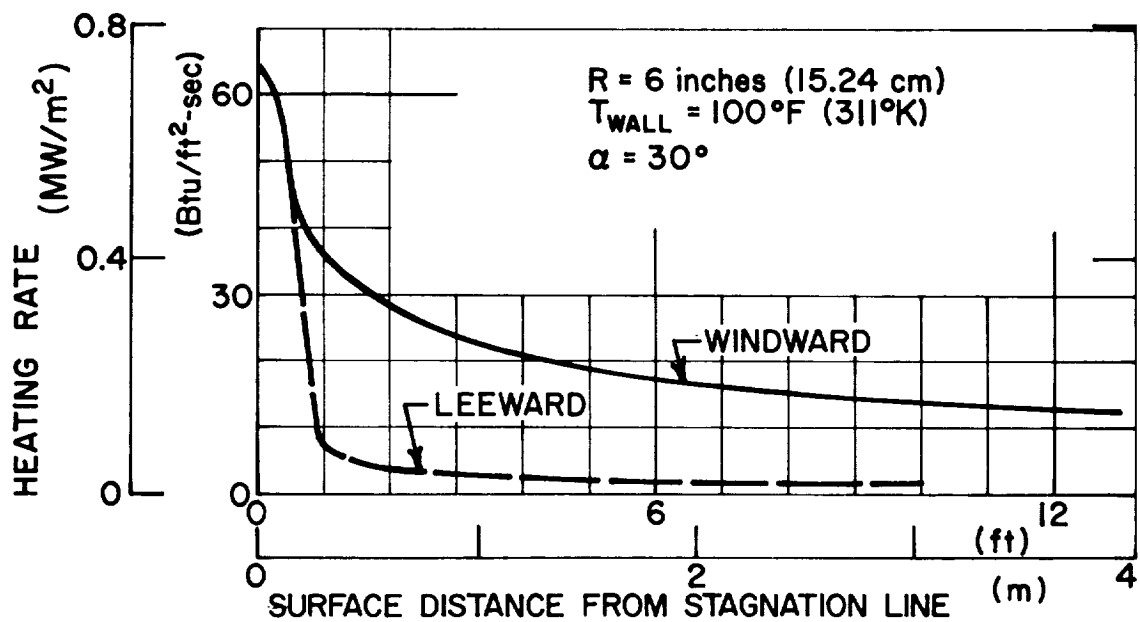


Figure 42.- Entry Heating Distribution around Wind Leading Edge for Reusable TPS Trajectory

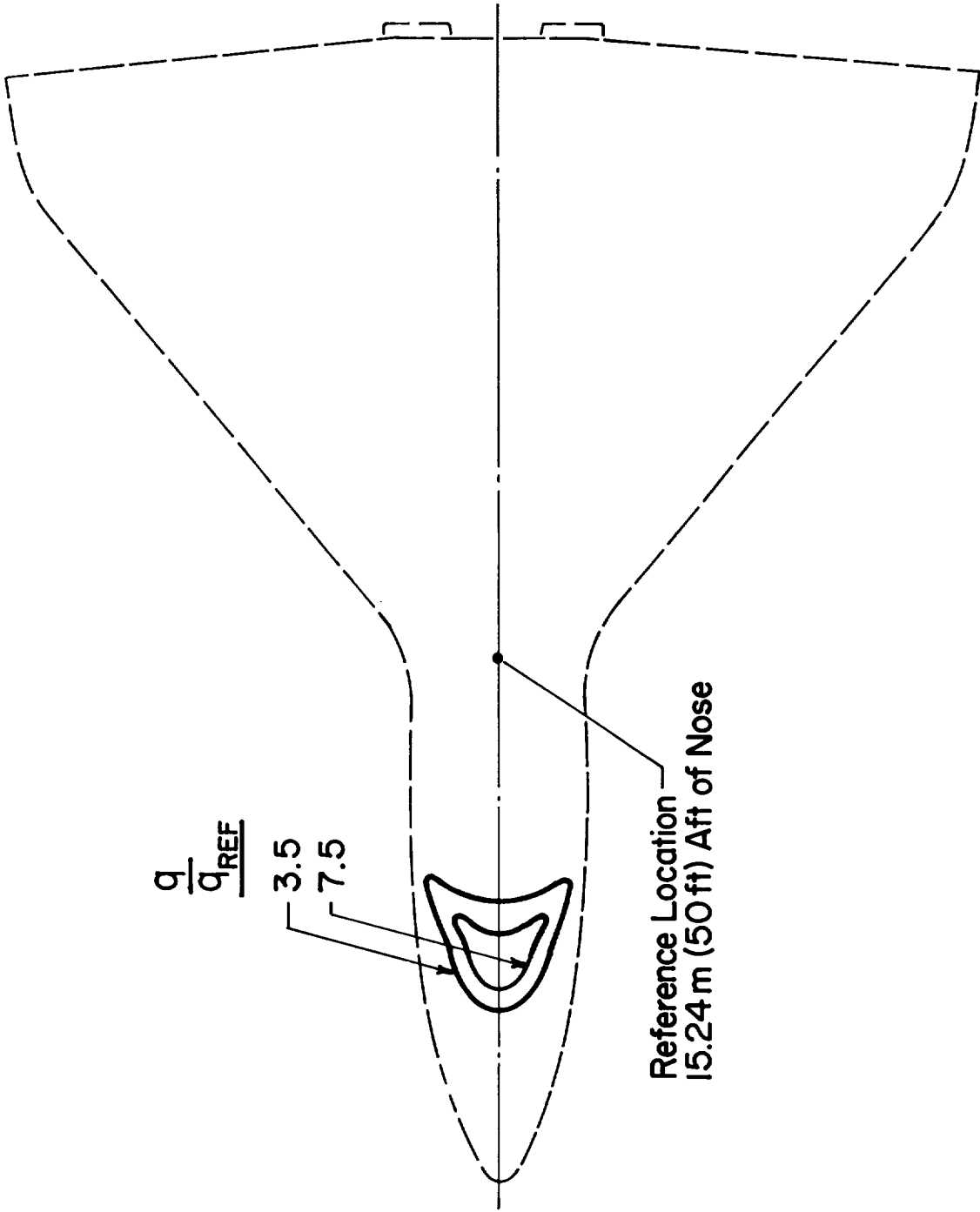


Figure 43.- Orbiter/External Tank Shock Interference Heating on Orbiter Lower Surface During Ascent

2. Local static pressures.- Local static pressure histories were obtained for the vehicle locations previously discussed for both ascent and entry using the methodology discussed in appendix B. These pressures were used to determine the heat shield design pressures presented in table 7 and also in the venting analysis of the standoff heat shield panels. Ascent local static pressures are presented in figure 44 while the entry static pressures are shown in figures 45 through 47.

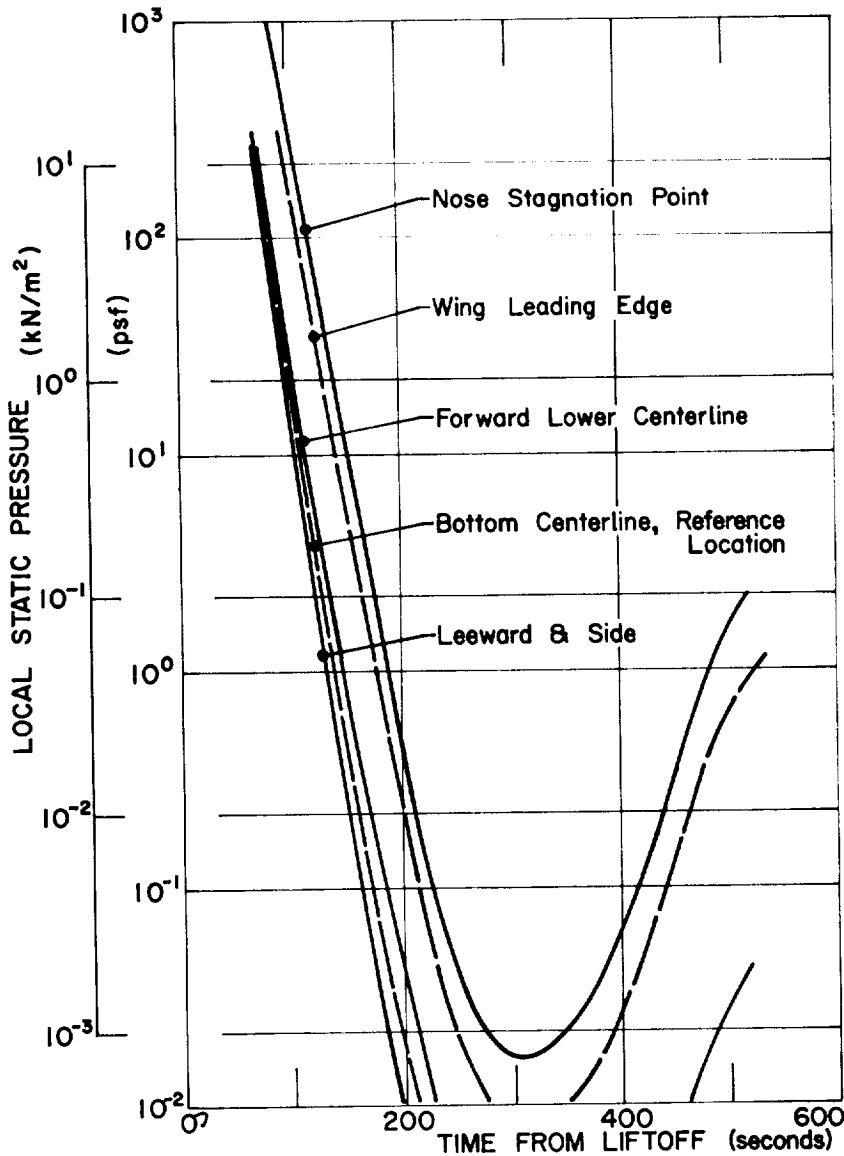
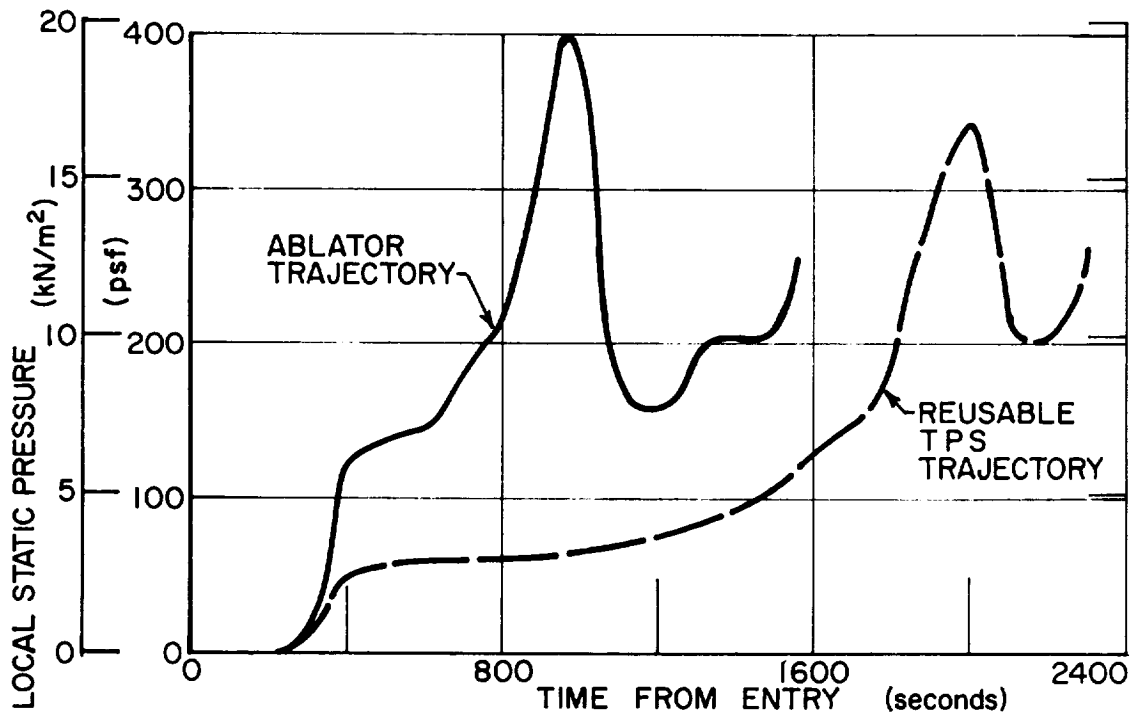
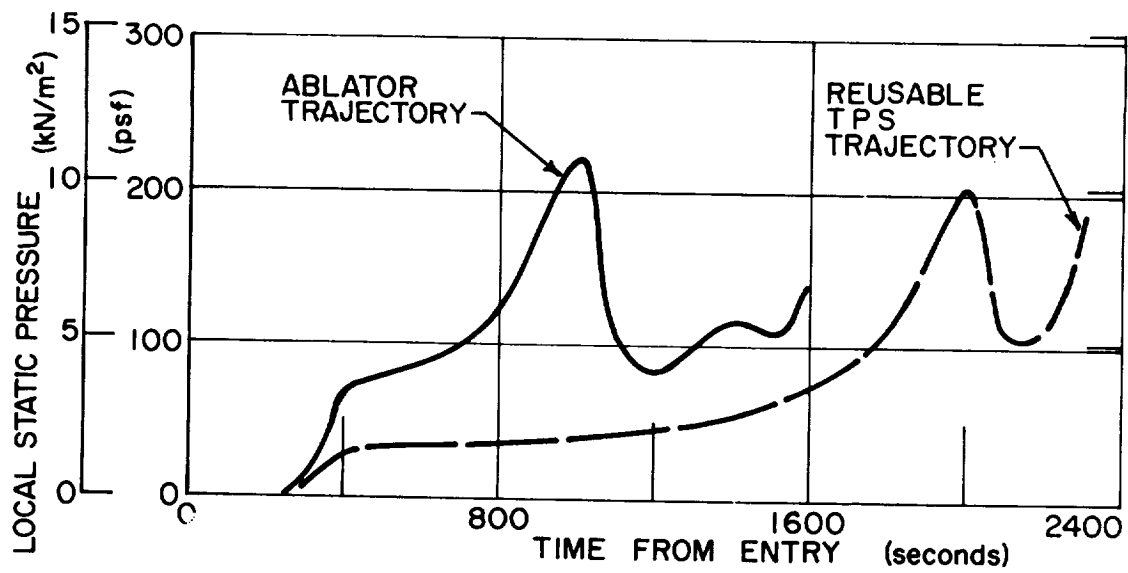


Figure 44.- Ascent Local Static Pressure History

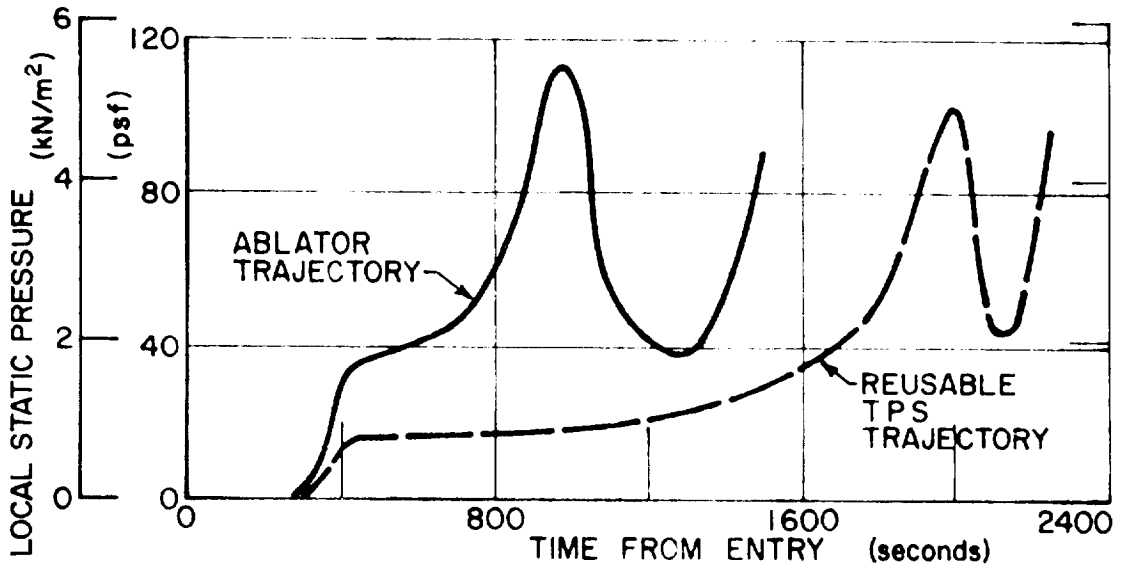


(a) Nose Cap

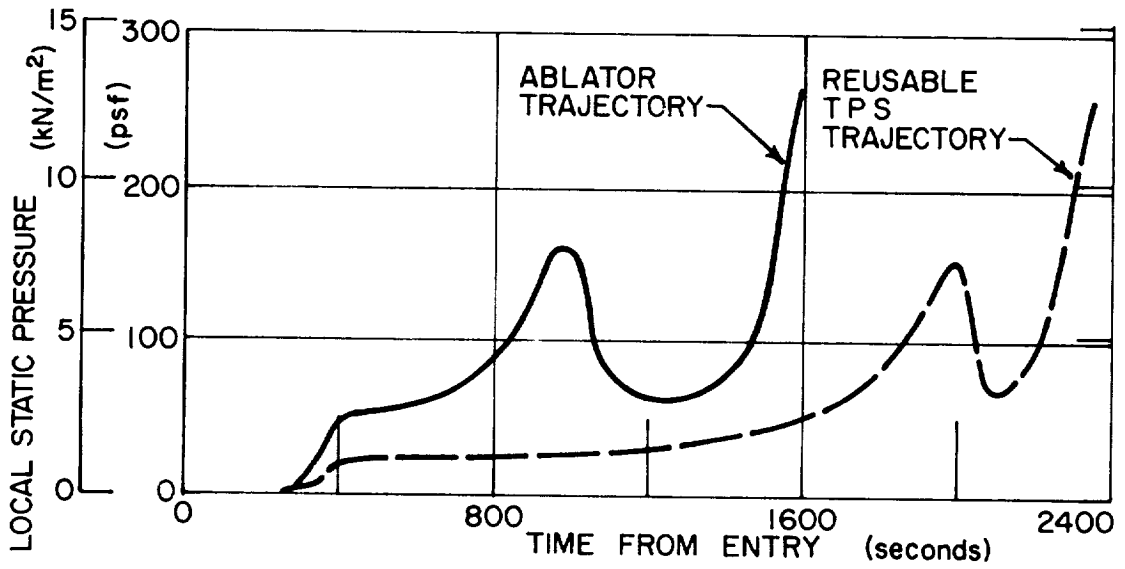


(b) Wing Leading Edge

Figure 45.- Entry Local Static Pressure Histories at Stagnation Regions



(a) Reference Location



(b) Forward Location

Figure 46.- Entry Local Static Pressure Histories along Body Lower Centerline

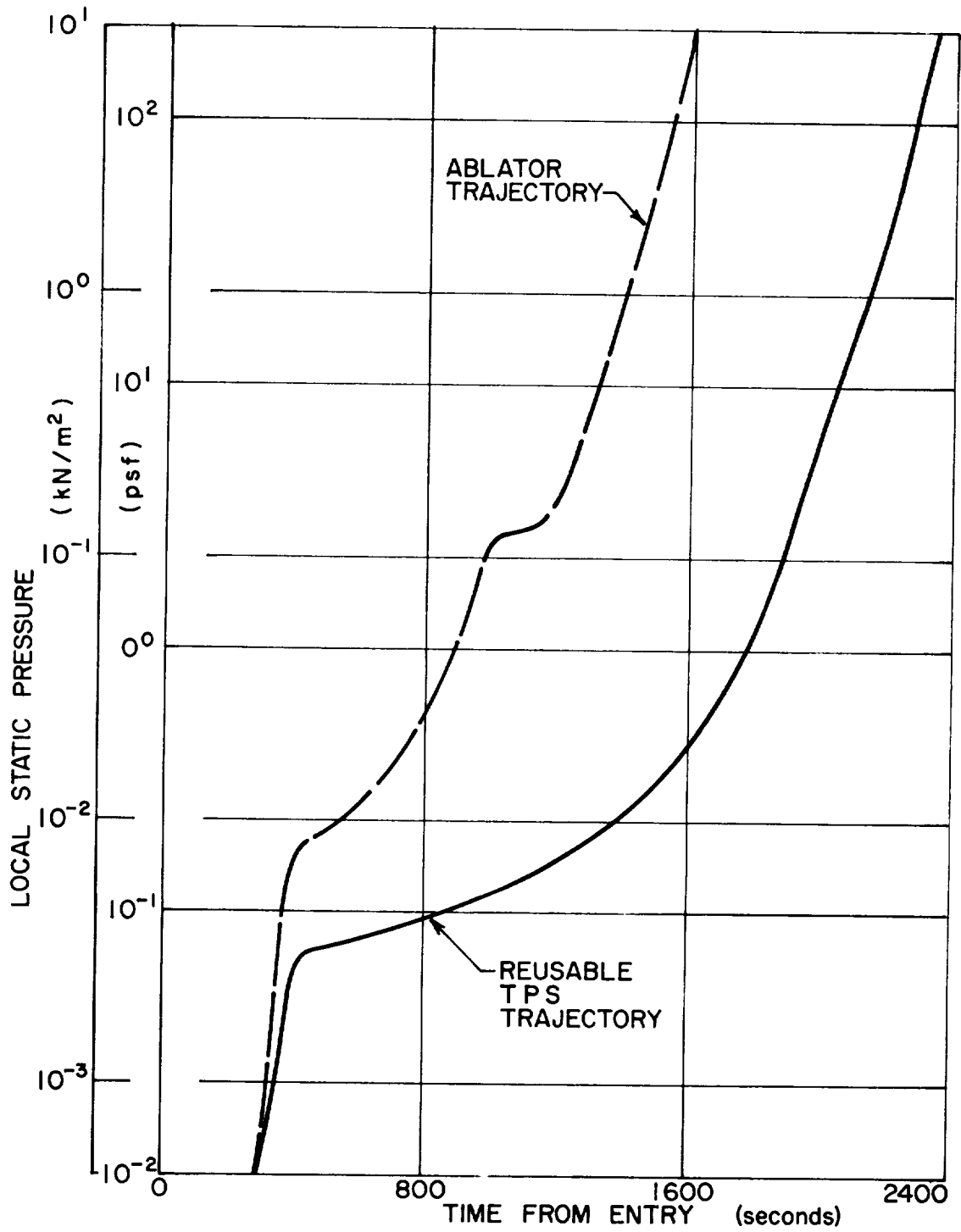


Figure 47.- Entry Local Static Pressure History at Leeward and Side Locations

3. Venting of standoff panels.- A venting analysis was performed for a typical standoff heat shield panel to determine if any of the panel design pressures as given in table 8 were exceeded for either ascent or entry. A typical panel 50.8 cm (20 in.) square with a standoff distance of 1.372 cm (0.54 in.) was chosen. The pressure differential ( $P_{\text{local}} - P_{\text{compartment}}$ ) was calculated based on an effective vent area of  $0.155 \text{ cm}^2$  ( $0.24 \text{ in.}^2$ ) for both ascent and entry for the bottom centerline reference location. Both positive (externally applied) and negative (internally applied) pressure differentials were assumed initially for both ascent and entry. In all cases, within several seconds the compartment vented to a pressure differential of  $\pm 6.895 \text{ N/m}^2$  ( $\pm 0.001 \text{ psi}$ ) and remained at this level throughout the trajectory. Since the maximum time rate of change of local pressure for the other locations listed in table 8 was four times the value at the reference location, it can conservatively be estimated that the maximum pressure differential is four times the reference point value. The effect of varying the volume is minimal. Thus, venting does not appear to be a problem for the standoff heat shield panels. Appendix B describes the pertinent equations and procedure used to perform the venting analysis.

#### IV HEAT SHIELD DESIGNS

With the establishment of a comprehensive design criteria, the achievement of shaped trajectories (one complementary to RSI TPS application and another taking advantage of inherent ablator TPS characteristics), and the definition of aerodynamic loads and heating histories (for each trajectory), the task of evaluating various ablative heat shield designs for the Space Shuttle Orbiter was undertaken.

The baseline vehicle was Grumman Orbiter Model 619, structurally defined as a semimonocoque aluminum construction using the conventional design approach of internal rings, frames, stringers, spars, etc., supporting a smooth exterior skin. This is the structure requiring thermal protection, primarily during mission reentry, to a maximum temperature of 450°K (350°F).

Two thermal protection systems were initially sized to establish baselines for subsequent comparisons with respect to vehicle TPS weight and/or program costs. These were: reusable surface insulation (RSI) attached to the aluminum exterior through a strain isolator system; and (2) Martin Marietta's ablator SLA-561 precast and bonded directly to the structure. In areas of high heating, alternative materials were added to each baseline, as indicated in table 13.

TABLE 13.- TPS MATERIALS<sup>a</sup> USED IN  
BASELINE DESIGNS

Region		RSI design	Ablator design
Nose cap		ESA-35-3560 HF	ESA-3560 HF
Wing leading edge	Upper	ESA-3560 HF	ESA-3560 HF
	Lower	ESA-3560 HF and ESA-5500M3	ESA-3560HF and ESA-5500M3
FIN		SLA-561	ESA-3560 HF
Acreage areas		LI-1500	SLA-561
<sup>a</sup> All materials indicated are Martin Marietta developed ablators except for thr RSI material LI1500.			

The RSI was Lockheed's LI-1500 [0.183 kg/m<sup>3</sup> (15 lb/ft<sup>3</sup>)], currently planned for the acreage areas of the Orbiter. The SLA-561 was originally developed for the Viking aeroshell TPS, scheduled for Mars entry in 1976. The special region ablators, all Martin Marietta materials, have a proven entry background on the PRIME vehicle.

The LI-1500 RSI modules require a thin outer coating for better emissivity characteristics and moisture-proofing. The SLA-561 ablator surfaces are coated with 0.127-cm (0.050 in.) thick DC 93-044 to provide an  $\alpha/\epsilon$  value of 0.31 for prelaunch environmental and orbital thermal control functions.

A summary of the Orbiter's TPS analysis points, configurations, and materials is presented in table 14. Eight locations on the vehicle exterior were selected for configuration tradeoff studies (fig. 48). These efforts concentrated on the four attachment configurations shown in figure 49: direct bond, direct attached plate, direct attached honeycomb subpanel, and standoff honeycomb subpanel. The tradeoff studies involved and integrated the disciplines of:

- 1) Detail design;
- 2) Feasibility, practicality considerations;
- 3) Stress analyses;
- 4) Thermal analyses;
- 5) TPS weigh-ins.

Discussions are presented in that sequence. The analyses uncovered areas requiring of experimental investigation and/or verification (Chapter V) and established the numbers for the TPS weight/program cost relationship analyses (Chapter VI).

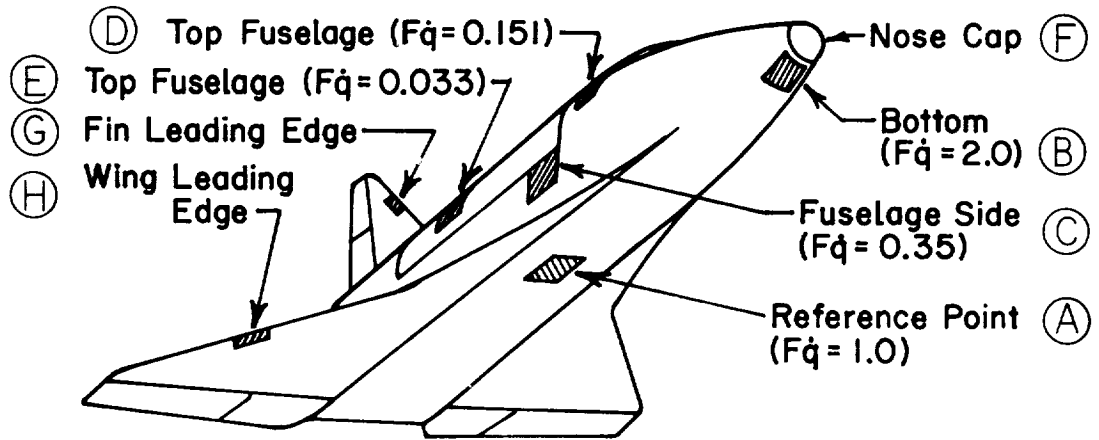


Figure 48.- Locations of Investigation Points

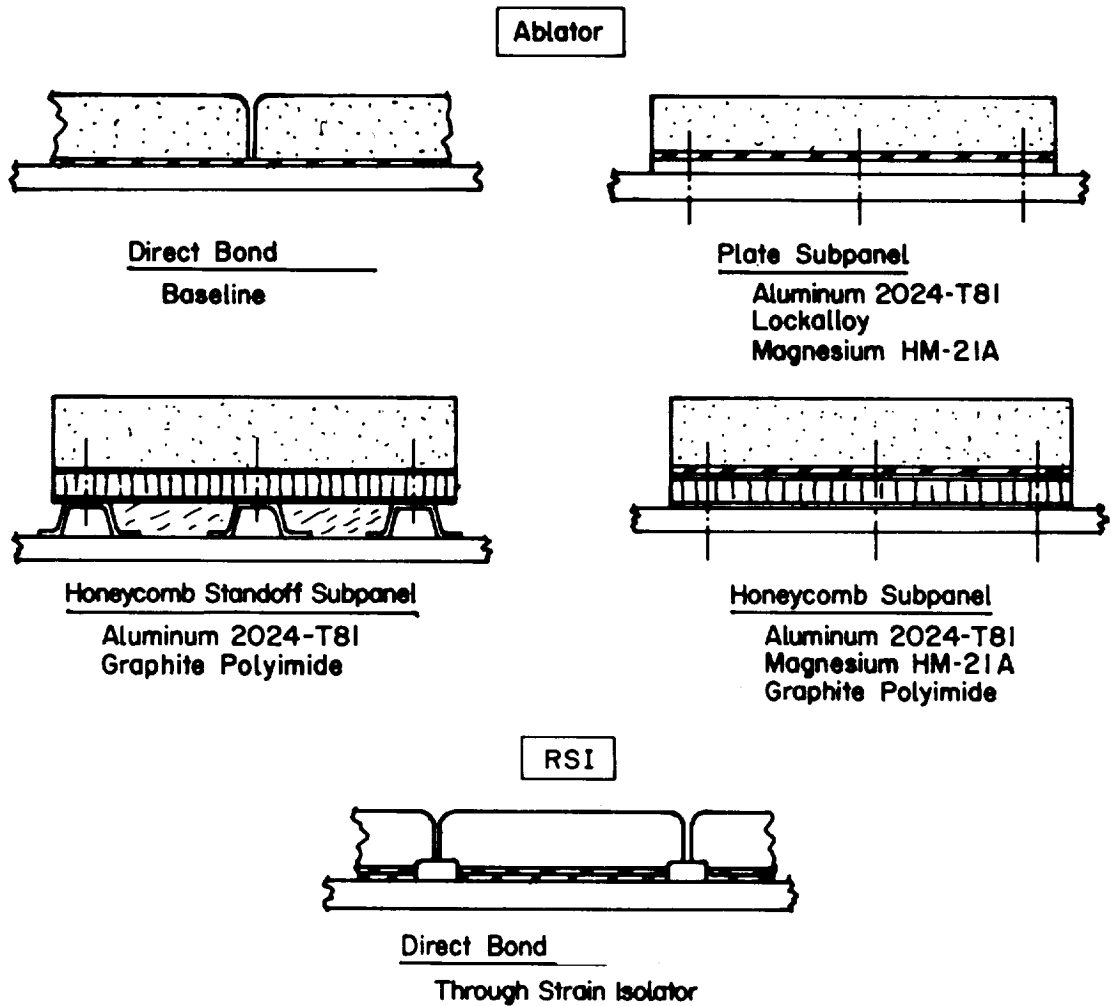


Figure 49.- Attachment Configurations

## A. Design Descriptions

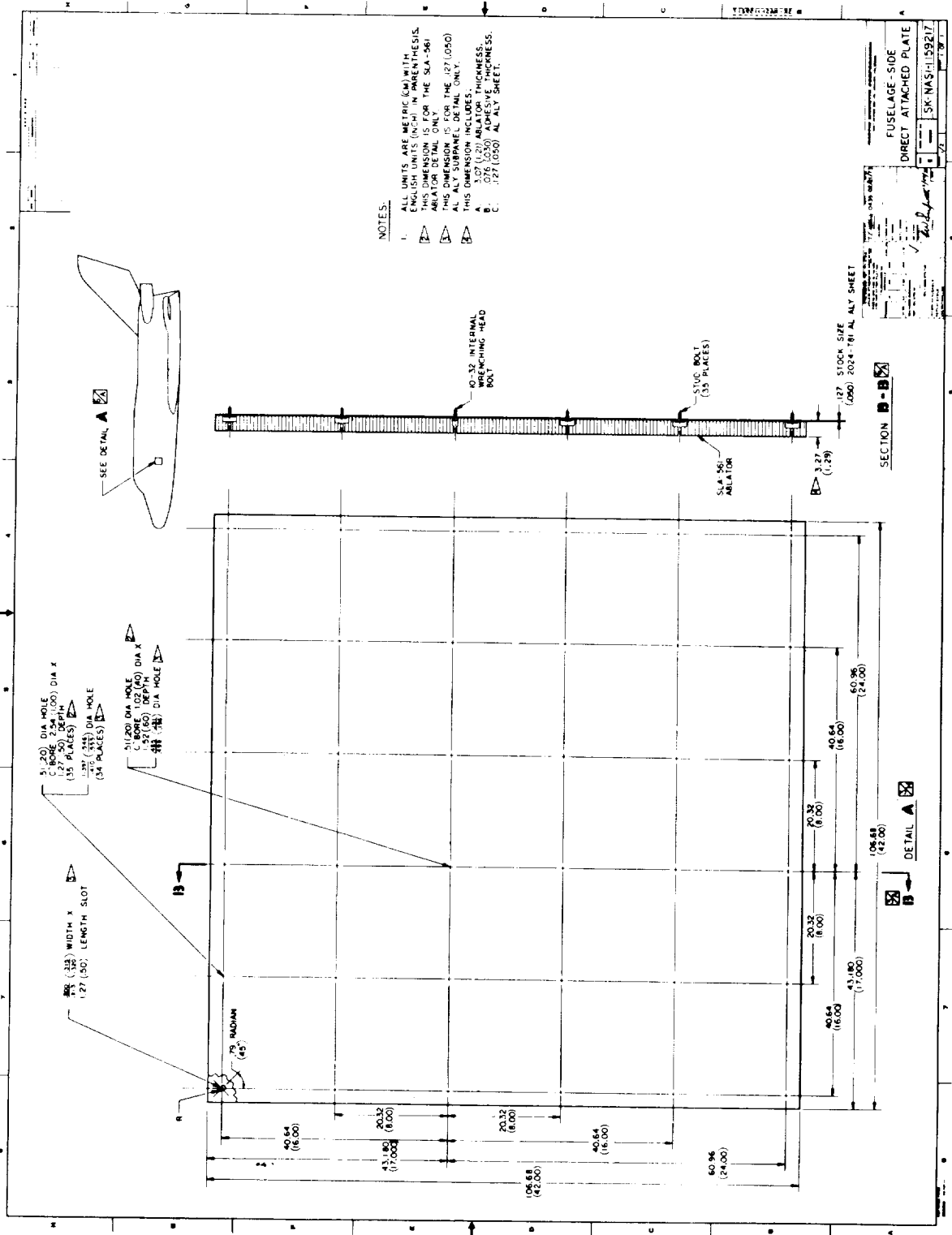
Depending on the location, one or more of the four TPS ablator attachment approaches of table 14 were applied. Presented here are summaries of the design details, materials required, gages, etc.

1. Side fuselage cabin area (point C).- The design for the side of the fuselage in the cabin area is illustrated in figure 50 as a direct attached aluminum alloy plate system. The panel is 106.68 cm (42.00 in.) square with no curvature. A 20.32-cm (8.00 in.) bolt spacing is shown for illustration only. The subpanel is a 0.127 cm (0.050 inch) 2024-T81 aluminum alloy sheet supporting a SLA-561 ablator thickness of 3.07 cm (1.21 in.). The backface of the subpanel is iridited to the specifications of reference 27 to increase radiation heat transfer from it to the vehicle structure.

The subpanel is mechanically attached directly to the orbiter structure with one centrally located fixed fastener ( to position the panel) and equally spaced floating fasteners. In addition, one fastener cutout in the subpanel corner is slotted to prevent panel rotation. A special fastener was designed to attach the subpanel to the Orbiter structure and to permit subpanel thermal expansion under the fastener head with the fastener torqued tightly to the structure (see fig. 51). Commercial standards do not include a lightweight fastener to perform this function without the need to limit the torque value to prevent clamping the subpanel. Since torquing 30 000 to 80 000 fasteners on each orbiter was considered impractical, the possible use of a commercial fastener was eliminated.

TABLE 14.- TPS CONFIGURATIONS AND MATERIALS

Location	TPS attachment configuration	Material	
		Subpanel	TPS
Reference point Sta 800 bottom fuselage centerline (point A)	Direct bond	None	SLA-561
	Direct bond	None	LI-1500
Max q for SLA-561 Sta 230 bottom fuselage centerline (point B)	Subpanel plate mechanically attached direct to Orbiter structure	Aluminum 2024-T81 Lockalloy Magnesium HM-21A	SLA-561
Side fuselage cabin Sta 495 WL 500 (point C)	Subpanel honeycomb mechanically attached direct to Orbiter structure	Aluminum faces 2024-T81 5052-H39	SLA-561
Sta 450 top fuselage centerline (point D)		Magnesium faces HM-21A Glass core HRH-327	
Forward of fin top fuselage centerline (point E)	Subpanel honeycomb mechanically attached through standoff fittings to Orbiter structure	Graphite polyimide faces Glass Glass core HRH-327	SLA-561
		Aluminum faces 2024-T81 Aluminum core 5052-H39  Graphite polyimide faces Glass core HRH-327	
Fuselage nose cap (point F)	Direct bond	None	SLA-561 ESA 3560HF ESA 5500  LI 1500 SLA-561 ESA 3560HF
Fin leading edge midspan (point G)	Direct bond	None	SLA-561 ESA 3560HF  LI 1500 SLA-561
Wing leading edge midspan (point G)	Direct bond	None	SLA-561 ESA 3560HF  LI 1500 SLA-561



(a) Direct attached Plate  
Figure 50.- Ablator Design, Fuselage Side



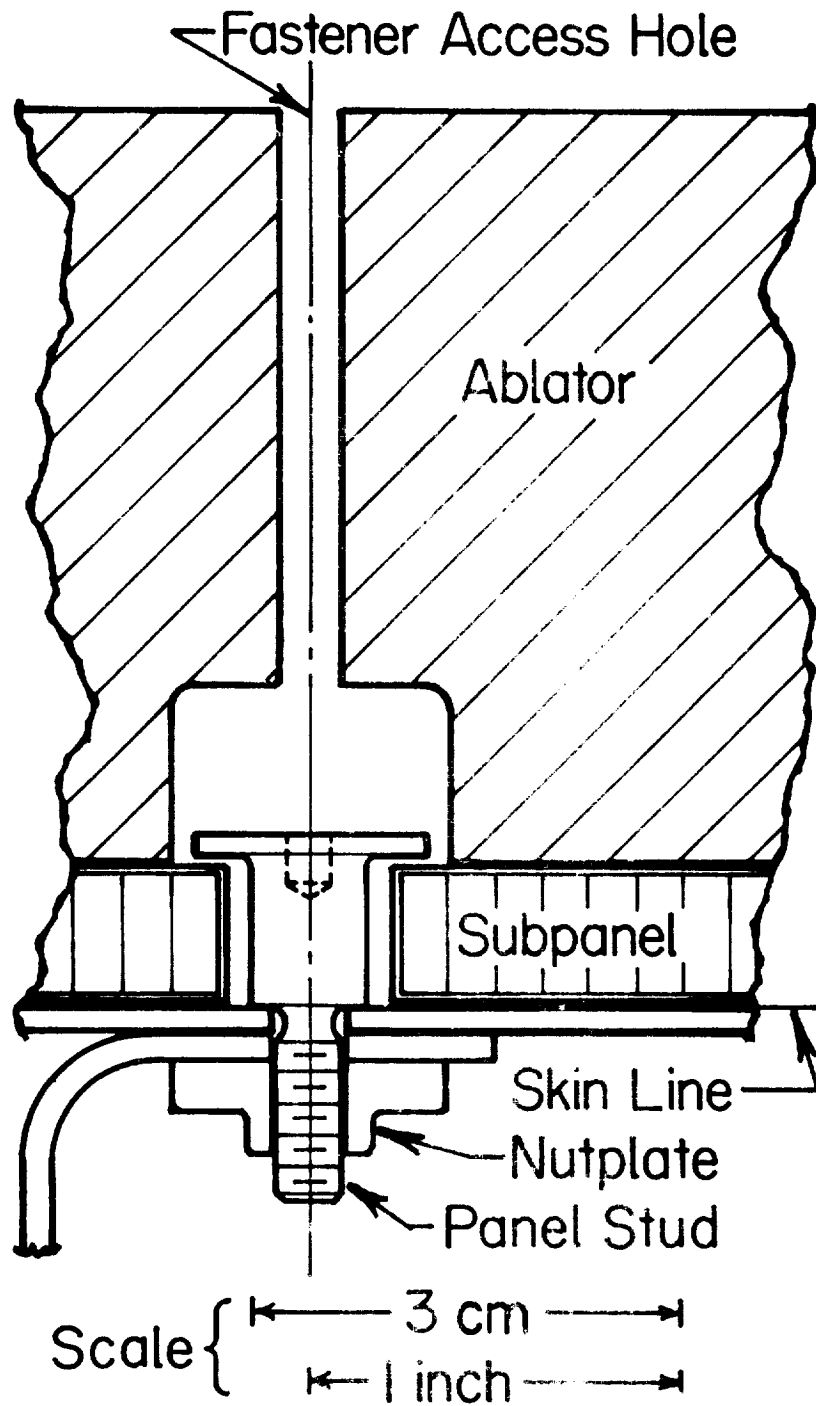


Figure 51.- Mechanical Fastener

2. Top fuselage, forward of fin (point fig.- Because of the low design heating rate in this area,  $15 \text{ kW/m}^2$  (1.31 Btu/ft<sup>2</sup>-sec), the SLA-561 ablator was considered for reuse incorporating the direct bond attachment design concept. This lead to the design drawing presented in figure 52.

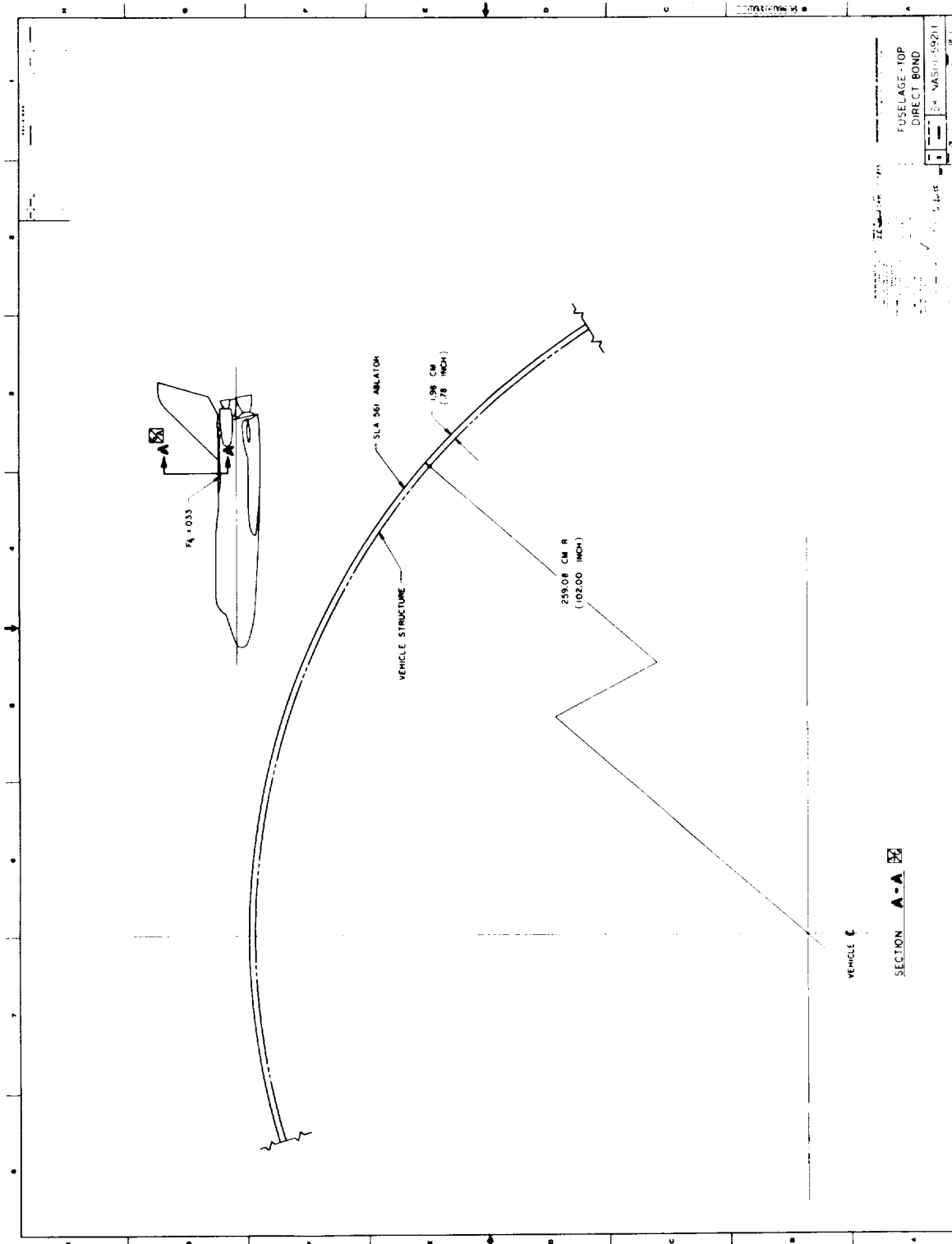


Figure 52.- Ablator Design, Fuselage Top,  $F_q = 0.033$ , Direct Bond

3. Bottom fuselage centerline (point A).- The first attachment configuration considered here was the subpanel honeycomb mechanically attached direct to the Orbiter structure. The honeycomb subpanel consists of 2024-T81 aluminum alloy 0.015-cm (0.006 in.) face sheets adhesively bonded to a core of 5052-H39 aluminum alloy 0.316 cm (0.125 in.) cell size with a density of 49.7 kg/m<sup>3</sup> (3.1 lb/ft<sup>3</sup>). The core edges are filled with HT-424 foam, Type 1 to form an edge member.

A 25.40-cm (10.00 in.) attachment grid was established using 3.16-cm (1.25 in.) diameter foam-filled areas to provide the bearing area for the fasteners. Oversized holes are drilled for the floating fasteners. The center fastener location is drilled to a shear tolerance to position the panel. One corner fastener location is slotted to prevent panel rotation. The subpanel backface is then iridited per reference 27.

The second attachment configuration is a direct mechanically attached subpanel plate. The subpanel plate is attached to the Orbiter structure in a manner similar to the honeycomb subpanel configuration.

The third TPS attachment configuration for the reference point is the graphite polyimide honeycomb standoff panel design (fig. 53). The honeycomb subpanel is flat 106.68 cm (42.00 in.) square with 0.028-cm (0.011 in.) face sheets and 1.40-cm (0.55 in.) thick Hexcel HRH 327 core. Fastener locations and edges are reinforced with HT-424 foam, Type 1. A 25.40-cm (10.00 in.) fastener spacing is illustrated.

The honeycomb subpanel backface temperature limit is increased from 450°K (350°F) to 589°F (600°F). This requires 1.04 cm (0.41 in.) of microquartz insulation to keep the vehicle structure temperature to the baseline of 450°K (350°F). The subpanel is attached to the standoff post with the floating stud bolt fastener.

4. Bottom centerline (point B).- The TPS attachment concept is a direct attached honeycomb subpanel with double curvature (fig. 54). The dimensions of the subpanel are 106.68 cm (42.00 in.) square. The subpanel is constructed with 0.013 cm (0.005 in.) 2024-T81 aluminum alloy face sheets and 0.457 cm (0.180 in.) 5052-H39 aluminum alloy Hexcel core. The fastener locations and edges are reinforced with HT-424 foam, Type 1. Fasteners are shown spaced at 25.40 cm (10.00 in.).





5. Fin leading edge (point G).- The fin leading edge design concept is shown in figure 55 for both the ablator and RSI trajectory requirements. Construction of the direct bond ablator support is a skin-frame panel 106.68 cm (42.00 in.) long with frames on a 25.40-cm (10.00 in.) spacing. The ablator is directly bonded to the aluminum alloy skin. The panels extend aft to the 5% chord line. Alternate segments overlap at both ends. The removal of the overlapping sections permits removal of the intermediate section. Fasteners attaching the leading edge are accessible through the outer ablator surface through access holes in the ablator.

6. Wing leading edge (point H).- The TPS attachment concept involves a removable and replaceable ablator panel section fastened to the wing structure forward of the wing front spar (fig. 56). The fastener interface plane is angled because the entry heating stagnation point is on the lower side of the wing leading edge. An ablator covered subpanel system is used aft of the removable leading edge for the all-ablator design. Access to the internally located fasteners is permitted by removal of the lower ablator subpanel forward of the spar, exposing an access door in the wing. (An alternative design for this access panel incorporates the removable ablator subpanel with the structure skin panel.)

The leading edge sections are 106.68 cm (42.00 in.) long. The substructure is an aluminum skin stiffened with formers with an upper and lower stringer for attachment points to interface with the wing structure.

A combination of three ablators is used to satisfy the ablator trajectory heating requirements. The ESA 5500 ablator extends both leeward and windward from the entry stagnation point along the aerodynamic surface 8.84 cm (3.48 in.). The ESA 3560HF extends leeward from the ESA 5500 7.92 cm (3.12 in.). The remaining ablator is SLA-561. (These are aerodynamic skin line measurements along a buttline cut at the wing midspan.)

The RSI trajectory leading edge is similar to the ablator trajectory leading edge and the fastener interface plane is the same as the ablator system. The differences appear in the types and thicknesses of the thermal protection materials used. The ESA 3560HF extends 12.19 cm (4.80 in.) leeward and windward from the entry stagnation point. The remaining portion of the leading edge ablator is SLA-561. The removable subpanel TPS is also SLA-561 and extends aft along the lower surface 92.96 cm (36.60 in.). The remaining TPS is directly attached LI-1500.



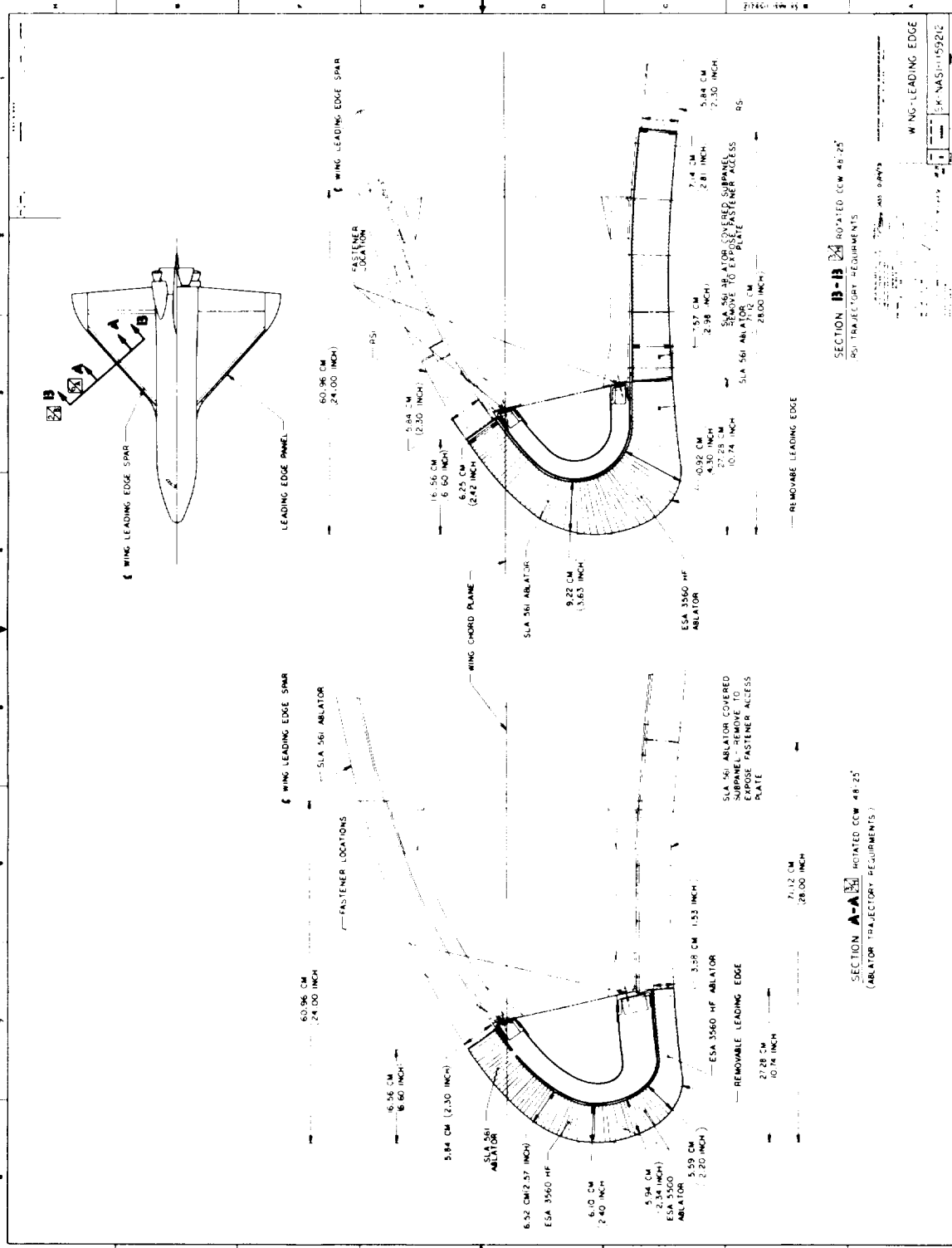


Figure 56.- TPS Design, Wing Leading Edge

7. Nose cap (point F).-- The nose cap TPS configurations considered were direct bond and direct attached subpanel. The direct bond configuration consists of a direct bond of the ablator to a fixed Orbiter skin with the refurbishment at the skin level. The direct attached subpanel configuration consists of bonding the ablator to a removable section of Orbiter structure which is refurbished or discarded following each mission (fig. 57).

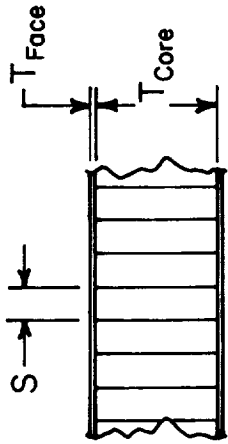
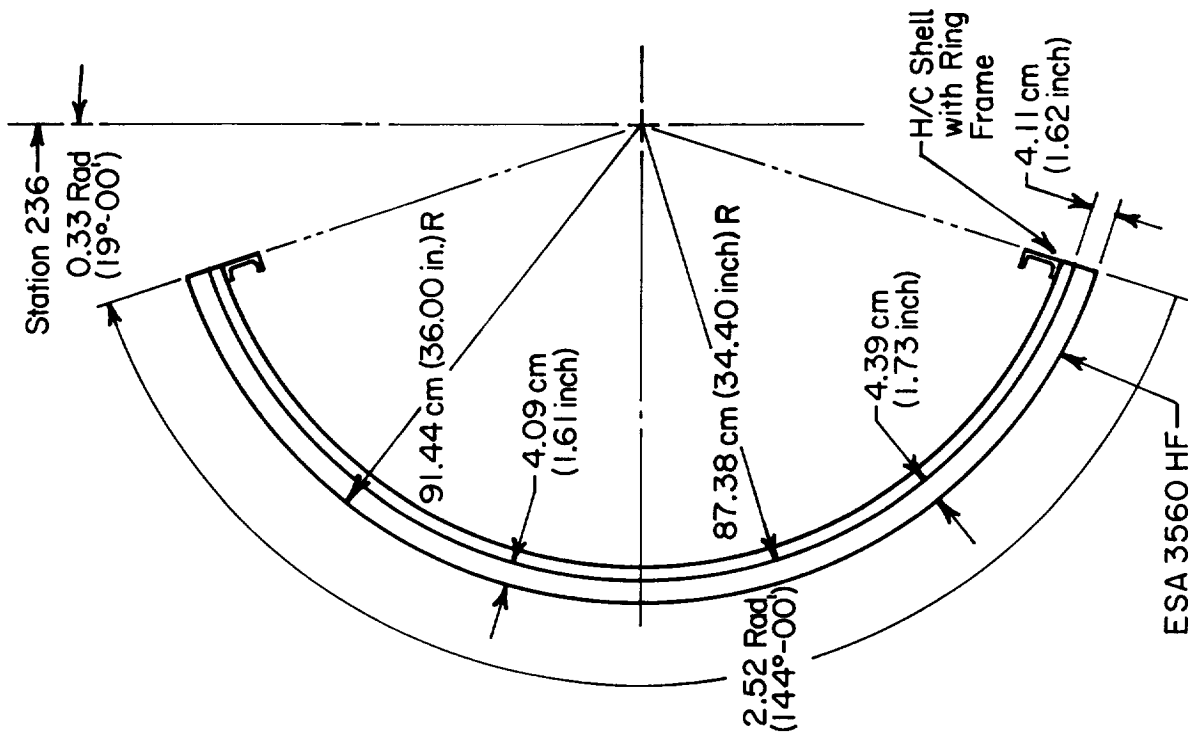
Two structural designs were considered for this removable Orbiter structure or spherical dome cap. These were a honeycomb sandwich spherical dome and a rib-supported sheet spherical dome. These dome caps encompass the total spherical section of the fuse-lage nose cap area, taking advantage of the strength-to-weight ratio of the spherical structure. The lightest structure is the aluminum sandwich spherical dome. This is a honeycomb shell with a continuous ring frame at the aft structural interface plane. In the rib-supported spherical dome, the ribs are structurally continuous through the center and are tied to a ring frame at the aft interface plane.

These structural designs are independent of the ablator material and thickness requirements that are specific for the mission trajectory. The ablator trajectory nose cap will be all ESA 3560HF ablator. The RSI trajectory nose cap will be all SLA-561 ablator.

The spherical dome nose cap is attached to the vehicle structure at an interface plane determined by the RSI mold line requirements. It can accommodate both the ablator and the RSI trajectory requirements.

#### B. Subpanel Selections

Numerous ablator heat shield support configurations and material combinations were considered, as indicated in table 15. The final selection of the subpanels to be carried through the remainder of the study was based on the factors of feasibility, costs, fabricability, and potential weight efficiency with respect to strengths, moduli, and heat capacities.



Configuration	T face, cm (in.)	T core, cm (in.)	S, cm (in.)	Wt-core, kg/m <sup>3</sup> lb/ft <sup>3</sup>
Al alloy faces & core	.025 (.010)	2.380 (.937)	.319 (.125)	49.7 (3.1)
Graphite polyimide faces & HRH	.041 (.016)	3.414 (1.344)	.476 (.187)	48.1 (3.0)
Titanium (6Al-4V) faces & core	.025 (.010)	1.753 (.690)	.476 (.187)	11.4 (4.9)
Glass phenolic faces & HRH 327 core	.051 (.020)	4.882 (1.922)	.476 (.187)	48.1 (3.0)

Figure 57.- TPS Design, Fuselage Nose Cap

TABLE 15.- SELECTION OF SUBPANELS FOR TRADEOFF STUDIES

Location	Configurations of support	Materials of Support	
		Preliminary	Final
Orbiter fuselage acreage areas (points A through E)	Ablator bonded to plate subpanels mechanically attached directly to the Orbiter structure.	2024-T81 HM-21A Lockalloy Beryllium Glass phenolic Graphite polyimide	2024-T81 HM-21A Lockalloy
	Ablator bonded to honeycomb sandwich subpanel mechanically attached directly to the Orbiter structure.	2024-T81 HM-21A graphite polyimide beryllium Lockalloy	2024-T81 HM-21A Graphite polyimide
	Ablator bonded to honeycomb sandwich subpanels mechanically attached through standoff fittings to the Orbiter structure.	2024-T81 Graphite polyimide HM-21A Titanium	2024-T81 Graphite polyimide
Fuselage nose cap (point F)	Ablator bonded to formed sheet monocoque nose cap		2024-T81 Titanium Graphite polyimide Glass phenolic
	Ablator bonded to honeycomb nose cap		2024-T81 Titanium Graphite polyimide Glass phenolic
	Ablator bonded to rib stiffened nose cap		2024-T8

C. Stress Analysis

Stress analysis of the ablator attachment alternatives for the acreage areas of the fuselage was accomplished with the aid of the computer program described in the appendix C. The nose cap was analyzed in the conventional manner (without computer utilization), and is also outlined in the appendix.

1. Load conditions.- The loads and environmental conditions used in the stress analysis of the ablator support structure are presented in table 16. Aerodynamic pressures, the equivalent static loads for acoustic pressures, flutter criteria, flutter conditions, ablator strain criteria and the natural environments that must be considered in the design and analysis of the thermal protection system were reviewed to determine design conditions.

TABLE 16.- DESIGN LOADING CONDITIONS

Configuration	Design condition	Design load	Design criteria reference
Plate subpanel mechanically attached directly to Orbiter structure	Plate bending stiffness	$\delta = 0.0125 \lambda$	Service life strength analysis
	Ablator strain limit of 1%	Airload (limit) = 3.45 kN/m <sup>2</sup> (0.5 psi)	Service life ablator strain Environments pressures
Honeycomb sub-panel mechanically attached directly to Orbiter structure	Intracell buckling of face sheet	Airload (ult) = 4.83 kN/m <sup>2</sup> (0.7 psi)	Environments pressures
Honeycomb sub-panel mechanically attached through standoff fittings to Orbiter structure	Intracell buckling of face sheet	Airload (limit) = 20.7 to 27.6 kN/m <sup>2</sup> (3 to 4 psi)	Environments pressures
	Ablator strain limit of 1% Panel flutter	Airload (ult) = 29.0 to 38.6 kN/m <sup>2</sup> (4.2 to 5.6 psi) $I = C\lambda^3/E$	Service life ablator strain Environments acoustics

The direct attached plate subpanels were designed by aerodynamic surface waviness limitations and by ablator strain limitations under aerodynamic pressures. The direct attached honeycomb subpanels are strength critical for aerodynamic pressures. The standoff attached honeycomb subpanels are strength critical for aerodynamic pressures and stiffness critical for panel flutter.

2. Method of analysis.- The minimum weight ablator subpanel configurations were determined by a computer program considering three modes of failure (appendix C).

- 1) Allowable strain of 1% in the ablator outer surface at ultimate load (plate and honeycomb sandwich subpanels);

- 2) Failure of the honeycomb sandwich subpanel face by face wrinkling;
- 3) Failure of the honeycomb sandwich subpanel face by intracell buckling.

Program inputs included ablator material properties and thicknesses, facing material properties and thicknesses, core material properties and cell sizes, and a range of bending moments. The range of bending moments was determined by considering the subpanel to be a continuous rectangular plate supported by rows of equidistant supports. The subpanels were subjected to acoustic and/or aerodynamic pressures at the corresponding temperature levels for these conditions.

The program optimized the subpanel by matching a configuration allowable bending moment with the maximum required bending moment.

The fuselage nose cap honeycomb sandwich and the formed sheet configurations were analyzed as spherical plate caps with a uniform external pressure distribution.

3. Summary of results.— The data resulting from the study analyses performed are summarized in table 17 and appendix C. These data present the required subpanel sizes for the various fastener spacing patterns and the various configurations studied at each of the four fuselage locations considered.

TABLE 17.— SUBPANEL GAGES REQUIRED FOR DIRECT ATTACHMENT APPLICATION

Subpanel a thickness identification	Attachment fastener spacing	Material	Vehicle station, cm(in.)	
			Nose <sup>a</sup> cap	584 to 2032 (230 to 800)
Plate thickness, cm(in.)	12.7 (5.0)	Aluminum	0.965 (0.380)	0.079 (0.031)
		Magnesium	---	0.091 (0.036)
		Lockalloy	---	0.058 (0.023)
Honeycomb, each face thickness, cm(in.)	25.4 (10.0)	Aluminum	0.025 (0.010)	0.013 (0.005)
		Magnesium	---	0.020 (0.008)
		Graphite	0.041 (0.016)	0.020 (0.008)

<sup>a</sup>Attachment fastener spacing does not apply for nose cap  
See appendix C for additional information

#### D. Thermal Analysis

The temperature response, thermal protection contribution, and required thickness of every component of each of the postulated combinations in tables 14 and 15 were evaluated using the thermal models, computer programs, and rationales presented in appendix D. The primary material design charts were the principal outputs of the thermal effort encompassing ablator and RSI designs. The analytical assumptions necessary to initiate the study were as follows:

- 1) Temperature distribution at the start of entry was uniform at 311°K (100°F);
- 2) Heat transfer through sandwich subpanels assumed conduction through the core coupled with radiation ( $VF = 1.0$ ) between the faces;
- 3) Heat transfer across the subpanel-primary structure faying surfaces assumed intimate contact and 100% conduction;
- 4) Primary material was sized based on a 450°K (350°F) peak structure temperature;
- 5) The structure was considered to be adiabatic;
- 6) The entire surface of the SLA-561 ablator was covered with the DC93-044 coating; the RSI, an emissivity coating;
- 7) Heating factors of safety and heating rates were as outlined in table 18;
- 8) Heating factors in the design curves must be increased by the appropriate safety factor. The curves are valid for  $SF \times \dot{F}q \leq 2.30$ . Interpolation between substructure thicknesses was considered permissible.

##### 1. Acreage area analysis.-

All-ablator designs: The thickness requirements of SLA-561 when considering direct bonding, plate subpanels directly attached, and honeycomb subpanels directly attached are presented in figures 58 to 64 for the large expanses of the Orbiter surface, bounded somewhat by several fixed subpanel gages. For subpanel and primary structural material and thicknesses other than shown on the ablator requirements curves, ablator thicknesses can be determined from the curves in figures 65 and 66.

TABLE 18.- DESIGN LOCATIONS AND HEATING LOADS

Point	Location	Heating factor of safety	Fq normalized to ref. point	Entry heating rates design, kW/m <sup>2</sup> (Btu/ft <sup>2</sup> -sec)	
				Ablator	RSI
A	Reference point Sta 800 Bottom fuselage centerline	1.15	1.00	341 (30)	170 (15)
B	Max q for SLA-561 Sta 230 Bottom fuselage centerline	1.15	2.00	681 (60)	341 (30)
C	Side fuselage cabin Sta 495, WL 500	1.32	0.35	139 (12.2)	68 (6)
D	Sta 450 Top fuselage centerline	1.50	0.150	68 (6)	34 (3)
E	Forward of fin Top fuselage centerline	1.50	0.033	15 (1.31)	7.5 (0.66)
F	Fuselage nose cap	1.15	N/A	1230 (108)	816 (72)
G	Fin leading edge midspan	1.15	N/A	965 (85)	500 (44)
H	Wing leading edge midspan	1.15	N/A	1370 (121)	953 (84)

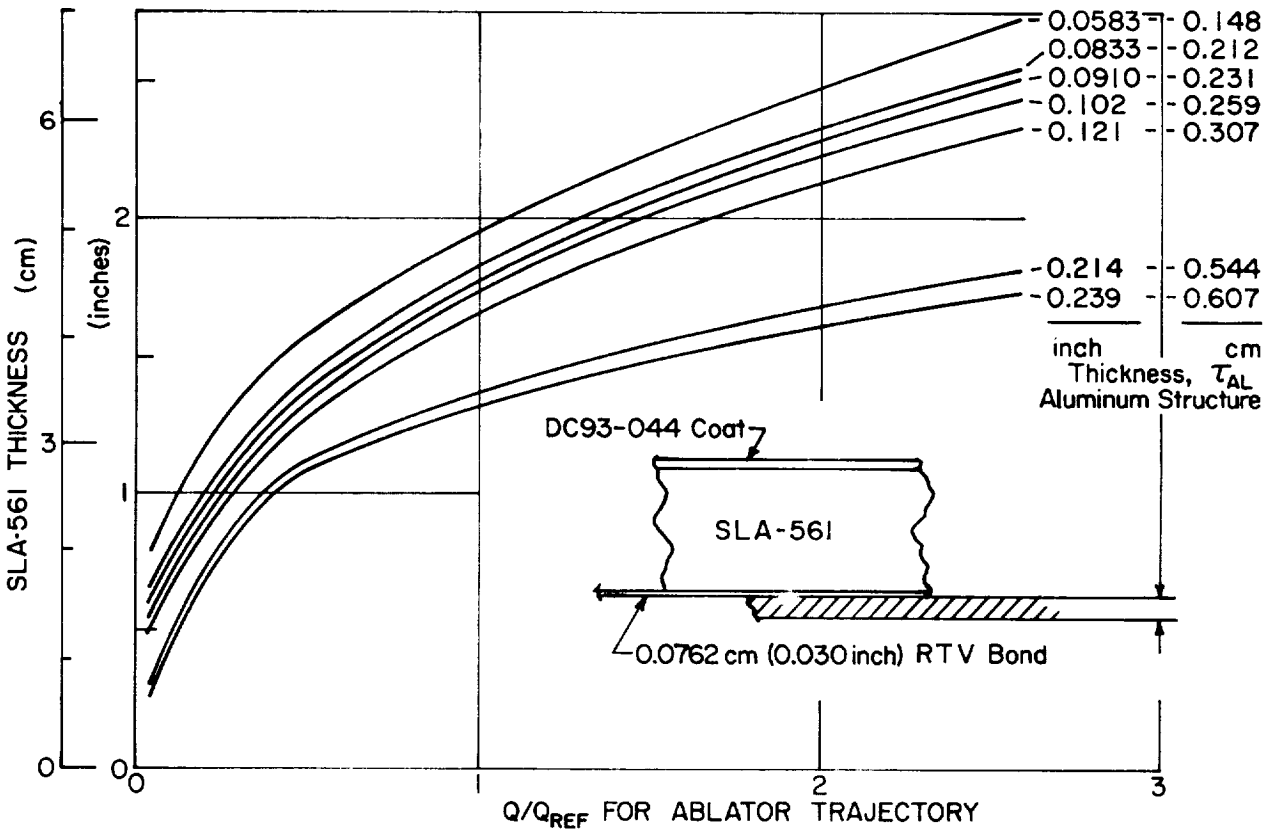


Figure 58.- SLA-561 Ablator Requirements, Direct Bond to the Orbiter Structure

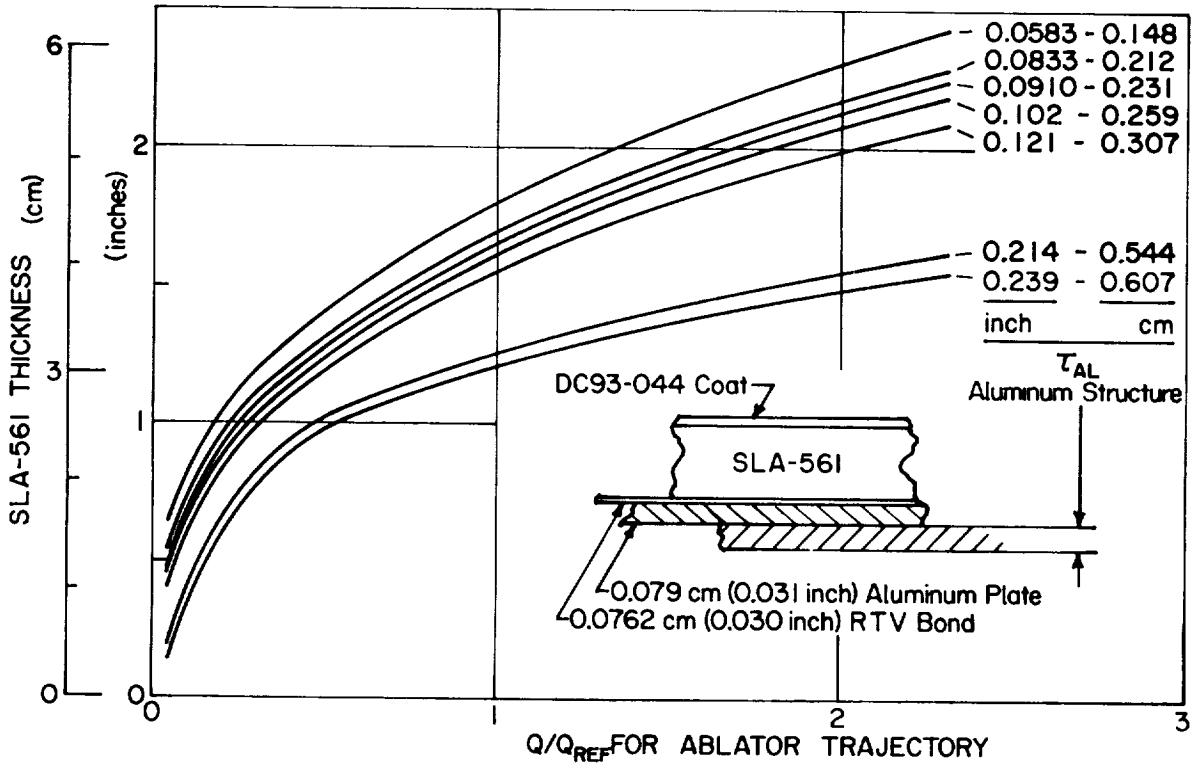


Figure 59.- SLA-561 Ablator Requirements, Aluminum Subpanel Mechanically Attached Directly to the Orbiter Structure

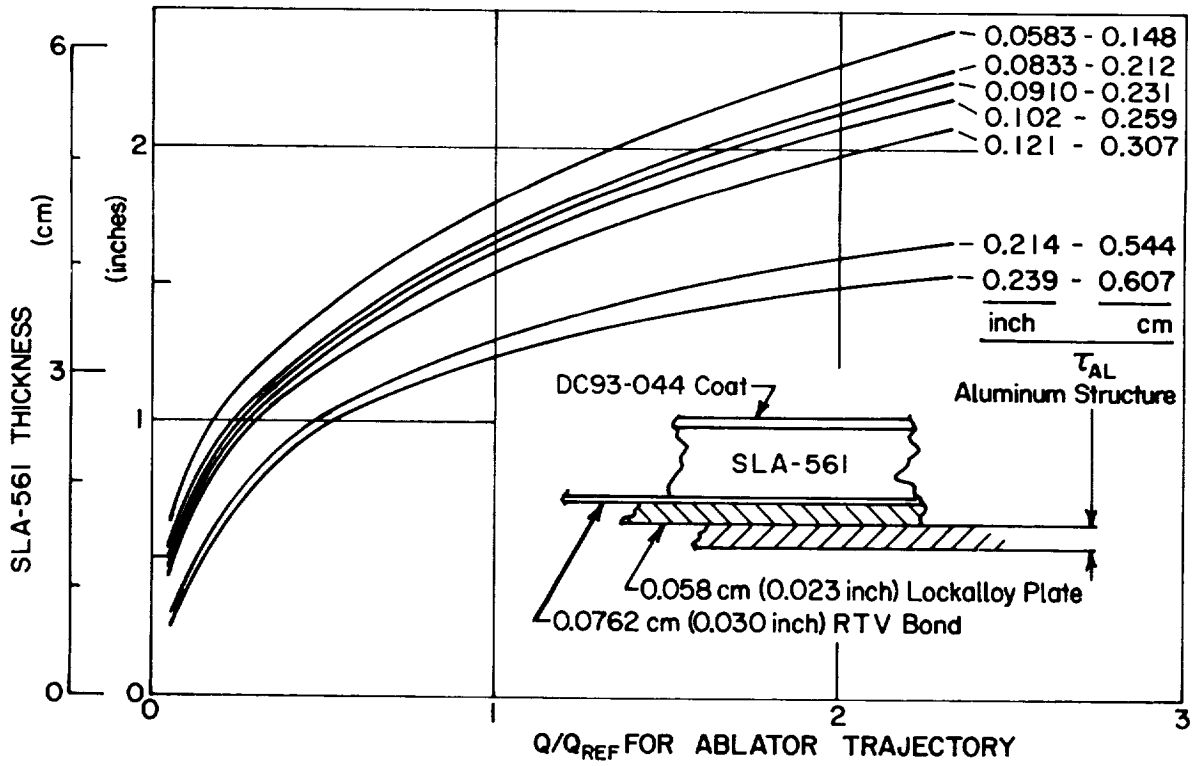


Figure 60.- SLA-561 Ablator Requirements, Lockalloy Subpanel Mechanically Attached Directly to the Orbiter Structure

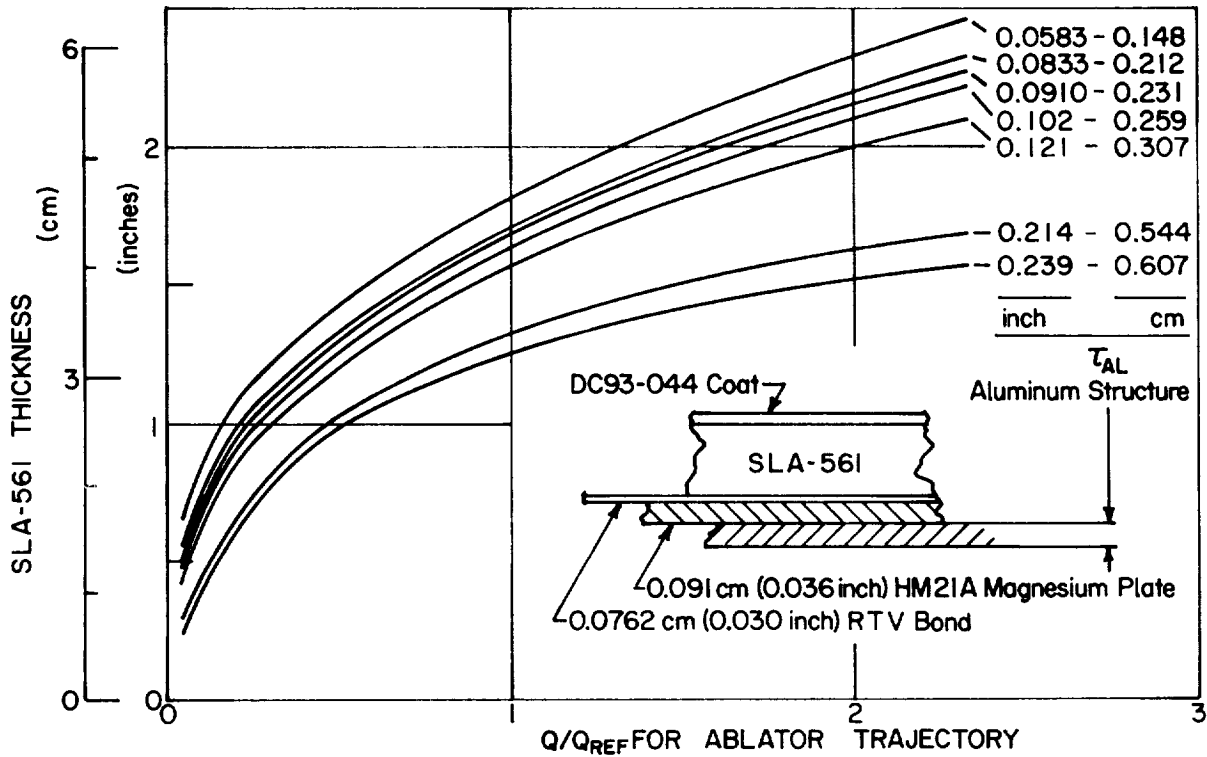


Figure 61.- SLA-561 Ablator Requirements, Magnesium Subpanel Mechanically Attached Directly to the Orbiter Structure

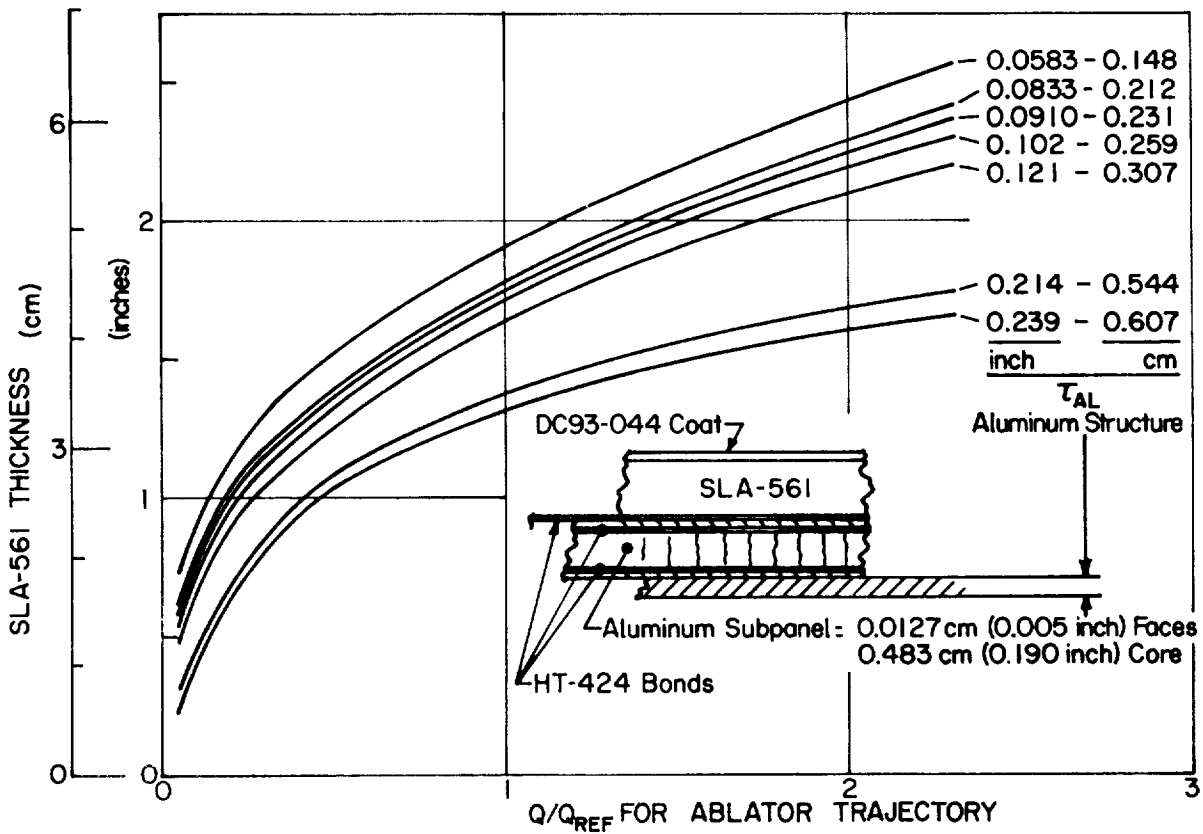


Figure 62.- SLA-561 Ablator Requirements, Aluminum Honeycomb Subpanel Mechanically Attached Directly to the Orbiter Structure

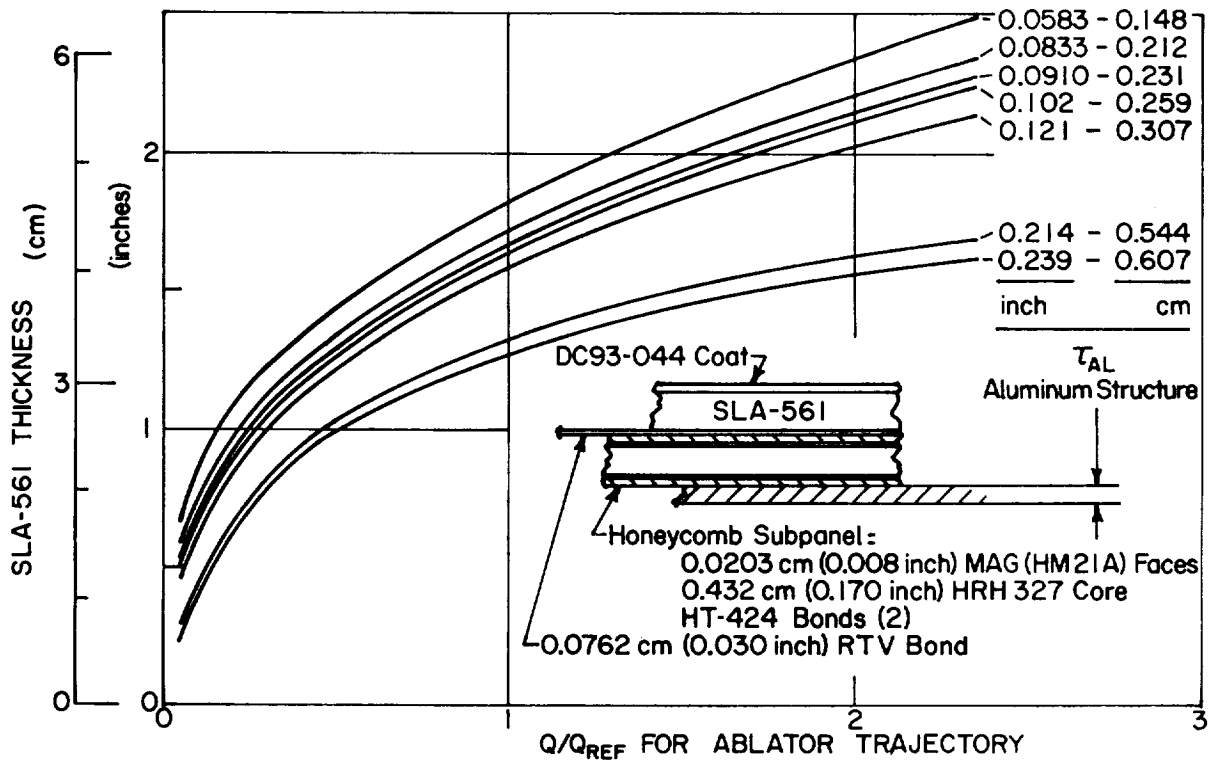


Figure 63.- SLA-561 Ablator Requirements, Magnesium Honeycomb Subpanel Mechanically Attached Directly to the Orbiter Structure

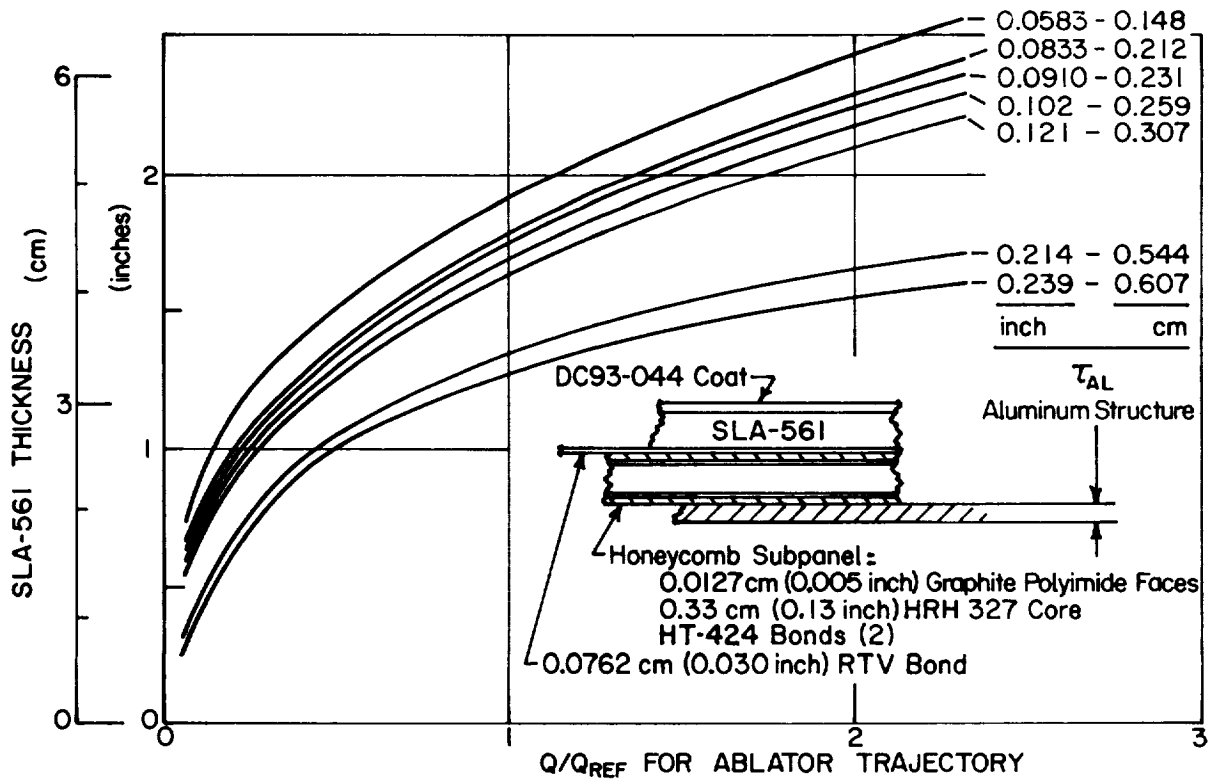


Figure 64.- SLA-561 Ablator Requirements, Graphite/Polyimide Honeycomb Subpanel Mechanically Attached Directly to the Orbiter Structure

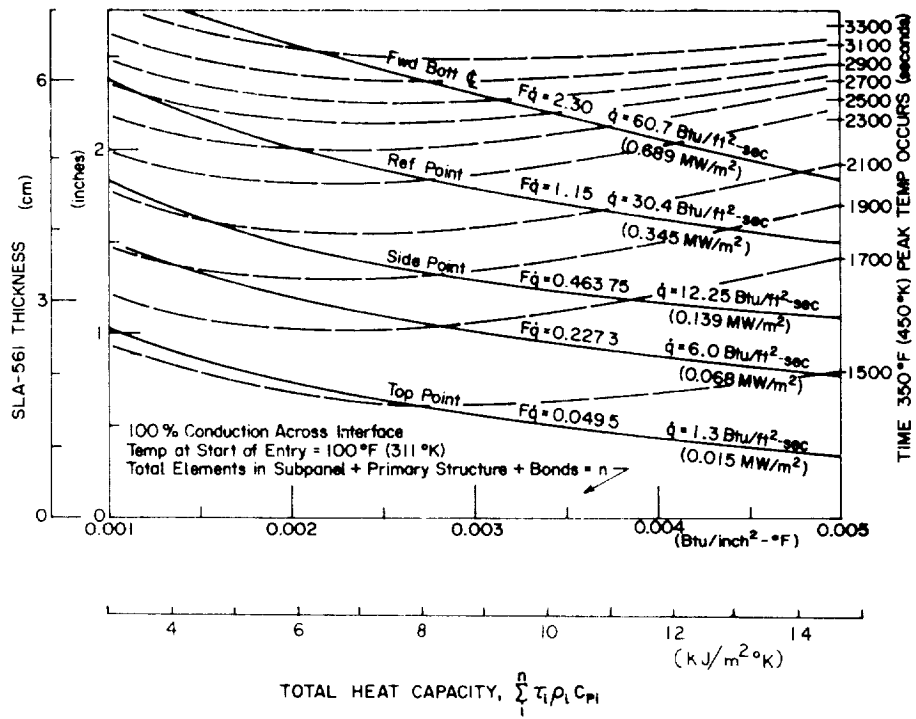


Figure 65.- SLA-561 Design Chart

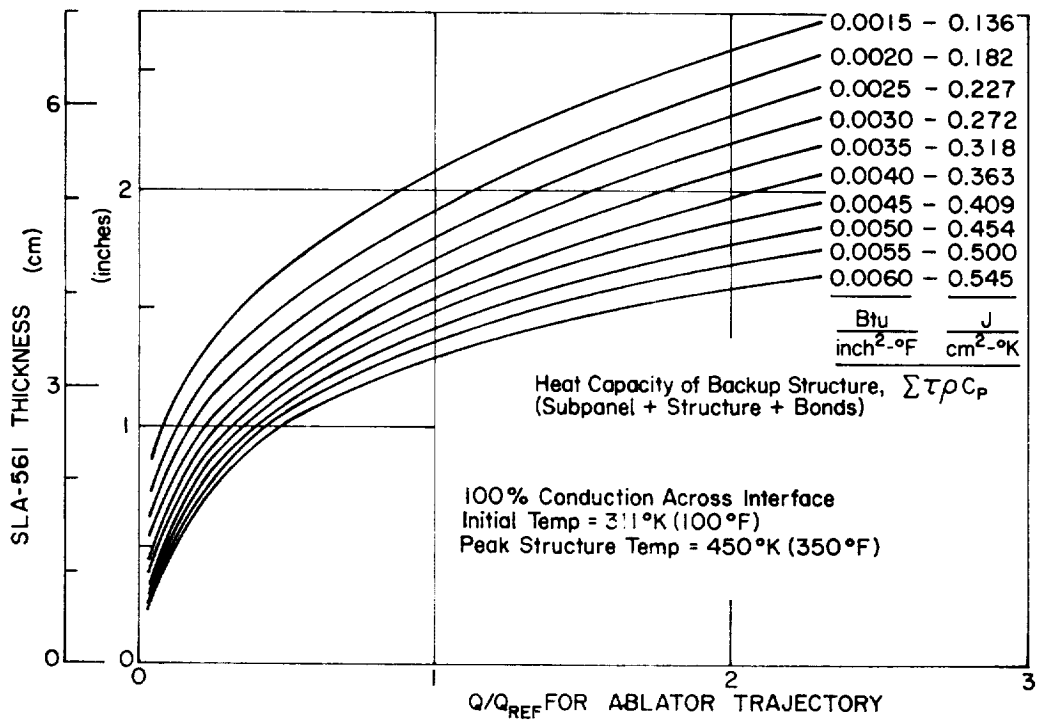


Figure 66.- SLA-561 Requirement versus  $Q/Q_{ref}$  versus Heat Capacity of Backup Structure for Direct Attach Subpanels

The most efficient standoff concept was a design in which the subpanel could be worked to a higher temperature than the primary structure. This concept requires insulation to thermally isolate the primary structure from the hot subpanel. The design charts in figures 67 and 68 are for two subpanel concepts or material variations, and for the two primary structure thicknesses identified on the curves. The charts are used by entering the curves at the desired  $SF \times Q/Q_{ref}$  and reading the prescribed insulation and ablator thickness corresponding to a given structure thickness. Note that a deviation from the insulation thickness given on the charts will change both subpanel and structure peak temperatures. Increasing the insulation thickness will increase the subpanel peak temperature and decrease the structure temperature, etc.

RSI design: Design charts for the LI-1500 TPS material (fig. 69) assumed a 0.025-cm (0.010 in.) coating, a 0.216-cm (0.085 in.) silicone rubber strain isolator, and 0.025-cm (0.010 in.) RTV bonds as shown in the figure. The maximum allowable surface temperature was taken to be 1561°K (2350°F), which occurs at a heating rate of approximately 306 kW/m<sup>2</sup> watt/meter (27 Btu/ft<sup>2</sup>-sec). This envelopes a major portion of the vehicle surface.

As a partial alternative, because of the possible reuse of the SLA-561 ablator in the lower heating rate areas using the RSI trajectory, the insulation (ablator) thickness requirement for the top fuselage point was established. This thickness was increased by 10% and then analytically cycled 10 times through the entry environment. Accumulative material degradation is illustrated in figures 70 and 71. The lambda variable shown is the progression of the ablative material from plastic ( $\lambda = 1.0$ ) to char ( $\lambda = 0.0$ ). The amount of material degradation decreases as the cycle increases. Since there is no material recession involved, reuse of the SLA-561 in select areas appears feasible.

Interior temperatures: Typical time-temperature histories for the various TPS concepts are shown in figures 72 and 73. The three basic approaches using SLA-561 ablator and LI-1500 insulation with their corresponding trajectories are shown. It is interesting to note the difference in structural temperature response for the various concepts.

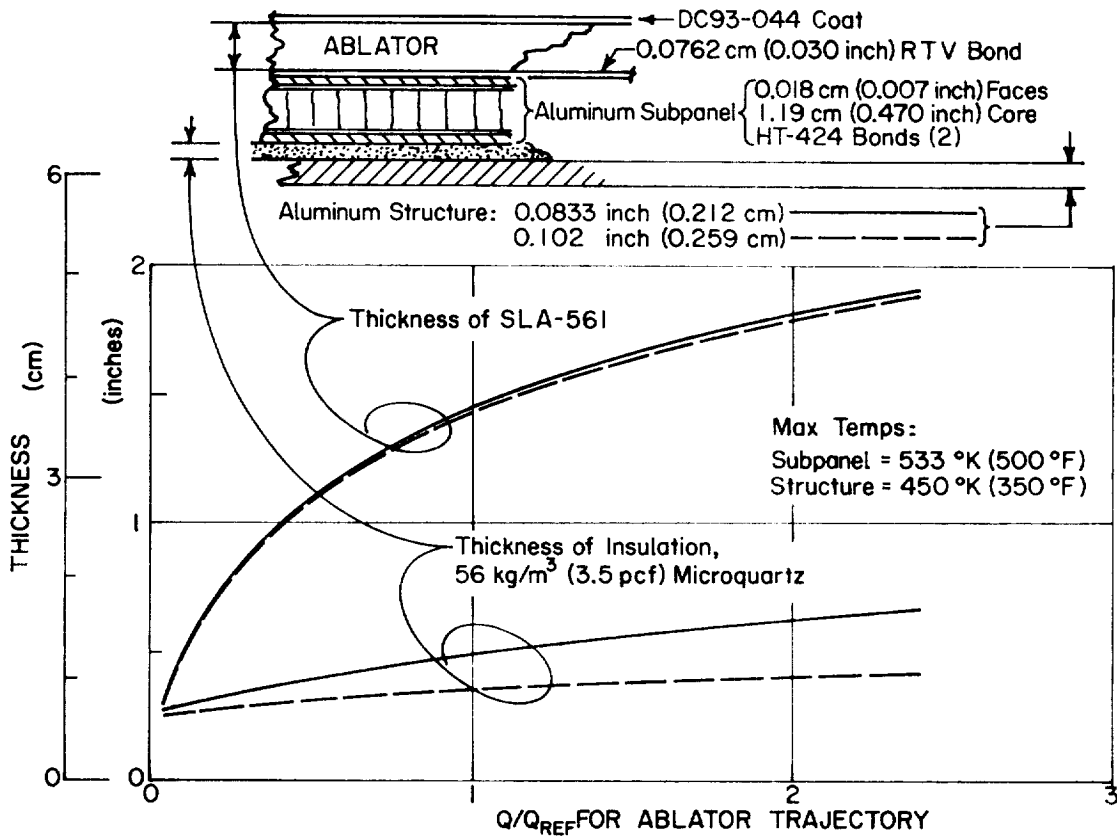


Figure 67.- SLA-561 Ablator Requirements, Aluminum Honeycomb Subpanel Mechanically Attached through Standoff Fittings to the Orbiter Structure

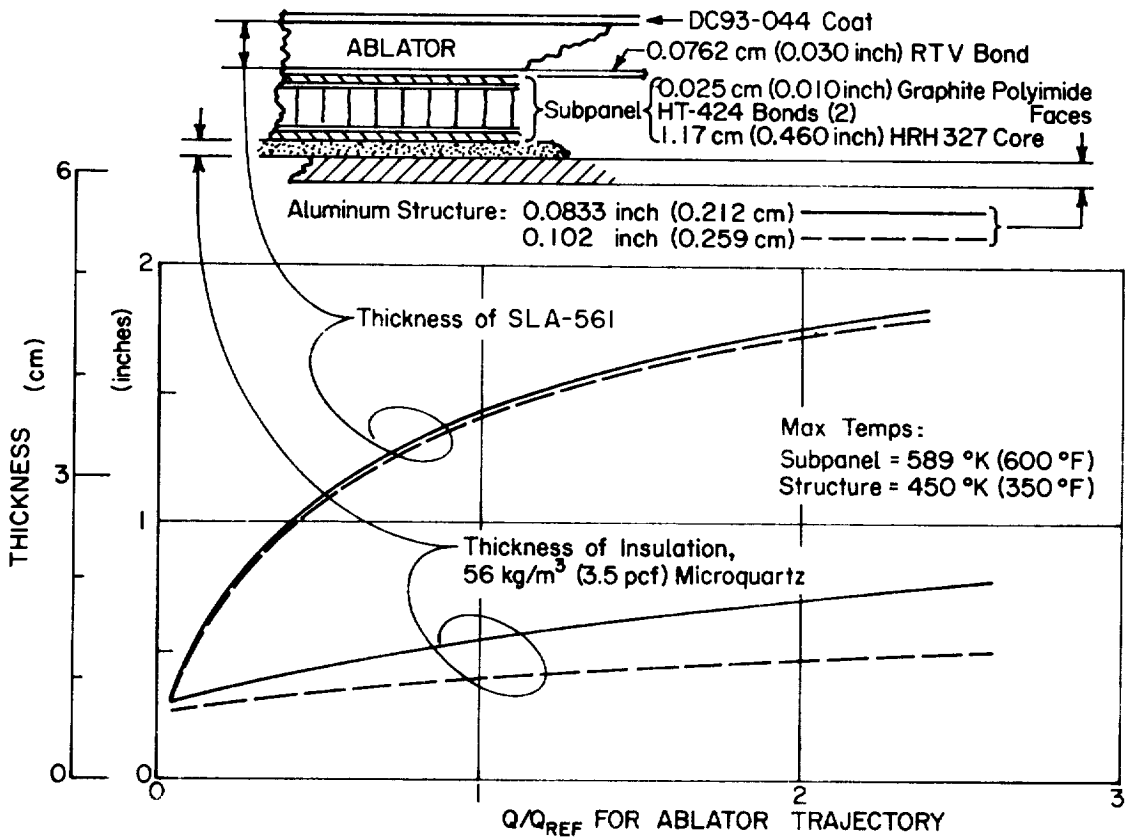


Figure 68.- SLA-561 Ablator Requirements, Graphite/Polyimide Honeycomb Subpanel Mechanically Attached through Standoff Fittings to the Orbiter Structure

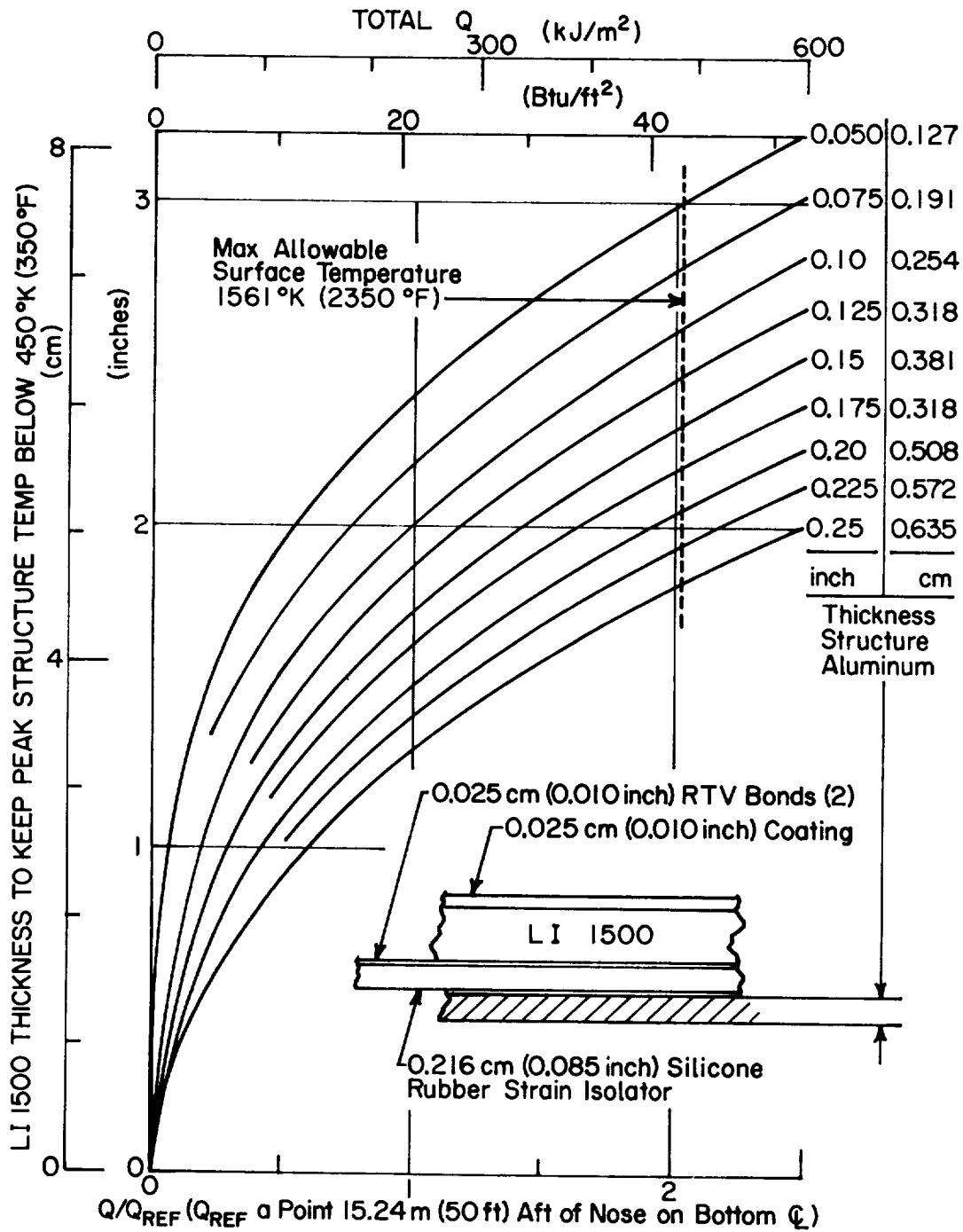


Figure 69.- RSI LI-1500 Requirements, Direct Bond to the Orbiter Structure

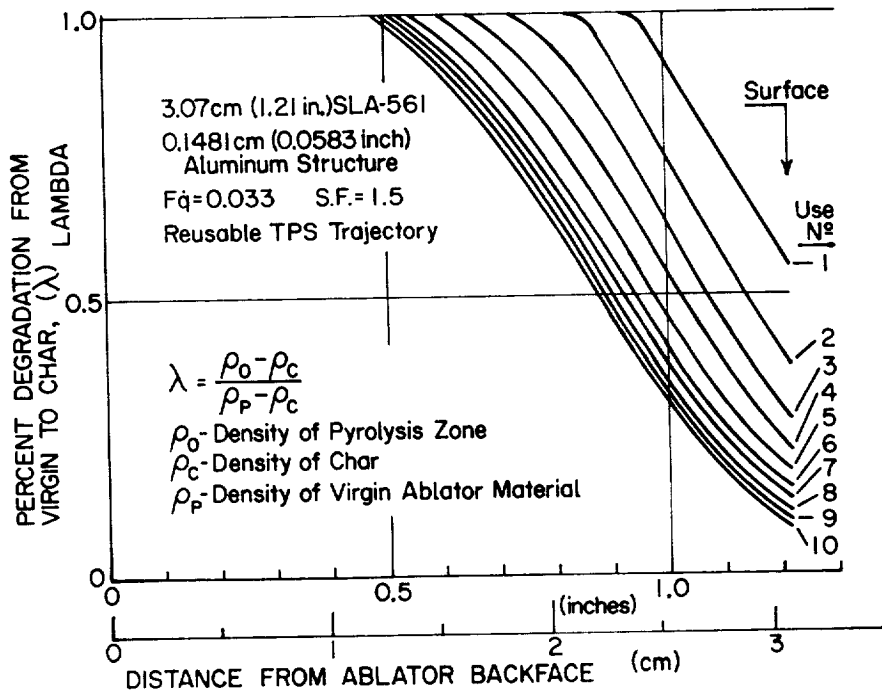


Figure 70.- Lambda Distributions at Top Fuselage, Reusable TPS Trajectory

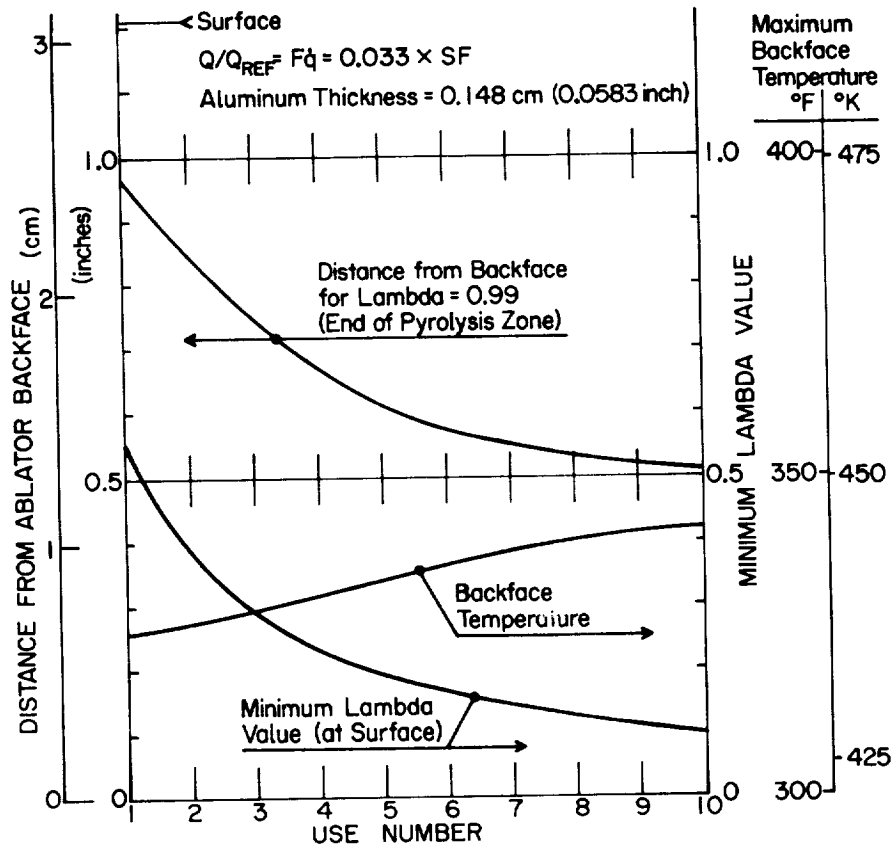


Figure 71.- RSI Trajectory, Lee Surface SLA-561 Ablator Reuse Assessment

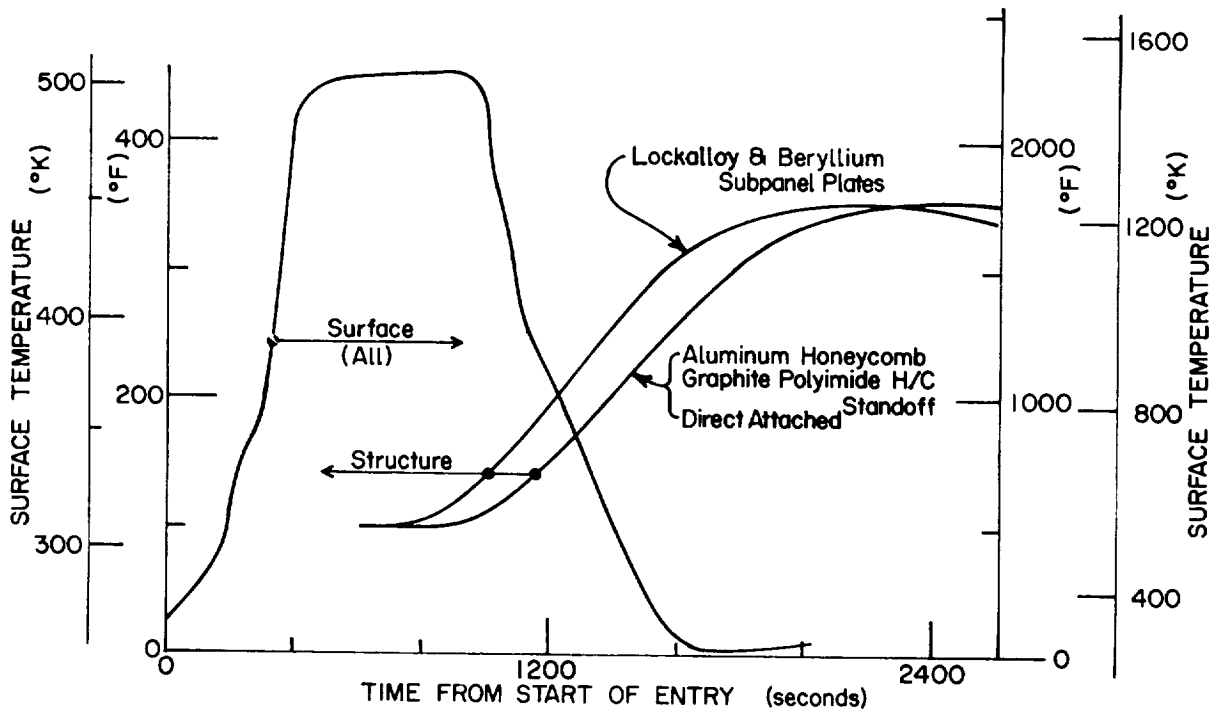


Figure 72.- Reference Point heating versus Ablator Trajectory Time

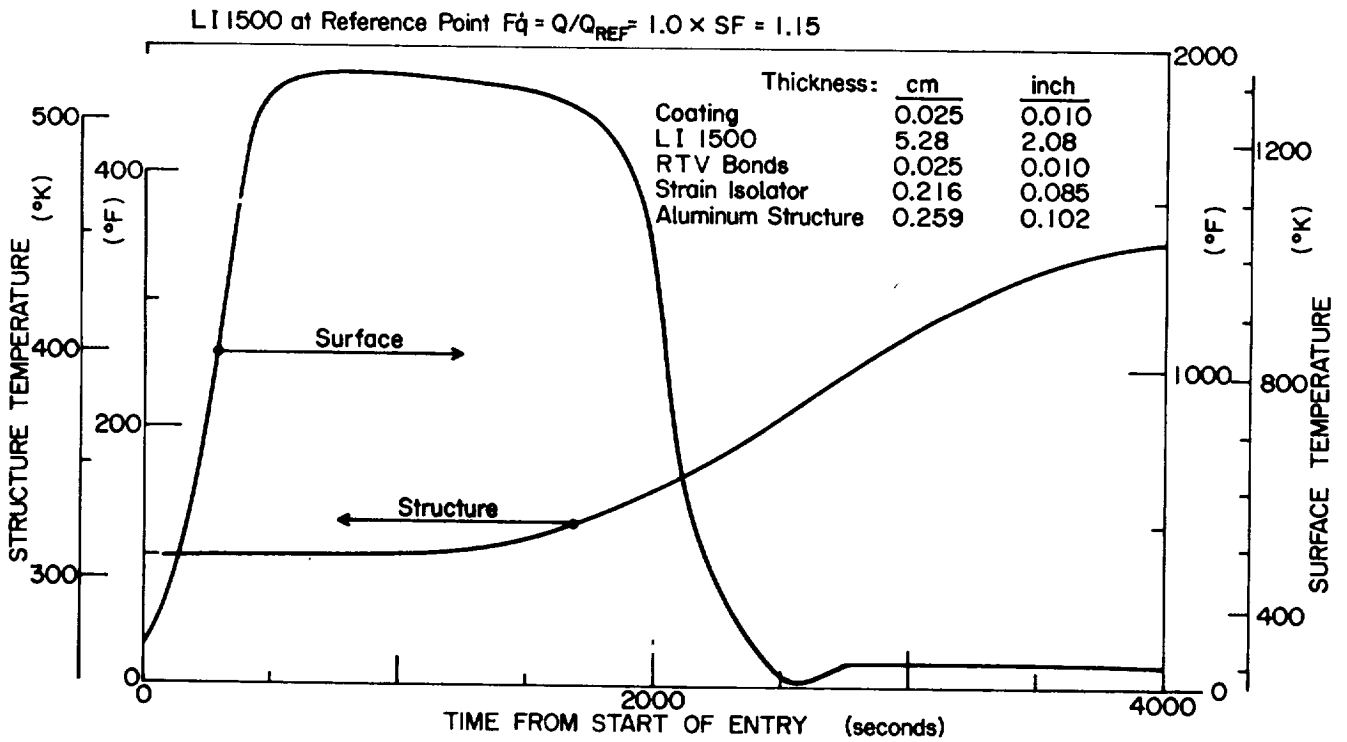


Figure 73.- Reference Point heating versus RSI Trajectory Time

2. Nose cap analysis.- Heating rates on the nose cap required consideration of higher density ablative materials. Significant degradation of these materials during ascent precluded the use of a coating for thermal control during orbit (appendix D). This required an analysis considering the ascent-orbit-entry environment rather than establishing initial temperatures at the beginning of entry and analyzing entry only, as done previously. The material considered and the limiting heating rates were:

Material	$\dot{q}_{\max}$	
	MW/m <sup>2</sup>	Btu/ft <sup>2</sup> -sec
SLA-561	0.68	60
ESA-3560HF	1.02	90
ESA-5500	1.14	over 100

Ablator thickness requirements from the stagnation point to the interfaces where the local heating rate drops to the previously described limiting heating rates are shown for the ablator and RSI trajectories in figures 74 to 77. Proper consideration was given to difference in the approximate location of the stagnation point region when coupling the ascent heating effects with those of entry.

The ablator trajectory requires the use of three ablator materials for optimum design. The RSI trajectory requires the use of two ablator materials for optimum design. It is recognized that final design of the nose caps must eventually be modified to facilitate manufacturing.

3. Wing and fin leading edges analysis.- The wing and fin leading edges required the same approach as for the nose cap. Again, three ablative materials were used for the ablator trajectory design and two for the RSI trajectory design, as indicated in figures 78 to 83.

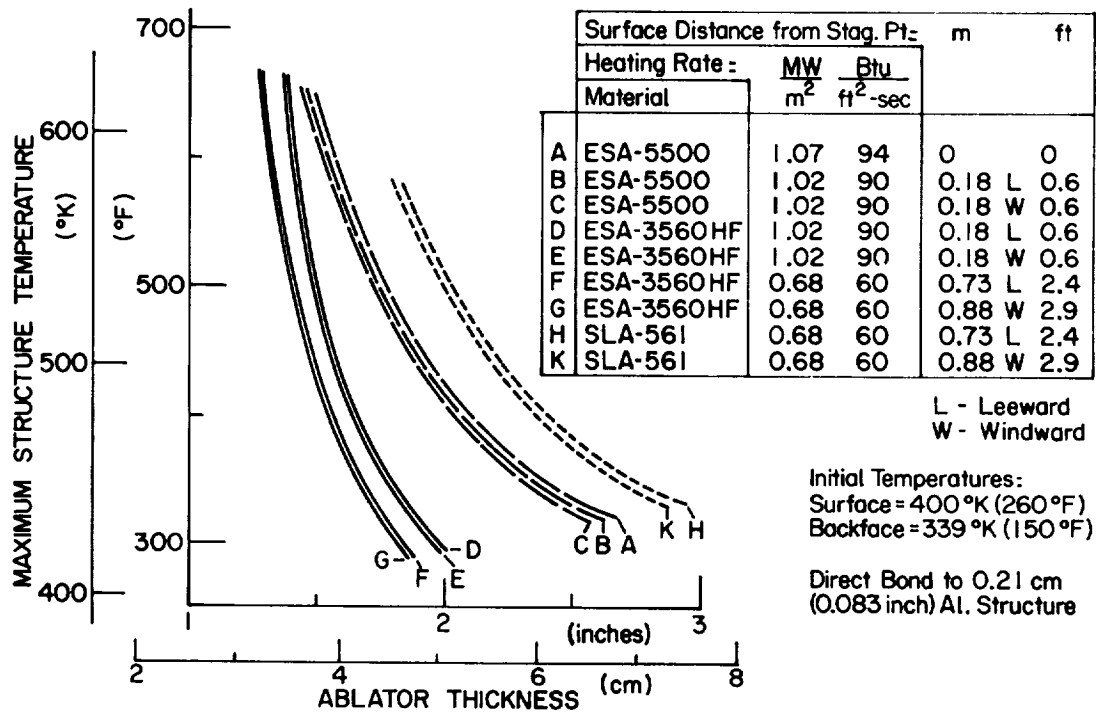


Figure 74.- Nose Cap Ablator Thickness for Ablator Trajectory, R = 91.4 cm (36 in.)

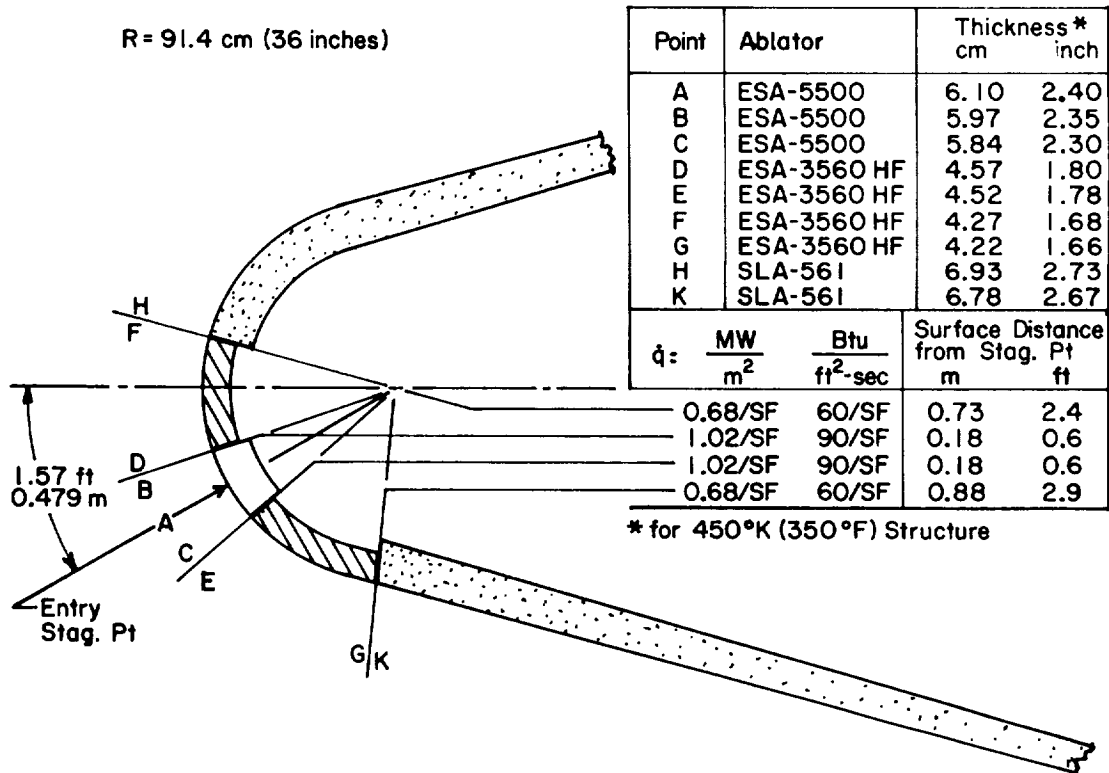


Figure 75.- Ablator Trajectory Nose Cap Design

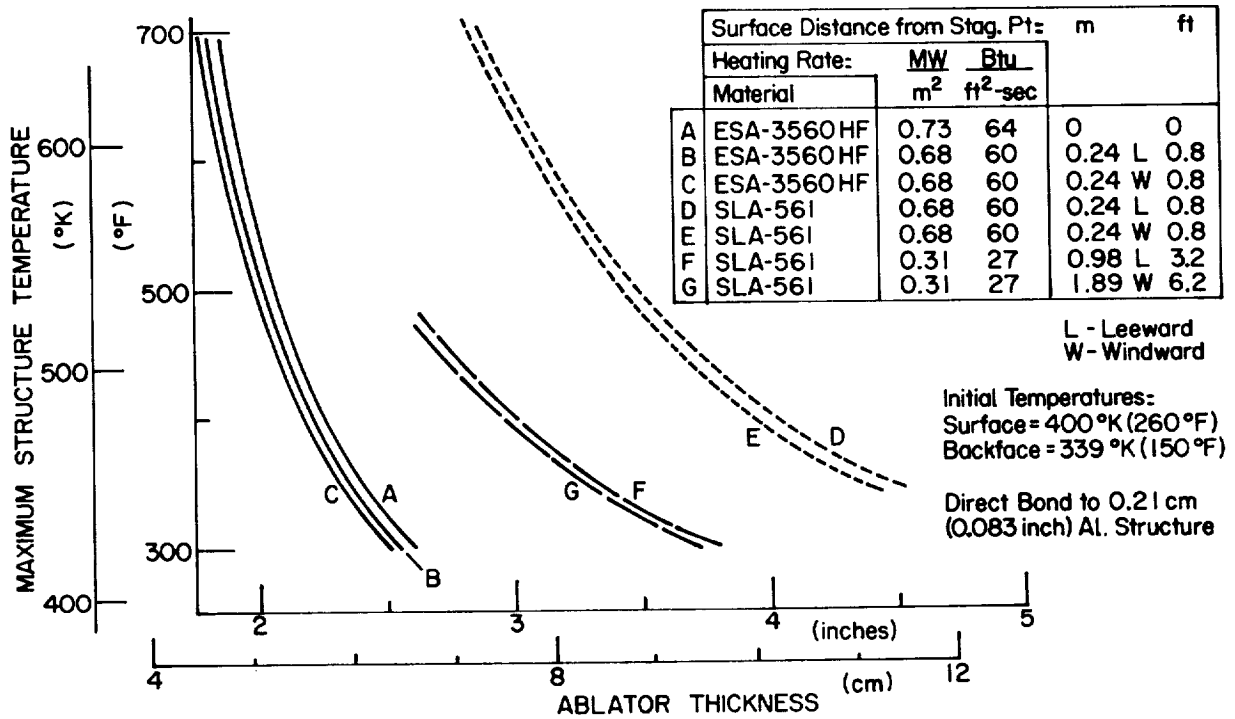


Figure 76.- Nose Cap Ablator Thickness for RSI Trajectory,  
R = 91.4 cm (36 in.)

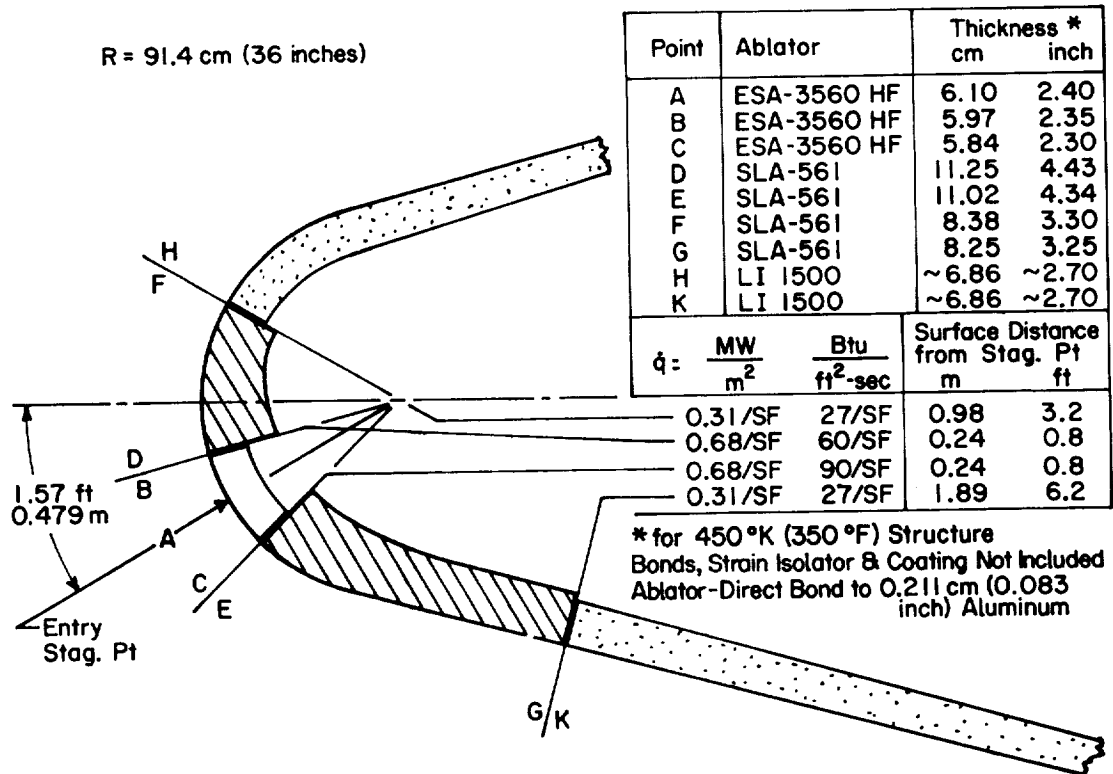


Figure 77.- RSI Trajectory Nose Cap Design

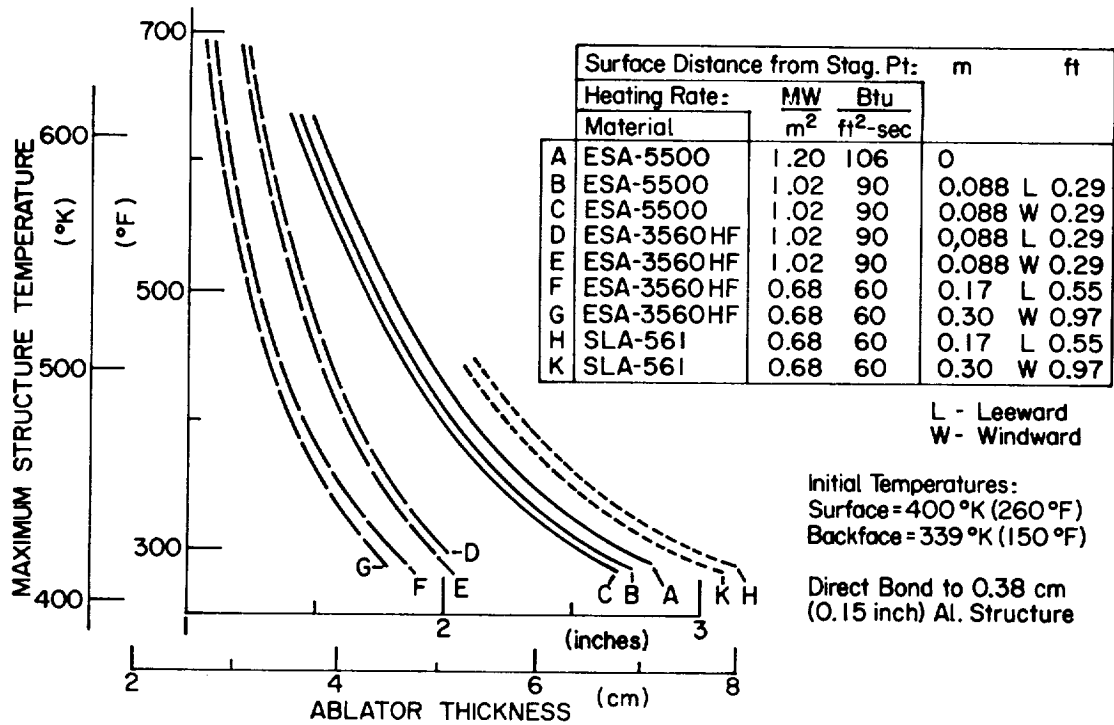


Figure 78.- Wing Leading Edge Ablator Thickness for Ablator Trajectory, R = 15.25 cm (6 in.)

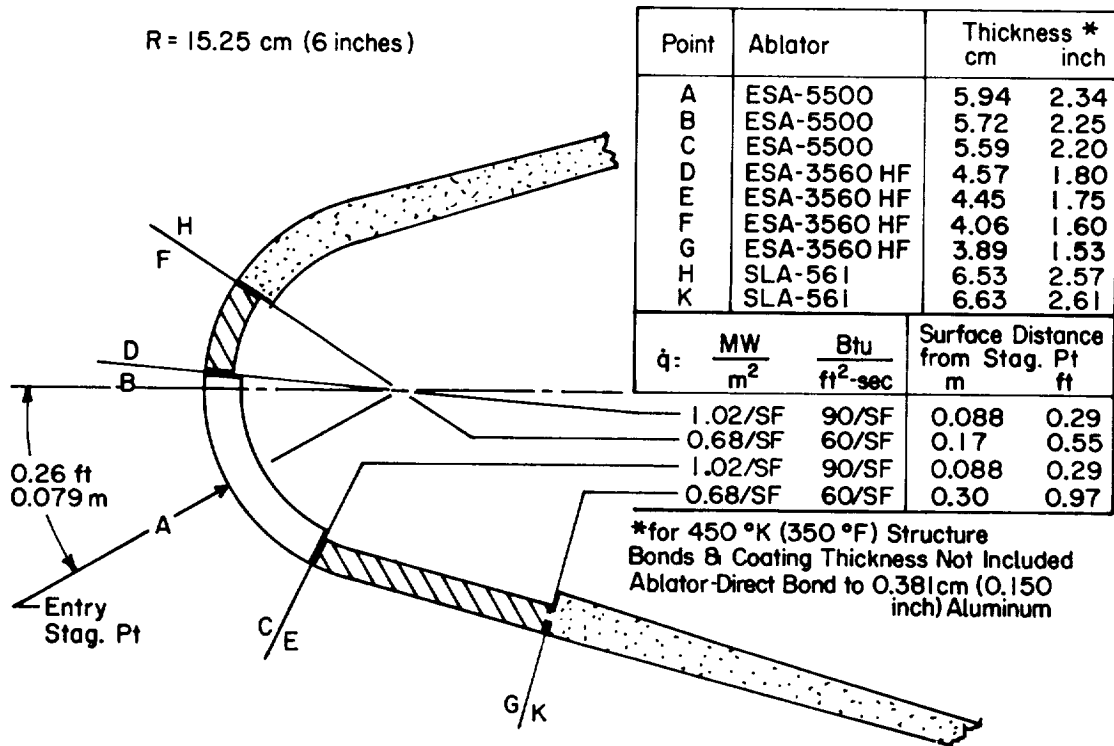


Figure 79.- Ablator Trajectory Wing Leading Edge Design

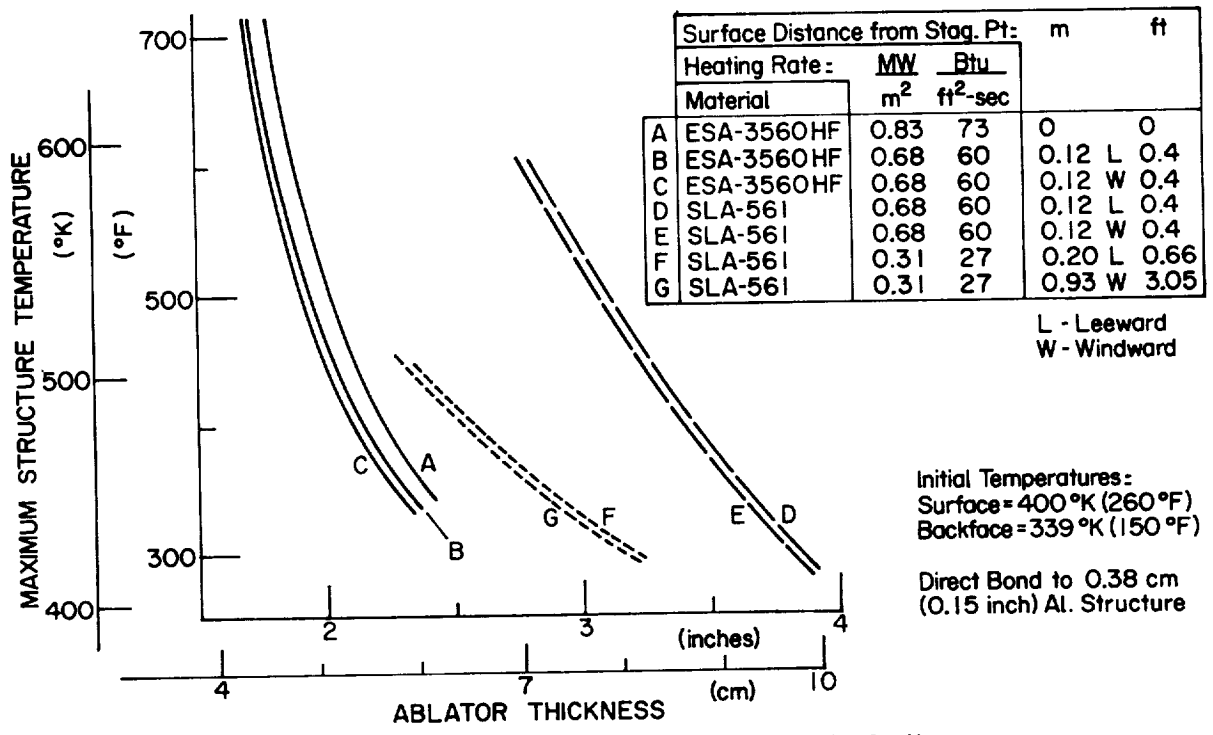


Figure 80.- Ablator Thickness for RSI Trajectory Wing Leading Edge, R = 15.25 cm (6 in.)

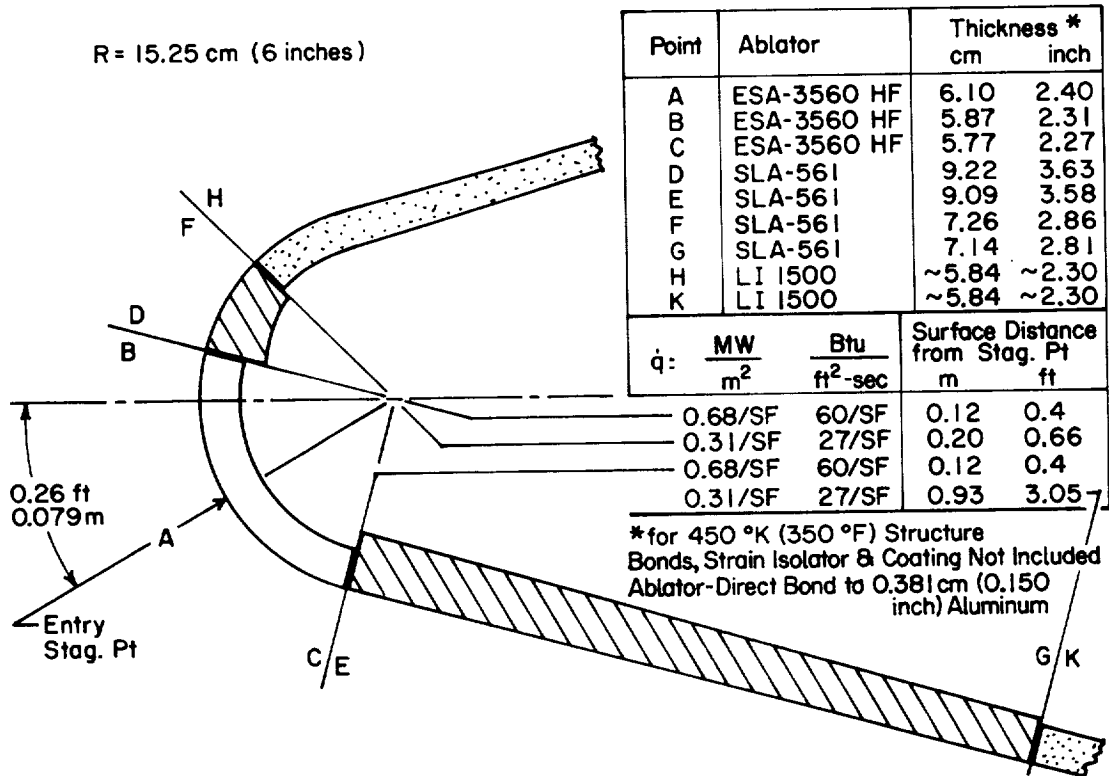


Figure 81.- RSI Trajectory Wing Leading Edge Design

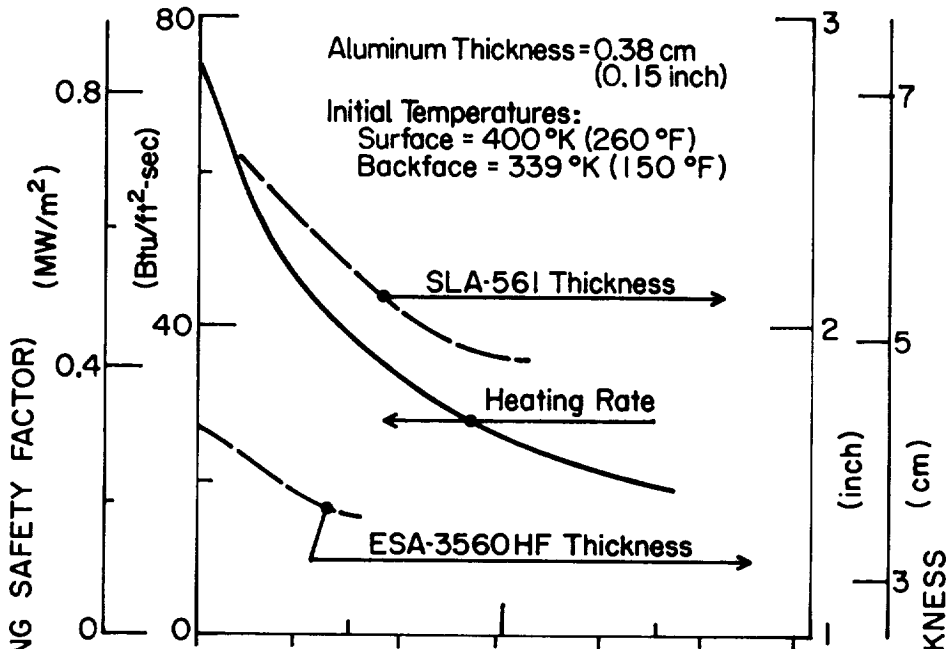


Figure 82.- Ablator Thickness for Ablator Trajectory Fin Leading Edge

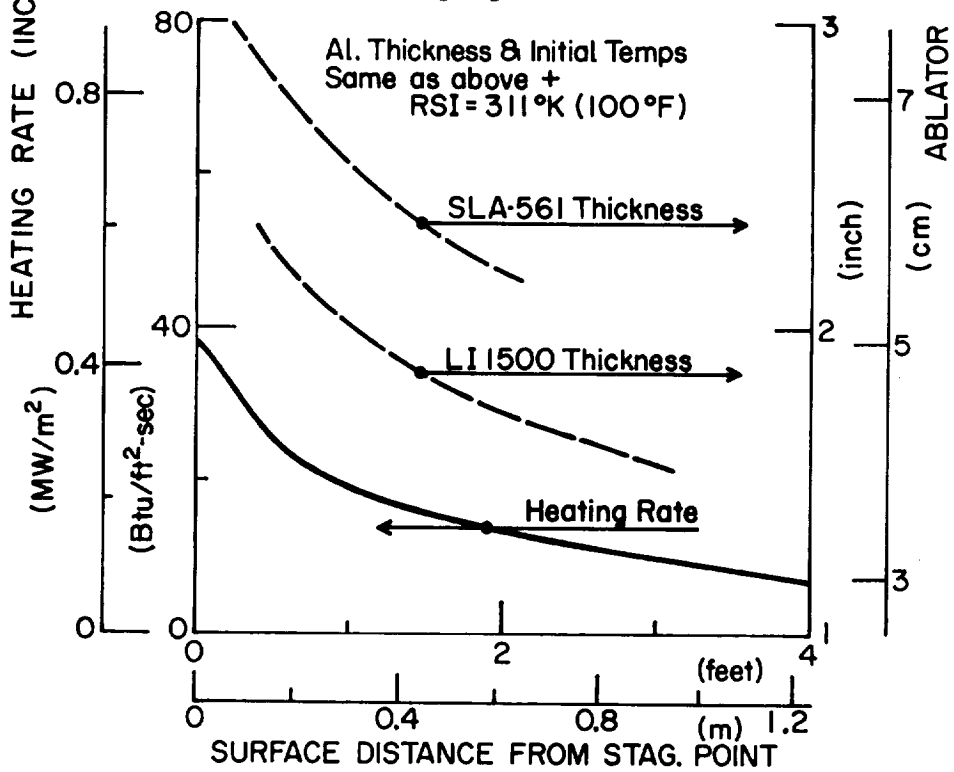


Figure 83.- Ablator Thickness for RSI Trajectory Fin Leading Edge

### E. TPS Weigh-Ins

All the inputs derived in the previous sections, (considerations of design, stress, and thermal effects for the matrix of TPS arrangements studied) were integrated into a TPS weights analysis. These weights will subsequently be the basis for the program weight/cost sensitivities discussed in Chapter VI. The process involved a bottoms-up approach for three key TPS configurations and a ratioing technique for the remainder. The unit weights used throughout were as follows:

Material	$\frac{\text{kg}}{\text{m}^3}$	$\frac{\text{lb}}{\text{ft}^3}$
Ablator, SLA-S61	0.177	14.5
Ablator, ESA-3560HF	0.367	30.0
Ablator, ESA-5500 M3	0.869	71.0
RSI, LI-1500	0.184	15.0
RSI, strain isolator	0.367	30.0

Material	$\text{kg/m}^2$	$\text{lb/ft}^2$
Ablator bond, GX-6300	0.002	0.177
Ablator coating, DC 93-044	0.003	0.235

Material	$\frac{\text{kg}}{1000}$	$\frac{\text{lb}}{1000}$
Plate fasteners	6.4	14.1
Honeycomb fasteners	7.3	16.1

Weight data presented does not include seals or allowance for weight contingency or weight growth.

1. Detailed weighing.- The weight components of the following items were analyzed in detail:

- 1) Ablator, direct bonded (table 19);
- 2) RSI, direct bonded (via strain isolator) (table 20);
- 3) Ablator, bonded to an aluminum sheet and directly mechanically attached (table 21).

TABLE 19.- ORBITER TPS WEIGHT, ABLATOR TRAJECTORY, SLA-561 DIRECT BOND

Description/Fq	Area, m <sup>2</sup>		Mass, kg			Area, ft <sup>2</sup>		Weight, lb			
	Bond	Total	Bond	Coating	Ablator	Bond	Total	Bond	Coating	Ablator	Total
Body											
Nose section	(13)	(214)	(16)	(24)	(174)	(139)	(214)	(33)	(52)	(385)	(470)
0.350	3	32	4	3	25	32	32	8	6	56	70
0.350 to 1.133	2	26	2	2	22	23	26	5	4	48	57
1.58	4	63	5	4	54	44	63	10	8	120	138
Nose cap (ESA 3560HF)	4	93	5	15 <sup>a</sup>	73	40	93	10	34 <sup>a</sup>	161	205
Cabin section	(90)	(1094)	(103)	(79)	(914)	(972)	(1094)	(228)	(171)	(2 014)	(2 413)
0.093 to 0.350	41	380	48	36	296	447	380	105	79	653	837
0.350 to 1.133	11	133	12	10	112	115	133	27	20	247	294
1.58 to 1.40	33	510	38	29	444	358	510	84	63	978	1 125
1.40 to 1.165	5	71	5	4	62	52	71	12	9	136	157
Forward section	(100)	(1252)	(115)	(85)	(1053)	(1074)	(1252)	(252)	(189)	(2 322)	(2 763)
0.093 to 0.350	24	216	27	20	169	256	216	60	45	372	477
0.350 to 1.133	13	158	15	11	132	140	158	33	25	291	349
1.133 to 1.40	16	233	19	14	200	175	233	41	31	442	514
1.40 to 1.165	22	274	25	19	274	240	274	56	42	603	701
1.165 to 1.00	17	230	20	15	196	182	230	43	32	433	508
1.00 to 0.93	8	97	9	6	82	81	97	19	14	181	214
Mid Section, lower	(34)	(357)	(39)	(29)	(290)	(366)	(357)	(85)	(64)	(637)	(786)
1.165 to 1.40	1	5	1	1	4	4	5	1	1	8	10
1.165 to 1.00	5	53	5	4	44	53	53	12	9	96	117
1.00 to 0.93	20	213	23	17	172	219	213	51	38	380	469
0.93 to 0.89	8	86	10	7	70	90	86	21	16	153	190
Mid Section, upper	(20)	(178)	(23)	(17)	(137)	(216)	(178)	(51)	(38)	(303)	(392)
0.093 to 0.350	20	178	23	17	137	216	178	51	38	303	392
Aft section, lower	(61)	(722)	(70)	(52)	(599)	(656)	(722)	(154)	(116)	(1 322)	(1 592)
0.93 to 0.89	27	270	31	23	216	288	270	68	51	477	596
0.89	34	452	39	29	383	368	452	86	65	845	996
Aft section, upper	(54)	(472)	(62)	(47)	(363)	(586)	(472)	(137)	(103)	(800)	(1 040)
0.093 to 0.350	54	472	62	47	363	586	472	137	103	800	1 040
OMS pod	(49)	(346)	(57)	(43)	(246)	(529)	(346)	(124)	(93)	(545)	(762)
0.143	4	33	5	4	24	44	33	10	8	54	72
0.143 to 0.070	14	103	16	12	75	149	103	35	26	166	227
0.070	31	210	36	27	147	336	210	79	59	325	463
Cargo doors	(180)	(1392)	(207)	(156)	(1031)	(1932)	(1392)	(454)	(342)	(2 272)	(3 068)
0.033	15	98	17	13	68	157	98	37	28	150	215
0.033 to 0.065	25	172	29	22	121	273	172	64	48	267	379
0.065 to 0.093	89	660	102	77	482	955	660	224	169	1 062	1 455
0.093 to 0.350	51	462	59	44	360	547	462	129	97	793	1 019
Total, body	601	6027	692	532 <sup>a</sup>	4808	6470	6027	1518	1168 <sup>a</sup>	10 600	13 286

<sup>a</sup>Includes aluminum honeycomb backup structure of 12 kg (27 lb)

TABLE 19.- ORBITER TPS WEIGHT, ABLATOR TRAJECTORY, SLA-561 DIRECT BOND - CONCLUDED

Description/eq	Area, m <sup>2</sup>	Mass, kg				Area, ft <sup>2</sup>	Weight, lb			
		Bond	Coating	Ablator	Total		Bond	Coating	Ablator	Total
<b>Wing</b>										
<b>Upper wing</b>										
Leading edge	(2)	(3)	(2)	(48)	(53)	(26)	(6)	(5)	(106)	(117)
PSA 3399BF	2	3	2	48	53	26	6	5	106	117
Blank	(162)	(185)	(139)	(982)	(1306)	(1739)	(408)	(306)	(2166)	(2 850)
0.007	89	102	77	440	619	957	225	169	971	1 365
0.007 to 0.145	33	38	28	168	234	353	83	62	371	516
0.145 to 0.260	18	20	15	108	143	189	44	33	238	315
0.260 to 2.00	22	25	19	266	310	240	56	42	586	684
PSA 3399BF	(66)	(76)	(57)	(354)	(487)	(712)	(167)	(126)	(781)	(1 074)
0.127	46	53	39	243	335	493	116	87	536	739
0.127 to 0.145	20	23	18	111	152	219	51	39	245	335
PSA 3399BF	(17)	(19)	(14)	(151)	(185)	(184)	(44)	(32)	(332)	(408)
0.007 to 2.00	1	1	1	19	21	14	3	2	41	46
0.007 to 0.917	4	4	3	41	49	42	10	7	91	108
0.917 to 0.967	7	9	6	59	73	79	19	14	129	167
0.967	5	5	4	32	42	49	12	9	71	92
PSA 3399BF	(7)	(9)	(7)	(316)	(330)	(78)	(18)	(14)	(695)	(727)
0.127 to 0.145	3	4	3	239	245	35	8	6	526	540
0.145 to 2.00	4	5	4	77	85	43	10	8	169	187
Blank	(150)	(170)	(129)	(1652)	(1953)	(1613)	(379)	(285)	(3642)	(4 756)
0.007 to 0.93	26	29	22	267	318	278	65	49	588	766
0.93 to 1.00	50	57	43	525	625	538	126	95	1157	1 514
1.00 to 1.165	30	34	26	327	387	322	76	57	720	933
1.165 to 1.450	26	30	23	306	360	284	67	50	676	895
1.450 to 2.00	18	20	15	227	263	191	45	34	501	663
PSA 3399BF	(66)	(75)	(56)	(709)	(842)	(712)	(167)	(125)	(1563)	(1 875)
0.127	49	56	42	521	619	528	124	93	1148	1 501
0.127 to 0.145	14	16	12	157	186	153	36	27	346	460
0.145 to 2.00	3	3	2	31	37	31	7	5	69	91
Blank	(17)	(21)	(16)	(201)	(234)	(184)	(44)	(32)	(442)	(518)
0.007	2	3	2	26	30	25	6	4	57	67
0.007 to 0.93	2	3	2	26	31	25	6	4	58	68
0.93 to 1.00	7	8	6	78	91	79	17	13	171	201
1.00 to 1.165	4	5	4	49	57	44	10	8	107	125
1.165 to 1.450	1	1	1	13	15	11	3	2	29	34
1.450 to 2.00	1	1	1	9	10	7	2	1	20	23
<b>Lower wing</b>	487	558	420	4413	5390	5248	1233	925	9727	11 885
<b>Tail</b>										
Leading edge	(2)	(2)	(1)	(23)	(26)	(18)	(4)	(3)	(51)	(58)
Blank	(58)	(68)	(52)	(507)	(627)	(630)	(149)	(112)	(1117)	(1378)
0.007 to 0.917	9	11	8	129	148	100	24	18	284	326
0.917 to 0.967	16	19	15	166	200	178	42	32	366	440
0.967 to 0.137	22	25	19	152	196	234	55	41	335	433
0.137	11	13	10	60	83	118	28	21	137	183
PSA 3399BF	(36)	(41)	(31)	(197)	(269)	(387)	(91)	(68)	(433)	(592)
0.127 to 0.145	4	5	4	24	33	46	11	8	52	71
0.145 to 2.00	32	36	27	173	236	341	80	60	381	521
<b>Wing total</b>	96	111	84	727	922	1035	244	183	1601	2028
<b>Wing total</b>	1184	1361	1036	9948	12 339	12 753	2 995	2 276	21 928	27 199

TABLE 20.- ORBITER TPS WEIGHT, REUSABLE TPS TRAJECTORY, LI 1500

Description/Fq average	LI 1500			LI 1500			Weight, lb
	Area, m <sup>2</sup>	Thickness, cm	Unit Mass, kg/m <sup>2</sup>	Mass, kg	Area, ft <sup>2</sup>	Thickness, in.	
Body							
Nose section	(13)			(238)	(139)		(524)
0.35	3	4.17	11.86	35	32	1.64	78
0.74	2	5.08	13.87	30	23	2.00	65
2.20	4	7.62	19.48	80	44	3.00	176
Nose cap (ESA 3560HF)	4			93	40		205
Cabin section	(91)			(1217)	(972)		(2 683)
1.48	33	6.30	16.75	557	358	2.48	1 228
0.74	11	4.95	13.82	147	115	1.95	325
1.30	5	6.22	16.75	81	52	2.45	178
0.22	42	3.56	10.40	432	447	1.40	952
Forward section	(100)			(1388)	(1074)		(3 059)
0.30	24	3.30	9.91	236	256	1.30	520
0.74	13	4.70	12.84	167	140	1.85	368
1.40	16	6.35	16.75	272	175	2.50	600
1.22	22	5.97	15.77	352	240	2.35	775
1.07	17	5.59	14.79	250	182	2.20	551
1.05	8	5.59	14.79	111	81	2.20	245
Mid section, lower	(34)			(384)	(366)		(847)
1.07	1	4.19	11.86	5	4	1.65	10
1.04	5	4.11	11.62	57	53	1.62	126
1.00	20	4.06	11.38	231	219	1.60	510
0.98	8	3.81	10.89	91	90	1.50	201
Mid section, upper	(20)			(184)	(216)		(406)
0.25	20	3.05	9.18	184	216	1.20	406
Aft section, lower	(61)			(797)	(656)		(1 757)
0.95	27	3.68	10.89	291	288	1.45	642
0.94	34	5.64	14.79	506	368	2.22	1 115
Aft section, upper	(54)			(462)	(586)		(1 019)
0.22	54	2.79	8.50	462	586	1.1	1 019
OMS pod	(49)			(394)	(529)		(868)
0.14	4	3.05	9.03	37	44	1.2	81
0.11	14	2.79	8.93	124	149	1.1	273
0.07	31	2.29	7.47	233	336	0.9	514
Cargo doors	(179)			(1696)	(1932)		(3 739)
0.03	15	2.03	6.98	102	157	0.8	143
0.05	24	2.29	7.47	190	273	0.9	225
0.08	89	3.05	9.03	801	955	1.2	418
0.22	51	4.32	11.86	603	547	1.7	1 767
Total, body	601			6760	6470		14 902

TABLE 20.- ORBITER TPS WEIGHT, REUSABLE TPS TRAJECTORY, L1 1500 - CONCLUDED

Description/Qty coverage	Area, m <sup>2</sup>	L1 1500			Area, ft <sup>2</sup>	L1 1500		Weight, lb
		Thickness, cm	Unit Mass, kg/m <sup>2</sup>	Mass, kg		Thickness, in.	Unit weight, lb/ft <sup>2</sup>	
<b>Wing</b>								
<b>Upper wing</b>								
Leading edge	(2)	-	-	(53)	(26)			(117)
ESA 360HF	2	-	-	53	26			117
Box	(262)			(1371)	(1739)			(3 020)
0.14	80	2.93	6.98	611	957	0.80	1.43	1 369
0.14	33	2.29	7.47	245	353	0.90	1.53	540
0.20	18	2.79	8.69	153	189	1.10	1.78	336
1.13	22	3.89	15.77	352	240	2.32	3.23	775
Elevon	(66)			(548)	(712)			(1 787)
0.13	36	2.54	8.20	276	293	1.00	1.68	828
0.14	25	2.67	8.45	172	219	1.05	1.73	379
ACS pod	(17)			(224)	(185)			(493)
1.46	1	7.11	18.70	75	14	1.80	3.83	54
0.65	3	3.98	13.87	55	32	2.00	2.84	119
0.29	7	3.95	13.33	98	79	1.95	2.73	216
0.22	3	3.56	16.50	47	39	2.50	2.13	104
<b>Lower wing</b>								
Leading edge	(7)			(330)	(78)			(227)
ESA 5500H	3	-	-	265	35			540
ESA 360HF	4	-	-	85	43			187
Box	(150)			(2162)	(1613)			(4 767)
0.95	26	3.93	13.82	357	278	1.98	2.83	787
0.97	50	3.08	13.87	693	538	2.00	2.84	1 528
1.02	30	3.21	14.06	320	322	2.05	2.88	927
1.23	26	3.39	14.89	393	283	2.20	3.05	866
1.76	18	6.48	16.84	299	191	2.55	3.45	659
Elevon	(66)			(978)	(712)			(2 157)
0.95	66	3.46	14.79	978	712	2.15	3.03	2 157
ACS pod	(17.09)			(265.8)	(184)			(586)
0.94	4.65	5.59	14.89	69.4	56	2.20	3.05	153
0.97	6.69	3.72	15.28	102.1	77	2.25	3.13	225
1.20	3.11	6.10	16.16	82.6	55	2.40	3.31	182
1.70	0.64	7.13	18.45	11.7	7	2.80	3.78	26
Total, wing	(587.54)			(5930.5)	(5348)			(13 074)
<b>Tail</b>								
Leading edge	(2)			(30)	(18)			(67)
2.0	2	6.99	18.21	39	18	1.75	3.73	67
Box	(39)			(702)	(630)			(1548)
1.46	9	6.86	17.72	165	130	2.70	3.63	363
3.64	17	3.98	13.87	239	178	2.00	2.84	506
0.25	22	3.23	9.91	215	234	1.35	2.03	475
0.14	11	2.79	8.45	92	118	1.10	1.73	204
Rudder	(38)			(295)	(387)			(611)
0.25	4	3.30	9.81	37	36	1.30	2.01	92
0.14	32	2.41	8.01	258	351	1.95	1.64	559
Total, tail	(96)			(1078)	(1035)			(2266)
Total, orbiter	(1183)			(13 718)	(12 753)			(30 254)

TABLE 21.- ORBITER TPS WEIGHT, ABLATOR TRAJECTORY, 0.079 CM (0.031 IN.) ALUMINUM  
 PLATE SUB PANEL DIRECT ATTACHMENT, FASTENER SPACING 12.7 CM (5 IN.)

Description/Fq	Area, m <sup>2</sup>	Mass, kg						Area, ft <sup>2</sup>	Weight, lb					Total	
		Fast.	Bond	Coat	Subpanel	Ablator	Total		Fast.	Bond	Coat	Subpanel	Ablator		
Body															
Nose section	(13)	(4)	(15)	(12)	(32)	(167)	(239)	(139)	(9)	(33)	(25)	(71)	(368)	(506)	
0,350	3	1	4	3	6	23	37	32	3	8	6	14	51	82	
0,350 to 1,133	2	1	2	2	5	20	30	23	2	5	4	10	44	65	
1,98	4	2	5	4	9	31	71	44	4	10	8	20	112	134	
nose cap (OSA 350HF)	4		4	3	12	73	92	40		10	7	27	161	205	
Cabin section	(90)	(41)	(103)	(78)	(197)	(854)	(1273)	(972)	(91)	(228)	(171)	(434)	(1882)	(2 806)	
0,093 to 0,350	41	19	48	36	91	277	471	447	42	105	79	200	610	1 036	
0,350 to 1,133	11	5	12	9	23	104	153	115	11	27	20	51	229	338	
1,98 to 1,50	13	15	38	29	73	416	571	358	33	84	63	160	917	1 257	
1,50 to 1,165	5	2	5	4	10	57	78	52	5	12	9	23	126	175	
Forward section	(100)	(45)	(115)	(85)	(217)	(981)	(1443)	(1074)	(98)	(252)	(189)	(478)	(2161)	(3 178)	
0,093 to 0,350	25	11	27	20	52	158	268	256	24	60	45	114	348	591	
0,350 to 1,133	13	6	15	11	28	121	181	140	13	33	25	62	267	400	
1,133 to 1,50	16	7	19	14	35	189	264	175	16	41	31	78	417	583	
1,50 to 1,165	22	10	25	19	49	253	356	240	22	56	42	107	557	784	
1,165 to 1,00	17	8	20	15	37	181	261	182	17	43	32	81	398	571	
1,00 to 0,93	8	3	9	6	16	79	113	81	6	19	14	36	175	249	
Mid section, lower	(65)	(15)	(38)	(30)	(74)	(229)	(386)	(366)	(33)	(85)	(65)	(164)	(584)	(931)	
1,165 to 1,50	1	-	-	1	1	3	5	4	0	1	1	2	7	11	
1,165 to 1,00	5	2	5	4	11	4	26	53	5	12	9	24	8	138	
1,00 to 0,93	20	9	23	18	44	160	254	219	20	53	39	98	352	560	
0,93 to 0,89	8	4	10	7	18	62	101	90	8	21	16	40	137	222	
Mid section, upper	(20)	(9)	(23)	(17)	(44)	(132)	(225)	(216)	(20)	(51)	(38)	(96)	(292)	(497)	
0,093 to 0,350	20	9	23	17	44	132	225	216	20	51	38	96	292	497	
Aft section, lower	(61)	(27)	(70)	(52)	(133)	(556)	(838)	(656)	(61)	(154)	(115)	(293)	(1,225)	(1 848)	
0,93 to 0,89	17	12	31	23	59	199	324	288	27	68	50	129	538	712	
0,89	34	15	39	29	74	357	514	368	34	86	65	164	787	1 146	
Aft section, upper	(34)	(24)	(62)	(46)	(119)	(341)	(592)	(586)	(54)	(137)	(103)	(262)	(753)	(1 309)	
0,093 to 0,350	18	8	20	15	39	117	199	193	18	45	34	86	259	442	
Mid, upper	33	11	28	21	53	139	252	261	24	61	46	117	306	554	
Aft, upper	12	5	14	10	27	85	141	132	12	31	23	59	188	313	
OMS pod	(59)	(22)	(30)	(43)	(107)	(230)	(432)	(529)	(49)	(124)	(93)	(237)	(506)	(1 009)	
0,153	4	2	5	4	9	24	44	44	4	10	8	20	52	94	
0,153 to 0,070	14	6	16	12	30	68	132	149	14	35	26	67	149	291	
0,070	31	14	9	27	68	138	256	336	31	79	59	150	305	624	
Cargo doors	(180)	(81)	(207)	(156)	(391)	(929)	(1764)	(1932)	(180)	(454)	(342)	(862)	(2049)	(3 887)	
0,033	15	7	17	13	32	56	125	157	15	37	28	70	123	273	
0,033 to 0,065	25	11	29	22	55	109	226	273	25	64	48	122	241	500	
0,065 to 0,093	89	40	102	77	193	434	846	955	89	224	169	426	958	1 866	
0,093 to 0,350	51	23	59	44	111	330	567	547	51	129	97	244	727	1 248	
Total, body	601	268	663	519	1 114	4419	7183	6470	595	1518	1141	2897	9820	15 971	

TABLE 21.- ORBITER TPS WEIGHT, ABLATOR TRAJECTORY, 0.079 CM (0.031 IN.) ALUMINUM  
 PLATE SUB PANEL DIRECT ATTACHMENT, FASTENER SPACING 12.7 CM (5 IN.) - CONCLUDED

Description/Eq	Area, m <sup>2</sup>	Mass, kg						Area, ft <sup>2</sup>	Weight, lb					
		Fast.	Bond	Coat	Subpanel	Ablator	Total		Fast.	Bond	Coat	Subpanel	Ablator	Total
<b>Wing</b>														
<b>Upper Wing</b>														
Leading edge ESA 3560HF	(2) 2		(3)	(2)		(48)	(53)	(26)		(6)	(5)		(106)	(117)
Box	(162)	(73)	(185)	(139)	(353)	(934)	(1684)	(1739)	(162)	(408)	(306)	(776)	(2057)	(3 759)
0.127	89	40	102	77	194	425	838	957	89	225	169	427	937	1 857
0.127 to 0.145	33	15	38	28	72	165	318	353	33	83	62	158	363	699
0.145 to 0.260	18	8	20	15	38	103	184	189	18	44	33	84	226	455
0.260 to 2.00	22	10	25	19	49	241	364	240	22	56	42	107	231	458
Elevon	(66)	(30)	(76)	(57)	(144)	(341)	(648)	(712)	(66)	(167)	(126)	(318)	(751)	(1 628)
0.127	46	21	53	39	100	235	448	493	46	116	87	220	518	987
0.127 to 0.145	20	9	23	18	44	106	200	219	20	51	39	98	233	441
ACS pod	(17)	(8)	(20)	(14)	(38)	(140)	(220)	(184)	(17)	(44)	(32)	(82)	(309)	(484)
0.917 to 2.00	1	1	1	1	3	17	23	14	1	3	2	6	38	52
0.367 to 0.917	4	2	5	3	9	39	58	62	4	10	7	19	85	125
0.217 to 0.367	7	3	9	6	16	54	88	79	7	19	14	35	119	174
0.217	5	2	5	4	10	40	51	49	5	12	9	22	67	113
<b>Lower wing</b>														
Leading edge ESA 5500M3 ESA 3560HF	(7) 3 4		(9) 4 5	(7) 3 4		(316) 239 77	(332) 246 86	(78) 35 43		(18) 8 10	(14) 6 8		(695) 256 169	(777) 360 287
Box	(150)	(69)	(170)	(129)	(326)	(1541)	(2235)	(1613)	(150)	(379)	(285)	(720)	(1397)	(3 111)
0.89 to 0.93	26	12	29	22	56	249	368	278	26	65	49	124	248	388
0.93 to 1.00	50	23	57	43	108	489	720	538	50	126	95	240	479	757
1.00 to 1.165	30	14	34	26	65	305	444	322	30	76	57	144	293	458
1.165 to 1.40	26	12	30	23	58	285	408	284	26	67	50	127	253	398
1.40 to 2.00	18	8	20	15	39	213	295	191	18	45	34	85	169	261
Elevon	(66)	(29)	(75)	(56)	(144)	(657)	(961)	(712)	(66)	(167)	(125)	(318)	(751)	(1 628)
0.89	49	22	56	42	107	486	713	528	49	124	93	236	497	774
0.89 to 0.93	14	6	16	12	31	142	207	153	14	36	27	68	144	219
0.93 to 1.30	3	1	3	2	6	29	41	31	3	7	5	14	35	51
ACS pod	(17)	(8)	(21)	(16)	(37)	(186)	(268)	(184)	(17)	(44)	(32)	(82)	(311)	(484)
0.89	2	1	3	2	5	24	35	25	2	6	4	11	23	36
0.89 to 0.93	2	1	3	2	5	24	35	25	2	6	4	11	23	36
0.93 to 1.00	7	3	8	6	15	72	105	77	7	17	13	32	68	102
1.00 to 1.165	4	2	5	4	9	45	65	44	4	10	8	20	43	64
1.165 to 1.40	4	1	1	1	2	12	17	11	1	3	2	5	11	16
1.40 to 2.0	1	-	1	1	1	9	12	7	1	2	1	3	7	10
Total, wing	487	217	559	420	1042	4163	6561	5248	477	1243	925	2296	5177	13 100
<b>Tail</b>														
Leading edge	(2)		(2)	(1)		(23)	(26)	(18)		(4)	(3)		(51)	(59)
Box	(58)	(27)	(68)	(52)	(127)	(475)	(749)	(640)	(59)	(149)	(112)	(281)	(1048)	(1649)
2.00 to 0.917	9	4	11	8	20	129	163	100	4	24	18	45	261	361
0.917 to 0.367	16	8	19	15	36	153	231	178	17	52	32	79	328	508
0.367 to 0.137	22	10	25	19	47	144	245	244	22	55	41	104	317	459
0.137	11	5	13	10	24	78	110	118	11	28	21	53	176	261
Rudder	(36)	(16)	(41)	(31)	(79)	(191)	(358)	(387)	(36)	(91)	(68)	(173)	(422)	(709)
0.367 to 0.137	4	2	5	4	10	73	114	114	4	11	8	21	51	75
0.137	32	14	36	27	69	168	314	351	32	80	60	152	371	534
Total, tail	96	43	111	84	206	639	1133	1035	95	244	183	453	1521	2097
Total, orbiter	1184	528	1333	1023	2562	9271	15 737	12 753	1168	2995	2249	5647	20 518	32 677

The total TPS weights, including the use of denser ablators in special areas (as previously discussed) and a total wetted area of 1184m<sup>2</sup> (12 753 ft<sup>2</sup>), were, respectively:

<u>table</u>	<u>kg</u>	<u>lb</u>
19	12 339	27 199
20	13 718	30 242
21	14 717	32 577

The bottoms-up weighing of the RSI design was performed for comparison purposes. Since no further extrapolation, RSI configuration, components arrangement, etc., had been considered for this material in this ablator program, it is the only RSI weight used in this study. The RSI modules were assumed to be 17 cm (6 2/3 in.) square, with coating on all surfaces except the bonding face. The unit weight as a function of RSI thickness, coating, and gap provisions is illustrated in figure 84.

2. Scaling of weight components.- The mechanically attached concepts require an attachment weight that varies with spacing; this value decreases with larger spacing. Conversely, the subpanel values increase, due to the increases in unsupported span. As a result of the subpanel thickening, however, its greater heat capacity reduces the amount of ablator required.

The expression used for obtaining total ablator material weight was:

$$W_i = W_B \left( \frac{H_B}{H_i} \right)$$

where:

W = ablator material weight

H = summation of heat sink elements behind ablator

B = baseline

i = alternative design

The summary of weights for the alternative ablator designs are presented in tables 22 through 29.

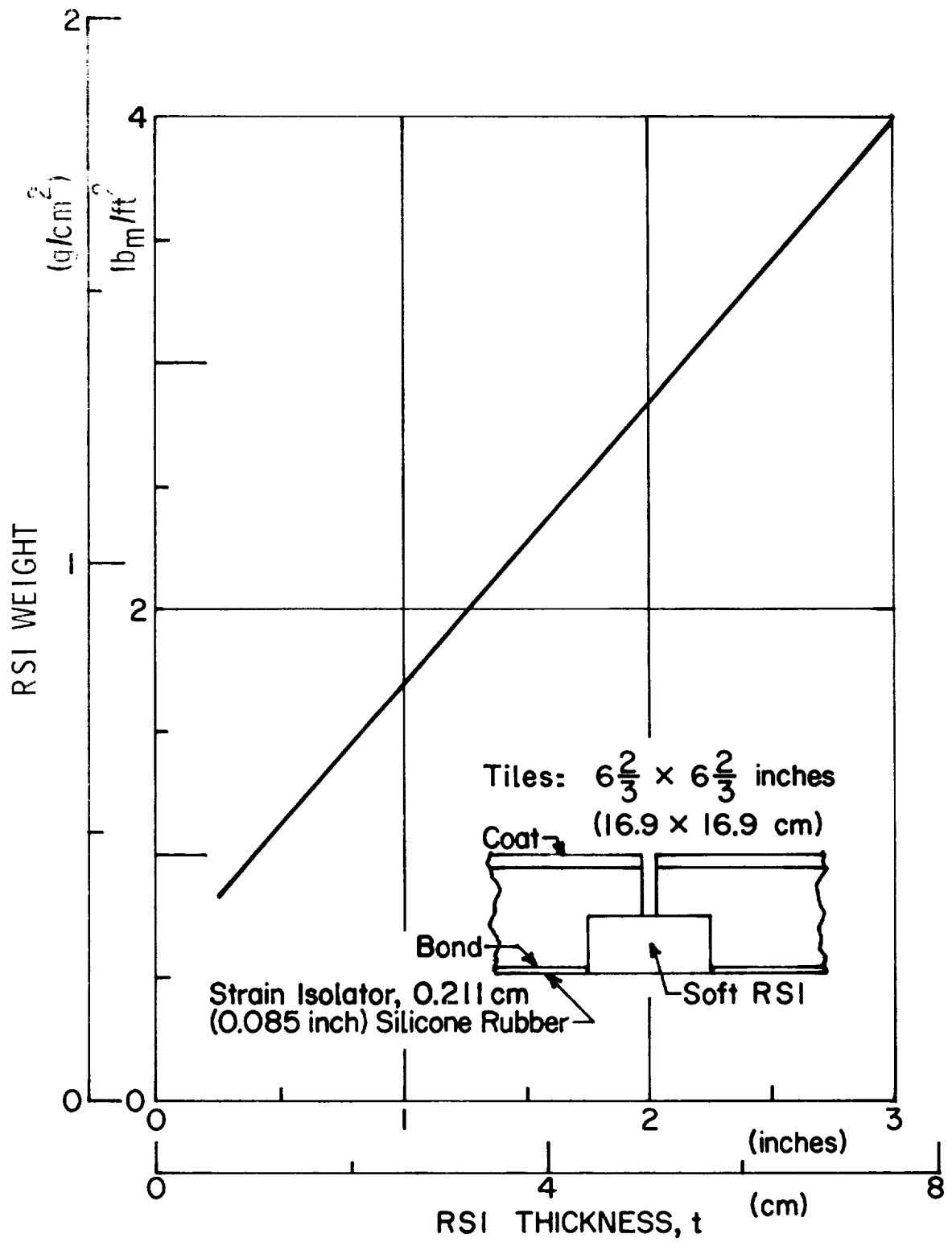


Figure 84.- RSI Thickness versus Weight

TABLE 22.- ALUMINUM (2024-T81) PLATE, DIRECT ATTACHED

Spacing	Mass, kg				Weight, lb			
	12.7 cm	25.4 cm	38.9 cm	50.8 cm	5 in.	10 in.	15 in.	20 in.
Ablator	9 307	8 853	7 621	6 236	20 518	19 518	16 800	13 748
Subpanel	2 562	5 716	12 043	19 060	5 647	12 601	26 550	42 020
Subpanel	2 378	2 378	2 378	2 378	5 244	5 244	5 244	5 244
Fasteners	530	200	85	65	1 168	440	188	142
Total	14 777	17 147	22 127	27 739	32 577	37 803	48 782	61 154

TABLE 23.- MAGNESIUM (4M-21A) PLATE, DIRECT ATTACHED

Spacing	Mass, kg				Weight, lb			
	12.7 cm	25.4 cm	38.9 cm	50.8 cm	5 in.	10 in.	15 in.	20 in.
Ablator	9 488	8 729	8 008	6 709	20 917	19 243	17 654	14 790
Subpanel	1 938	4 450	9 345	13 858	4 273	9 811	20 601	30 552
Bond & Coating	2 378	2 378	2 378	2 378	5 244	5 244	5 244	5 244
Fasteners	530	200	85	65	1 168	440	188	142
Total	14 334	15 757	19 816	23 010	31 602	34 738	43 687	50 728

TABLE 24.- LOCKALLOY PLATE, DIRECT ATTACHED

Spacing	Mass, kg				Weight, lb			
	12.7 cm	25.4 cm	38.9 cm	50.8 cm	5 in.	10 in.	15 in.	20 in.
Ablator	9 310	8 746	7 684	6 450	20 525	19 281	16 939	14 220
Subpanel	1 431	2 986	5 817	9 467	3 155	6 584	12 823	20 871
Bond & coating	2 378	2 378	2 378	2 378	5 244	5 244	5 244	5 244
Fasteners	530	200	85	64	1 168	440	188	142
Total	13 649	14 310	15 964	18 359	30 092	31 549	35 194	40 477

TABLE 25.- ALUMINUM HONEYCOMB, DIRECT ATTACHED

Spacing	Mass, kg				Weight, lb			
	12.7 cm	25.4 cm	38.9 cm	50.8 cm	5 in.	10 in.	15 in.	20 in.
Ablator	9 846	9 846	9 846	9 846	21 707	21 707	21 707	21 707
Subpanel	1 887	2 443	2 988	3 449	4 160	5 386	6 586	7 604
Bond & coating	2 378	2 378	2 378	2 378	5 244	5 244	5 244	5 244
Fasteners	475	187	137	86	1 047	412	302	189
Total	14 586	14 854	15 349	15 759	32 158	32 749	33 839	34 744

TABLE 26.- MAGNESIUM HONEYCOMB, DIRECT ATTACHED

Spacing	Mass, kg				Weight, lb			
	12.7 cm	25.4 cm	38.9 cm	50.8 cm	5 in.	10 in.	15 in.	20 in.
Ablator	9 450	9 450	9 450	9 450	20 834	20 834	20 834	20 834
Subpanel	1 704	2 413	2 956	3 402	3 757	5 321	6 518	7 500
Bond & coating	2 378	2 378	2 378	2 378	5 244	5 244	5 244	5 244
Fasteners	475	187	137	85	1 047	412	302	189
Total	14 008	14 429	14 922	15 316	31 482	31 811	32 898	33 767

TABLE 27.- GRAPHITE POLYIMIDE HONEYCOMB, DIRECT ATTACHED

Spacing	Mass, kg				Weight, lb			
	12.7 cm	25.4 cm	38.9 cm	50.8 cm	5 in.	10 in.	15 in.	20 in.
Ablator	9 507	9 507	9 507	9 507	20 959	20 959	20 959	20 959
Subpanel	1 675	2 339	2 910	3 368	3 694	5 157	6 416	7 427
Bond & coating	2 378	2 378	2 378	2 378	5 244	5 244	5 244	5 244
Fasteners	475	187	137	86	1 047	412	302	189
Total	14 036	14 412	14 933	15 340	30 944	31 772	32 921	33 819

TABLE 28.- ALUMINUM HONEYCOMB, STANDOFF

Spacing	Mass, kg				Weight, lb			
	12.7 cm	25.4 cm	38.9 cm	50.8 cm	5 in.	10 in.	15 in.	20 in.
Ablator	8 450	8 450	8 450	8 450	18 628	18 628	18 628	18 628
Subpanel	2 674	3 831	5 786	7 104	5 895	8 446	12 757	15 661
Bond & coating	2 378	2 378	2 378	2 378	5 244	5 244	5 244	5 244
Fasteners	475	187	137	86	1 047	412	302	189
Standoff fittings	1 625	405	177	97	3 582	892	390	214
Insulation	400	400	400	400	883	883	883	883
Total	16 002	15 651	17 328	35 279	34 505	38 204	38 204	40 819

TABLE 29.- GRAPHITE POLYIMIDE HONEYCOMB, STANDOFF

Spacing	Mass, kg				Weight, lb			
	12.7 cm	25.4 cm	38.9 cm	50.8 cm	5 in.	10 in.	15 in.	20 in.
Ablator	8 280	8 280	8 280	8 280	18 255	18 255	18 255	18 255
Subpanel	2 596	3 810	5 655	6 915	5 722	8 400	12 467	15 245
Bond & coating	2 378	2 378	2 378	2 378	5 244	5 244	5 244	5 244
Fasteners	475	187	137	86	1 047	412	302	189
Standoff fittings	3 913	963	424	264	8 617	2 122	934	581
Insulation	456	456	456	456	1 006	1 006	1 006	1 006
Total	18 098	16 074	17 330	18 379	39 901	35 439	38 208	40 520

3. Observations.- The TPS configuration weights are plotted against fastener spacing in figure 85. This graph also shows the reference weights for the direct bond ablator and the RSI designs. Note that at large attachment spacing, the plate thickness and weight is rising rapidly. The bending strength of honeycomb panels can be increased with small weight penalties by core thickness increase as fastener spacing goes up. The standoff configurations weight is large for low fastener spacing due to the large weight of the many standoff fittings. With increased fastener spacing, the number and weight of standoff fittings is reduced while subpanel weight becomes large. While standoff configuration weights only vary over a range of 3292 kg (7258 lb), compared to a variance of 12 963 kg (28 577 lb) for the direct attached aluminum plate configuration, their weights are greater than the minimum weight direct attached configurations.

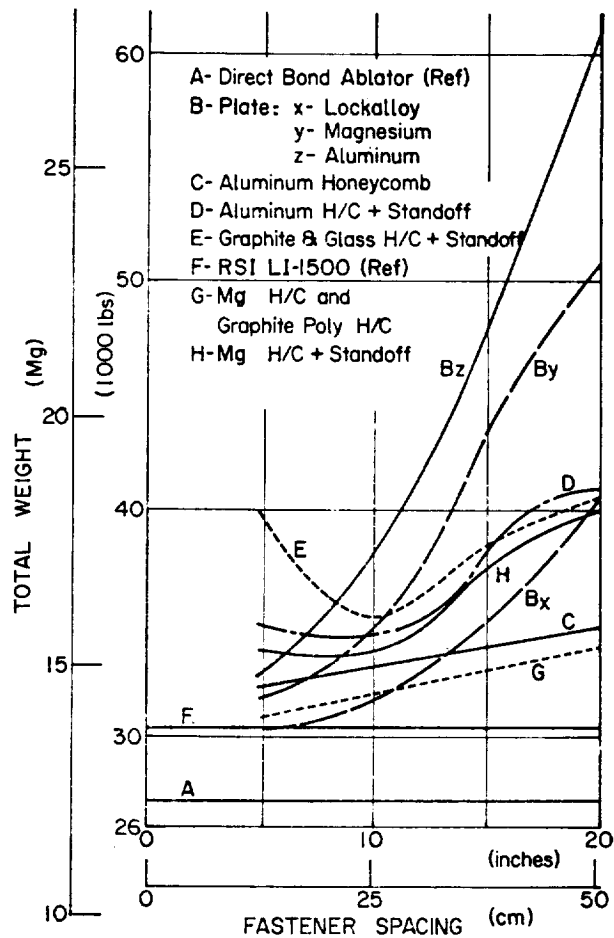


Figure 85.- TPS Attachment Configuration Weight versus Fastener Spacing

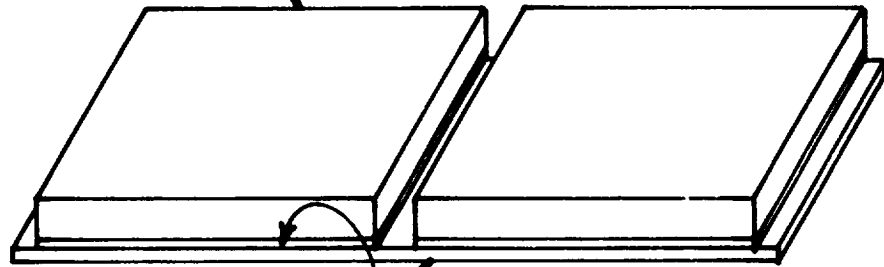
## V. DESIGN VERIFICATION

Eight attachment concepts were evaluated analytically in the program. One of the more efficient concepts determined from the weight and cost studies, the aluminum subpanel concept, was selected for additional evaluation through a verification test series. The objective of these tests was to obtain quantitative data on representative sized configurations when subjected to simulated ascent and reentry thermal loadings. Two panel test series were established: open gap and sealed gap. A corollary series to the sealed-gap work entailed testing various sealer materials for use in the sealed-gap testing.

The primary objective in the panel testing was to evaluate the concepts of gap sealing without the use of a sealer material (open gap) and gap sealing using sealer material (sealed gap). Secondary objectives in both tests were to verify freedom of subpanel motion relative to the primary structure plate to determine the temperature distribution around the stud-bolt counterbore.

The configuration selected for test consisted of a composite panel of two ablator panels bonded to two aluminum subsheets that were then mechanically attached to a stiffened aluminum primary structure sheet. Thicknesses of the components were established from those required at the reference point location (Sta (800)) on the underside of the Orbiter. The ablator thickness was 4.39 cm (1.73 in.), the aluminum subpanel sheet was 0.102 cm (0.040 in.), the aluminum subpanel sheet was 0.103 cm (0.040 in.), and the aluminum primary structure sheet was 0.254 cm (0.10 in.). The analytical studies had indicated an optimum panel size of approximately 1.12 m (44 in.) square. The radiant heat test facility permitted a composite panel length of approximately 1.22 m (48 in.). Therefore, a subpanel size of 55.88 cm (22 in.) square was chosen so that uniform heating would extend beyond the panel edges. The composite test panel configuration is shown in fig. 86. Attachment of each subpanel was at a fixed point in the center of the subpanel and at eight other points, which permitted motion parallel to the subpanel, but prevented displacement perpendicular to the panel (fig. 87).

**Ablator Subpanel**  
4.39x55.88x55.88 cm  
(1.73x22x22 inch)



**Aluminum Subpanel Sheet**  
0.102x55.88x55.88 cm  
(0.040x22x22 inch)

**Aluminum Primary Structure Sheet**  
0.254x55.88x116.84 cm  
(0.10x22x46 inch)

Figure 86.- Composite Test Panel Configuration

**Panel Floating Relative to Primary Structure (16 Places)**

**Panel Fixed Relative to Primary Structure**

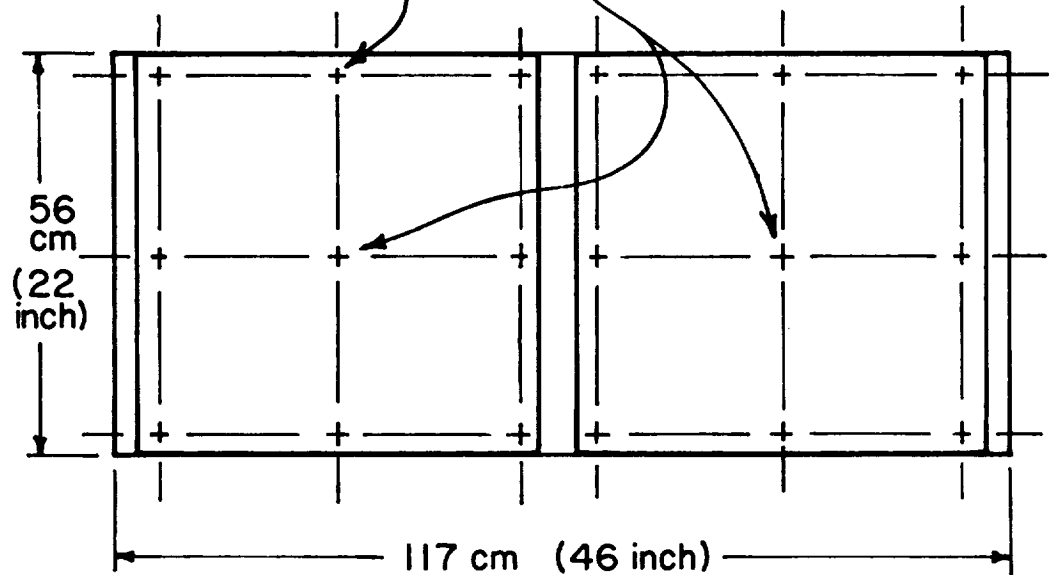


Figure 87.- Subpanel Attachment

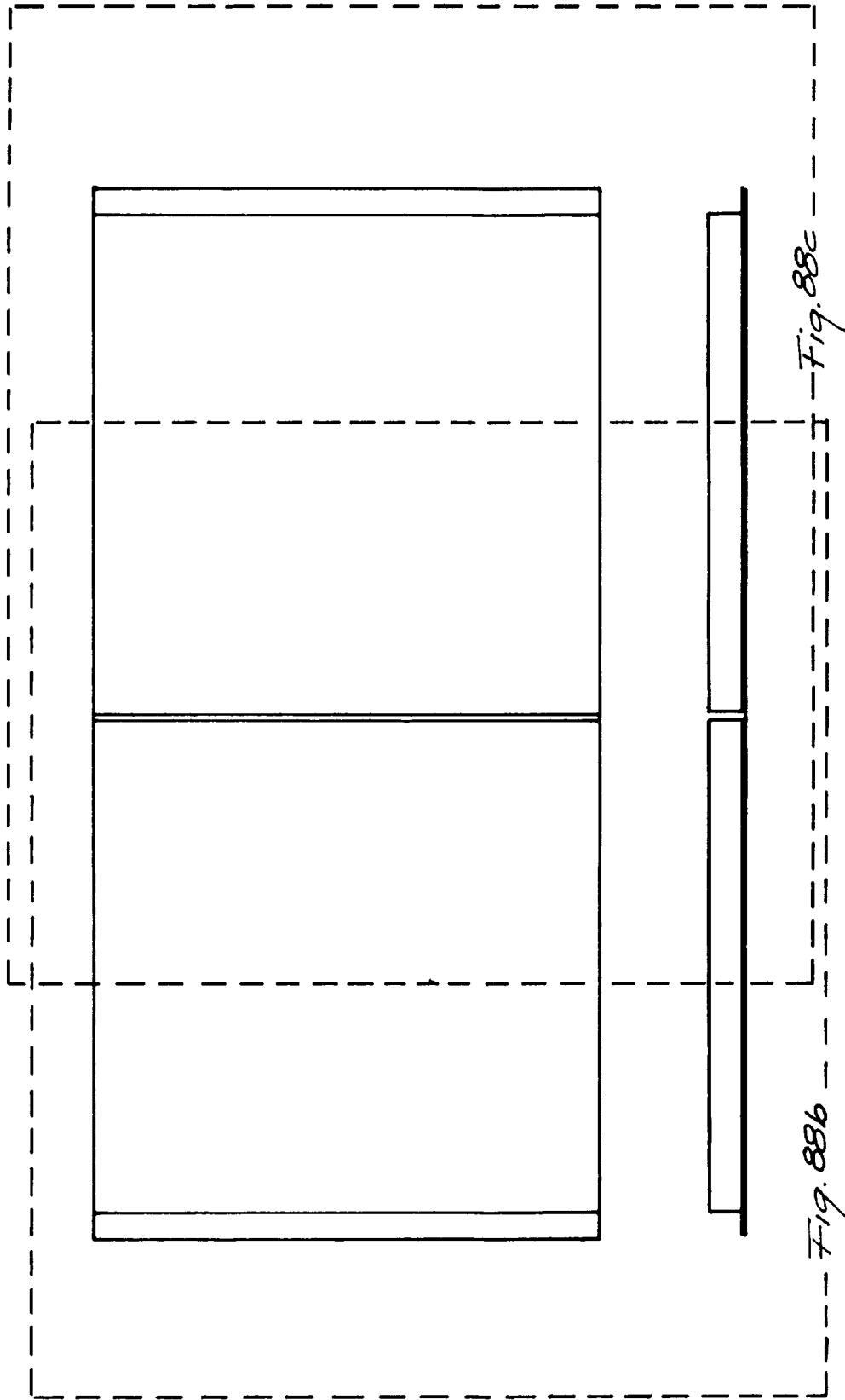
### A. Open-Gap Panel Test

The panel test specimen is shown in figures 88 (a), (b), and (c) complete with instrumentation details. Two portions of the engineering drawing are shown. Four sets of gap-closure pins were incorporated into the panel. One set each of three pins was set at 1.143 cm (0.45 in.), 2.286 cm (0.90 in.), 3.429 cm (1.35 in.) and 3.937 cm (1.55 in.) above the top surface of the aluminum subpanel. During gap closure from the thermal loading, the pin ends were designed to contact a conducting plate on the opposite subpanel ablator. X-ray analysis was used to determine the distance between the pins and the copper conducting plates (fig. 89) following assembly of the subpanels on the primary structure sheet. Two sets of pins are shown in the photo. The test plan for the test is given in appendix E.

Quartz lamps were used to provide the radiant heat input to the panel in the test system shown in figure 90. The panel was mounted vertically in the fixture. Nitrogen gas was dispensed through a manifold into the space between the lamps and the panel to sweep the panel surface free of combustion products. A venting system, consisting of a hood, a centrifugal fan, and an exhaust duct, was used to collect and exhaust the combustion products to the atmosphere outside the building.

For the open-gap panel test, only reentry (descent) heating was simulated. The effects of ascent heat were deferred until the test of the sealed-gap panel. The nominal descent heating profile at the reference point is shown in figure 91.

At approximately 678 s into the heating profile simulation, the cooling water lines to the upper quartz-lamp arrays sprang leaks, necessitating a premature ending of the test. The large amount of heat input to the specimen had caused considerable charring of the ablator, which precluded retesting that particular composite panel. It was determined in the posttest evaluation that an excessive amount of heat was reradiated from the vent hood to the upper surface of the lamp bank where the cooling lines were arranged. The excessive heat caused failure of the lines.



a. Guide to Panel Views

Figure 88.- Open-Gap Test Panel

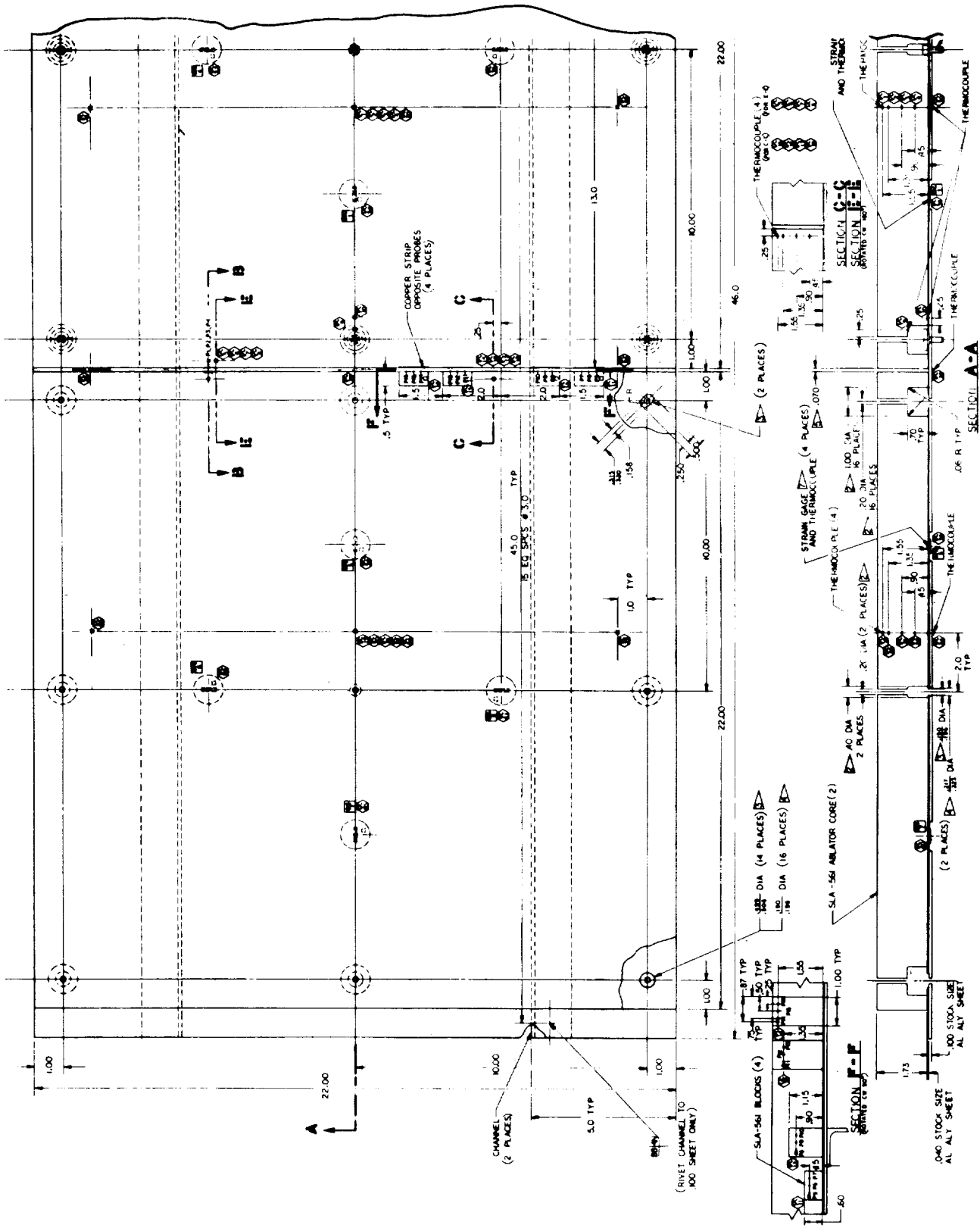


Figure 88.- Continued

b. Left End



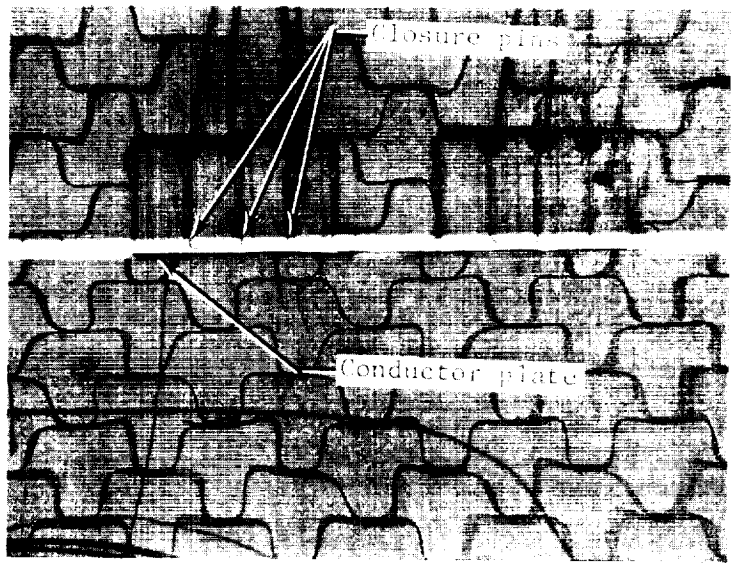


Figure 89.- X-Ray of Gap Closure Pins

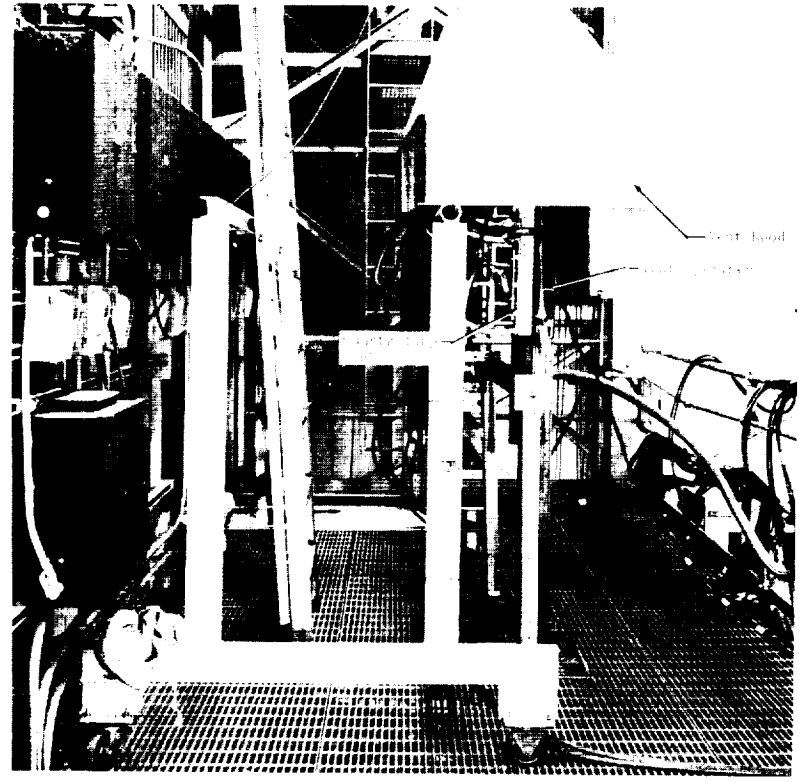


Figure 90.- Radiant-Heat Test Facility (Ablator Panel)

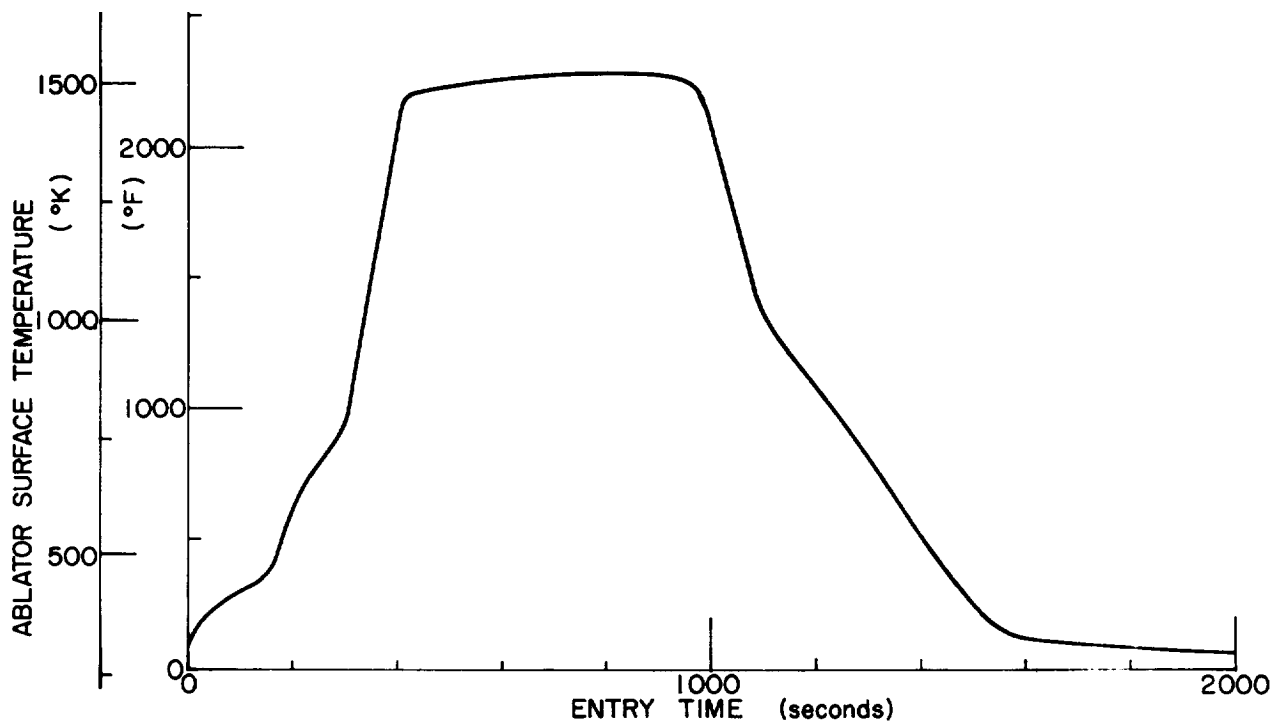


Figure 91.- SLA-561 Reference Point Heating (Descent)

The test data and an examination of the test specimen indicated the following:

- 1) Heat input to the panel was not as uniform as that determined in a calibration test.
- 2) The top and back of the panel were insufficiently insulated and heat was radiated from the vent hood to the panel rear surface. Thermocouple (T/C) 33 on the outstanding leg of the aluminum support channel registered a maximum of 463°K (374°F). T/C 32 on the inner channel leg had a reading of 445°K (341°F) at the same time. T/C 35, mounted on the bottom of the 0.102 cm (0.040 in.) aluminum subpanel sheet, read 337°K (148°F) and T/C 29 on the bottom of the 0.254-cm (0.100 in.) aluminum primary structure read 402°K (264°F) at the time that T/C 33 indicated 463°K (374°F). Heat was obviously getting to the panel rear surface other than through the panel front surface.

- 3) The premature ending of the test did not permit the full thermal pulse to be transferred through the ablator. As a result, back surface temperatures did not have a chance to reach their expected peaks. In addition, to recall, early in the heat exposure the rear surface ("structure") temperatures were higher than those on the subpanel sheets.

Eight strain gages had been bonded to the 0.102 cm (0.040 in.) aluminum subpanel sheets to monitor subpanel deformation that might have occurred as a consequence of binding between subpanel and primary structure through the attachments. The nonuniform heating and premature ending of the test caused the responses shown in figures 92 and 93. Apparently binding at the attachments did occur. With rear surface temperatures higher than subpanel sheet temperatures, the latter were put into tension. Conversely, as additional heat was transferred through the ablator and stored in the ablator at test shutdown, the subpanel became hotter than the primary structure panel and the subpanel sheet was put into compression. Recorded temperature differences between subpanel sheet and primary structure substantiated these data. The magnitude of the resulting subpanel stresses indicate that only a fraction of the anticipated movement freedom was realized, implying that additional development work is necessary with the "floating" bolt attachment system.

- 4) Table 30 presents a compilation of the gap-movement information as determined from the variable length electrical switch probes. The switch closure distances were measured from the x-ray photos previously described. Switch closure predictions were taken from the data presented in Chapter IV of this report. Feasibility of the switch operation was shown in the experiment. However, due to all of the test deficiencies, the amount of information obtained from the 16 switches was meager. Correlation between analysis and experiment for the operative switches was good.
- 5) Nine thermocouples (23 through 31) were installed on the 0.254-cm (0.100 in.) primary structure sheet to determine temperature variation across the panel and compare protected areas with that of the gap. Table 31 presents the data. T/C 25 and 28 indicated higher temperatures at the top of the panel. Temperatures in the gap (T/C 27 and 28) were higher than those at comparable locations on one part of the panel (T/C 24 and 25) but lower than that at

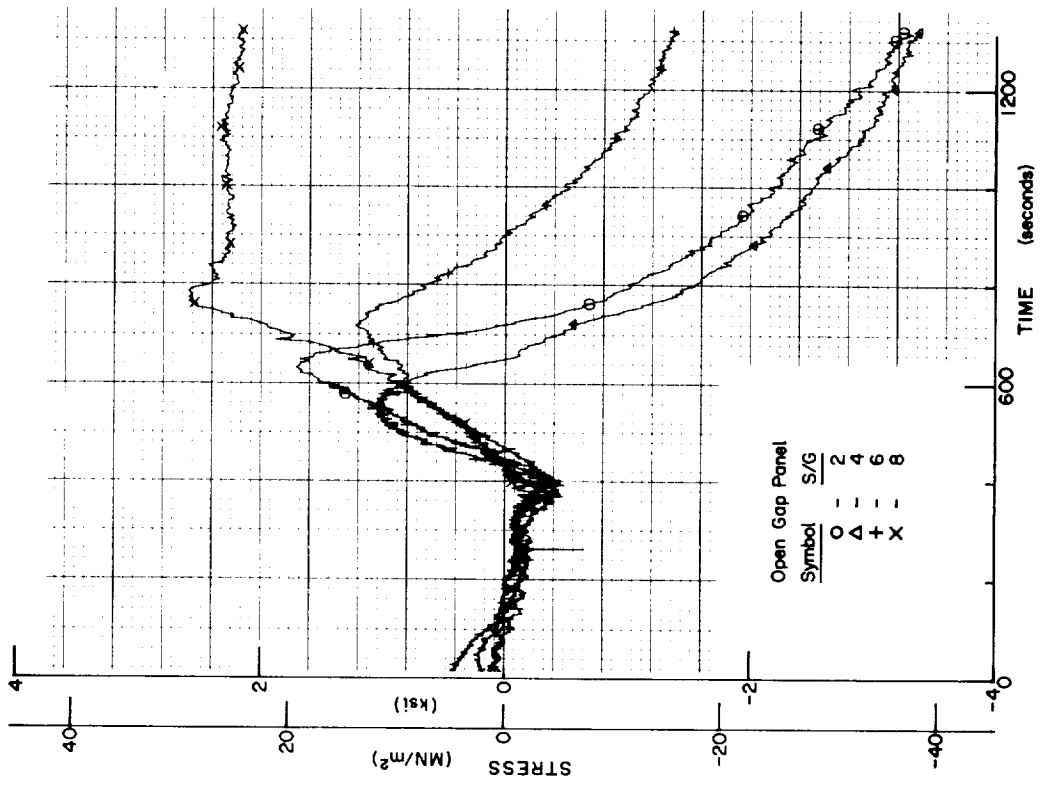


Figure 92.- Strain Gage Data (S/G 1, 3, 5, and 7)

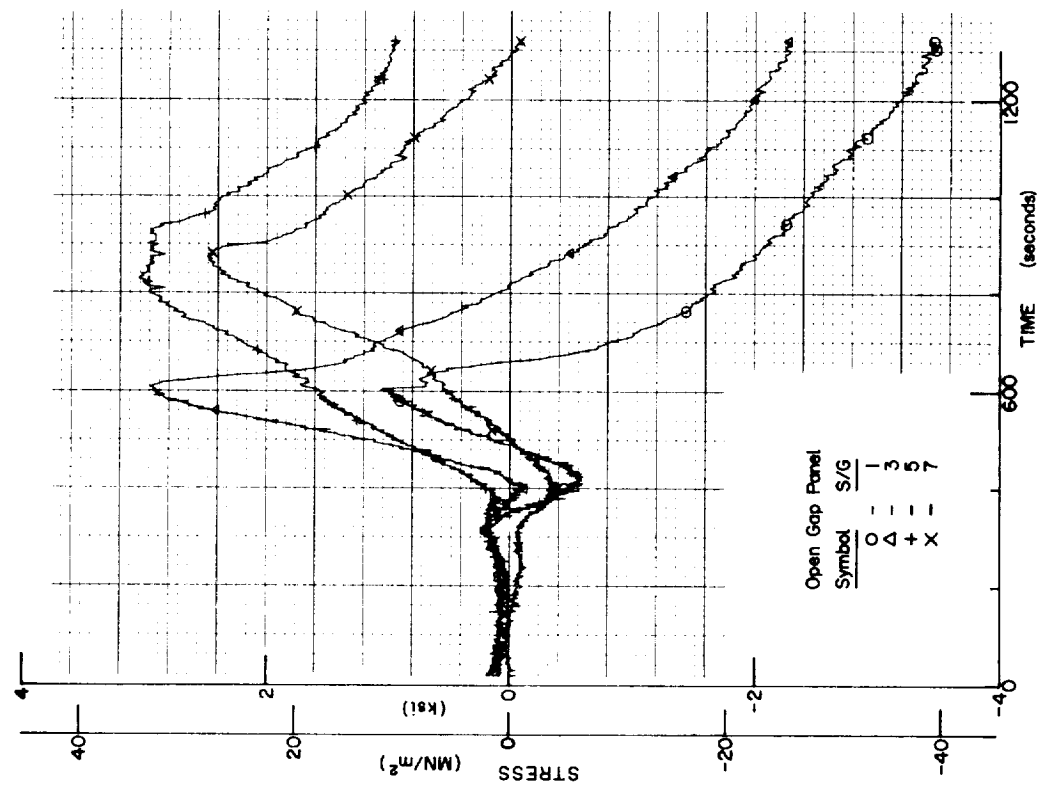


Figure 93.- Strain Gage Data (S/G 2, 4, 6, and 8)

TABLE 30.1. SWITCH-HEAT-FLUX-TO-WEAR MOVEMENT

Switch number	Location above bottom of ablator, cm (in.)	Measured distance from channel web, cm (in.)	Time switch closed, sec (ms from initiation of test)		Measured temperature at switch location at time of switch closure	
			Actual	Predicted	T/C number	°K (°F)
1	3.937 (1.55)	0.149 (0.059)	b	190	5	---
2	3.429 (1.35)	0.143 (0.056)	a	275	6	364 (195)
3	2.286 (0.90)	0.143 (0.056)	a	745	7	---
4	1.143 (0.45)	0.081 (0.032)	c	650	8	---
5		0.075 (0.030)	c	590		---
6	1.143 (0.45)	0.143 (0.056)	a	520	11	---
7		0.143 (0.056)	a	835		---
8		0.143 (0.056)	a	350		---
9	2.286 (0.90)	0.143 (0.056)	a	475	12	---
10		0.143 (0.056)	a	---		---
11		0.143 (0.056)	a	190		---
12	3.429 (1.35)	0.143 (0.056)	a	295	13	332 (139)
13		0.143 (0.056)	a	275		---
14		0.143 (0.056)	a	90		---
15	3.937 (1.55)	0.143 (0.056)	a	260	14	352 (174)
16		0.143 (0.056)	a	180		396 (254)
<p><sup>a</sup> Could not be determined from microanalysis (switch shielded by aluminum channel web)</p> <p><sup>c</sup> No indication</p> <p><sup>b</sup> Ambiguous data</p>						

another (T/C 30). Due to the thermal deficiencies noted previously, no conclusive results were obtained from the thermocouple data alone. An examination of the gap surfaces indicated definite gap closure in some areas (i.e., virgin ablator material) while in other areas, charring appeared to be substantial (see fig. 94). The charring occurred in locations where the switch plugs were bonded into the parent ablator. This was apparently due to high evolution of gases from the silicone adhesive and subsequent combustion. Figure 95 illustrates a cross section through one sub-panel showing the char pattern across the edge of the ablator panel.

TABLE 31.- GAP TEMPERATURE COMPARISON

Time	Temperature at Given Thermocouple, °K (°F)					
	T/C 24	T/C 25	T/C 27	T/C 28	T/C 29	T/C 30
At heat cut-off	384 (232)	433 (320)	410 (279)	466 (379)	394 (249)	417 (292)
Maximum temperature for given T/C	387 (238)	439 (331)	416 (289)	469 (384)	402 (265)	423 (302)
T/Cs 23, 26, and 31 were inoperative.						

- 6) T/C 9 was installed in a stud-bolt counterbore and T/C 10 was installed adjacent to T/C 9 between the ablator and aluminum subpanel sheet to determine if excessive temperatures would be experienced due to the cavity. The data shown in table 32 indicate that counterbore temperatures were comparable to corresponding values in the solid ablator.

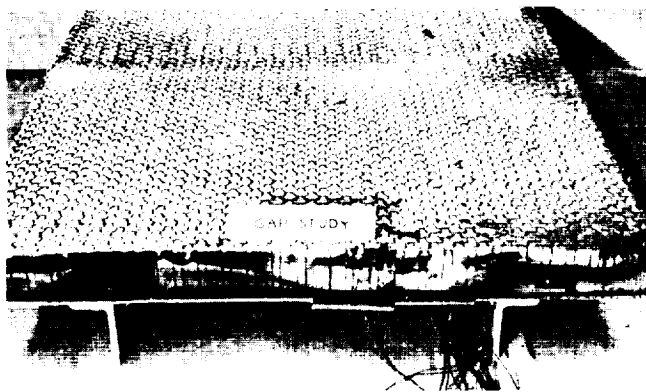


Figure 94.- Posttest Condition of Gap Area (Open-Gap Panel)

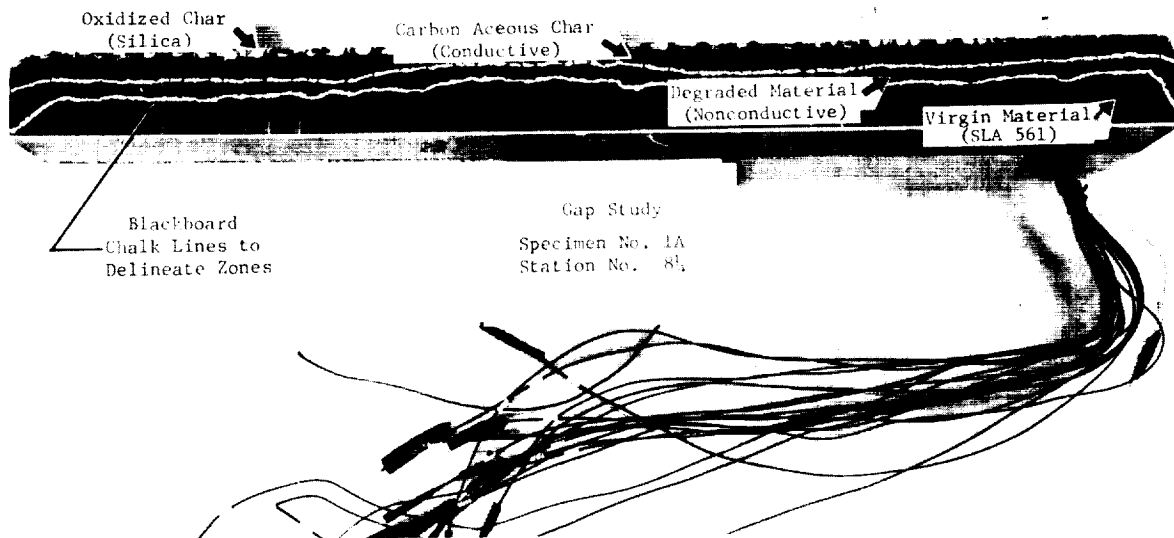


Figure 95.- Cross Section of Tested Subpanel (Open-Gap Panel)

TABLE 32.- STUD-BOLT COUNTERBORE HEATING COMPARISON,  
OPEN-GAP PANEL

Location	T/C number	Temperature at given time, °K (°F)	
		Time from start of test	
		11 min 20 sec (maximum heat termination)	14 min 40 sec (maximum temp in counterbore)
Center of panel, 1.78 cm (0.7 in.) from bottom	1-4	544 (520)	616 (650)
Near gap, 1.78 cm (0.7 in.) from bottom	5-8	469 (385)	550 (530)
Top of counterbore near gap, 1.78 cm (0.7 in.) from bottom	9	472 (390)	580 (584)
Next to counterbore between ablator and aluminum sheet	10	401 (263)	411 (281)

Plots of the recorded thermocouple data for this test are presented in appendix E.

## B. Gap-Sealer Material Resiliency Tests

As part of the preparation for the sealed-gap panel testing, gap-sealer material resiliency tests were planned to measure candidate material springback when subjected to deformations at high temperatures, which simulated ablator expansion at reentry temperatures. A test fixture (fig. 96) was designed to provide a space corresponding to initial installation compression of the sealer and subsequent ablator expansion compression. Two types of sealer materials were evaluated: high resiliency Fiberfrax H blanket and Fiberfrax rope (both are products of the Carborundum Company, Niagara Falls, New York).

Due to its method of manufacture, the Fiberfrax H blanket material is transversely isotropic (fig. 97). That is, in the X-Y plane the properties, both mechanical and thermal, are constant and independent of orientation. Properties in the Z-direction are different than in the X-Y plane. The method of fabrication of the blanket orients the ceramic fibers so that the thermal conductivity in the Z-direction is low. Conductivity in the X-Y plane is much higher. Therefore, orienting the sealer in such a way that the Z-direction would be parallel to the gap would reduce heat transfer down the gap. Unfortunately, however, loading the Z-direction material, as the ablator would compress it, could cause delaminations. Adequate resiliency might remain however, and Z-direction specimens were fabricated. The Fiberfrax rope specimens were fabricated as shown in figure 98. The Irish Refrasil cloth was used to contain the rope. (This cloth would also be used with an actual blanket material sealer to aid in handling.)

The testing procedure was as follows:

- 1). Specimens were measured before the test;
- 2) One specimen was installed in each test fixture and six fixtures were placed in the high temperature kiln;
- 3) Dead load silica weights were placed on each of the fixtures to fully compress the test specimen to the test thickness;

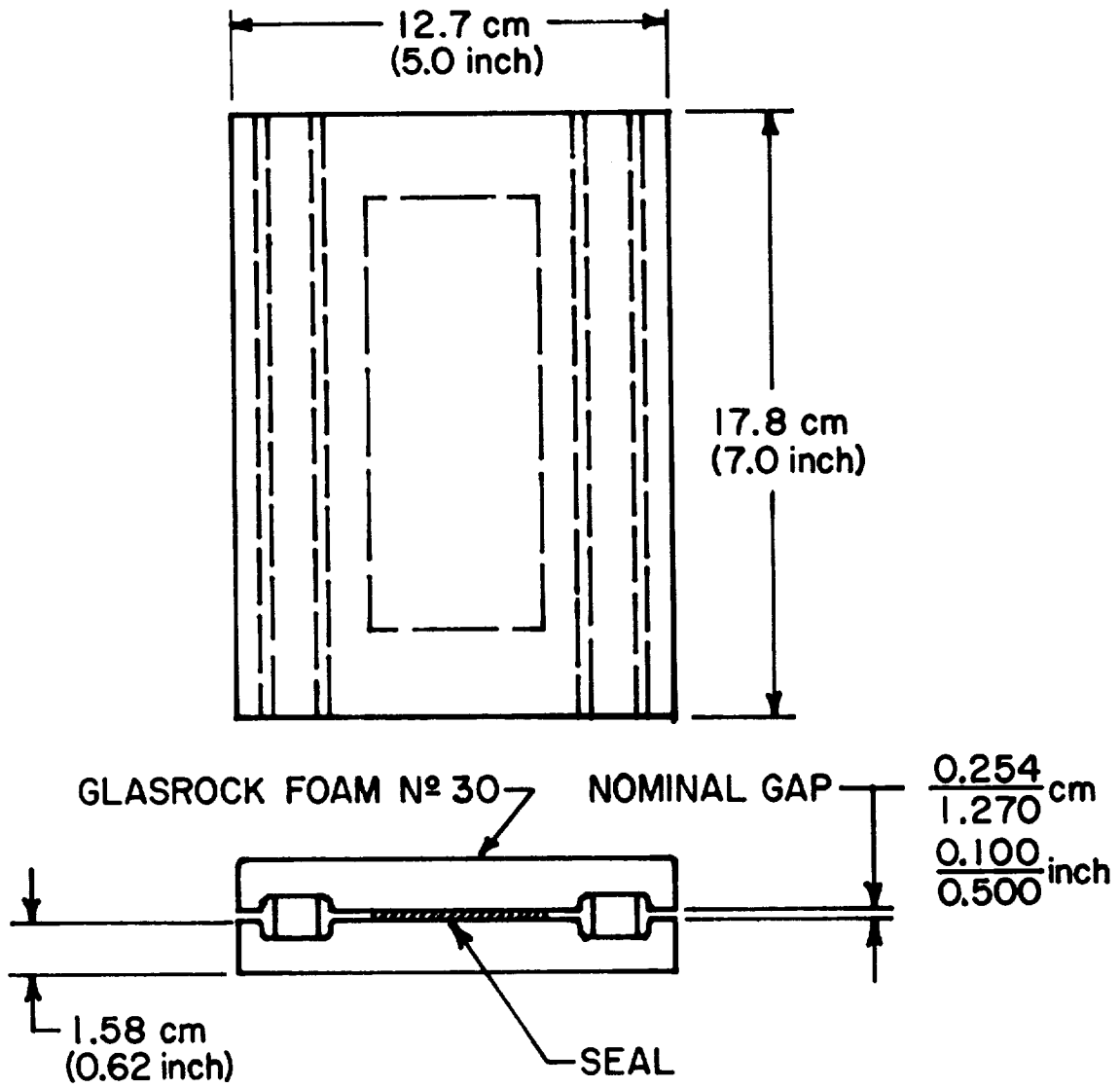


Figure 96.- Test Fixture, Gap Sealer Material

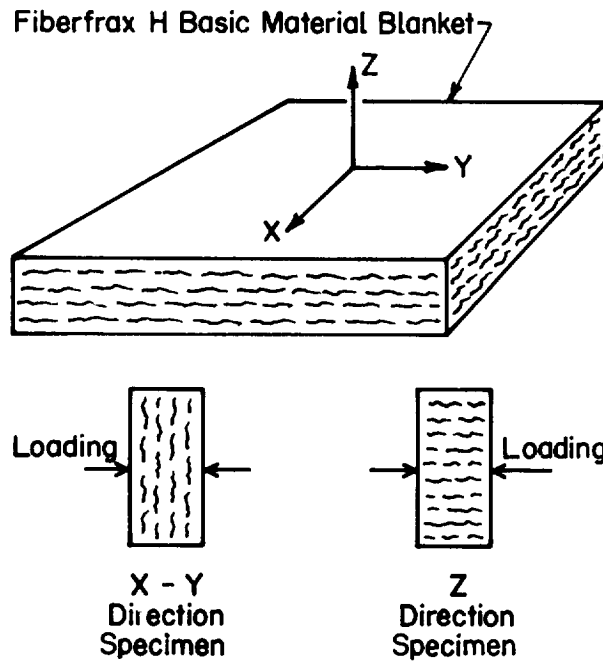


Figure 97.- Blanket Material Specimens

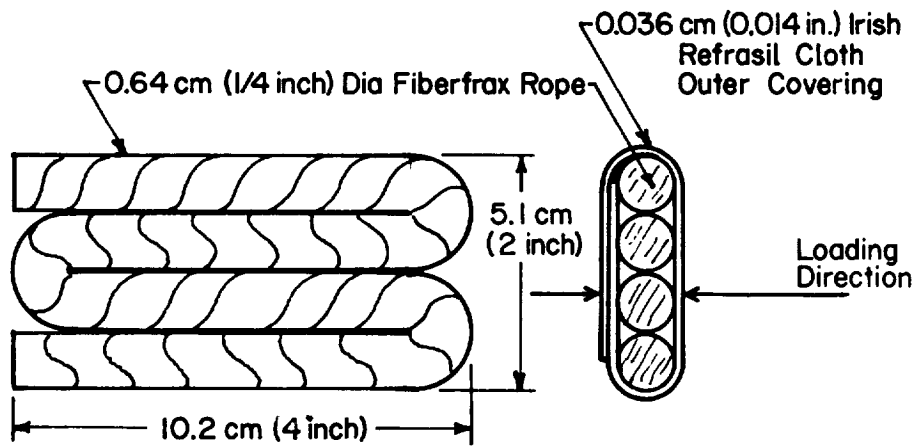


Figure 98.- Fiberfrax Rope Specimen

- 4) The kiln was heated to 1366°K (2000°F) (elapsed time approximately 3¼ hours), the temperature kept constant for 15 minutes, and then heat input immediately stopped. Twenty hours were required to cool the kiln to approximately 339°K (150°F) to remove the test fixtures;
- 5) The dead weights were removed sequentially from each fixture and each specimen was measured immediately thereafter.

A total of 17 specimens were tested. The results are shown in table 33. For the X-Y plane specimens, the thicker blanket material, nominally 2.032 cm (0.8 in.) thick, exhibited more resiliency than the thinner, nominally 1.016 cm (0.4 in.) thick, material. All of the Z-direction specimens became severely delaminated during the initial compression process. Springback on both thicknesses after heating was poor. Springback of the rope material was nonexistent. This was disappointing in that the rope is much more rugged and easier to handle when compared to the blanket material. Based on these data, it was decided that 2.032-cm (0.8 in.) thick, X-Y plane, blanket material would be used with a 1.143-cm (0.45 in.) gap for the sealed-gap panel test.

TABLE 33.- GAP SEALER RESILIENCY TESTING

Specimen identification	Specimen number	Initial thickness		Thickness after compression		Springback after decompression	
		cm (in.)	cm (in.)	cm (in.)	cm (in.)	cm (in.)	cm (in.)
Fiberglass blankets, X-Y plane specimens <sup>a</sup>	1	0.960 (0.378)	0.249 (0.098)	0.711 (0.279)	0.435 (0.171)	0.084 (0.033)	0
	2	0.960 (0.378)	0.249 (0.098)	0.711 (0.279)	0.435 (0.171)	0.084 (0.033)	0
	3	0.960 (0.378)	0.249 (0.098)	0.711 (0.279)	0.435 (0.171)	0.084 (0.033)	0
	4	1.016 (0.399)	0.273 (0.107)	0.743 (0.292)	0.468 (0.184)	0.110 (0.043)	0
	5	1.016 (0.399)	0.273 (0.107)	0.743 (0.292)	0.468 (0.184)	0.110 (0.043)	0
	6	1.016 (0.399)	0.273 (0.107)	0.743 (0.292)	0.468 (0.184)	0.110 (0.043)	0
	7	1.016 (0.399)	0.273 (0.107)	0.743 (0.292)	0.468 (0.184)	0.110 (0.043)	0
	8	1.016 (0.399)	0.273 (0.107)	0.743 (0.292)	0.468 (0.184)	0.110 (0.043)	0
	9	1.016 (0.399)	0.273 (0.107)	0.743 (0.292)	0.468 (0.184)	0.110 (0.043)	0
	10	1.016 (0.399)	0.273 (0.107)	0.743 (0.292)	0.468 (0.184)	0.110 (0.043)	0
Fiberglass blankets, Z-direction specimens <sup>a</sup>	1	0.960 (0.378)	0.249 (0.098)	0.711 (0.279)	0.435 (0.171)	0.084 (0.033)	0
	2	0.960 (0.378)	0.249 (0.098)	0.711 (0.279)	0.435 (0.171)	0.084 (0.033)	0
	3	0.960 (0.378)	0.249 (0.098)	0.711 (0.279)	0.435 (0.171)	0.084 (0.033)	0
	4	0.960 (0.378)	0.249 (0.098)	0.711 (0.279)	0.435 (0.171)	0.084 (0.033)	0
	5	0.960 (0.378)	0.249 (0.098)	0.711 (0.279)	0.435 (0.171)	0.084 (0.033)	0
	6	0.960 (0.378)	0.249 (0.098)	0.711 (0.279)	0.435 (0.171)	0.084 (0.033)	0
Fiberglass rope	1	0.960 (0.378)	0.249 (0.098)	0.711 (0.279)	0.435 (0.171)	0.084 (0.033)	0
	2	0.960 (0.378)	0.249 (0.098)	0.711 (0.279)	0.435 (0.171)	0.084 (0.033)	0
	3	0.960 (0.378)	0.249 (0.098)	0.711 (0.279)	0.435 (0.171)	0.084 (0.033)	0

<sup>a</sup>See Figure 58 for identification of test fixtures.

### C. Sealed-Gap Panel Test

The configuration of the sealed-gap panel is shown in figure 99. Instrumentation details (i.e., strain gages and thermocouples) are also shown in the figure. The pretest appearance of the panel is shown in figure 100. Eight surface thermocouples used to control power to the quartz-lamp bank can be seen.

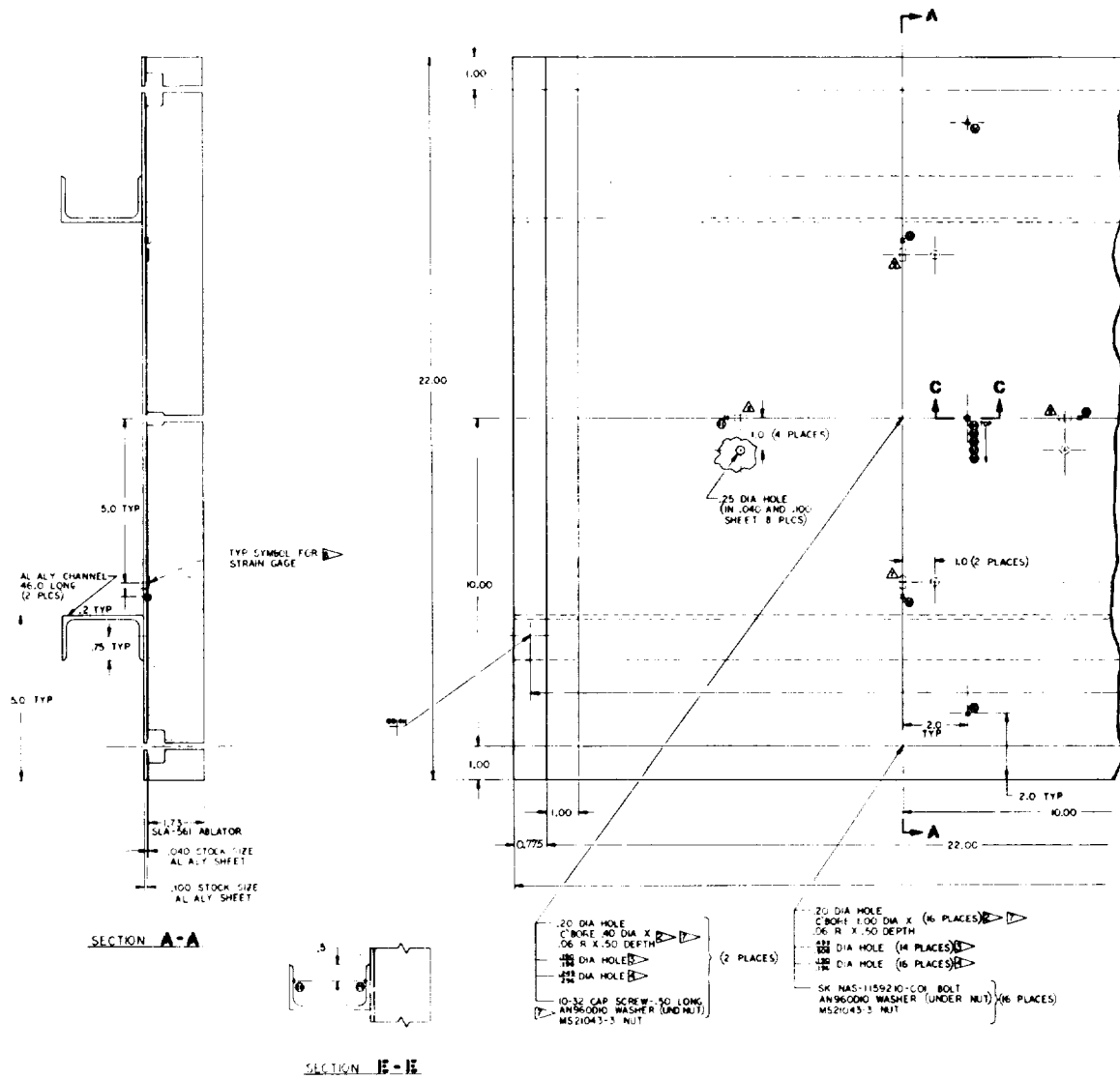
Based upon the results of the gap-sealer resiliency tests, the gap sealer was fabricated of 2.032 cm (0.8 in.) thick, X-Y plane, Fiberfrax H blanket material. One layer of Irish Refrasil cloth was wrapped around the blanket material to aid in handling. The gap between panels was established at 1.143 cm (0.45 in.).

The complete test plan for the panel is given in appendix E. The panel was subjected to two heating conditions, an ascent heating profile (fig. 101) and a descent heating profile (fig. 91).

1. Ascent heating.— The physical appearance of the panel and gap sealer did not change from that in the untested condition. A review of the recorded digital data indicated that gap sealing by use of the Fiberfrax H blanket was satisfactory. However, temperature changes for the ascent heating test condition were so low that it was difficult to reach a definite conclusion, i.e., maximum temperature of the back surface of the 0.254 cm (0.100 in.) primary structure sheet was 304°K (88°F).

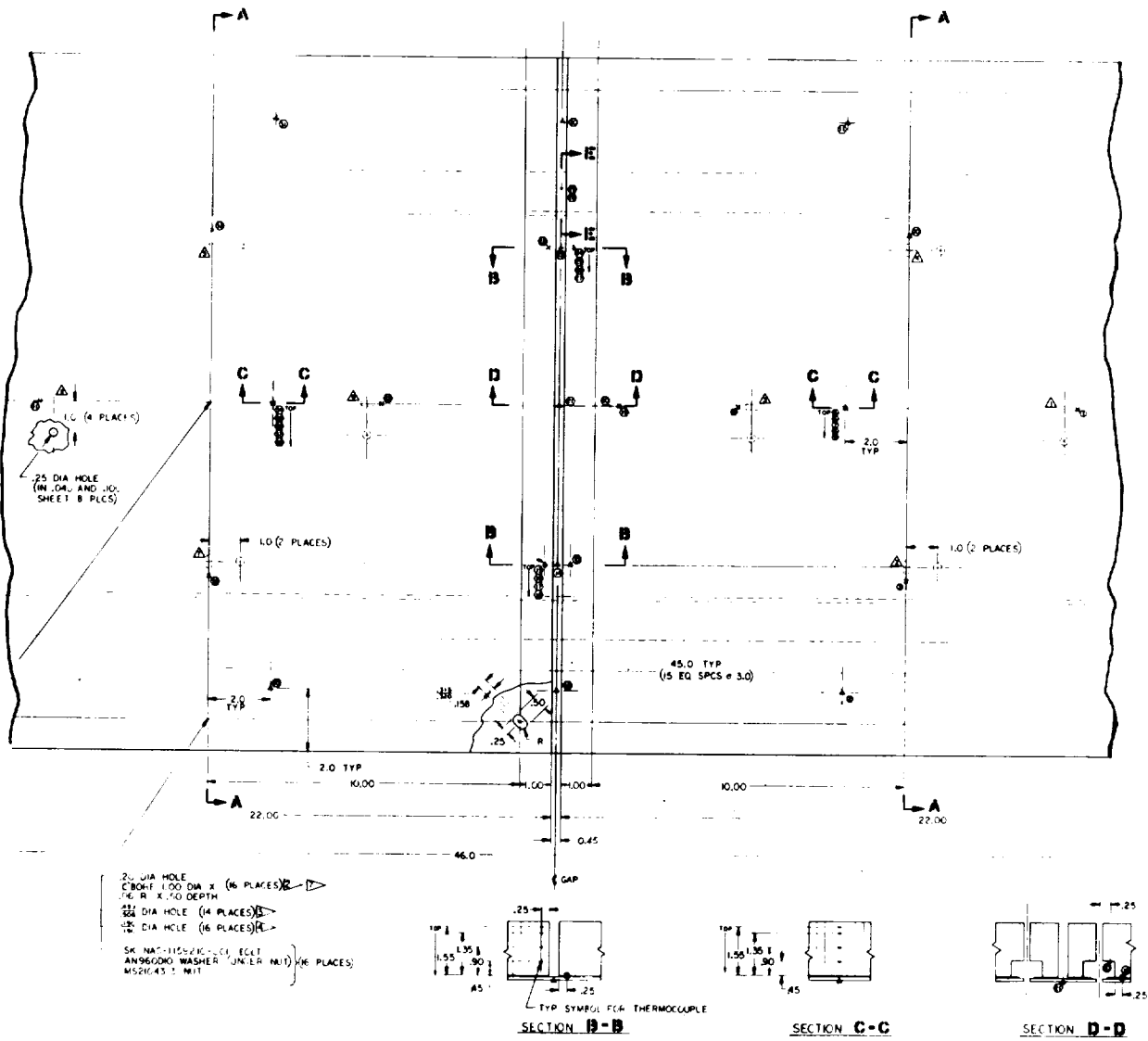
2. Descent heating.— The panel was subjected to the complete descent heating profile. The test data and an examination of the test specimen indicated the following:

- 1) Four zones on the panel were monitored and used to control the power to the quartz-lamp bank. Recorded temperatures were within  $\pm 28^{\circ}\text{K}$  ( $\pm 50^{\circ}\text{F}$ ) of the nominal curve shown in figure 101.
- 2) Ten thermocouples (31, 30, 11, 38, 23, 9, 40, 12, and 2) were installed on the 0.254-cm (0.100 in.) primary structure sheet to determine temperature variation across the panel and to compare protected areas with that of the gap. Figure 102 presents the maximum temperature and corresponding time from start of test for each of the T/C locations. T/C 2 and 11 were inoperative during the test. The results indicate that the temperature was not uniform in the primary structure sheet. Gap temperatures at the panel top and bottom were significantly higher than those of the surrounding structure. This indicates that the sealer in



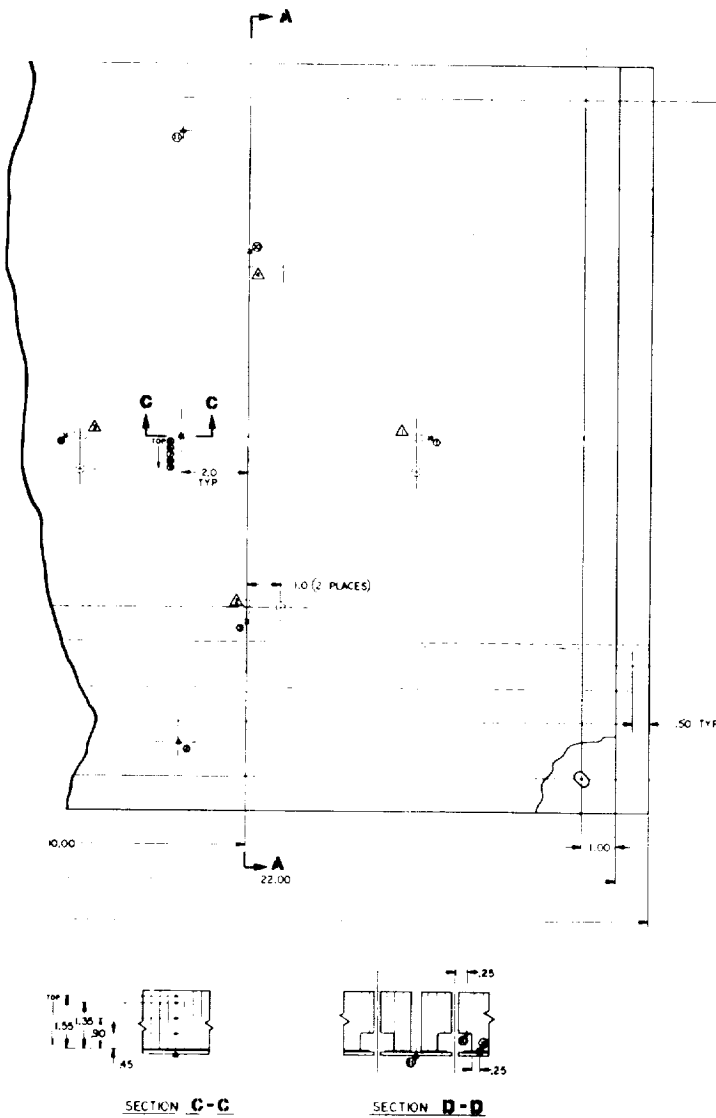
a. Left End

Figure 99.- Sealed-Gap Test Panel



b. Center

Figure 99.- Continued



**NOTES:**

1. BREAK ALL SHARP EDGES.
2. THIS DIMENSION IS FOR THE SLAB ABLATOR - THIS ONLY.
3. THIS DIMENSION IS FOR THE JOO AL ALY SHEET - THIS ONLY.
4. THIS DIMENSION IS FOR THE JOO AL ALY SHEET - THIS ONLY.
5. THE FOLLOWING SYMBOLS ARE USED ON THIS DRAWING:
  - OR ⊖ - STRAIN GAGE
  - ▲ OR △ - THERMOCOUPLE - BACK FACE OF JOO SHEET
  - ⊖ OR ⊕ - THERMOCOUPLE - INTER-FACE OF SLAB AND JOO AL ALY SHEET
  - OR - - THERMOCOUPLE - IN THE SLAB ABLATOR AND OTHER
  - ⊖ OR ⊕ - INSTRUMENTATION - THERMOCOUPLE NUMBER
  - △ - INSTRUMENTATION - STRAIN GAGE NUMBER
6. FILL ALL FASTENER ACCESS HOLES WITH ABLATOR PLUS. BOND WITH CLEAR ABLATOR RESIN AFTER X-RAY AND INSTRUMENTATION CONTINUITY CHECKOUT.
7. BOND JOO TO JOO AL ALY SHEET AFTER X-RAY AND INSTRUMENTATION CONTINUITY CHECKOUT WITH A HIGH TEMPERATURE ADHESIVE.
8. BOND STRAIN GAGES TO JOO AL ALY SHEET WITH FACTAN 90 HT OR ANY OTHER ADHESIVE WITH A MINIMUM TEMPERATURE CAPABILITY OF 250°F.
9. JOO AND JOO SHEET DETAILS ARE TO BE MATCHED DRILLED PER DIMENSIONS SHOWN. FINAL DRILL HOLE SIZES ARE TO BE DONE INDIVIDUALLY.
10. INSTALL FASTENERS INTO JOO SHEETS. BOND DRILLED AND INSTRUMENTED ABLATOR SLABS TO THE JOO SHEET DETAILS. TAKE CARE TO ASSURE THE ADHESIVE DOES NOT FLOW INTO FASTENER HOLES IN ABLATOR AND PERMANENTLY FIX FASTENERS.

DATE: 04/15/02/75

GAP TEST-CEALED

SK-NAS1-1159220

c. Right End

Figure 99.- Concluded

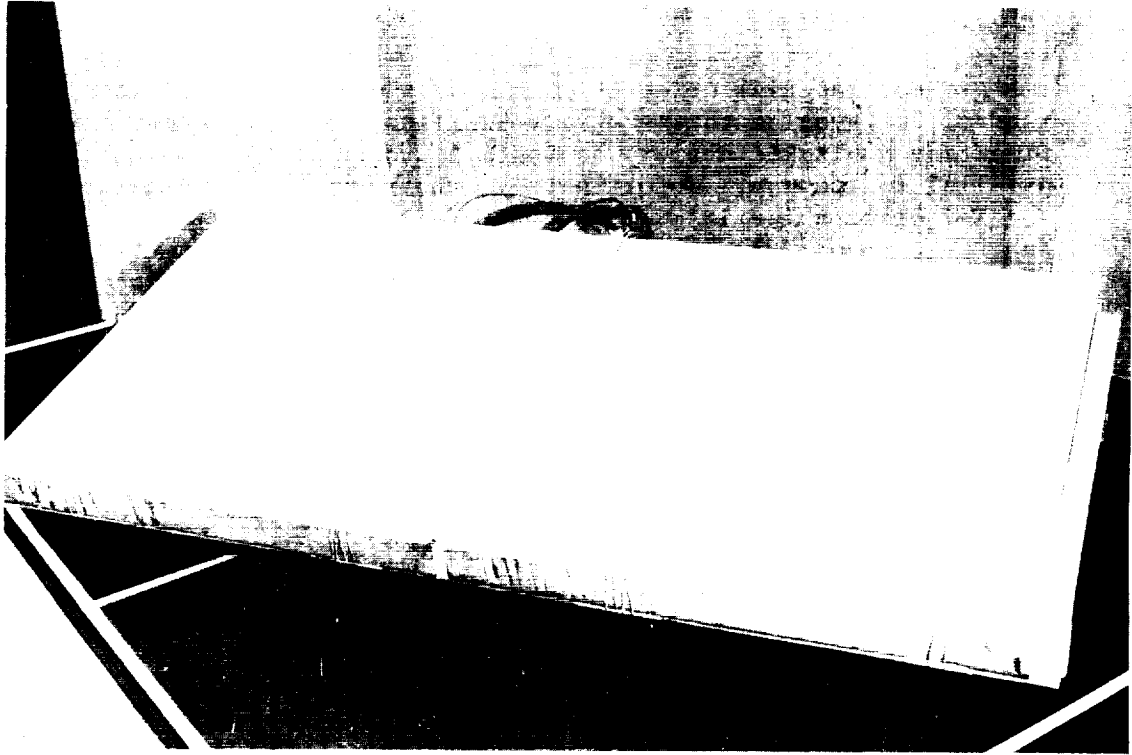


Figure 100.- Sealed-Gap Panel, Pretest Appearance

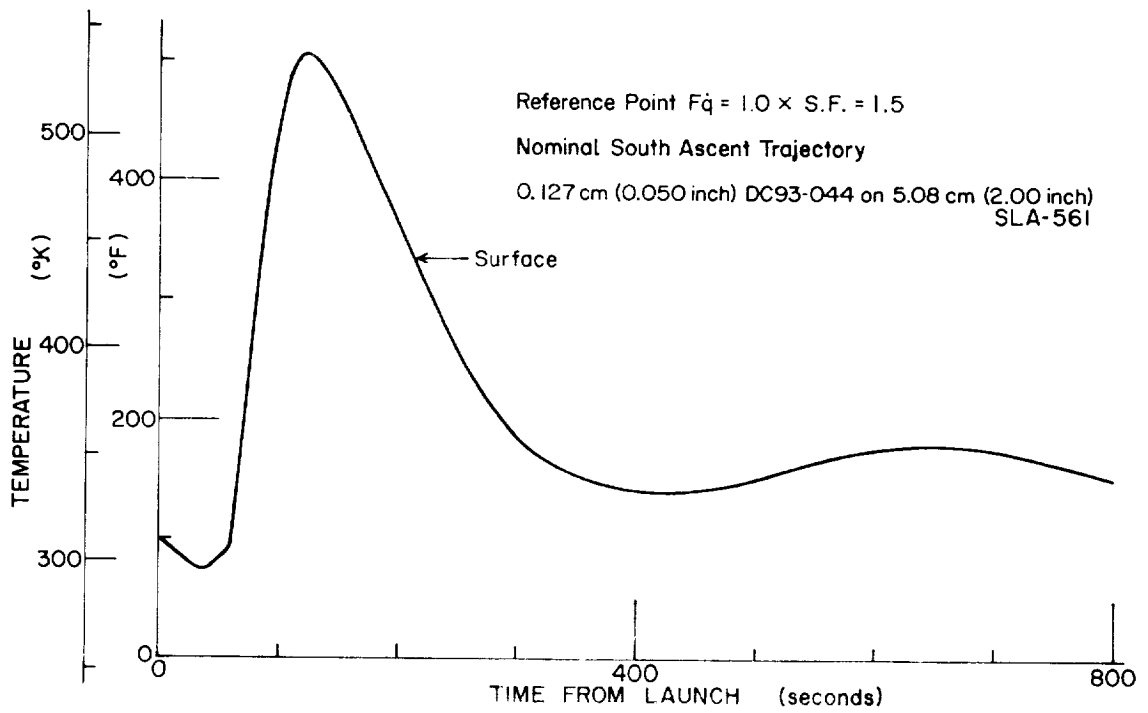
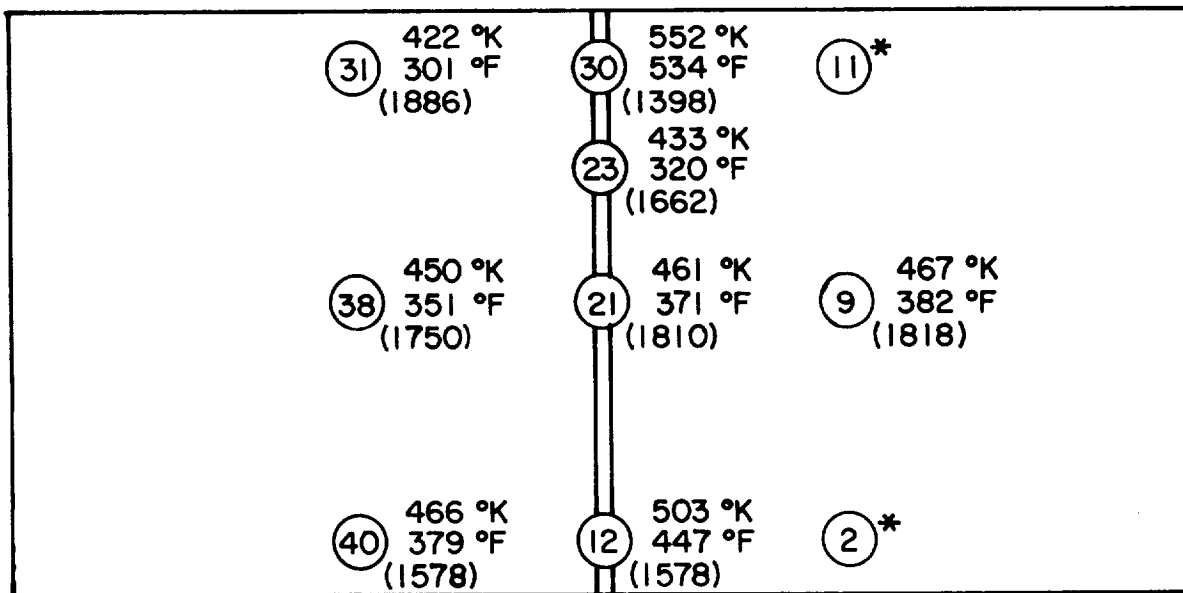


Figure 101.- SLA-561 Reference Point Heating (Ascent)

its present material orientation did not work as well as intended. To provide the necessary resiliency in the sealer, the Fiberfrax H blanket sealer was installed with the X-Y orientation parallel to the gap. Unfortunately, the thermal conductivity in the X-Y orientation is much higher than that in the Z-direction and, as a result, a significant amount of heat was conducted through the sealer. The temperature differential between the top surface and primary structure plate was approximately 1300°K (1700°F). Additional development effort is required in future programs to design the required thermal barrier. Feasibility of the concept has been demonstrated in this program, however.



- - T/C Location and Number
- ( ) - Time in seconds to Reach Given Maximum Temperature

Figure 102.- Temperature Uniformity and Gap Temperature Comparison, Back of 0.254-cm (0.10 in.) Primary Structure Sheet

3) T/C 20 was installed in and T/C 19 was installed adjacent to a stud-bolt counterbore to determine if excessive temperature would be experienced in the cavity. The data shown in table 34 indicate that maximum temperature in the counterbore was significantly higher than those in comparable points in the solid ablator. Future development effort is necessary in this design area since the temperature differential found in the test of the open-gap panel did not shown this large temperature difference.

TABLE 34.- STUD-BOLT COUNTERBORE HEATING COMPARISON,  
SEALED-GAP PANEL, DESCENT HEATING

Location	Thermocouple number	Temperature °K at given time from start of test, s
Center of panel, 1.27 cm (0.5 in.) from bottom	5 thru 8	648°K(707°F) (≈1240)
Near gap, 0.127 cm (0.5 in.) from bottom	24 thru 27	583°K(590°F) (≈1380)
Top of counterbore near gap, 1.27 cm (0.5 in.) from bottom	20	886°K(590°F) (1012)
Next to counterbore between ablator and aluminum subpanel sheet	19	460°K(369°F) (1622)
Near counterbore, in gap, on back of primary structure plate	21	461°K(371°F) (1810)

- 4) The sides of the ablator panels at the gap did not exhibit as much charring as occurred with the open-gap panel. Virgin ablator remained in about the lower third of each panel at the gap.
- 5) Eight strain gages were bonded to the 0.102-cm (0.040 in.) aluminum subpanel sheet to monitor subpanel deformations. Figures 103 and 104 present the strain gage data. Anomalous results were obtained since some of the indicated stresses were higher than those that would be predicted from a fully-fixed attachment condition and the temperature differential between subpanel and primary structure plate. The attachment bolts for this panel were selected to provide an ample clearance for subpanel motion. From the data, the subpanels were restrained. Additional effort would be required in attachment design in future programs. Figure 105 presents the maximum temperatures of the aluminum subpanel sheets recorded at each of the strain gage locations.
- 6) The posttest appearance of the panel is shown in Figure 106. Plots of the recorded thermocouple data for the descent heating test are presented in Appendix E.

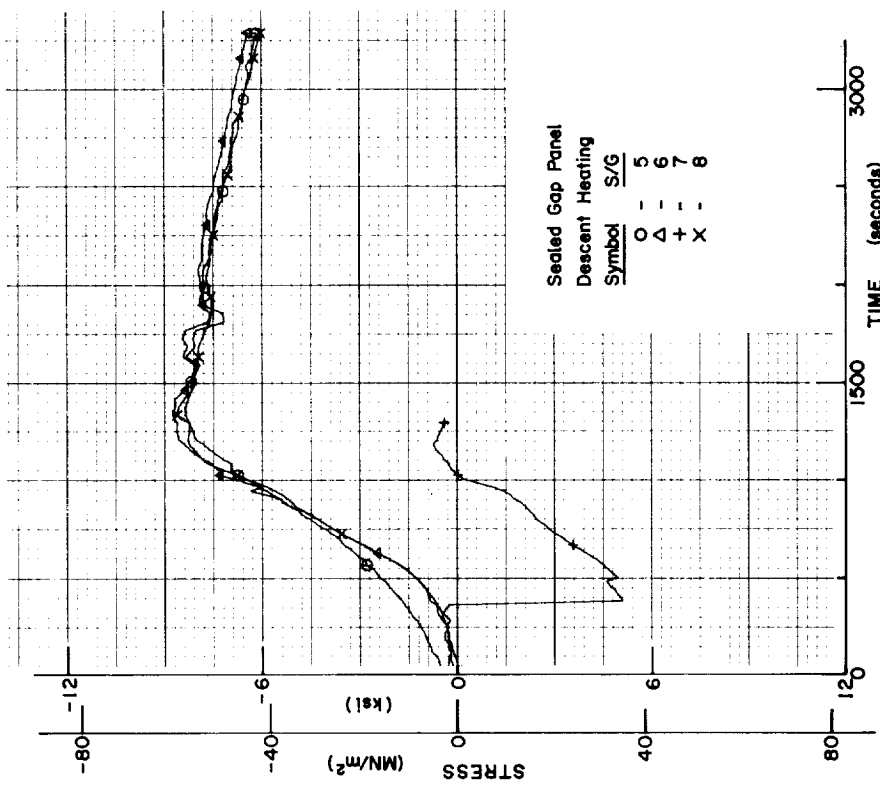


Figure 103.- Strain Gage Data (S/G 1, 2, 3, and 4)

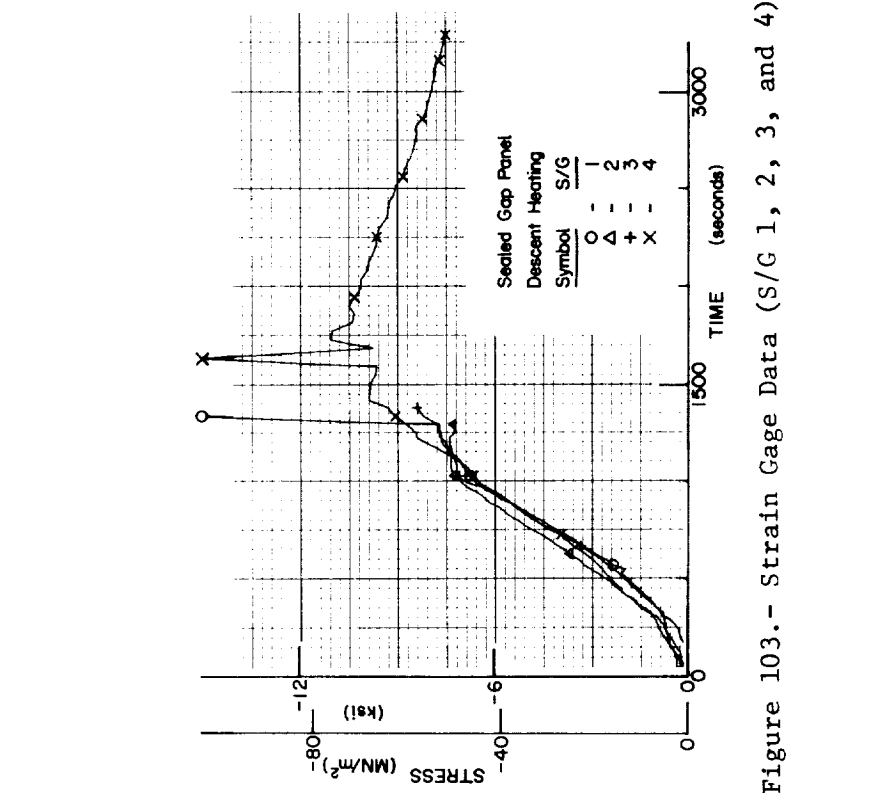
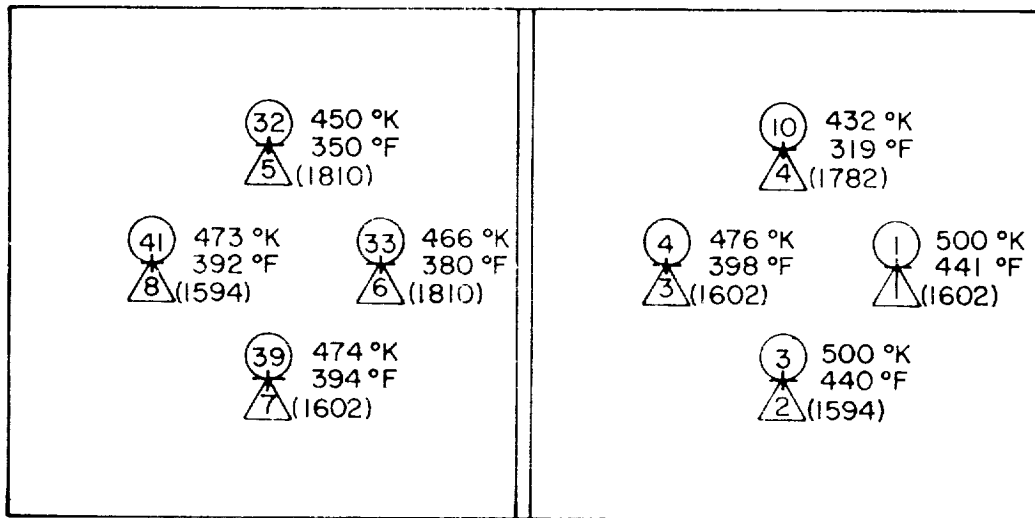


Figure 104.- Strain Gage Data (S/G 5, 6, 7, and 8)



- - T/C Number
- △ - Location
- △ - Strain Gage Number
- ( ) - Time in seconds to Reach Given Maximum Temperature

Figure 105.- Maximum Temperature at Strain Gages, Gages between Ablator and 0.102-cm (0.040 in.) Sheet

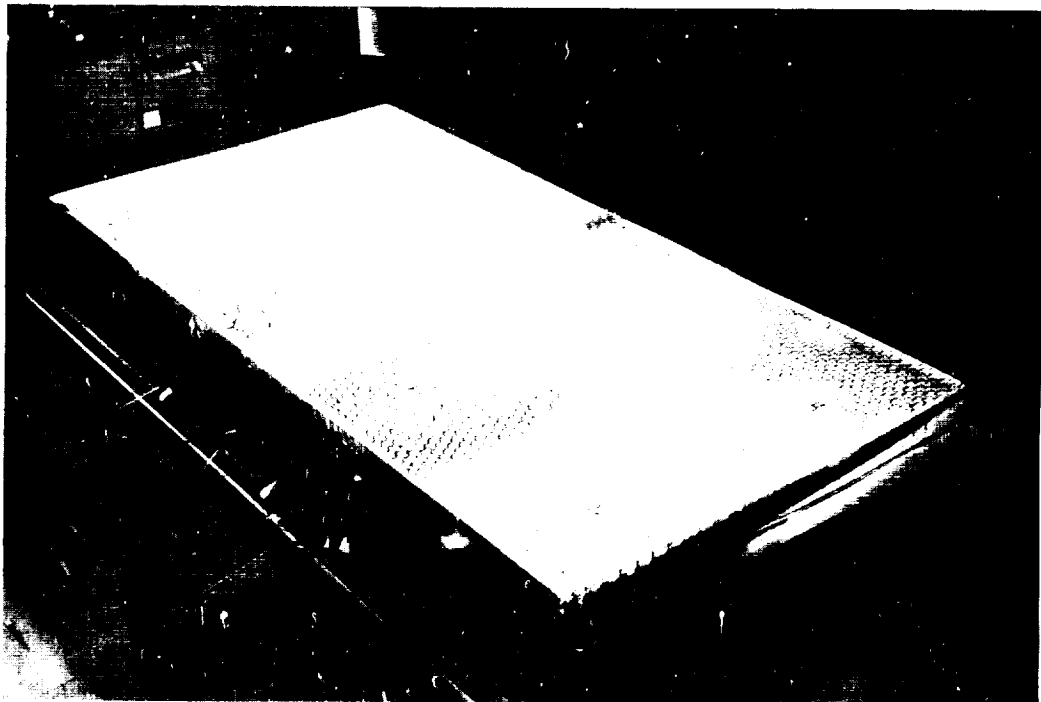


Figure 106.- Sealed-Gap Panel, Posttest Appearance

D. General Summary

Table 35 presents a summary of the three test series conducted in the design verification testing.

TABLE 35.- VERIFICATION TEST PROGRAM

Heat Shield Component	Test Objective	Test Environment/ Test Facility	Test Specimens	Results
Open Gap/ Attachments (Panel Test)	PRIMARY: Feasibility of self-closing gap concept  SECONDARY: a. Motion of subpanel plate under stud bolt b. Temperature distribution around stud bolt counterbore	Reentry Heating/ Structures Laboratory, Radiant Heat Facility	1 specimen approximate size 1.12 x 0.56 m (44 x 22 in.)	- Full heating profile not achieved - Indications of incomplete gap sealing - Indications of inadequate subpanel motion - No abnormally high heating in counterbore
Gap Seale (Component Test)	Resiliency after high temperature deformations	Dead load compression and uniform heating/ Advanced Structures and Materials Ceramics	17 specimens, approximate size 5.08x15.24x0.250 to (2 x 6 x 0.1 to 0.5 in.)	- Blanket material showed adequate resiliency - Rope material non-resilient
Sealed Gap/ Attachments (Panel Test)	PRIMARY: Feasibility of sealed-gap concept  SECONDARY: a. Motion of subpanel plate under stud bolt b. Temperature distribution around stud bolt counterbore	Ascent and Reentry Heating/ Structures Laboratory, Radiant Heat Facility	1 specimen, approximate size 1.12 x 0.56 m (44 x 22 in.)	- Ascent heating - no apparent effect on panel - Descent heating - some backface temp. > 450°K (350°F) - High temp. in gap - Indications of inadequate subpanel motion - High temperature in counterbore

## VI. WEIGHT AND COST ANALYSES

Weight and cost estimates were determined as functions of the Orbiter area covered with ablator. Estimates were made for ablator TPS weight and cost for Orbiter areas with equilibrium surface temperatures equal to or greater than 422°K (300°F), 700°K (800°F), 922°K (1200°F), 1144°K (1000°F), 1366°K (2000°F), 1589°K (2400°F), and 1811°K (2800°F). In addition, weight and cost estimates were made for the fuselage nose cap and the leading edges of the wing and fin. Detailed weight estimates were made of candidate ablator configurations. Cost estimates are total program costs and include operational costs, reliability costs, and payload weight penalty costs.

### A. Payload Weight Penalty Costs

The payload weight penalty costs are derived by determining a cost per pound to orbit. All program costs are apportioned against all the payload weight. Consideration was given to the number of flights which could conceivably use an ablative TPS. A ground rule was established for study purposes limiting the application of ablative TPS to the first five years of the operational phase of the program. Then an analysis of the traffic model for the time considered was made to determine total payload planned usage. From these data, a payload penalty per pound was determined. The traffic model used was from reference 1. The payload weights for the first 151 flights are listed in Table 36. The payload penalty per pound was developed as follows:

TABLE 36.- PAYLOAD WEIGHT IN FIRST 151 FLIGHTS

Year	No. of Flights	Planned Payload Mg (lb)
1979	14	129.7 (285 940)
1980	21	218.4 (481 450)
1981	30	349.2 (769 950)
1982	34	364.3 (803 180)
1983	52	1006.6 (2 219 210)
Total	151	2068.3 (4 559 730)

Data for the total Space Shuttle Program are derived from current estimates and presented here for developing the expense aspect of cost penalties in TPS weights:

Total flights = 445  
 All systems operations associated with a mission @ 10.5M \$/flight  
 Total DDT&E = \$5,150M

Therefore, the DDT&E apportionment over the total program is:

$$\frac{\$5,150M}{445 \text{ flights}} = \$11.57M/\text{flight}$$

From table 36:

No. of flights in first five years = 151  
 Total of payload weights in 151 flights = 2 068 294 kg (4 559 730 lb)

So, for 151 flights:

DDT&E apportionment	=\$1747.5M
<u>All systems operations costs</u>	<u>=\$1585.5M</u>
Total 151 cost	=\$3333.0M

The expense of extra TPS weight in the first 151 (ablator protected) flights can then be computed as:

$$\text{Weight penalty per pound} = \frac{\text{Total 151 cost}}{\text{Total 151 payload}} = 1612 \text{ \$/kg (731 \$/lb)}$$

Note: This unit weight penalty is applied only when:

Ablator TPS weight	>	RSI TPS weight + Unused payload bay capability
--------------------	---	--

Sample calculations of this penalty are presented in table 37.

TABLE 37.- SAMPLE CALCULATION, WEIGHT PENALTY COST, 1981 MODEL

Flight no. (a) (payload no.)	15 (NCN-10)		18 (NE2-44)		20 (NEO-16)	
Payload loading factor	0.31		0.38		0.83	
Mission capability	29 484 kg	65 000 lb	20 412 kg	45 000 lb	20 412 kg	45 000 lb
Payload bay load	9 140 kg	20 150 lb	7 757 kg	17 100 lb	16 942 kg	37 350 lb
Unused capacity	20 344 kg	44 850 lb	12 655 kg	27 900 lb	3 470 kg	7 650 lb
RSI design weight	13 717 kg	30 240 lb	13 717 kg	30 240 lb	13 717 kg	30 240 lb
Mission standard weight	34 061 kg	75 090 lb	26 372 kg	58 140 lb	17 187 kg	37 890 lb
38.1-cm (15 in.) fastener spacing, direct attach aluminum plate TPS system weight	22 128 kg	48 782 lb	22 128 kg	48 782 lb	22 128 kg	48 782 lb
Weight penalty @ \$1612/kg (\$731/lb)	-0-	-0-	-0-	-0-	4 941 kg	10 892 lb
	-0-	-0-	-0-	-0-	\$7 962 052	(\$7 962 052)

Note: All weight penalties for all flights are added for the first 5 years (151 flights). For the case of 38.1 cm (15 in.) spacing direct attach aluminum plate:

Year	Penalty \$K
1979	-0-
1980	-0-
1981	\$ 15 924
1982	-0-
1983	348 484
Total	\$364 408K

$$\boxed{\text{Average Weight Penalty (This TPS System)}} = \frac{\$364\,408\text{K}}{151} = \$2413\text{K/Flight}$$

<sup>a</sup>Reference 1 nomenclature.

Rationale for application of the penalty factor is given below:

- 1) RSI-TPS has been selected as the Shuttle TPS. TPS weight comparisons are made versus the RSI design weight.
- 2) For most missions shown in the traffic model for the first five years, a considerable excess payload capacity exists. Therefore, no actual weight penalty is imposed until the excess capacity is used.
- 3) Then, for purposes of determining weight penalties in terms of dollars per pound in cost trades:

$$\boxed{\text{Penalty pounds}} = \boxed{\text{Weight of TPS considered} - \text{RSI system weight} + \text{excess capacity}}$$

(Never less than zero)

- 4) Penalty pounds are calculated for each flight and are converted to weight penalty dollar amounts at \$1,612/penalty kg (\$731/penalty lb).
- 5) The total penalty dollar amounts for a given system (151 flights) is obtained as a sum of the individual flight penalties, then apportioned on a per flight basis.

$$\frac{\text{Total weight penalty dollar}}{151} = \text{Average weight penalty dollar/flight}$$

System weight penalties were calculated for a direct bond ablator system (no penalty), a direct mechanical attachment of aluminum plate, magnesium plate, lockalloy plate, aluminum honeycomb, magnesium face honeycomb, and graphite/polyimide composite honeycomb. Standoff mechanical attachment systems for aluminum honeycomb and graphite/polyimide honeycomb were also assessed. Further, for each mechanically attached system, 12.7, 25.4, 38.1 and 50.8 cm (5, 10, 15, and 20 in.) fastener spacings were studied. Weight penalties are summarized in Table 38 for each of the 32 mechanical configurations and for the direct bond configuration. Note that most of the weight penalties are encountered in 1983. Table 38 illustrates this for each configuration. The data have been grouped and the calculations made in the tradeoffs so that weight

TABLE 38.- PAYLOAD WEIGHT PENALTY COSTS

Material and attachment concept	Subpanel configuration			Weight penalty (1000 \$)							Totals thru 1983	Total/flight thru 1979 thru 1983	
	Attachment spacing	Heat shield system mass		1979	1980	1981	1982	1983	Totals thru 1979 thru 1983				
		cm	in.							kg			lb
Plate	Aluminum 2024-T81	12.7	5	14 777	32 577	-0-	-0-	-0-	-0-	10 605	10 605	70	
		25.4	10	17 147	37 803	-0-	-0-	-0-	-0-	76 862	76 862	509	
	Magnesium HM-21A	38.1	15	22 128	48 782	-0-	15 924	-0-	-0-	348 484	364 408	2413	
		50.4	20	27 739	61 154	42 728	64 232	93 645	709 886	996 261	6598		
	Lockalloy 62Be38A	12.7	5	14 335	31 602	-0-	-0-	-0-	3 624	3 624	24		
		25.4	10	15 757	34 738	-0-	-0-	-0-	34 886	34 886	231		
	Direct	Aluminum 2024-T81	38.1	15	19 816	43 687	-0-	8 475	-0-	214 404	222 879	1476	
			50.4	20	23 010	50 728	-0-	18 943	1 838	400 043	421 698	2793	
	Honeycomb	Magnesium HM-21A	12.7	5	13 650	30 092	-0-	-0-	-0-	-0-	-0-	-0-	-0-
			25.4	10	14 311	31 549	-0-	-0-	-0-	3 276	3 276	22	
Aluminum 2024-T81		38.1	15	15 964	35 194	-0-	-0-	-0-	39 596	39 596	262		
		50.4	20	18 360	40 477	-0-	3 782	-0-	130 644	134 427	890		
Graphite composite		12.7	5	14 587	32 158	-0-	-0-	-0-	7 329	7 329	49		
		25.4	10	14 855	32 749	-0-	-0-	-0-	11 988	11 988	79		
Standoff		Aluminum 2024-T81	38.1	15	15 349	33 839	-0-	-0-	-0-	23 057	23 057	153	
			50.4	20	15 760	34 744	-0-	-0-	-0-	34 965	34 965	232	
Direct bond ablator		Graphite composite	12.7	5	14 008	30 882	-0-	-0-	-0-	469	469	3	
			25.4	10	14 429	31 811	-0-	-0-	-0-	4 999	4 999	33	
Direct bond RSI	Aluminum 2024-T81	38.1	15	14 923	32 898	-0-	-0-	-0-	13 228	13 228	88		
		50.4	20	15 317	33 767	-0-	-0-	-0-	22 110	22 110	146		
Standoff	Aluminum 2024-T81	12.7	5	14 059	30 994	-0-	-0-	-0-	602	602	4		
		25.4	10	14 418	31 772	-0-	-0-	-0-	4 743	4 743	31		
Direct bond ablator	Graphite composite	38.1	15	14 933	32 921	-0-	-0-	-0-	13 430	13 430	89		
		50.4	20	15 340	33 819	-0-	-0-	-0-	22 794	22 794	151		
Standoff	Aluminum 2024-T81	12.7	5	16 003	35 279	-0-	-0-	-0-	42 005	42 005	278		
		25.4	10	15 651	34 505	-0-	-0-	-0-	31 820	31 820	211		
Direct bond ablator	Graphite composite	38.1	15	17 329	38 204	-0-	459	-0-	84 349	84 808	562		
		50.4	20	18 515	40 819	-0-	4 282	-0-	138 929	143 212	948		
Standoff	Aluminum 2024-T81	12.7	5	18 099	39 901	-0-	2 940	-0-	118 252	121 192	803		
		25.4	10	16 075	35 439	-0-	-0-	-0-	44 110	44 110	292		
Direct bond ablator	Graphite composite	38.1	15	17 331	38 208	-0-	465	-0-	84 428	84 892	562		
		50.4	20	18 380	40 520	-0-	3 845	-0-	131 587	135 432	897		
Standoff	Aluminum 2024-T81	12.7	5	12 337	27 199	-0-	-0-	-0-	-0-	-0-	-0-	-0-	
		25.4	10	13 717	30 240	-0-	-0-	-0-	-0-	-0-	-0-	-0-	

penalty assessments could be made quickly for different time periods; i.e., other than the first five years.

#### B. Operational Costs, TPS

Operational costs are those costs incurred in the fabrication and refurbishment of the ablator TPS during the 151-flight period. These costs include:

- 1) Ablator slab raw materials and fabrication including scrappage (this accounts for 3/4 of the operational cost);
- 2) Subpanel raw materials and assembly costs, including scrappage;
- 3) Assembly of ablator slab to the subpanel;
- 4) Tools and labor to install the ablator panel assembly;
- 5) Tools and labor to remove used ablator panels;
- 6) Materials and labor to repair damage from handling during packing, shipping, storage, and installation.

These costs are tabulated in table 39.

#### C. Reliability Costs

Reliability costs are those costs incurred in the performance of Quality Assurance during the fabrication and refurbishment of the ablator TPS during the 151-flight period. These costs include:

- 1) Bond line inspection;
- 2) Mechanical fastener inspection;
- 3) Subpanel fabrication inspection;
- 4) Refurbishment cleanliness inspection;
- 5) Inspection for damage following ablator installation;
- 6) Inspection of repaired areas.

These costs are tabulated in table 40.

TABLE 39.- OPERATIONAL COSTS FOR 151 FLIGHTS (\$K)

	Ablator panels	Sub-panels	Panel assembly	Instl tools	Instl labor	Removal tools	Ablator removal	Repair matls	Repair labor	Operl cost
Direct Bond	125 722	----	----	287	15 181	1823	10 620	2485	1887	158 010
Aluminum plate										
12.7 cm (5 in.)	120 713	1 241	8 665	287	10 601	892	10 158	3486	3079	159 122
25.4 cm (10 in.)	117 160	1 130	8 462	287	5 911	892	8 152	3372	2604	148 179
38.1 cm (15 in.)	107 505	1 394	8 429	287	5 034	892	7 750	3132	2494	136 866
50.8 cm (20 in.)	96 663	1 534	8 396	287	4 306	892	7 498	2622	2365	124 564
Magnesium plate										
12.7 cm (5 in.)	122 130	1 767	8 665	287	12 055	895	11 122	3557	3202	163 690
25.4 cm (10 in.)	116 183	1 855	8 462	287	6 815	895	8 724	3323	2677	149 371
38.1 cm (15 in.)	110 539	2 571	8 429	287	5 775	895	8 242	3283	2554	142 524
50.8 cm (20 in.)	100 364	3 047	8 396	287	4 951	895	7 939	2807	2421	131 124
Lockalloy plate										
12.7 cm (5 in.)	129 738	31 095	10 398	287	12 055	1070	12 190	3523	3301	194 657
25.4 cm (10 in.)	116 318	49 131	10 155	287	6 765	1070	9 783	3565	2770	199 844
38.1 cm (15 in.)	107 999	40 504	10 115	287	5 775	1070	9 301	3192	2650	180 842
50.8 cm (20 in.)	98 339	55 254	10 075	287	4 967	1070	8 998	2741	2518	184 250
Aluminum/aluminum honeycomb										
12.7 cm (5 in.)	124 937	8 703	8 665	287	12 055	1096	12 258	3698	3258	174 957
25.4 cm (10 in.)	124 937	7 767	8 462	287	6 765	1096	9 850	3961	2733	165 858
38.1 cm (15 in.)	124 937	8 152	8 429	287	5 775	1096	9 368	4003	2611	164 607
50.8 cm (20 in.)	124 937	8 057	8 396	287	4 967	1096	9 065	4035	2478	163 319
Magnesium/HRH honeycomb										
12.7 cm (5 in.)	121 835	12 203	8 665	287	13 510	1099	13 231	3543	3378	177 751
25.4 cm (10 in.)	121 835	12 047	8 462	287	7 618	1099	10 422	3806	2803	168 379
38.1 cm (15 in.)	121 835	14 989	8 429	287	6 519	1099	9 860	3848	2674	169 489
50.8 cm (20 in.)	121 835	16 744	8 396	287	5 631	1099	9 506	3880	2531	169 910
Graphite polyimide HRH honeycomb										
12.7 cm (5 in.)	122 279	14 975	8 665	287	12 055	1096	12 258	3565	3258	178 438
25.4 cm (10 in.)	122 279	17 177	8 462	287	6 765	1096	9 850	3828	2733	172 477
38.1 cm (15 in.)	122 279	20 554	8 429	287	5 775	1096	9 368	3870	2611	174 218
50.8 cm (20 in.)	122 279	24 941	8 396	287	4 967	1096	9 065	3902	2478	177 412
Standoff aluminum/aluminum honeycomb										
12.7 cm (5 in.)	113 999	8 972	8 665	311	20 277	1114	18 336	3300	3820	178 794
25.4 cm (10 in.)	113 999	7 866	8 462	311	12 328	1114	13 641	3513	3082	164 335
38.1 cm (15 in.)	113 999	8 363	8 429	311	10 993	1114	12 556	3569	2919	162 202
50.8 cm (20 in.)	113 999	8 445	8 396	311	9 539	1114	12 134	3598	2750	160 287
Standoff graphite polyimide HRH honeycomb										
12.7 cm (5 in.)	112 674	18 582	8 665	311	21 290	1114	18 336	3284	3820	188 076
25.4 cm (10 in.)	112 674	27 609	8 462	311	12 799	1114	13 641	3489	3082	183 181
38.1 cm (15 in.)	112 674	36 096	8 429	311	11 367	1114	12 556	3522	2919	188 937
50.8 cm (20 in.)	122 674	46 660	8 396	311	9 888	1114	12 134	3550	2750	197 478

TABLE 40.- RELIABILITY COSTS FOR 151 FLIGHTS (\$K.)

	Bond line inspection	Mech fastener inspection	Subpanel inspection	Reliability inspection	Damage inspection	Repair inspection	Reliability subtotal
Direct bond	3150	-	-	3138	-	482	6 770
Aluminum plate							
12.7 cm (5 in.)	1422	3959	305	1506	1242	786	9 220
25.4 cm (10 in.)	1370	2099	177	1506	730	665	6 547
38.1 cm (15 in.)	1362	1639	297	1506	627	637	6 068
50.8 cm (20 in.)	1353	1072	297	1506	563	604	5 395
Magnesium plate							
12.7 cm (5 in.)	1422	4331	401	1506	1490	817	9 967
25.4 cm (10 in.)	1370	2317	347	1506	876	683	7 099
38.1 cm (15 in.)	1362	1828	381	1506	753	652	6 482
50.8 cm (20 in.)	1353	1241	389	1506	686	618	5 783
Lockalloy plate							
12.7 cm (5 in.)	1706	4331	401	1807	1490	843	10 578
25.4 cm (10 in.)	1644	2317	347	1807	876	707	7 698
38.1 cm (15 in.)	1634	1828	381	1807	753	677	7 080
50.8 cm (20 in.)	1624	1241	389	1807	676	643	6 380
Aluminum/aluminum honeycomb							
12.7 cm (5 in.)	1422	4331	2182	1851	1490	832	12 108
25.4 cm (10 in.)	1370	2317	1882	1851	876	698	8 994
38.1 cm (15 in.)	1362	1939	1939	1851	753	666	8 399
50.8 cm (20 in.)	1353	1241	1885	1851	676	632	7 638
Magnesium/HRH honeycomb							
12.7 cm (5 in.)	1422	4702	2422	1851	1739	862	12 998
25.4 cm (10 in.)	1370	2535	2089	1851	1022	716	9 583
38.1 cm (15 in.)	1362	2018	2167	1851	878	682	8 958
50.8 cm (20 in.)	1353	1411	2110	1851	788	646	8 159
Graphite polyimide HRH honeycomb							
12.7 cm (5 in.)	1422	4331	2115	1851	1490	832	12 041
25.4 cm (10 in.)	1370	2317	2014	1851	876	698	9 126
38.1 cm (15 in.)	1362	1828	2054	1851	753	666	8 514
50.8 cm (20 in.)	1353	1241	2180	1851	676	632	7,933
Standoff aluminum/aluminum honeycomb							
12.7 cm (5 in.)	1422	5674	2182	1851	3042	975	15 146
25.4 cm (10 in.)	1370	3140	1882	1851	1843	787	10 873
38.1 cm (15 in.)	1362	2591	1939	1851	1566	745	10 054
50.8 cm (20 in.)	1353	1853	1885	1851	1459	702	9 193
Standoff graphite polyimide HRH honeycomb							
12.7 cm (5 in.)	1422	5674	2115	1851	3042	975	15 079
25.4 cm (10 in.)	1370	3140	2014	1851	1843	787	11 005
38.1 cm (15 in.)	1362	2591	2054	1851	1567	745	10 170
50.8 cm (20 in.)	1353	1853	2180	1851	1459	702	9 498

#### D. Total Program Costs for the Total TPS

The payload weight penalty costs, the operational costs, and the reliability costs are summed up for each of the 32 mechanical attachment configurations and for the direct bond configuration, and are listed in tables 41 through 44.

The direct bond ablator is lighter than all other configurations studied (including the RSI LI-1500 by 1361 kg (3000 lb)). The 151 flight program costs for the lowest cost six configurations are:

Direct bond	\$165M
Magnesium plate at 12.7 cm (5 in.)	\$177M
Aluminum plate at 12.7 cm (5 in.)	\$179M
Magnesium honeycomb at 25.4 cm (10 in.)	\$183M
Graphite/polyimide honeycomb at 25.4 cm (10 in.)	\$186M
Aluminum honeycomb at 25.4 cm (10 in.)	\$187M

The large TPS weights of the standoff configurations make them noncompetitive. Much of this weight is in the large number of standoff fittings at small fastener spacing. The lockalloy TPS weight is low due to the light subpanel, but the high material costs in thin gages makes this configuration noncompetitive.

Direct bond, by our ground rules of minimum total cost, is the first choice. The magnesium plate directly attached system is the second choice, both from low weight and low cost. The aluminum plate directly attached system is a close third choice by cost; however, it is almost 454 kg (1000 lb) heavier than the magnesium plate system.

#### E. Program Costs and TPS Weights by Temperature Regions

The program costs for the various mechanically attached configurations and the direct bonded system have all been computed on the basis of total Orbiter area and weight. To determine the weight and cost distributions to the required thermal zones, the

TABLE 41.- WEIGHT AND COST SUMMARY, 12.7-cm (5-in.) FASTENER SPACING

Attachment method	Weight, kg (lb)	Cost, \$M				Total cost
		Weight	Reliability	Operational		
Direct bond	12 337 (27 199)	-----	6.770	158.010		165
Direct mechanical attachment						
Aluminum plate subpanel	14 833 (32 577)	10.605	9.220	159.122		179
Magnesium plate subpanel	14 777 (31 602)	3.624	9.967	163.690		177
Lockalloy plate subpanel	13 650 (30 092)	-----	10.578	194.657		205
Aluminum honeycomb subpanel, aluminum core	14 587 (32 158)	7.329	12.108	174.957		194
Magnesium face/HRH 327 core	14 008 (30,882)	0.469	12.998	177.751		191
Graphite polyimide face/ HRH 327 core	14 059 (30,994)	0.602	12.041	178.438		191
Standoff mechanical attachment						
Aluminum honeycomb subpanel	16 003 (35 279)	42.005	15.146	178.794		236
Graphite polyimide honeycomb subpanel	18 099 (39 901)	121.192	15.079	188.076		324

TABLE 42.- WEIGHT AND COST SUMMARY, 25.4-cm (10 in.) FASTENER SPACING

Attachment method	Weight, kg (lb)	Cost, \$M				Total cost
		Weight	Reliability	Operational		
Direct bond	12 337 (27 119)	-----	6.770	158.010		165
<b>Direct mechanical attachment</b>						
Aluminum plate subpanel	17 147 (37 803)	76.862	6.547	148.170		232
Magnesium plate subpanel	15 757 (34 738)	34.886	7.099	149.371		191
Lockalloy plate subpanel	14 311 (31 549)	3.276	7.698	199.844		211
Aluminum honeycomb subpanel	14 855 (32 749)	11.998	8.994	165.858		187
Magnesium face/HRH 327 core	14 429 (31 811)	4.999	9.583	168.379		183
Graphite polyimide face/ HRH 327 core	14 412 (31 772)	4.743	9.126	172.477		186
<b>Standoff mechanical attachment</b>						
Aluminum honeycomb subpanel	15 651 (34 505)	31.820	10.873	164.335		207
Graphite polyimide honeycomb subpanel	16 075 (35 439)	44.110	11.005	183.181		238

TABLE 43.- WEIGHT AND COST SUMMARY, 38.1-cm (15 in.) FASTENER SPACING

Attachment method	Weight, kg (lb)	Cost, \$M				Total cost
		Weight	Reliability	Operational		
Direct bond	12 337 (27 199)	-----	6.770	158.010	165	
Direct mechanical attachment						
Aluminum plate subpanel	22 128 (48 782)	364.408	6.068	136.866	507	
Magnesium plate subpanel	19 816 (43 687)	222.879	6.482	142.524	372	
Lockalloy plate subpanel	15 964 (35 194)	39.596	7.080	180.842	228	
Aluminum honeycomb subpanel	15 349 (33 839)	23.057	8.399	164.607	196	
Magnesium face/HRH 327 core	14 923 (32 898)	13.228	8.958	169.489	192	
Graphite polyimide face/ HRH 327 core	14 933 (32 921)	13.430	8.514	174.218	196	
Standoff mechanical attachment						
Aluminum honeycomb subpanel	17 329 (38 204)	84.808	10.054	162.202	257	
Graphite polyimide honeycomb subpanel	17 331 (38 208)	84 892	10.170	188.937	284	

TABLE 44.- WEIGHT AND COST SUMMARY, 50.8-cm (20 in.) FASTENER SPACING

Attachment method	Weight, kg (lb)	Cost, \$M			
		Weight	Reliability	Operational	Total cost
Direct bond	12 337 (27 199)	-----	6.770	158.010	165
Direct mechanical attachment					
Aluminum plate subpanel	27 739 (61 154)	996.261	5.395	124.564	1126
Magnesium plate subpanel	23 010 (50 728)	421.698	5.783	131.124	559
Lockalloy plate subpanel	18 360 (40 477)	134.427	6.380	184.250	325
Aluminum honeycomb subpanel	15 760 (34 744)	34.965	7.638	163.319	206
Magnesium face/HRH 327 core	15 317 (33 767)	22.110	8.159	169.910	200
Graphite polyimide face/ HRH 327 core	15 340 (33 819)	22.794	7.933	177.412	208
Standoff mechanical attachment					
Aluminum honeycomb subpanel	18 515 (40 819)	143.212	9.103	160.287	313
Graphite polyimide honeycomb subpanel	18 380 (40 520)	135.432	9.398	197.478	342

Orbiter TPS weights were plotted against  $F_q$  determined from the detailed weight estimates (fig. 107). Superimposing surface equilibrium temperatures on the  $F_q$  values gives us TPS weight versus temperature. The surface area distribution against heating rate and equilibrium temperature (fig. 108) was determined from figure 109. By calculating the operational costs against area and weight, one is able to determine the operational costs for the thermal zones. Payload weight penalty costs were assessed against weight and reliability costs against area. The operational costs were apportioned to weight and area as follows:

- 1) Ablator slab fabrication                    --weight;
- 2) Subpanel materials and fabrication--weight and area;
- 3) Panel assembly                                --area;
- 4) Installation tools                            --area;
- 5) Installation labor                            --area;
- 6) Removal tools                                --area;
- 7) Ablator removal labor                        --area;
- 8) Repair materials                             --weight;
- 9) Repair labor                                 --area.

Four configurations were examined in detail: (1) direct bond; (2) magnesium plate; (3) aluminum plate; and (4) graphite polyimide honeycomb.

With the program costs assigned to weight and the weight distribution against temperature from figure 107, the weight cost is distributed in the same proportion. The area cost is distributed to the thermal zones in the proportions from figure 108. The area and weight cost distributions are summed and plotted on figure 110 against weight and cost with the thermal zones identified. Figure 109 also defines the TPS panel distributions and curvatures.

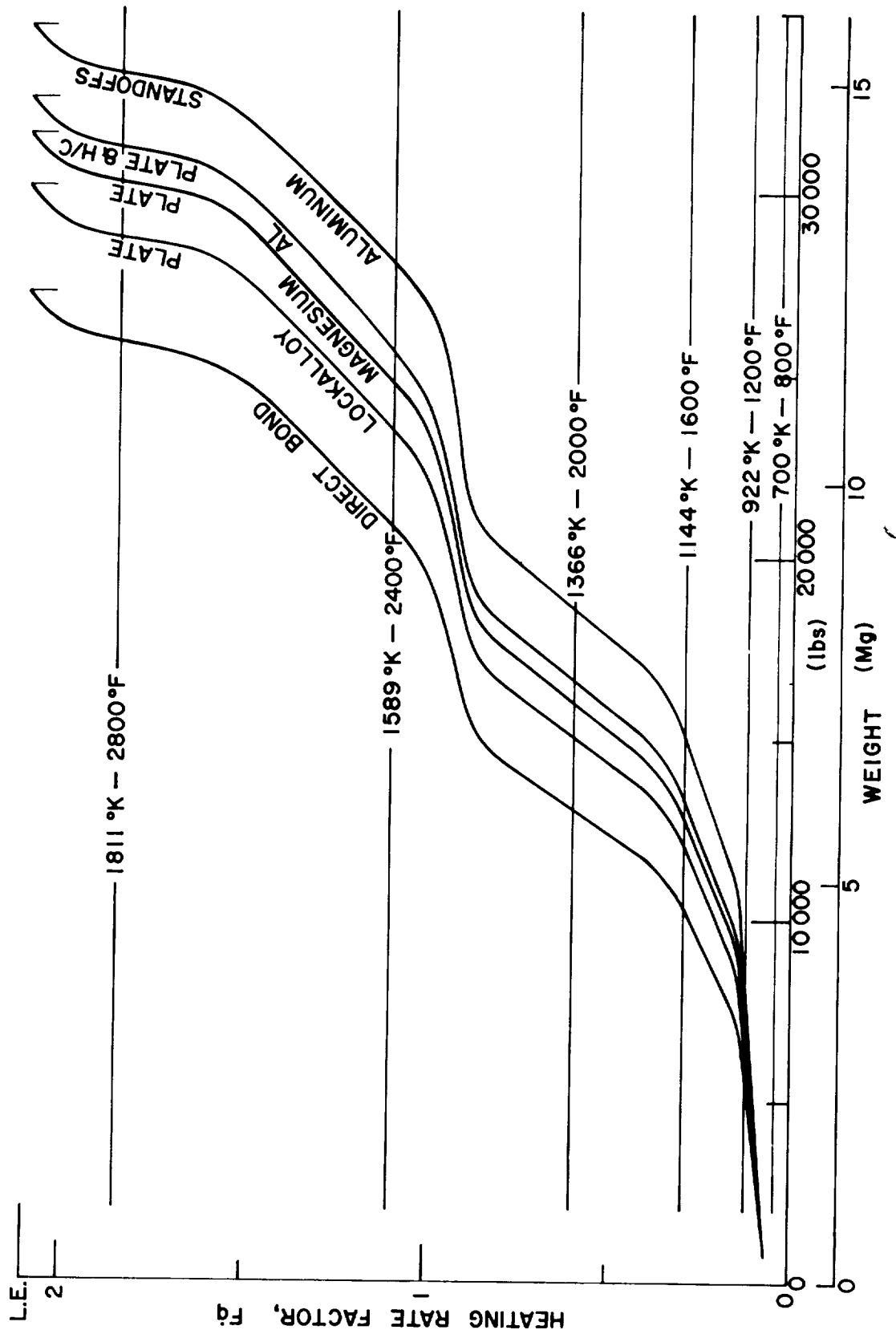


Figure 107.- Orbiter TPS Weight vs. Fq

	m <sup>2</sup>	ft <sup>2</sup>
Area of: Nose Cap =	3.72	40
Wing, L. E. =	9.66	104
Tail, L. E. =	1.67	18
Body, Upper =	398.91	4 294
Body, Lower =	198.43	2 136
Wing, Upper =	244.42	2 631
Wing, Lower =	233.46	2 513
Tail =	94.48	1 017
<b>Total Orbiter Area =</b>	<b>1184.75</b>	<b>12 753</b>

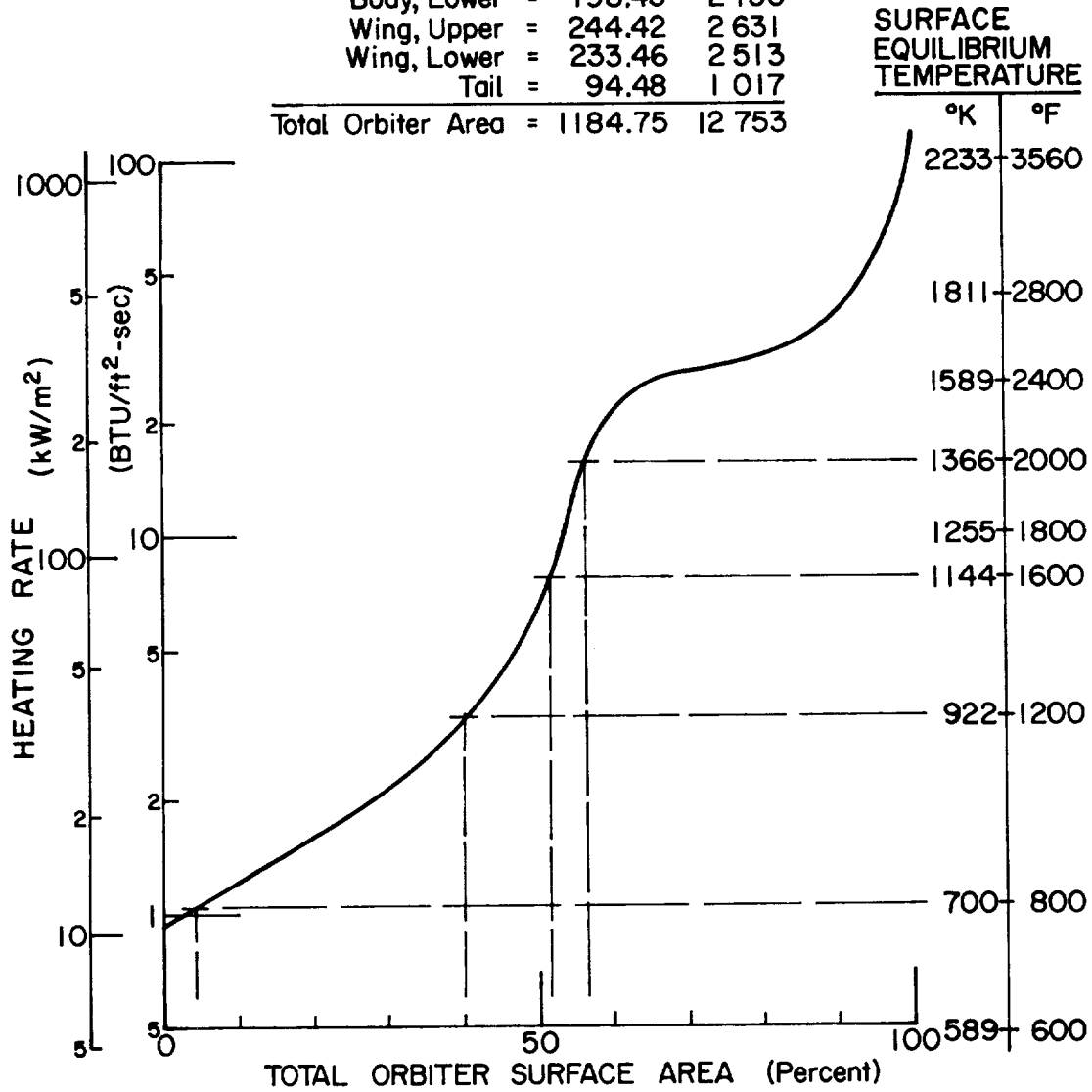


Figure 108.- Heat Load vs. Area

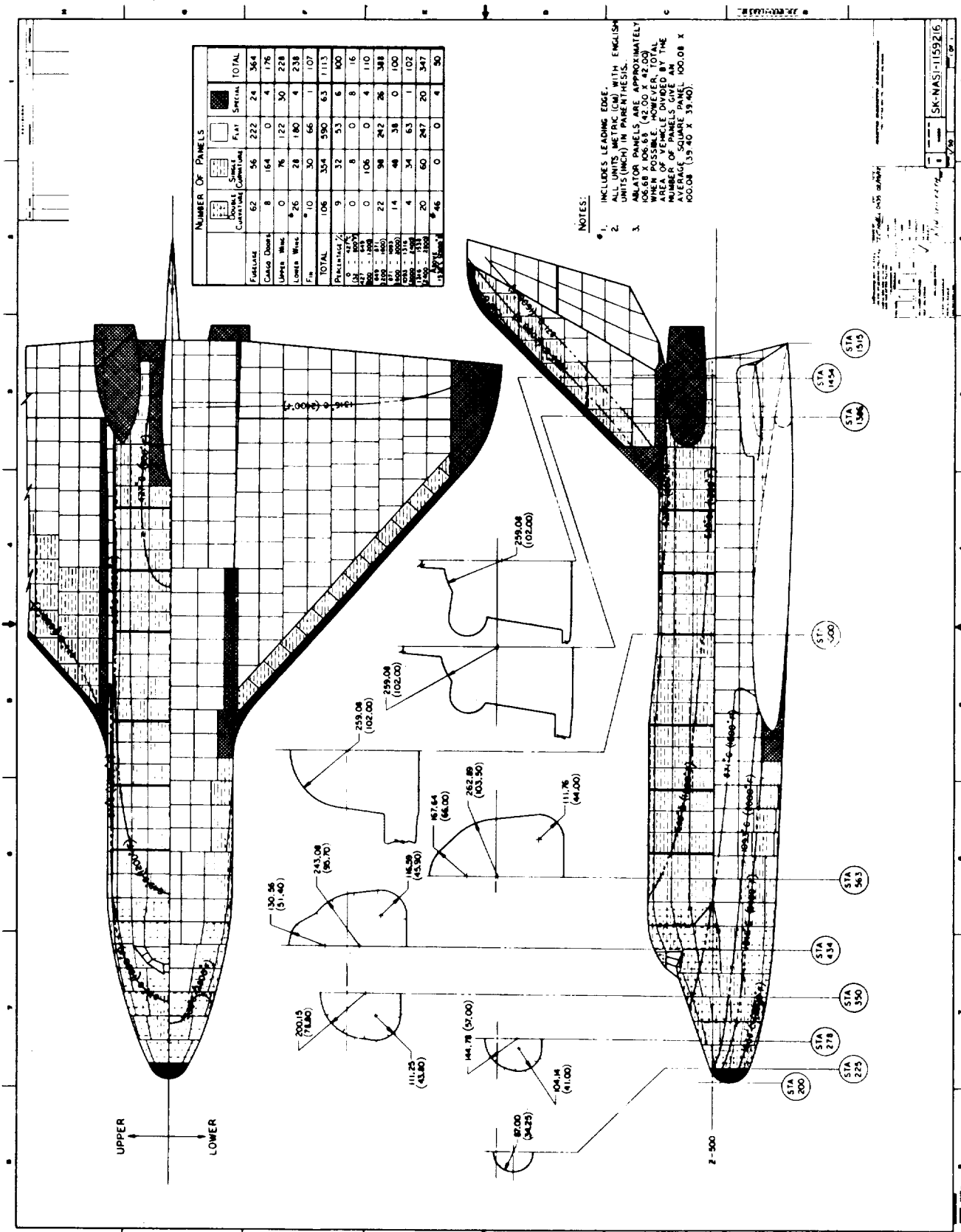


Figure 109.- Orbiter General Panel Location and Quantity



The cost of applying ablative materials to the Orbiter includes the reliability costs, installation tools, installation labor, removal tools, removal labor, and repair labor (table 45). For the direct bond SLA-561 TPS, this cost is \$36.6M, and is identified as "area cost". The remaining cost is identified as "weight cost" and considers fabrication of ablator slabs, including raw materials and repair materials. For the direct bond SLA-561 TPS, this cost is \$128.2M.

TABLE 45.- ABLATOR MATERIAL COSTS

Ablator Material	Raw Material Costs \$/kg (\$/lb) (includes G&A)	Ablator Slab as Fabricated Costs \$/kg (\$/lb) (includes G&A)
SLA-561	49.38 (22.40)	85.89 (38.96)
ESA 3560HF	42.67 (19.34)	59.41 (26.95)
ESA 5500	18.10 ( 8.21)	25.22 (11.44)

## F. Leading Edge and Nose Cap Costs and Weights

Leading edge and nose cap costs are estimated on the basis of area covered and the weight and ablative material used in each location. The nose cap and leading edge configurations are assumed identical for the various ablator configurations examined. Weight and areas are derived from the detailed weight analysis and summarized in table 46.

Nose cap and leading edge TPS costs are estimated by:

$$\text{TPS Cost} = \text{Area Cost} + \text{Weight Cost}$$

$$\text{Area Cost} = \frac{\text{Direct Bond Area Cost}}{(\text{Total Orbiter Area})(151 \text{ Flights})}$$

$$\text{Area Cost} = \frac{\$36.6\text{M}}{1,184.8 \text{ m}^2 (151)} = \$204.58/\text{m}^2$$

$$\text{or: } \frac{\$36.6\text{M}}{(12,753 \text{ ft}^2)(151)} = \$19.01/\text{ft}^2$$

$$\text{Weight Cost} = (\text{Ablator Weight}) \times (\text{Ablator Fab. Slab Cost}) \times (151 \text{ Flights})$$

Example:

$$\text{Nose Cap Cost} = (\text{Nose Cap Area Cost}) + (\text{Nose Cap Weight Cost})$$

$$\begin{aligned} \text{Nose Cap Area Cost} &= (\text{Area Cost})(\text{Nose Cap Area})(151 \text{ Flights}) \\ &= 204.58 \times 3.716 \times 151 = \$115\text{K, or} \\ &= (19.01)(40)(151) \\ &= \$115\text{K} \end{aligned}$$

$$\begin{aligned} \text{Nose Cap Weight Cost} &= 80.75 (59.41) 151 = 724\text{K, or} \\ &= (178)(26.95)(151) \\ &= \$724\text{K} \end{aligned}$$

$$\begin{aligned} \text{Nose Cap Cost} &= \$115\text{K} + \$724\text{K} \\ &= \$839\text{K} \end{aligned}$$

The leading edge costs are determined in the same manner, see table 47.

TABLE 46.- NOSE CAP AND LEADING EDGE TPS AREAS AND WEIGHTS

Element	Ablator	Area, m <sup>2</sup> (ft <sup>2</sup> )	Weight, kg (lb)			
			Bond	Coating	Ablator	Total
Nose cap	ESA 3560HF	3.72 (40)	4.54 (10)	3.18 (7)	73.03 (161)	80.75 (178)
Leading edges (wing and fin)	SLA-561	1.67 (18)	1.81 (4)	1.36 (3)	23.13 (51)	26.31 (58)
	ESA 3560HF	6.41 (69)	7.26 (16)	5.90 (13)	124.74 (275)	137.90 (304)
	ESA 5500	3.25 (35)	3.63 (8)	2.72 (6)	238.59 (526)	244.94 (540)
Total		11.33 (122)	12.70 (28)	9.98 (22)	386.46 (852)	409.14 (902)

TABLE 47.- NOSE CAP AND LEADING EDGE COSTS

Element	Ablator	Total program costs, \$K		
		Area cost	Weight cost	Total cost
Nose cap	ESA 3560HF	115	724	839
Leading edges	SLA-561	52	273	325
	ESA 3560HF	198	1237	1435
	ESA 5500	100	933	1033
Total		350	2443	2793

## VII. CONCLUSIONS AND RECOMMENDATIONS

### A. Conclusions

- The design criteria for ablative thermal protection systems on a Space Shuttle Orbiter are comprehensive and complete in scope.
- A range of entry trajectories is available that fully uses an ablative TPS--all within  $2\frac{1}{2}$  g limitations. At one end of this spectrum is a short time, high peak heating rate entry that would demand considerable usage of dense ablator materials. Extending the time duration of entry reduces the heating conditions to levels which permits lightweight ablators over most of the vehicle.
- Direct bonding of an all-ablator TPS (low density SLA-561) to the Orbiter structure yielded the lowest TPS weight of all the heat shield systems evaluated [weight factor (WF) =  $\text{TPS}(i)/\text{TPS}(\text{RSI}) = 0.90$ ]. An RSI TPS was next lowest (WF = 1.00), followed by a series of designs involving mechanically attached subpanels supporting SLA-561 (WF = 1.00 to 2.00). Fastener spacing was influential in the total weights of the latter designs.
- A feasible cost model, involving a weight penalty of \$1610/kg (\$731/lb) was derived based on an apportionment of program costs to the first 151 flights (assumed duration of utilization of all-ablator TPS) and the total payload weight carried in these flights. This penalty was employed in every instance where the total heat shield weight exceeded a given parameter.
- The direct bond ablator system had the lowest program cost of all the ablator configurations examined (the RSI system was not costed). No weight penalty (dollars) was required for this system.
- The next best cost ablative system, magnesium HM-21A subplates, directly attached, would incur \$12 million more than the direct bonded arrangement. This was closely followed by the similar system using 2024-T81 aluminum (\$14 million more).
- In the three candidate ablator designs highlighted above, approximately  $\frac{3}{4}$  of the TPS operational cost involves the fabrication of the ablator slab. The other quarter encompasses assembly, installation, removal, tooling, repair, and inspection. A typical TPS operational cost is approximately 10% of the total program's estimated operational cost.

- The use of a nonablator, insulative material in the gaps between panels tended to make the structure along these lines hotter than the remainder, as demonstrated in a large scale test.
- A test to investigate the feasibility of experiencing gap closure before high heating was encountered was inconclusive because of poor heat distribution in the test assembly.
- A concept of a fastener design that would provide some degree of movement between ablator subpanels and the structure was established.
- An early decision in the design of an ablative TPS must be made concerning the incorporation of anchor nuts in the structure of an Orbiter to accommodate fasteners.

#### B. Recommendations

- Cost reductions with respect to ablative systems should concentrate on the basic slab fabrication--materials, processes, inspection, etc.
- Additional effort should be expended to find an acceptable gap sealer; i.e., caulking, etc.
- Additional investigations should be made on the concept of self-sealing of gaps before the high heat time period.
- The fastener presented should be reevaluated for greater tolerances and, possibly, Teflon coating.
- The feasibility of reuse of silicone ablators installed in low heat regions should be further examined.



## APPENDIX A

### TRAJECTORY ANALYSIS

The method by which a given mission is flown defines a specific trajectory in terms of velocity and altitude time histories which, in turn, establishes the relevant heat shield entry parameters of total heat, heating rate, pressure, enthalpy, and viscous shear. Many different methods of flying the Orbiter for a given mission can be applied that will alter these parameters. Thus, the trajectories can be shaped for a given mission to provide an optimum set of entry environmental parameters to minimize the weight for a given heat shield system. For example, the metallic and the external insulation heat shield systems impose lower peak heating rate limits than an ablative system. These limits can be met for a given mission by shaping the trajectory, at the expense of an increase in the entry time and total heat. Conversely, an ablative system may not be heating-rate limited and, if it is, the limit would be much higher than for a reusable system. To minimize the system weight, a trajectory shaped to minimize total heat and entry time is desirable.

All trajectories for the studies conducted during this contract were generated using Martin Marietta's "Program to Optimize Shuttle Trajectories" (POST), which was developed under contract, (ref. 28). This program iterates on the trajectory shape for a given set of control variables to optimize selected parameters such as the sum of the heat shield weight and retrorocket propellant weight. The program can also compute the value of a selected control parameter, e.g., bank angle, to maintain selected parameters, such as heating rate of acceleration level, at specified values.

#### A. Vehicle Characteristics

The vehicle configuration used in this study was the Grumman Configuration 619. This configuration is similar to the current North American configuration as far as entry weight and surface are concerned. The Grumman configuration entry weight is 93 000 kg (205 000 lb) with a 18 000-kg (40 000 lb) payload. The North American configuration entry weight is 98 800 kg (217 620 lb) with a 18 000-kg (40 000 lb) payload weight. The surface area for the Grumman 619 configuration is 348 m<sup>2</sup> (3750 ft<sup>2</sup>), whereas the North American configuration has a surface area of 299 m<sup>2</sup> (3200 ft<sup>2</sup>). The corresponding wing loading ratios are 2610 N/m<sup>2</sup> (54.4 psi) and 3230 N/m<sup>2</sup> (67.5 psf), respectively.

## APPENDIX A

The aerodynamic coefficients used were for a forward center-of-gravity condition. These coefficients are shown in figures 111 and 112. The angle-of-attack versus Mach number envelopes are shown in figure 113.

### B. Heat Shield Panel Model

The vehicle was divided into nine panels, which had ratios relating the heating on each panel to the reference point. The reference point was located on the bottom centerline of the vehicle approximately 15.24 m (50 ft) aft of the nose. The heating for the reference point was determined as a trivariant function of angle of attack, altitude, and relative velocity using Martin Marietta's version of the MINIVER aerothermal analysis program. Heat shield unit weight-versus-total heat curves were used for the SLA-561 ablative material. These curves are shown in figure 114. The heating rate distributions and areas of the different panels are shown in table 48.

### C. Entry Trajectory Shaping Methodology

The trajectory shaping technique minimized the total heat and entry time for any given heat rate or acceleration limit. This minimization is obtained by achieving the desired heat rate or acceleration limit as early as possible and then following the limit as long as possible before deviating from the limit to obtain the required crossrange.

The initial bank angle for the baseline trajectory was  $180^\circ$ . The bank angle was reduced at a rate of  $2^\circ/\text{s}$  to  $45^\circ$  at the time selected to achieve a pullout at the desired value of heating rate. For the minimum heating rate trajectory, the bank angle was held constant at  $60^\circ$  until the desired heating rate was reached.

After pullout was performed, the bank angle was modulated to follow the prescribed heating rate or acceleration limits to minimize the entry time. These limits were flown as late into the trajectory as possible while still achieving the desired crossrange. Rollout to  $0^\circ$  bank angle was initiated at Mach 5 for the entries from the  $55^\circ$  inclination orbits because this technique provided adequate crossrange without further optimization. For the 185-km (100 n. mi.) polar orbits with 2040-km (1100 n. mi.) crossrange, the altitude actually increased slightly after deviating from the acceleration limit to achieve the desired crossrange.

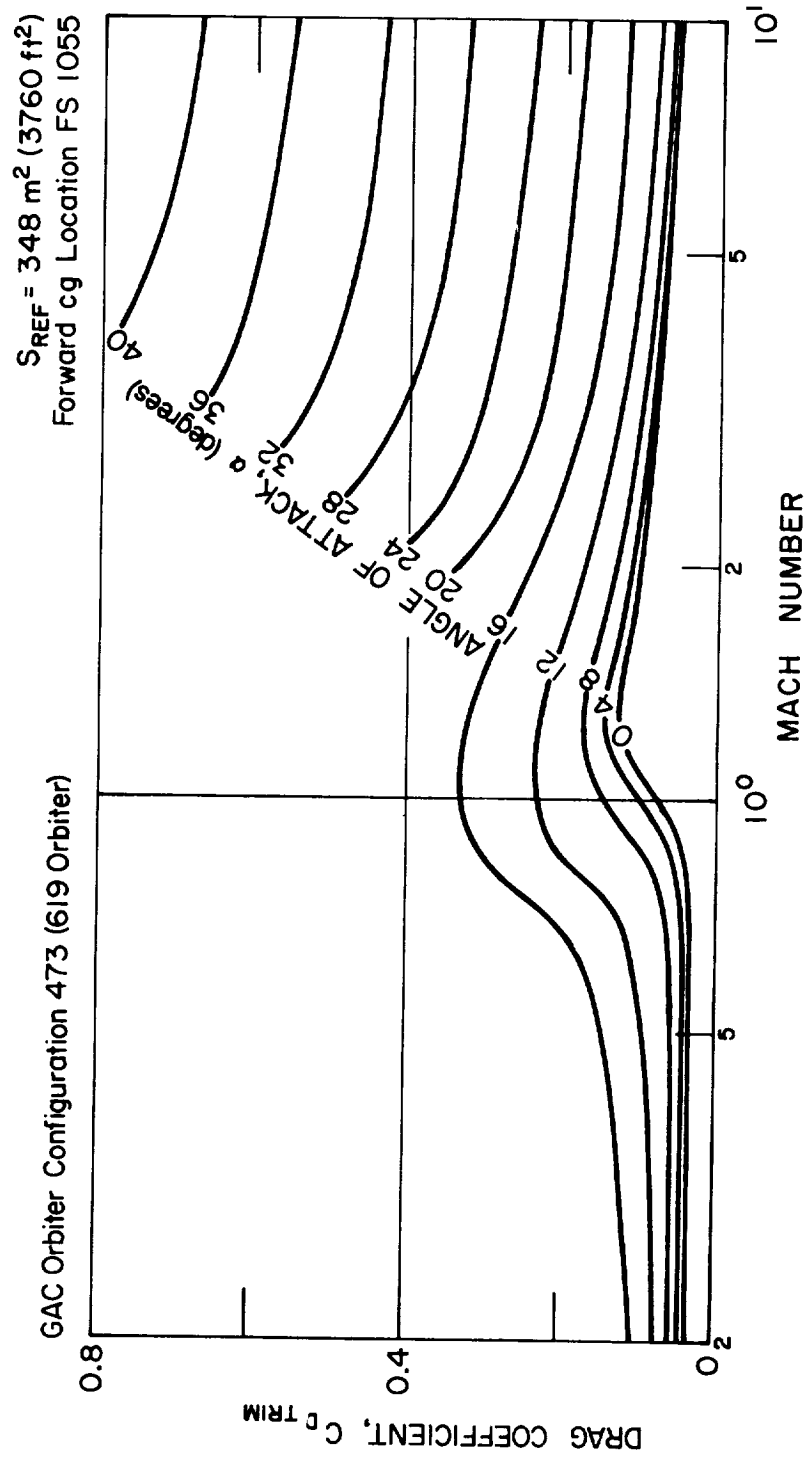


Figure 111.- GAC Orbiter Drag Coefficients

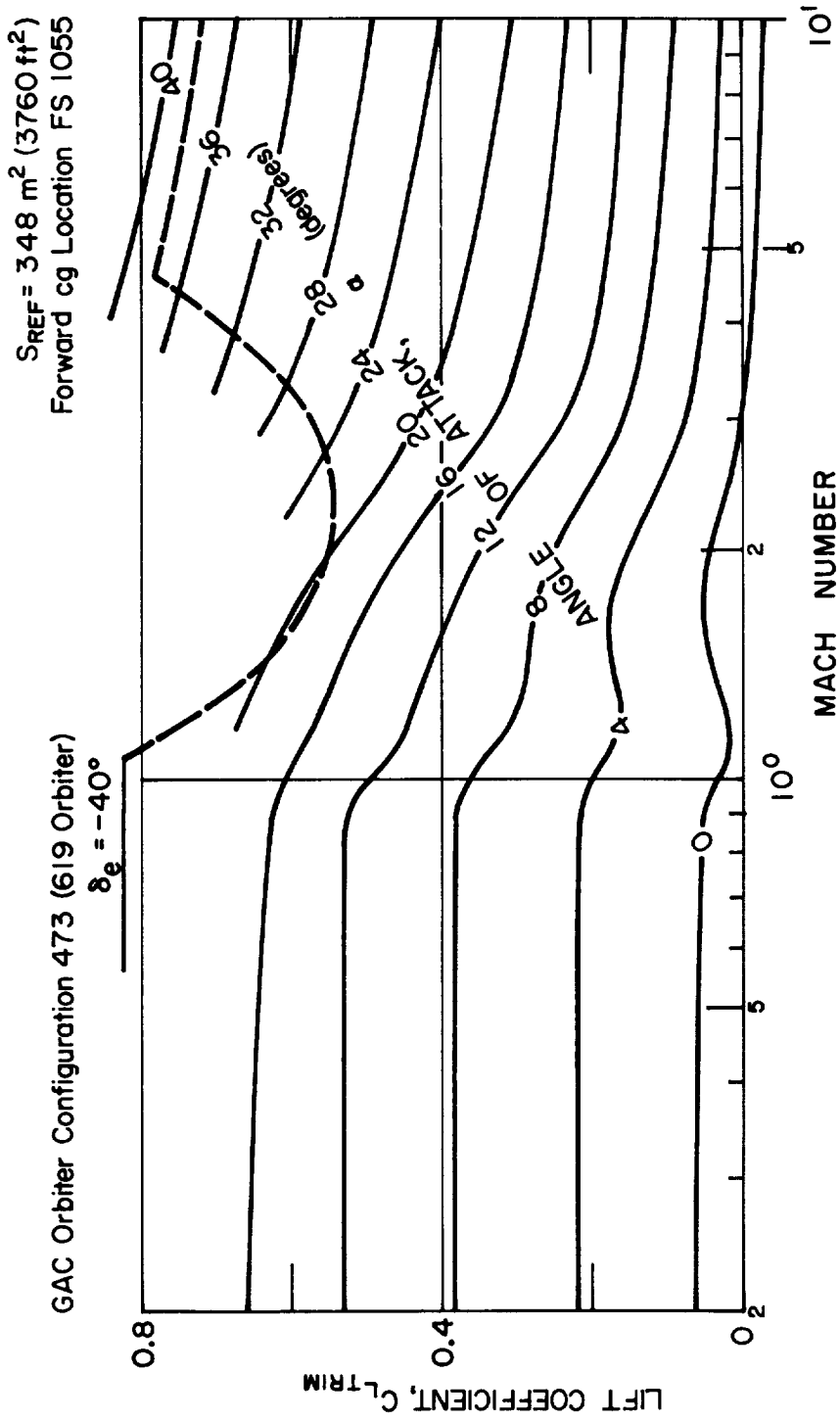


Figure 112.- GAC Orbiter Lift Coefficients

NOTE: 1) Trim Limit C.G. at  $0.65 \Omega_B$  2) Stability C.G. at  $0.67 \Omega_B$  3) FRL = Fuselage Reference Line. 4)  $\delta_{FR}$  = Rudder Flair Angle. 5)  $\delta_e$  = Elevator Deflection

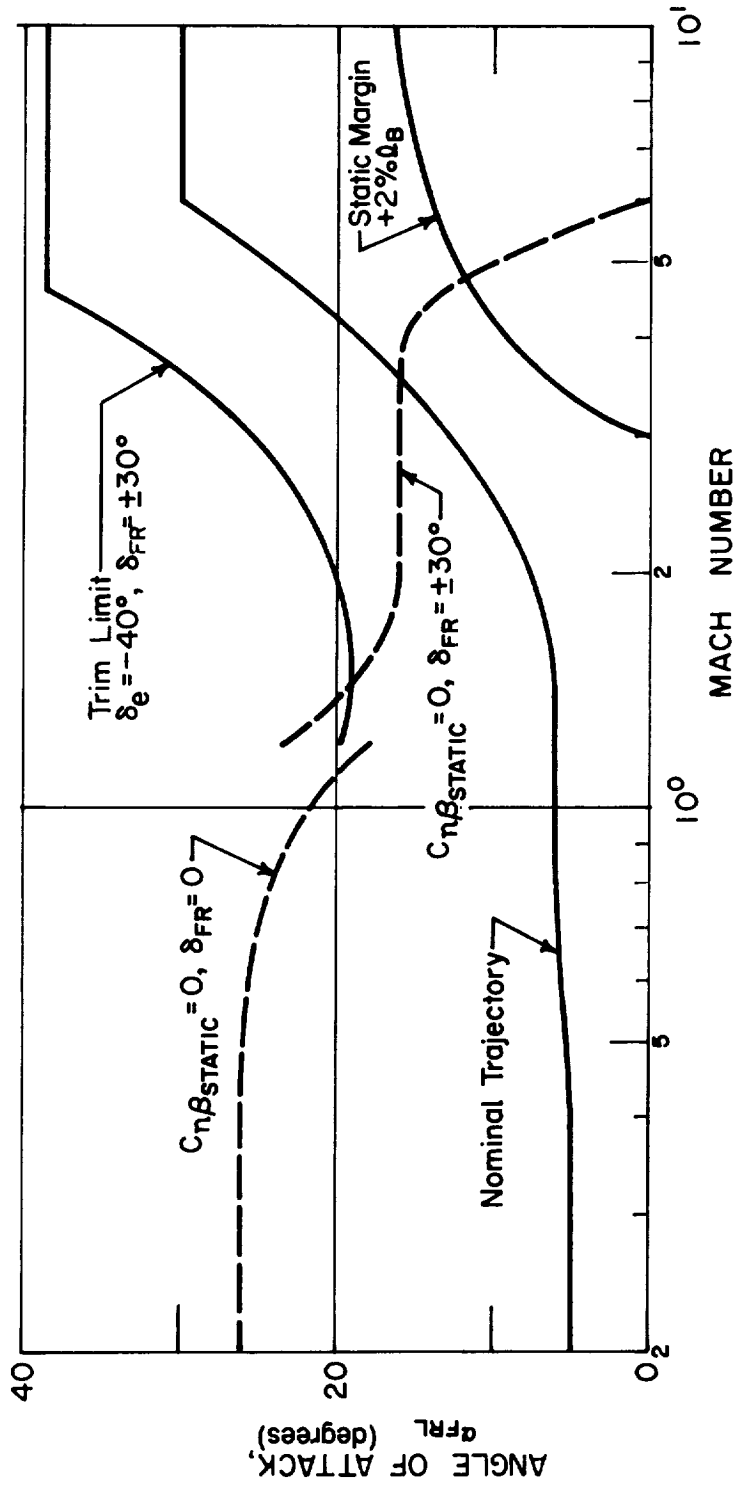


Figure 113.- GAC Orbiter Angle of Attack

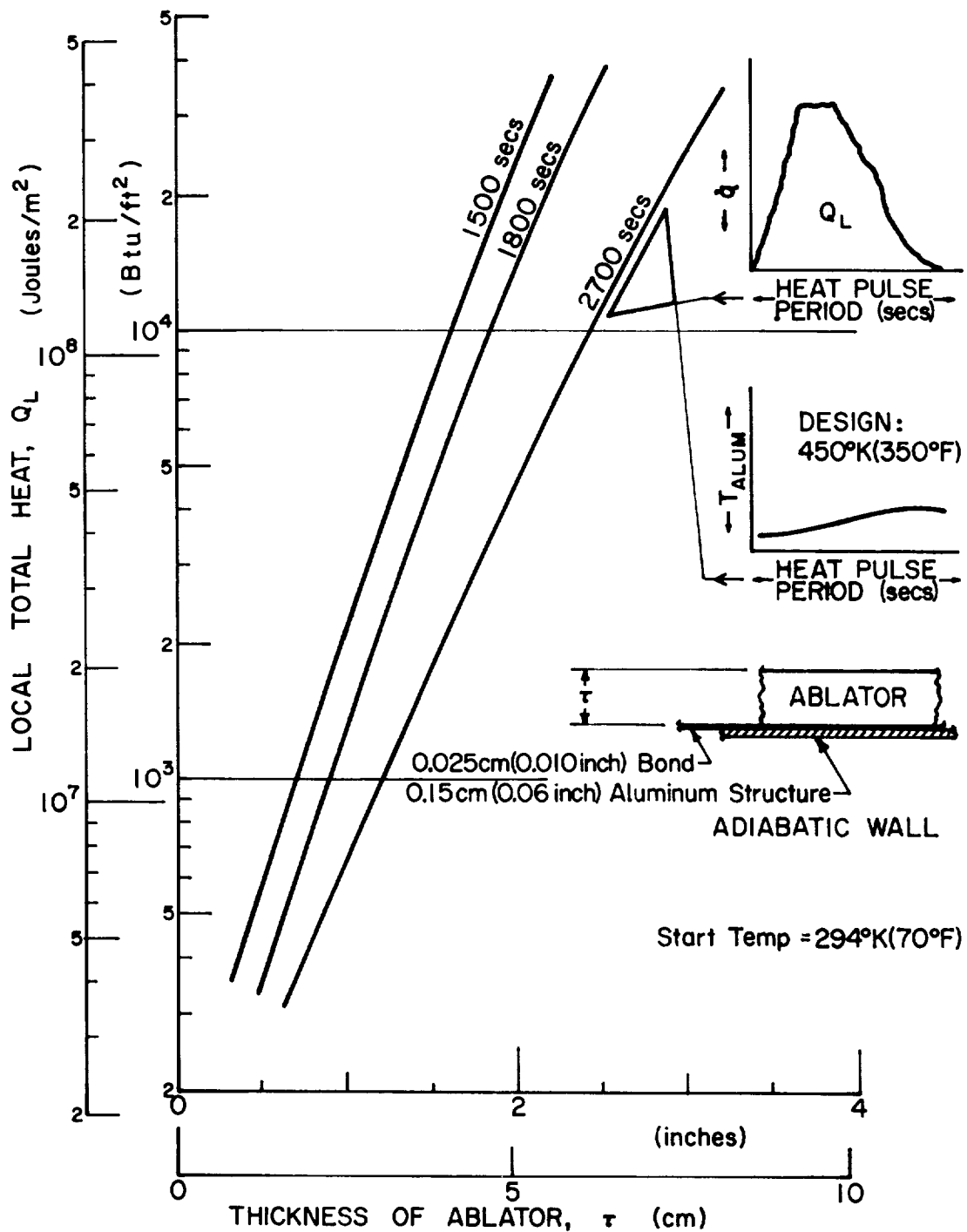


Figure 114.- Design Chart, SLA-561 Direct Bond Orbiter Entries

APPENDIX A

TABLE 48.- HEATING RATE DISTRIBUTION AND AREAS<sup>a</sup>

Panel number	1	2	3	4	5	6	7	8	9
q/q <sub>ref</sub>	0.01 to 0.11	0.12 to 0.22	0.23 to 0.64	0.65 to 0.92	0.93 to 1.00	1.01 to 1.24	1.25 to 2.0	2.01 to 3.0	3.01 to 4.0
q/q <sub>ref</sub> avg	0.06	0.17	0.43	0.78	0.97	1.12	1.62	2.5	3.5
Areas, m <sup>2</sup> (ft <sup>2</sup> )	40.2 (433) 87.9 (946) 25.1 (270) 14.5 (156) 13.7 (148) 30.8 (332) 13.2 (142) 6.1 (66) 19.9 (214) 17.7 (191) 24.1 (259) 12.2 (131)	11.0 (118) 31.7 (341) 32.5 (350) 88.2 (949) 20.2 (217) 45.4 (489) 10.1 (109) 4.1 (44)	14.3 (154) 21.7 (234) 4.3 (46) 5.2 (56) 17.4 (187) 11.7 (126)	4.8 (52) 2.6 (28) 22.9 (247) 15.5 (167) 38.2 (411) 20.2 (217) 6.8 (73) 26.5 (285) 33.8 (364)	5.8 (62) 21.8 (235)	49.1 (529) 19.8 (213) 2.0 (21) 9.9 (107) 14.2 (153) 8.1 (87) 2.0 (22) 6.7 (72) 7.1 (76) 7.3 (79) 4.6 (49)	34.5 (371) 5.8 (62) 17.0 (183) 1.0 (11) 19.6 (211) 13.2 (142)	10.8 (116) 2.5 (27) 9.0 (97)	2.7 (29) 10.3 (111)
Area Totals, m <sup>2</sup> (ft <sup>2</sup> )	305.5 (3288)	274.6 (2955)	74.6 (803)	171.3 (1844)	27.6 (297)	130.8 (1408)	91.0 (980)	22.3 (240)	110.6 (11955)
% area	27.5	24.7	6.7	15.5	2.5	11.8	8.2	2.0	1.1
Accumulated % area	27.5	52.2	58.9	74.4	76.9	88.7	96.9	98.9	100.0

<sup>a</sup>Does not include leading edges and base heat shields.

## APPENDIX A

This slight increase in altitude could probably be eliminated by deviating from the acceleration limit earlier with a corresponding increase in entry time and total heat if required from a guidance implementation standpoint.

The bank angle modulation was implemented with a linear feedback technique that uses both displacement and rate gains that are determined empirically to allow the desired heating rate or acceleration limits to be followed within acceptable tolerances. The bank angle command is calculated as

$$\text{Bank angle } (\sigma) = \sigma_{\text{nom}} + k_D (\Delta f) + k_R (\Delta \dot{f})$$

where:

$\sigma_{\text{nom}}$  = an input nominal bank angle time history

$k_D, k_R$  = displacement and rate gains for the function to be followed

$\Delta f, \Delta \dot{f}$  = the displacement and rate errors in the function being followed.

## APPENDIX B

### AEROTHERMAL ANALYSIS

#### A. Heating Rate Distributions

All of the aerothermal tasks except the ascent interference heating and standoff heat shield venting analyses were performed using the FD 330 (MINIVER) computer program. FD 330 incorporates the methodology recommended by the Thermal Panel of the Aerothermodynamics Working Group (ref. 29). Local flow properties for all windward (vehicle bottom) locations were determined from conical shock relations assuming the surface at the point in question was an equivalent cone whose half-angle was equal to the local body slope plus the angle of attack. Stagnation point properties were determined from normal shock relations while wing leading edge properties were predicted using swept cylinder expressions for a parallel shock. Flow properties for the leeward surface in the vicinity of the nose cap and wing leading edge were obtained assuming ambient pressure at these locations. Laminar heating rates for all but the nose cap and wing leading edge were predicted using Eckert's reference enthalpy method (ref. 30) while Spalding and Chi's skin friction correlation (ref. 31) with Colburn's Reynolds analogy factor (ref. 32) was used for turbulent values. Cross-flow effects were also included. The nose cap stagnation point heating rates were calculated using the method of Fay and Riddell (ref. 33) while the wing leading edge stagnation line heating rates were calculated using the method of Beckwith and Gallagher (ref. 34). Laminar heating rates for the remainder of the nose and wing leading edge were calculated using Lee's similarity solution (ref. 35), while turbulent values were determined from the method of Deltra and Hidalgo (ref. 36). Leeward surface heating rates were obtained from GAC/Martin Marietta Phase C proposal and were unchanged except in the vicinity of the nose and wing leading edge. All heating rates were based on a 311°K (100°F) wall temperature.

For the nominal south ascent trajectory, heating rates were determined for only the nose cap, wing leading edge, interference region, and bottom centerline reference location. These were shown in figures 37, 40, 43, and 35, respectively.

APPENDIX B

Heating rates were obtained at additional locations on the body lower centerline and wing bottom at the midspan location for both the ablator and reusable TPS entry trajectories. The additional locations on the body centerline are for distances of 3.05, 6.10, 9.14, and 12.19 m (10, 20, 30, and 40 ft) from the nose stagnation point while the locations on the wing bottom are for distances of 1.52, 3.05, 4.57, 6.10, and 7.62 m (5, 10, 15, 20, and 25 ft) from the wing stagnation line. Figures 115 and 116 present the body lower centerline location heating rate histories for the ablator and reusable TPS entry trajectories respectively, while figures 117 and 118 show the heating rate histories for the wing bottom locations. As discussed in Chapter III, flow transition for locations near the nose stagnation point and wing stagnation line occurs several hundred seconds after the transition of the reference point. This transition from laminar to turbulent flow and the corresponding increase in heating rate is evident in figures 115 thru 118.

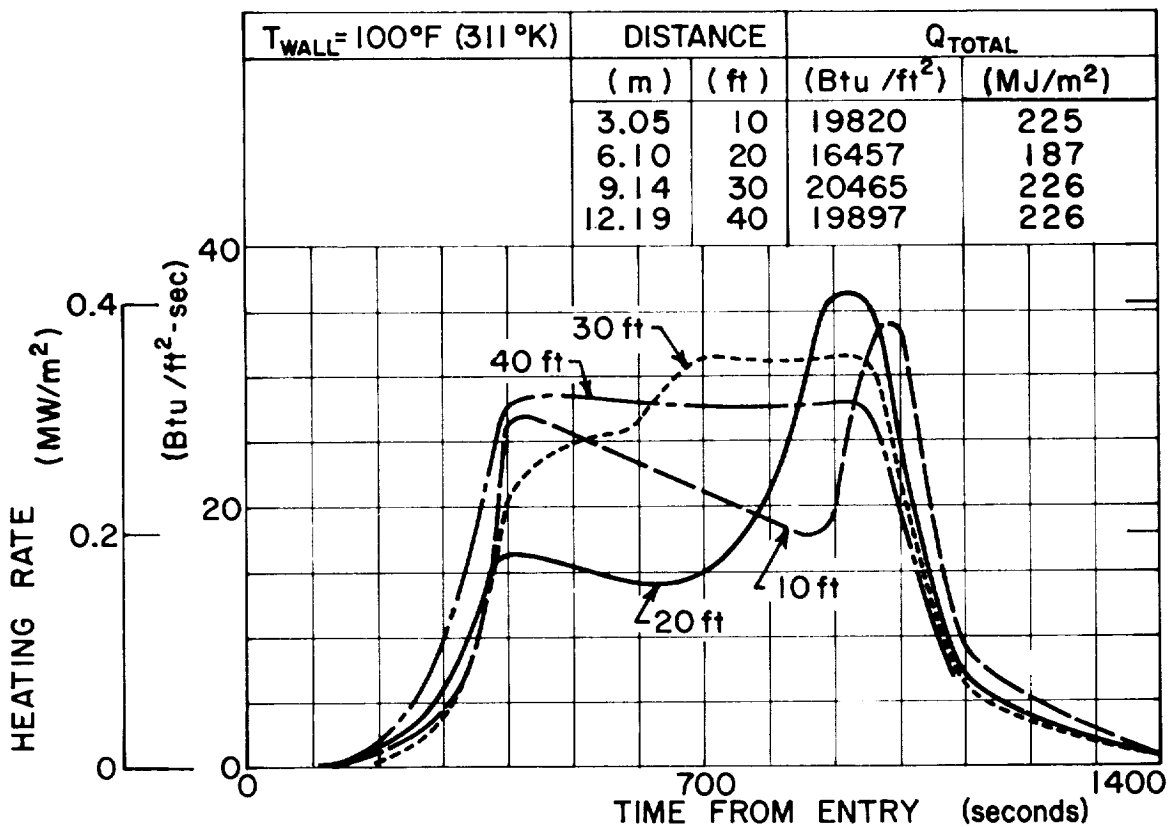


Figure 115.- Entry Heating Rate Histories on the Forward Portion of the Body Lower Centerline for Ablator Trajectory

APPENDIX B

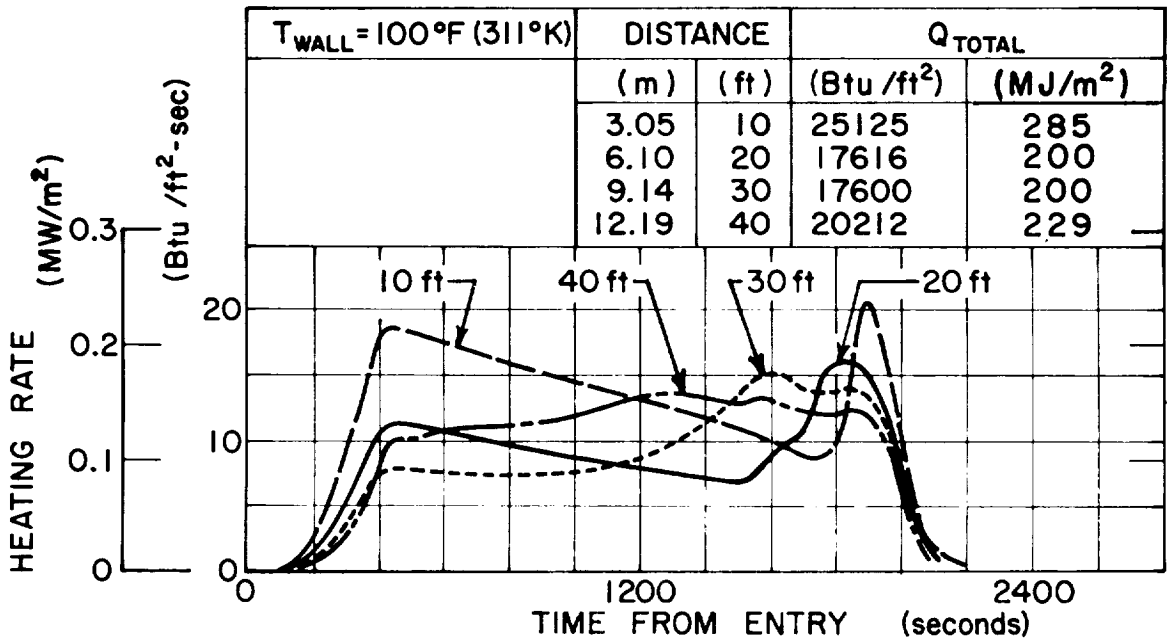


Figure 116.- Entry Heating Rate Histories on the Forward Portion of the Body Lower Centerline for the Reusable TPS Trajectory

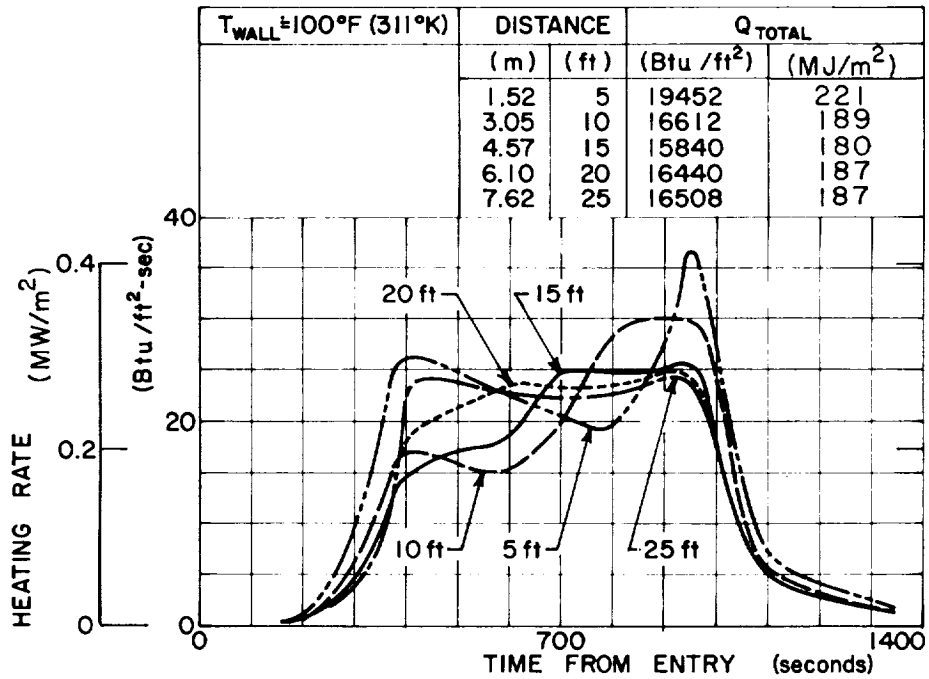


Figure 117.- Entry Heating Rate Histories on Bottom of Wing (Midspan Location) for Ablator Trajectory

APPENDIX B

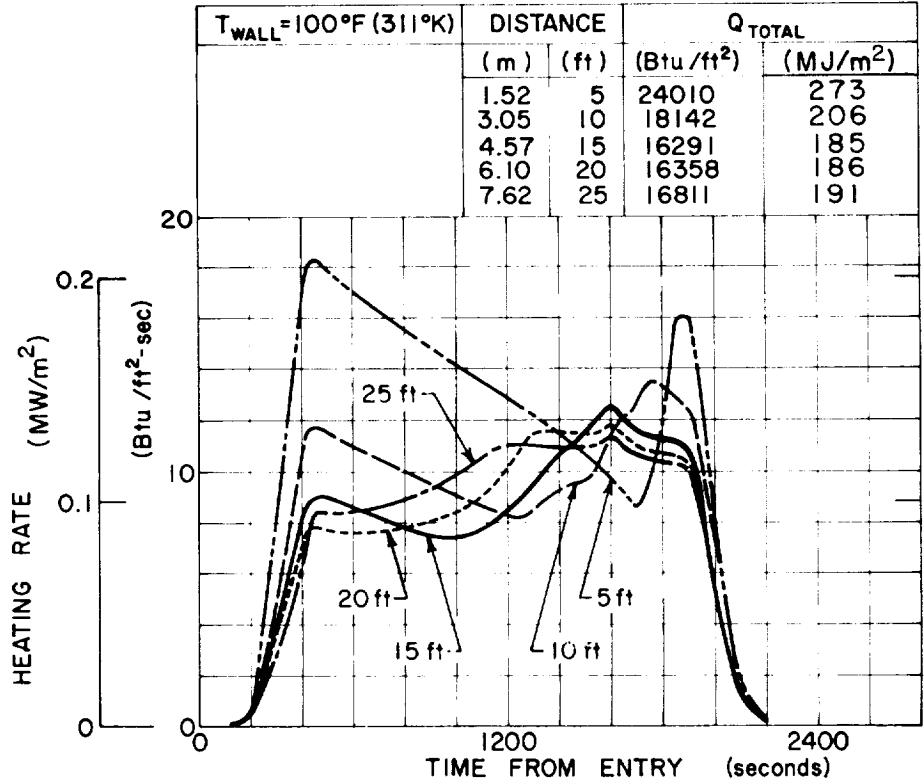


Figure 118.- Entry Heating Rate Histories on Bottom of Wing (Midspan Location) for Reusable TPS Trajectory  
 B. Aerodynamic Pressure Distributions

The local static and dynamic pressures and local Mach number were all determined using the methods described for the local flow properties. (The local dynamic pressure is defined as  $1/2$  the product of the local velocity squared times the local density.) The aerodynamic shear stress was determined from the skin friction coefficient and the local dynamic pressure. Plots of these variables for each applicable location [e.g.,  $M_L$  and  $\tau_w$  (shear stress) = 0 for the nose stagnation point] are presented first for the nominal south ascent trajectory and then for both the ablator and reusable TPS trajectories. Ascent local static pressures were shown in figure 44, ascent local dynamic pressures in figure 119, ascent local Mach numbers in figures 120 and 121, and ascent aerodynamic shear stresses in figures 122 and 123 for the nose stagnation point, bottom centerline reference location, wing leading edge, forward lower centerline, and for the body leeward and side locations. Both the ablator and reusable TPS entry time histories for a given aerothermal characteristic and location are presented on a single graph for ease of comparison. Entry static pressures were presented in figures 47 through 49, entry local dynamic pressures in figures 124 through 127, entry local Mach numbers in figures 128 through 131, and entry aerodynamic shear stresses in figures 132 through 135.

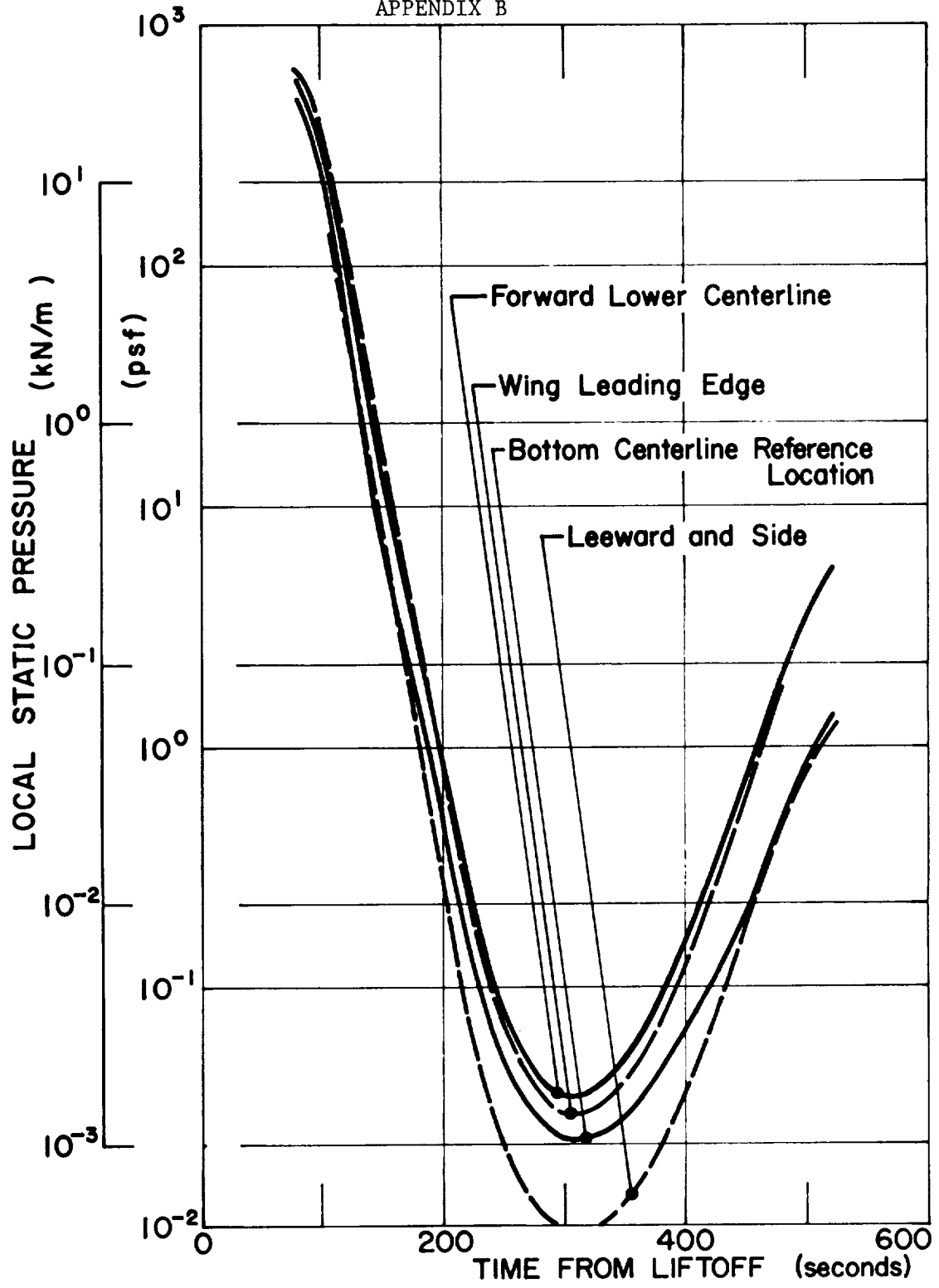


Figure 119.- Ascent Local Dynamic Pressure History

APPENDIX B

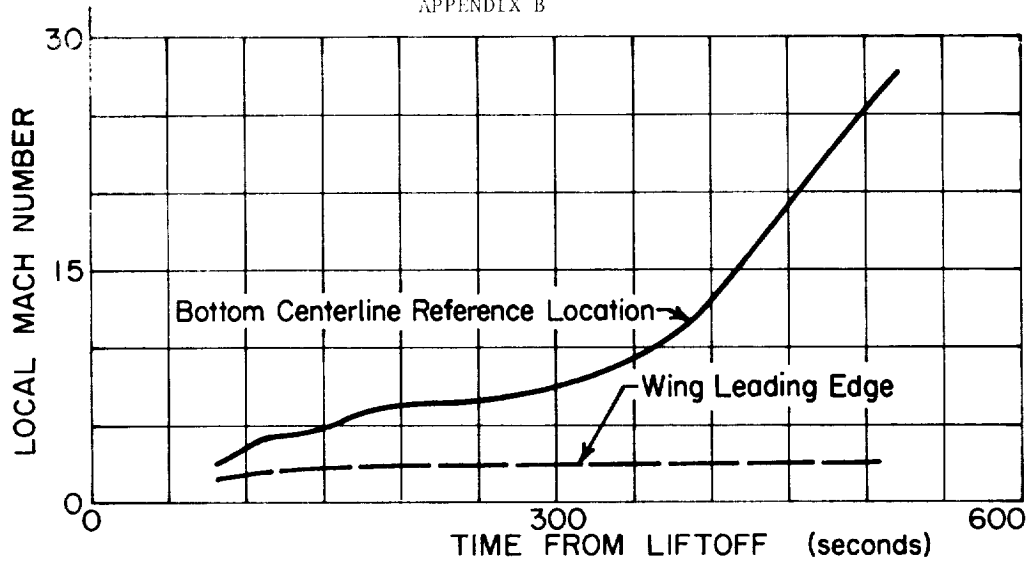


Figure 120.- Ascent Local Mach Number History at Body Lower Centerline Reference Location and at Stagnation Line of Wing Leading Edge

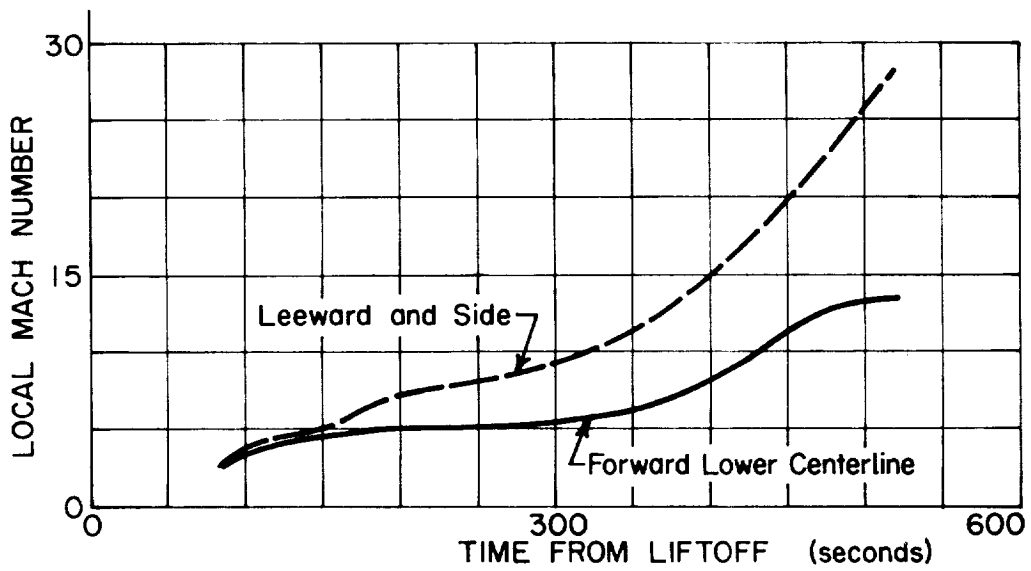


Figure 121.- Ascent Local Mach Number History at Forward Centerline and at Leeward and Side Locations

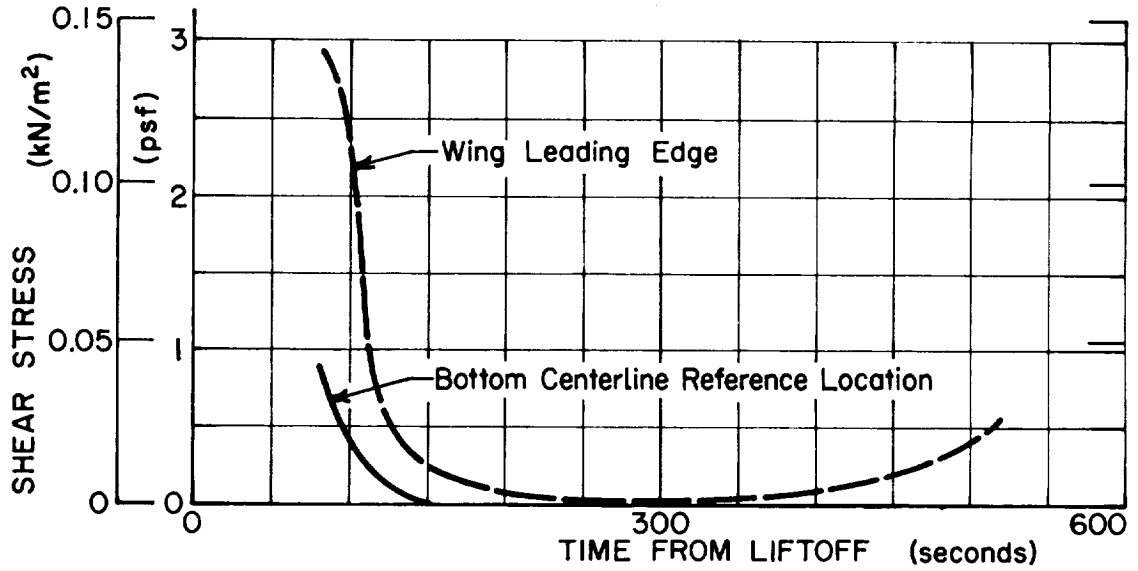


Figure 122.- Ascent Shear Stress History at Body Lower Centerline Reference Location and at Stagnation Line of Wing Leading Edge

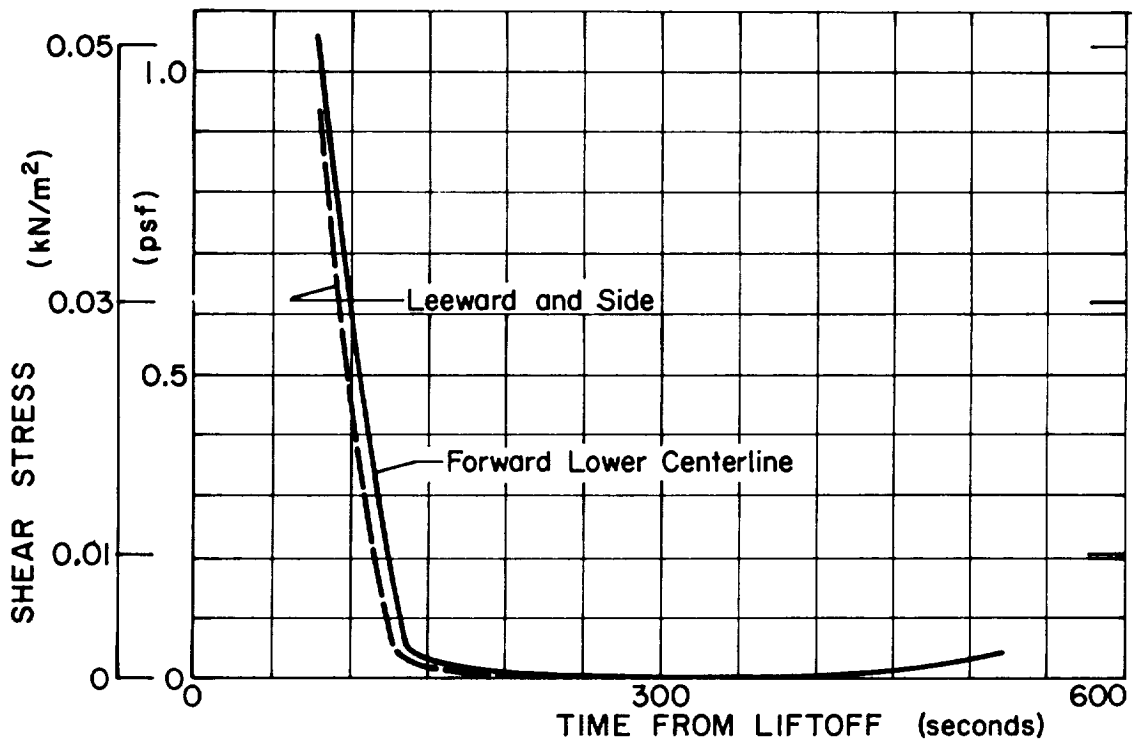


Figure 123.- Ascent Shear Stress History at Forward Lower Centerline and at Leeward and Side Locations

APPENDIX B

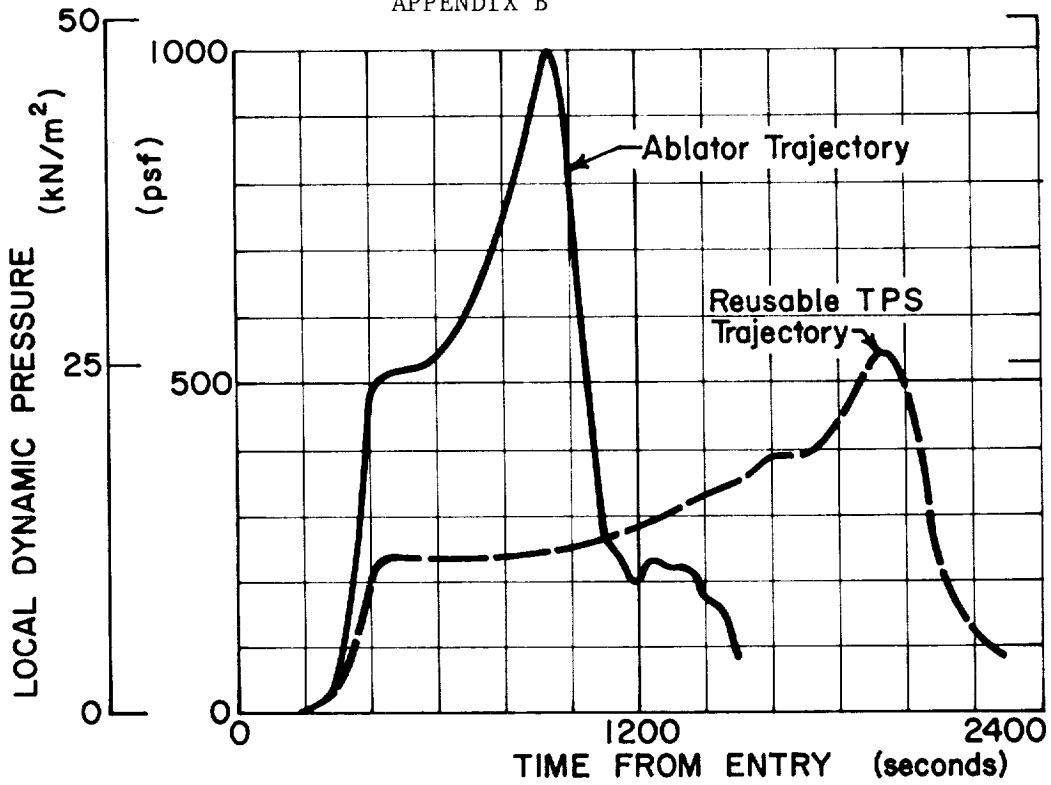


Figure 124.- Entry Local Dynamic Pressure History at Body Lower Centerline Reference Location

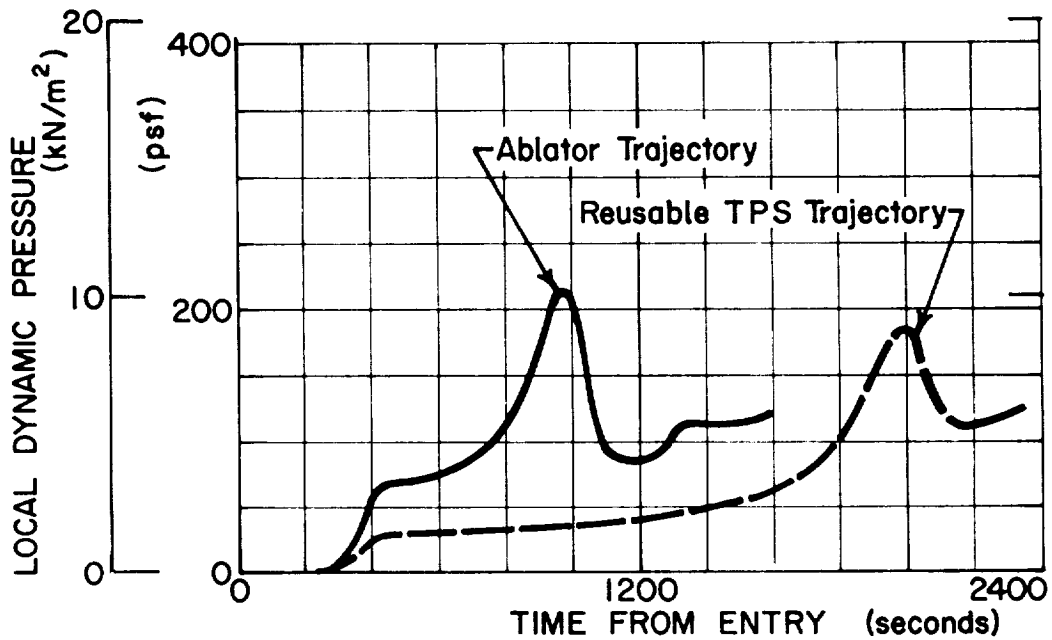


Figure 125.- Entry Local Dynamic Pressure History at Stagnation Line of Wing Leading Edge (Midspan Location)

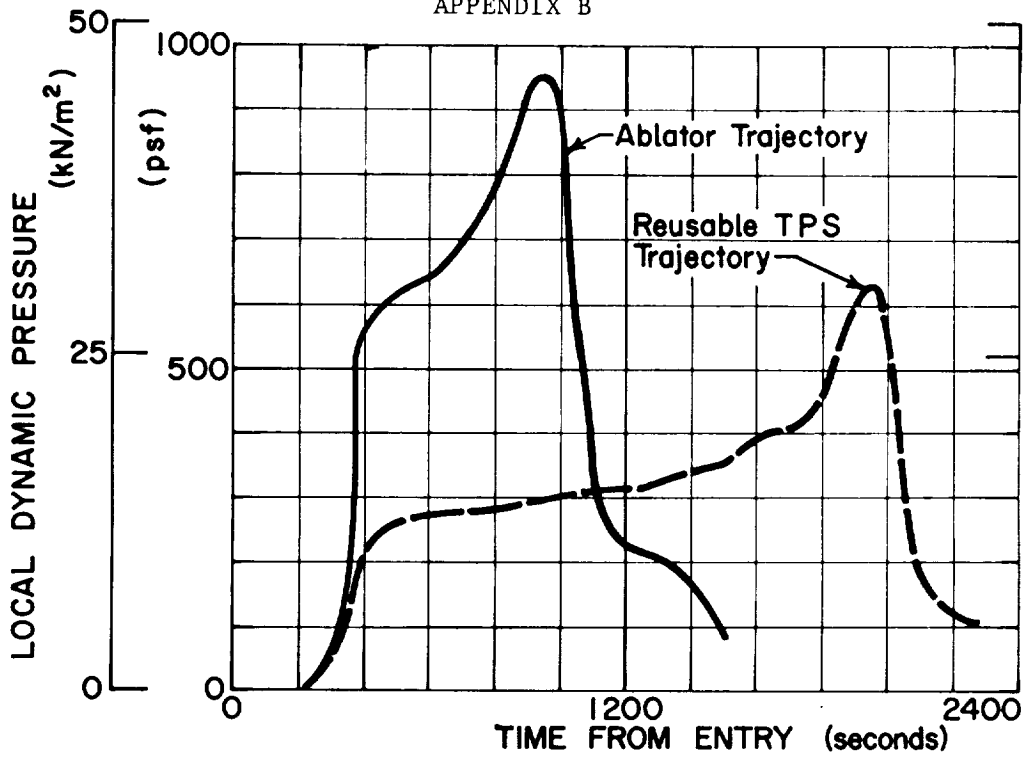


Figure 126.- Entry Local Dynamic Pressure History at the Forward Lower Centerline Location

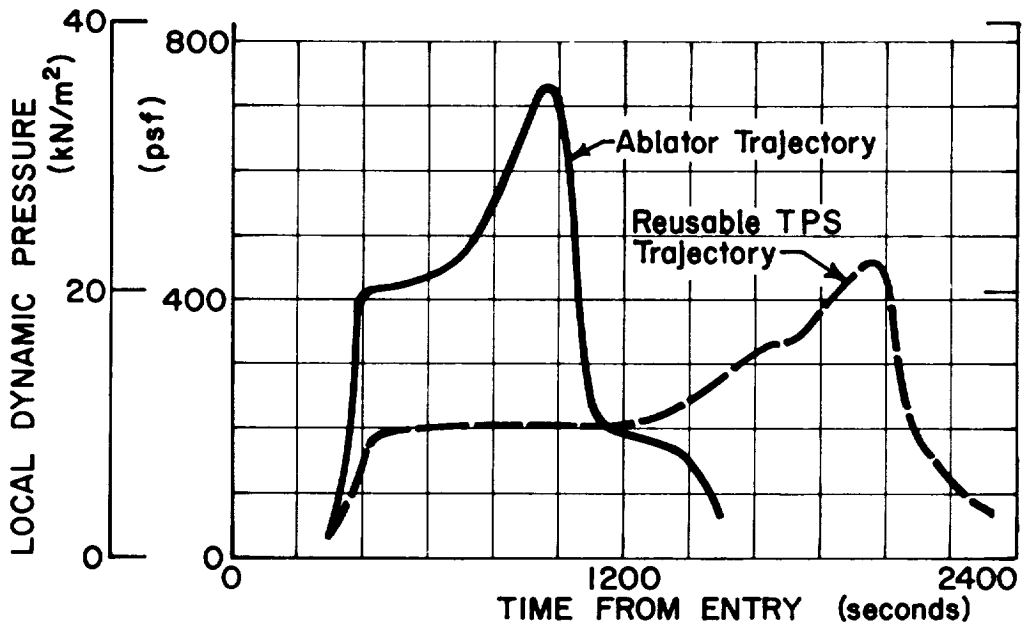


Figure 127.- Entry Local Dynamic Pressure History at Leeward and Side Locations

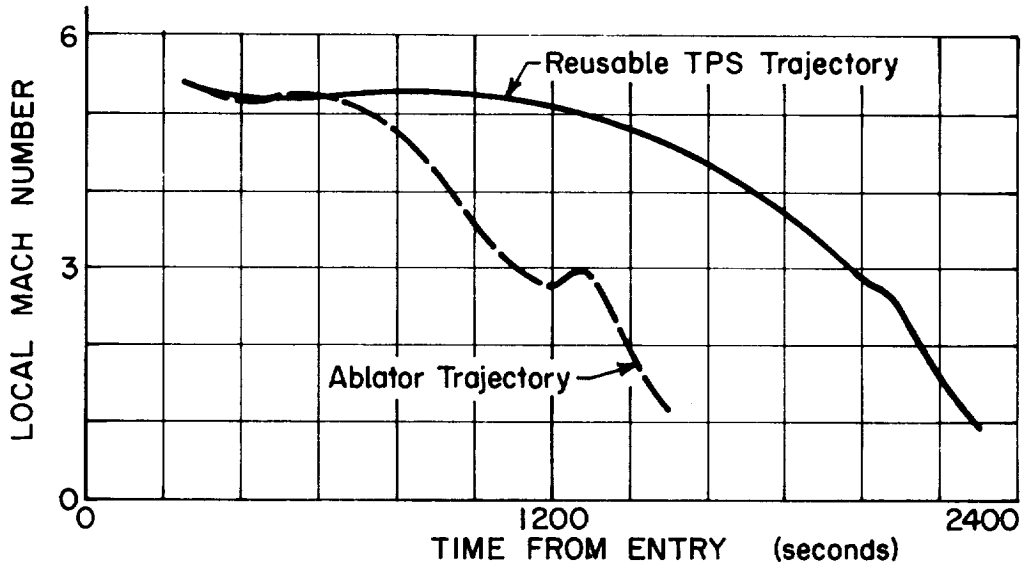


Figure 128.- Entry Local Mach Number History at Body Lower Centerline Reference Location

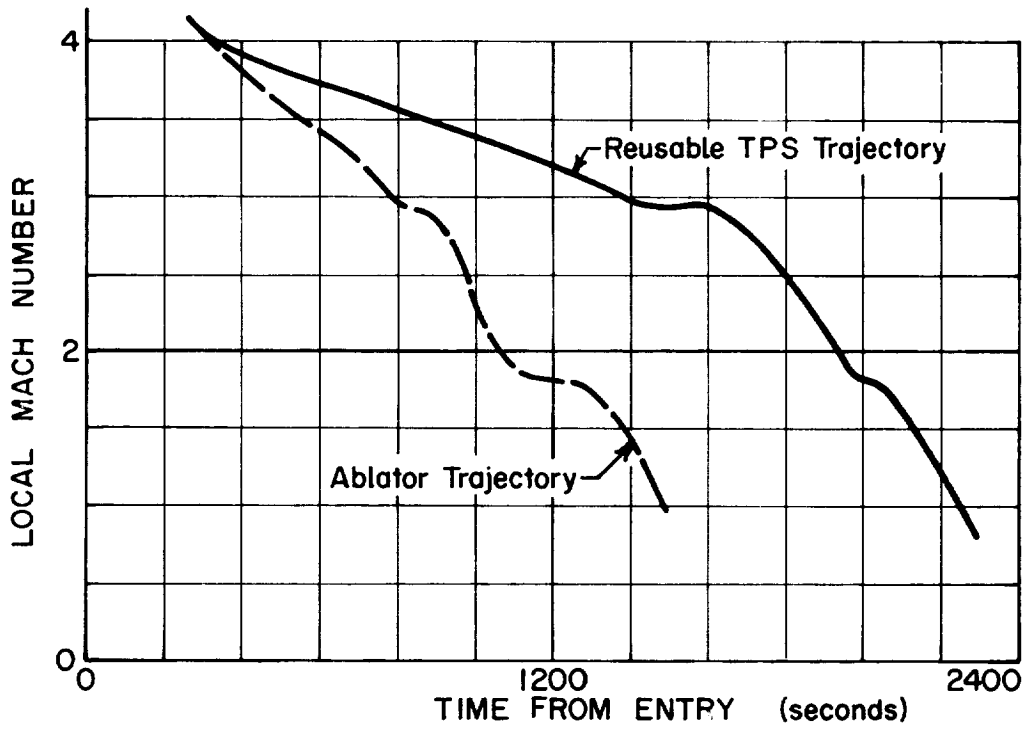


Figure 129.- Entry Local Mach Number History at Stagnation Line of Wing Leading Edge (Midspan Location)

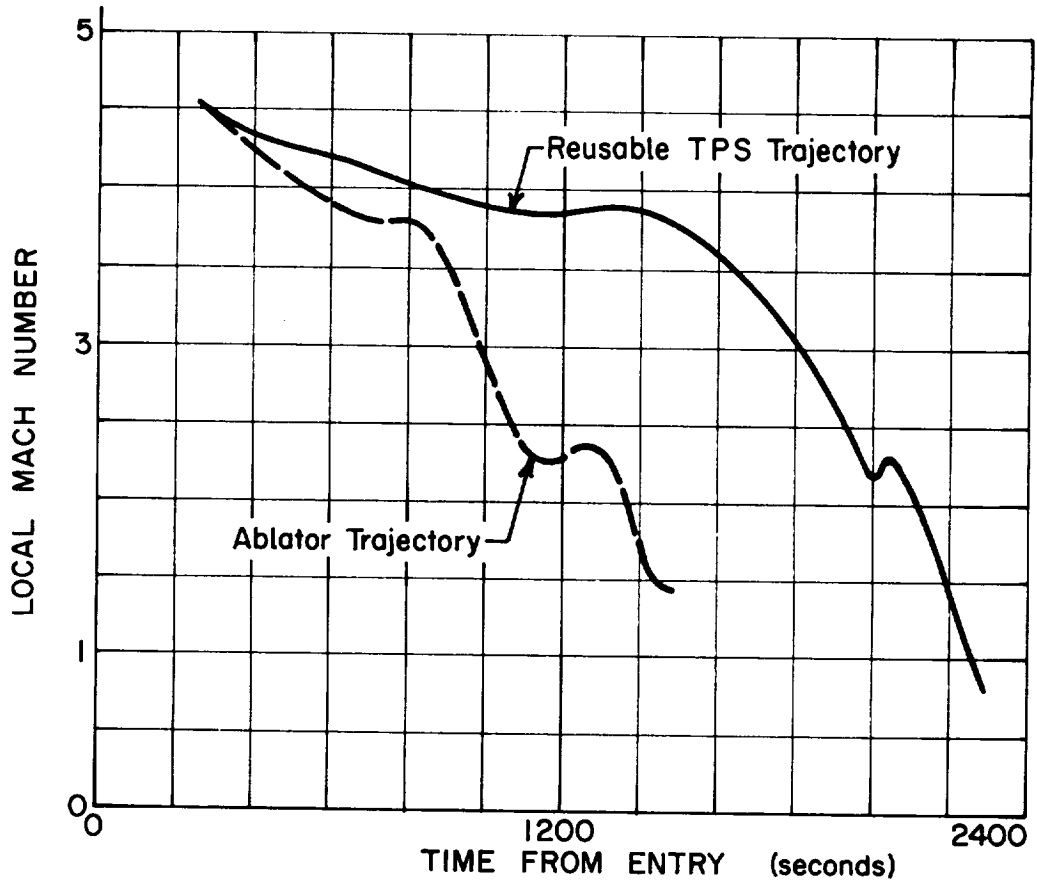


Figure 130.- Entry Local Mach Number History at the Forward Lower Centerline Location

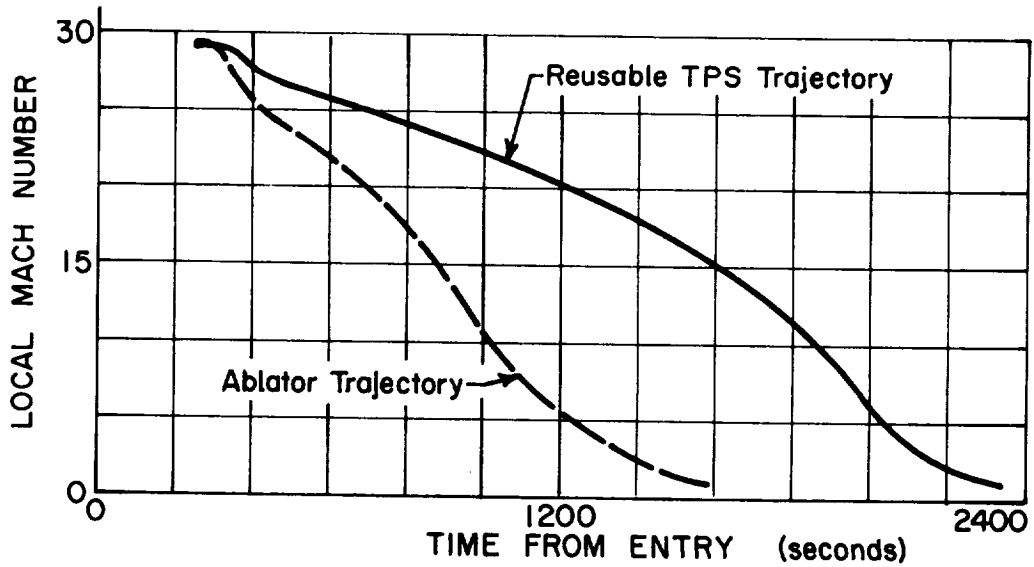


Figure 131.- Entry Local Mach Number History at Leeward and Side Locations

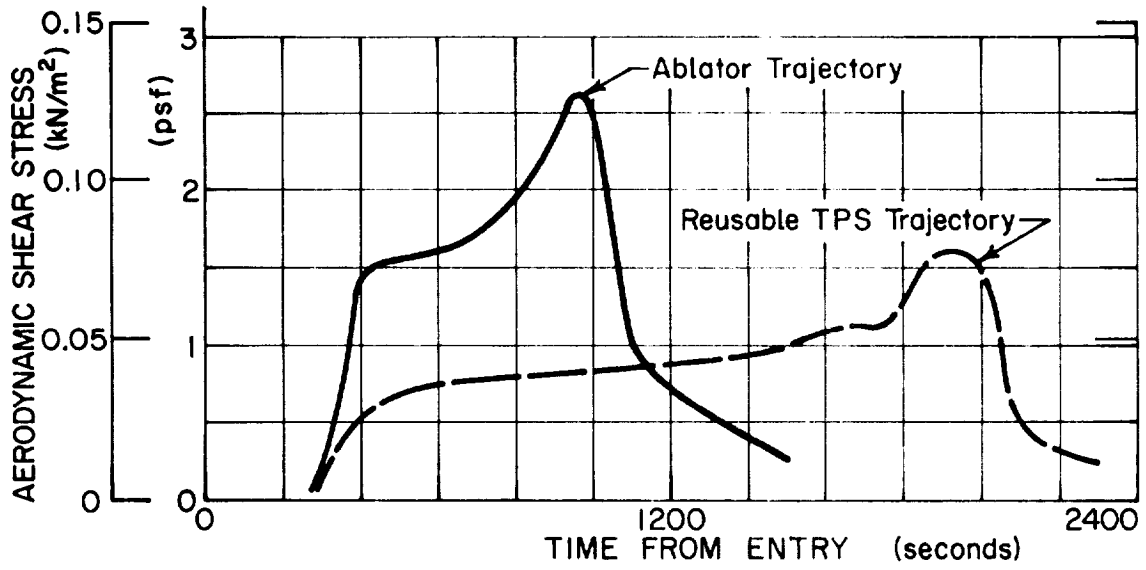


Figure 132.- Entry Shear Stress History at Body Lower Centerline Reference Location

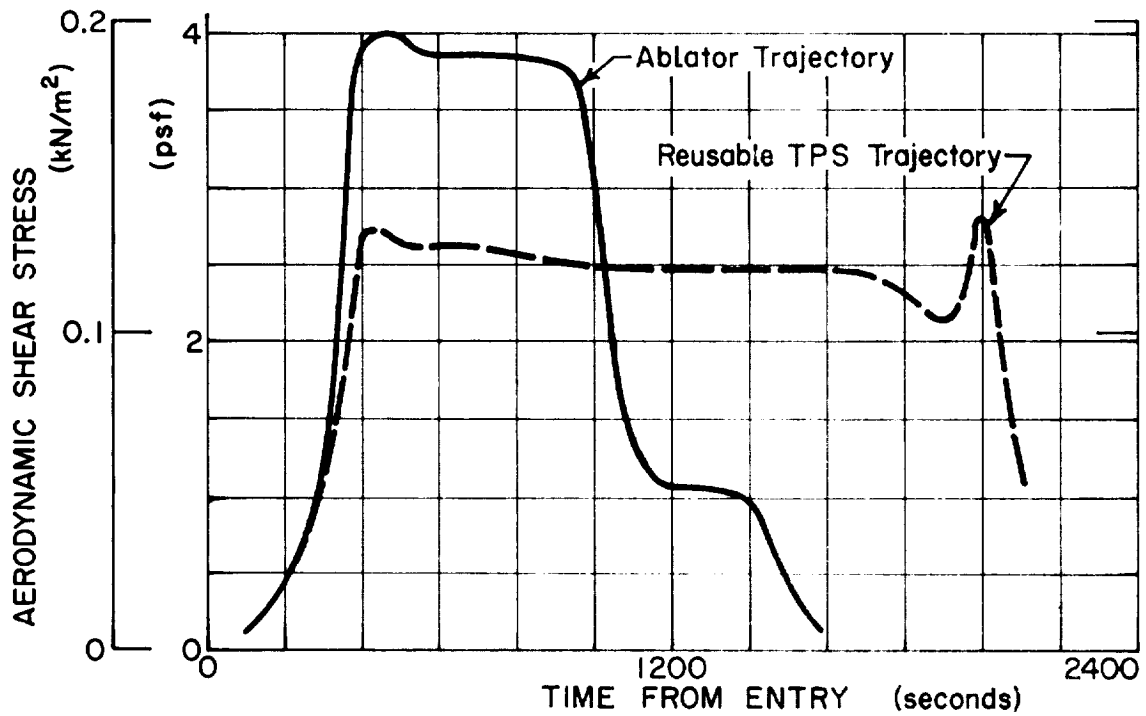


Figure 133.- Entry Shear Stress History at Stagnation Line of Wing Leading Edge (Midspan Location)

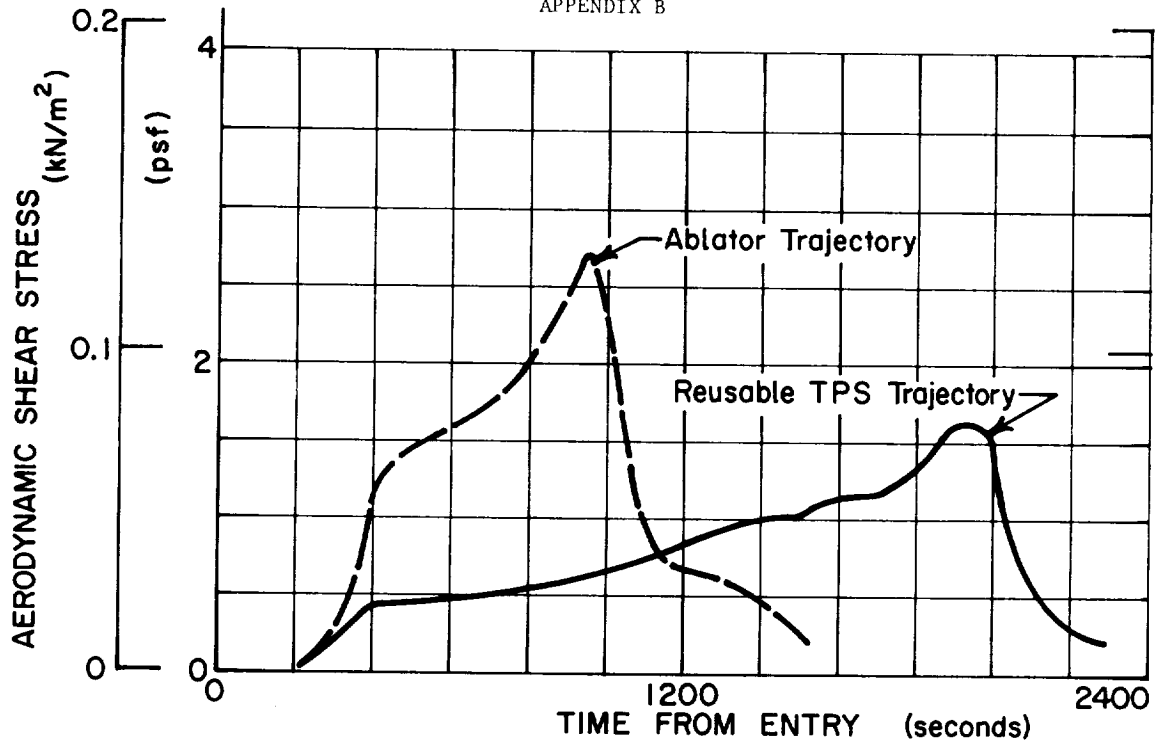


Figure 134.- Entry Shear Stress History at the Forward Lower Centerline Location

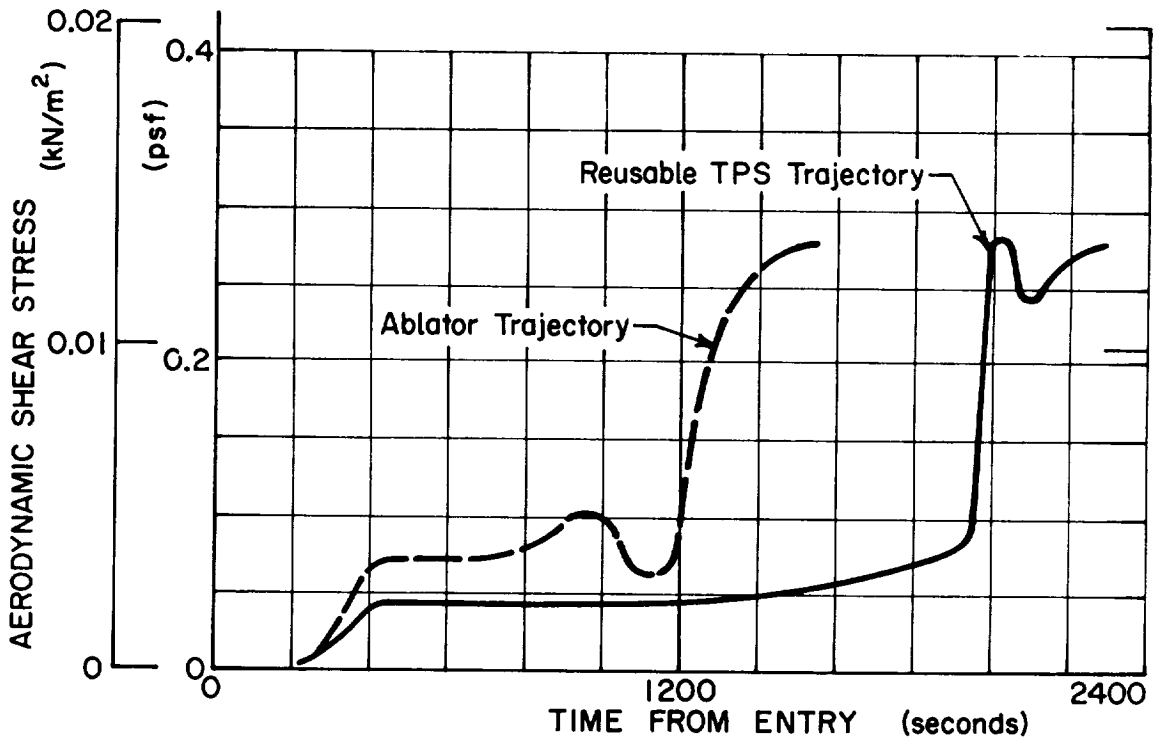


Figure 135.- Entry Shear Stress History at Leeward and Side Locations

## APPENDIX B

### C. Venting of Standoff Panels

The standoff heat shield panel venting analysis was performed using the compartment venting digital computer program, FD275 (ref. 37). A typical panel 50.8 cm (20-in.) square with a standoff distance of 1.372 cm (0.54 in.) was chosen with a vent area of 0.258 cm<sup>2</sup> (0.04 in.<sup>2</sup>). The vent area was assumed to be 60% effective, which resulted in an effective area of 0.155 cm<sup>2</sup> (0.024 in.<sup>2</sup>). The FD275 venting program uses the law of conservation of mass so that the rate of change of mass within the compartment equals the net total mass flow in and out of the compartment. Isentropic adiabatic, perfect gas flow equations were used to calculate the mass flow. The calculation time interval is varied by the program until the mass conservation is balanced within 1.0 percent, and the mass flow rate to within 0.1 percent. The following equations are used to calculate the compartment conditions once conservation of mass and mass flow rate is achieved.

$$\frac{dP_c}{dt} = \frac{\delta R T_L}{V} \left( \frac{dm}{dt} \right)$$

$$\frac{dT_c}{dt} = \left( \frac{\delta T_L - T_c}{\rho_c V} \right) \frac{dm}{dt}$$

where:

$dP_c/dt$  = time rate of change of compartment pressure

$dT_c/dt$  = time rate of change of compartment temperature

$dm/dt$  = mass flow rate

$V$  = compartment volume

$\rho_c$  = density of gas in compartment

$T_c$  = temperature of gas in compartment

$T_L$  = local gas temperature (outside compartment)

$\delta$  = ratio of specific heats for air

$R$  = gas constant for air

The temperature of the gas in the compartment was assumed to be the total temperature. All aerothermal characteristics required for the venting analysis were obtained by the methods described previously.

APPENDIX C

STRESS ANALYSIS

A. Acreage Area Subpanels

The computer program used is the Subpanel Design Optimization for Ablator Thermal Protection Systems (ref. 38). It is capable of determining honeycomb face thicknesses and core thickness for least-weight subpanels.

To obtain least-weight subpanel configurations for a range of bending moments, the computer program considers three modes of failure:

- 1) An allowable strain of 1% in the ablator outer fibers at ultimate load;
- 2) Failure of the Subpanel face by face wrinkling;
- 3) Failure of the subpanel face by intracell buckling.

Program inputs include ablator material properties and thicknesses, facing material properties and thicknesses, core material properties and cell size, and a table of bending moments. The range of bending moments was determined by considering the subpanel to be a continuous rectangular plate supported by rows of equidistant support posts. In this case, a square array pattern of fasteners attached the heat shield panels to the primary structure (table 49).

TABLE 49.- APPLIED LOADINGS

Condition	Equation	Reference
Airload bending	$\text{Moment} = \frac{q\ell^2}{4\pi} \left[ (1+\mu) \log \frac{\ell}{c} - (\alpha+3\mu) \right]$ $= 0.106 q\ell^2 \left( \log \frac{\ell}{c} - 0.811 \right)$	Ref. 21
Airload deflection	$\delta = \frac{12\alpha_1 q\ell^4 (1-\mu^2)}{Eh^3}$ $= \frac{0.062 q\ell^4}{Eh^3}$	

For subpanels on equidistant supports:

$\ell$  = Attachment spacing

$\alpha_1 = 0.00581$  (for deflection at center)

$\alpha = \beta = 0.811$  (for moment at support)

$C = 1.588$  cm (0.625 in.) radius of support post

$q$  = Aerodynamic airload pressure

$\mu$  = Poisson's ratio

$E$  = Young's modulus

$h$  = Core height or plate thickness

Allowable bending moments and deflections for the plate-ablator combinations and honeycomb-ablator combinations are listed in table 50.

TABLE 50.- ALLOWABLE LOADINGS

Critical element	Equation	Reference
Ablator strain due to subpanel bending	$MAS = \frac{\epsilon EI}{(1-\mu^2)(Y)} = \frac{0.01 EI}{(1-\mu^2)Y}$	$\epsilon = 0.01$ strain design criteria
Panel bending deflection	$\delta = 0.0125\ell$	Design criteria
Honeycomb face wrinkling	$MFW = (0.33) \left[ E_{\text{core}} E_{\text{face}} (h) \right]^{1/2} (t)^{3/2}$	Refs. 6 and 39
Honeycomb intra-cell buckling	$MJB = \frac{(0.833) E_{\text{face}} (h+t) (t^3)}{(1-\mu^2)(S^2)}$	

## APPENDIX C

For which:

MAS = allowable bending moment based on 1% ablator strain

MFW = allowable bending moment based on face wrinkling buckling

MIB = allowable bending moment based on face intracell buckling

I = moment of inertia of subpanel cross section

$E_{\text{face}}$  = Young's modulus of elasticity for the sandwich face material in the direction of the bending stress

$E_{\text{core}}$  = smeared out compressive modulus of the sandwich core

$\bar{Y}$  = distance from the calculated neutral axis to the outer fiber of the ablator

t = facing thickness

S = honeycomb core cell size

Sample calculation (tables 51 through 53).-

Problem: Design the optimum combination of SLA-561 ablator bonded to a 2024-T81 aluminum subpanel mechanically attached to an aluminum Orbiter structure at fuselage Sta 450 (top centerline) with screws at 12.7 cm (5 in.), 25.4 cm (10 in.), 38.1 cm (15 in.) and 50.8 cm (20 in.)

From table 16: Design airload  $q = 4.8 \text{ kN/m}^2$  ( $0.7 \text{ lb/in.}^2$ ) ultimate; heating rate ratio to ref. point  $Fq = 0.151$  (table 18).

From table 49:

$$\text{Airload Moment} = 0.106 q \ell^2 \left( \log \frac{\ell}{c} - 0.811 \right)$$

$$\text{Deflection} = \frac{0.062 q \ell^4}{Eh^3} = 0.0125 \ell$$

APPENDIX C

TABLE 51.- AIRLOAD BENDING MOMENT AND MINIMUM THICKNESS<sup>a</sup>

s		Moment		Min. Thickness	
cm	in.	N-m	in.-lb	cm	in.
12.7	5	0.266	2.35	0.079	0.031
25.4	10	1.60	14.20	0.157	0.062
38.1	15	4.46	39.44	0.234	0.092
50.8	20	8.89	78.69	0.312	0.123

<sup>a</sup>To limit deflection to 0.0125s, final subpanel thickness must  $\geq$  min. thickness as determined by airload moment requirements.

From table 50:

$$MAS = \frac{0.01 EI}{(1-\nu^2)\bar{Y}} = \frac{0.01122 EI}{\bar{Y}}$$

TABLE 52.- PLATE THICKNESS REQUIRED FOR MAS  $\geq$  AIRLOAD MOMENT

s		Ablator, t		MAS		t	
cm	in.	cm	in.	N-m	in.-lb	cm	in.
12.7	5	2.67	1.05	1.29	11.41	0.079	0.031
25.4	10	2.41	0.95	1.62	14.37	0.218	0.086
38.1	15	2.16	0.85	4.55	40.33	0.406	0.160
50.8	20	2.16	0.85	9.60	84.97	0.549	0.216

Since this check is being made for a plate subpanel, MFW and MIB are not applicable.

TABLE 53.- SUMMARY OF PLATE t TO MEET DEFLECTION AND MAS

s		Plate, t		Criticality
cm	in.	cm	in.	
12.7	5	0.079	0.031	Deflection
25.4	10	0.218	0.086	MAS
38.1	15	0.406	0.160	MAS
50.8	20	0.549	0.216	MAS

## APPENDIX C

Table 54 "subpanel gages" lists the final thickness for all materials and configurations investigated.

### B. Nose Cap Subpanels

The structure of the fuselage nose cap was analyzed as a spherical cap under uniform external collapsing pressure. Aerodynamic airload pressures were taken from table 7 while the analysis used the methods defined in reference 40, Section C 3.0, p 86.

Classical collapsing pressure for a spherical shell is obtained by:

$$P_{CL} = \frac{2E}{[3(1-\mu^2)]^{1/2}} \left(\frac{t}{R}\right)^2$$

$P_{CL}$  = Collapsing pressure

$E$  = Young's modulus

$\mu$  = Poisson's ratio

$t$  = Shell thickness

$R$  = Shell radius

The value of  $P_{CL}$  must be modified to make it consistent with test data by:

$$P_{CR} = P_{CL} \left(0.14 + \frac{3.2}{\lambda^2}\right)$$

where:

$$\lambda = [12(1-\mu^2)]^{1/4} \left(\frac{R}{t}\right)^{1/2} \left(2 \sin\left(\frac{\phi}{2}\right)\right)$$

$P_{CR}$  = critical collapsing pressure

$\phi$  = shell half angle

APPENDIX C

TABLE 54.- SUBPANEL GAGES

Material	Sta 230		Sta 450		Sta 495		Sta 800		Sta 230		Sta 450		Sta 495		Sta 800		
	Fastener Spacing, cm	t, face cm	h, core cm	t, face in.	h, core in.												
Aluminum 2024-T81	12.7	0.079	NA	0.079	NA	0.079	NA	0.079	NA	0.031	NA	0.031	NA	0.031	NA	0.031	NA
	25.4	0.157	NA	0.157	NA	0.157	NA	0.152	NA	0.062	NA	0.086	NA	0.062	NA	0.060	NA
	38.1	0.234	NA	0.411	NA	0.411	NA	0.376	NA	0.092	NA	0.160	NA	0.162	NA	0.148	NA
Magnesium HM-21A	50.8	0.554	NA	0.564	NA	0.564	NA	0.579	NA	0.218	NA	0.216	NA	0.222	NA	0.228	NA
	12.7	0.091	NA	0.091	NA	0.091	NA	0.091	NA	0.036	NA	0.036	NA	0.036	NA	0.036	NA
	25.4	0.183	NA	0.183	NA	0.183	NA	0.183	NA	0.072	NA	0.102	NA	0.072	NA	0.072	NA
Lockalloy 62Be-38A2	38.1	0.277	NA	0.488	NA	0.488	NA	0.432	NA	0.109	NA	0.188	NA	0.192	NA	0.170	NA
	50.8	0.640	NA	0.671	NA	0.671	NA	0.686	NA	0.252	NA	0.252	NA	0.264	NA	0.270	NA
	12.7	0.058	NA	0.058	NA	0.058	NA	0.058	NA	0.023	NA	0.023	NA	0.023	NA	0.023	NA
Aluminum 2024-T81	25.4	0.117	NA	0.117	NA	0.117	NA	0.117	NA	0.046	NA	0.052	NA	0.046	NA	0.046	NA
	38.1	0.239	NA	0.277	NA	0.277	NA	0.239	NA	0.094	NA	0.107	NA	0.109	NA	0.094	NA
	50.8	0.389	NA	0.389	NA	0.389	NA	0.389	NA	0.153	NA	0.153	NA	0.153	NA	0.153	NA
Aluminum 2024-T81	12.7	0.013	0.076	0.013	0.076	0.013	0.076	0.013	0.076	0.005	0.030	0.005	0.030	0.005	0.030	0.005	0.030
	25.4	0.013	0.457	0.013	0.457	0.013	0.457	0.013	0.483	0.005	0.180	0.005	0.190	0.005	0.180	0.005	0.190
	38.1	0.015	0.737	0.015	0.737	0.015	0.737	0.015	0.762	0.006	0.290	0.006	0.300	0.006	0.290	0.006	0.300
Magnesium HM-21A	50.8	0.020	0.635	0.018	1.118	0.018	1.143	0.018	1.067	0.008	0.250	0.007	0.440	0.007	0.450	0.007	0.420
	12.7	0.013	0.279	0.013	0.279	0.013	0.279	0.013	0.279	0.005	0.110	0.005	0.110	0.005	0.110	0.005	0.110
	25.4	0.020	0.432	0.020	0.432	0.020	0.432	0.020	0.432	0.008	0.170	0.008	0.170	0.008	0.170	0.008	0.170
Graphite composite	38.1	0.025	0.584	0.025	0.813	0.025	0.610	0.025	0.584	0.010	0.230	0.009	0.320	0.010	0.240	0.010	0.230
	50.8	0.030	0.686	0.025	1.194	0.025	1.194	0.025	1.194	0.012	0.270	0.010	0.470	0.010	0.470	0.010	0.470
	12.7	0.013	0.356	0.013	0.330	0.013	0.330	0.013	0.356	0.005	0.140	0.005	0.130	0.005	0.130	0.005	0.140
Aluminum 2024-T81	25.4	0.020	0.508	0.020	0.508	0.020	0.508	0.020	0.508	0.008	0.200	0.008	0.200	0.008	0.200	0.008	0.200
	38.1	0.028	0.533	0.025	0.787	0.025	0.711	0.028	0.533	0.011	0.210	0.010	0.310	0.010	0.280	0.011	0.210
	50.8	0.033	0.635	0.025	1.448	0.025	1.448	0.028	1.194	0.013	0.250	0.010	0.570	0.010	0.570	0.011	0.470
Graphite composite	12.7	0.013	0.610	0.013	0.457	0.013	0.533	0.013	0.457	0.005	0.240	0.005	0.180	0.005	0.210	0.005	0.180
	25.4	0.018	1.372	0.018	1.194	0.018	1.346	0.018	1.219	0.007	0.540	0.007	0.470	0.007	0.530	0.007	0.480
	38.1	0.028	2.565	0.023	2.286	0.025	2.261	0.023	2.286	0.011	1.010	0.009	0.900	0.010	0.890	0.009	0.900
Graphite composite	50.8	0.041	3.759	0.033	2.946	0.038	2.616	0.036	2.515	0.016	1.480	0.013	1.160	0.015	1.030	0.014	0.990
	12.7	0.020	0.711	0.020	0.508	0.020	0.584	0.020	0.508	0.008	0.280	0.008	0.200	0.008	0.230	0.008	0.200
	25.4	0.020	1.422	0.025	1.626	0.028	1.549	0.028	1.397	0.012	0.560	0.010	0.640	0.011	0.610	0.011	0.550
Graphite composite	38.1	0.048	2.845	0.041	2.261	0.046	2.286	0.041	2.286	0.019	1.120	0.016	0.890	0.018	0.900	0.016	0.900
	50.8	0.069	3.734	0.064	2.438	0.066	2.794	0.058	2.972	0.027	1.470	0.025	0.960	0.026	1.100	0.023	1.170

APPENDIX C

The values  $P_{CL}$  and  $P_{CR}$  are developed for shells with "clamped" edges. Because the nose cap is assumed to have "simply supported" edges, calculated shell thicknesses are increased by a factor of 4.4, derived from table XVI of reference 20. The geometry of the fuselage nose cap is illustrated in figure 136. Aerodynamic pressure on the cap is  $51.7 \text{ kN/m}^2$  (7.5 psi), limit, or, with a factor of 1.4,  $72.4 \text{ kN/m}^2$  (10.5 psi), ultimate. When the structure was assumed to be honeycomb, the cross sectional moments of inertia were assumed equivalent to a plate using the relationship:

$$I_{\text{plate}} = I_{\text{honeycomb}}$$

$$\frac{t^3}{12} = \frac{t_{\text{face}}}{2} (t_{\text{face}} + t_{\text{core}})^2$$

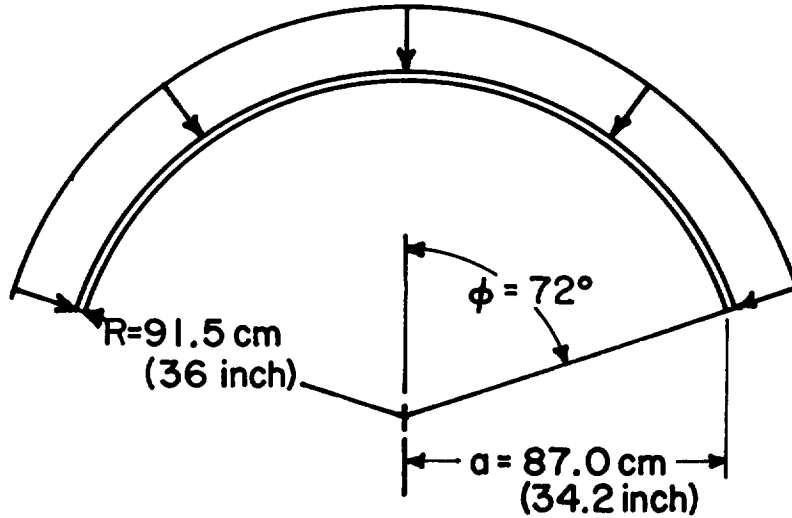


Figure 136.- Fuselage Nose Cap Geometry

The mechanical properties used are listed in table 55. A summary of the nose cap structural gages is presented in table 56.

APPENDIX C

TABLE 55.- MATERIAL PROPERTIES

Material	Youngs modulus x 10 <sup>6</sup>		μ
	kN/m <sup>2</sup>	lb/in. <sup>2</sup>	
2024-T81 Aluminum	72.4	10.5	0.33
6Al-4V Titanium	110.0	16.0	0.31
Graphite Polyimide	34.5	5.0	0.20
Glass Phenolic	20.7	3.0	0.20

TABLE 56.- NOSE CAP CONFIGURATIONS

Configuration	Material	Sandwich		Sheet	
		Face thickness, cm (in.)	Core thickness, cm (in.)	Sheet thickness, cm (in.)	Rib thickness, cm (in.)
Honeycomb sandwich spherical dome	2024-T81 aluminum alloy faces and 5052-H39 aluminum foil honeycomb core	0.025 (0.010)	2.38 (0.937)	--	--
	Titanium 6Al-4V alloy faces and core	0.025 (0.010)	1.75 (0.690)	--	--
	Graphite polyimide faces and Hexcel HRH 327 glass reinf plastic honeycomb core	0.041 (0.016)	3.41 (1.344)	--	--
	Glass phenolic faces and Hexcel HRH 327 glass reinf plastic honeycomb core	0.051 (0.020)	4.88 (1.922)	--	--
Formed sheet spherical dome	2024-T81 Al alloy	--	--	0.965 (0.380)	--
	Titanium 6Al-4V alloy	--	--	0.785 (0.309)	--
	Graphite polyimide	--	--	1.42 (0.560)	--
	Glass phenolic	--	--	1.84 (0.723)	--
Rib-supported sheet spherical dome	2024-T81 aluminum alloy sheet and ribs	--	--	2.16 (0.085)	1.63 (0.064)

## APPENDIX D

### THERMAL ANALYSIS

Thermal analysis for this study used two existing computer programs. To use these programs effectively, proper modeling of the problem is necessary. This appendix presents the modeling studies that were conducted and the conclusions of these studies.

Thermal analysis for ablator sizing was carried out with the Thermochemical Ablation Program (TCAP III) (ref. 41). Data input to this program includes trajectory data, i.e., velocity, altitude, heating rate, and recovery enthalpy; thermophysical properties for the ablator material and backup structure materials; ablation kinetics; and geometry of the model being analyzed. Analysis results include time-temperature distributions throughout the model and a time-density profile through the ablative material.

Analysis for sizing the RSI material and for developing back-up structure modeling techniques was carried out with the Three Dimensional Heat Transfer program (ref. 42). Data input and analysis results are similar to TCAP III except that an ablation process is not considered. Both programs allow for variations of conductivity with pressure as well as temperature.

#### A. Modeling of Honeycomb Sandwich Subpanels

Three methods of modeling a honeycomb sandwich subpanel were considered. The first model consisted of a simple three-element configuration with heat transfer through the model by conduction only. The center, or core element, was assigned a reduced density to simulate the reduced solid cross-sectional area of a honeycomb core. The second model was the same as the first with the addition of radiant heat transfer between the face elements with a shape factor of 1.0. The third model, representing the best analytical description of the panel, was a six-sided box with the top and bottom elements representing the sandwich face sheets and the sides representing the cell walls. Heat transfer was by conduction between adjacent elements and by radiation between all elements.

The analysis was conducted by defining the temperature on the top face element and comparing responses of the bottom face elements. Figures 137 and 138 show typical results for high (0.88) and low (0.2) emissivity materials. Since models 2 and 3 gave comparable results and the reduction in radiation paths and greater simplicity of model 2 represent a significant savings in computational time, this model was used in subsequent analysis.

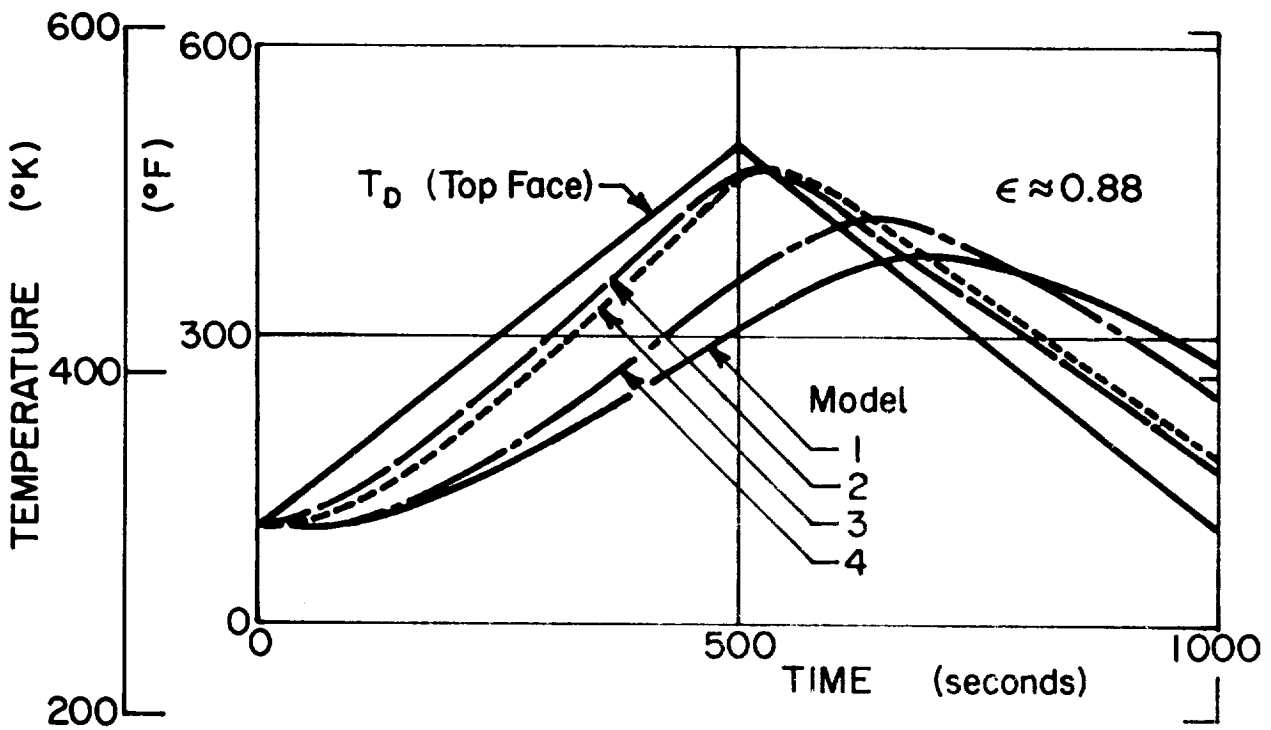
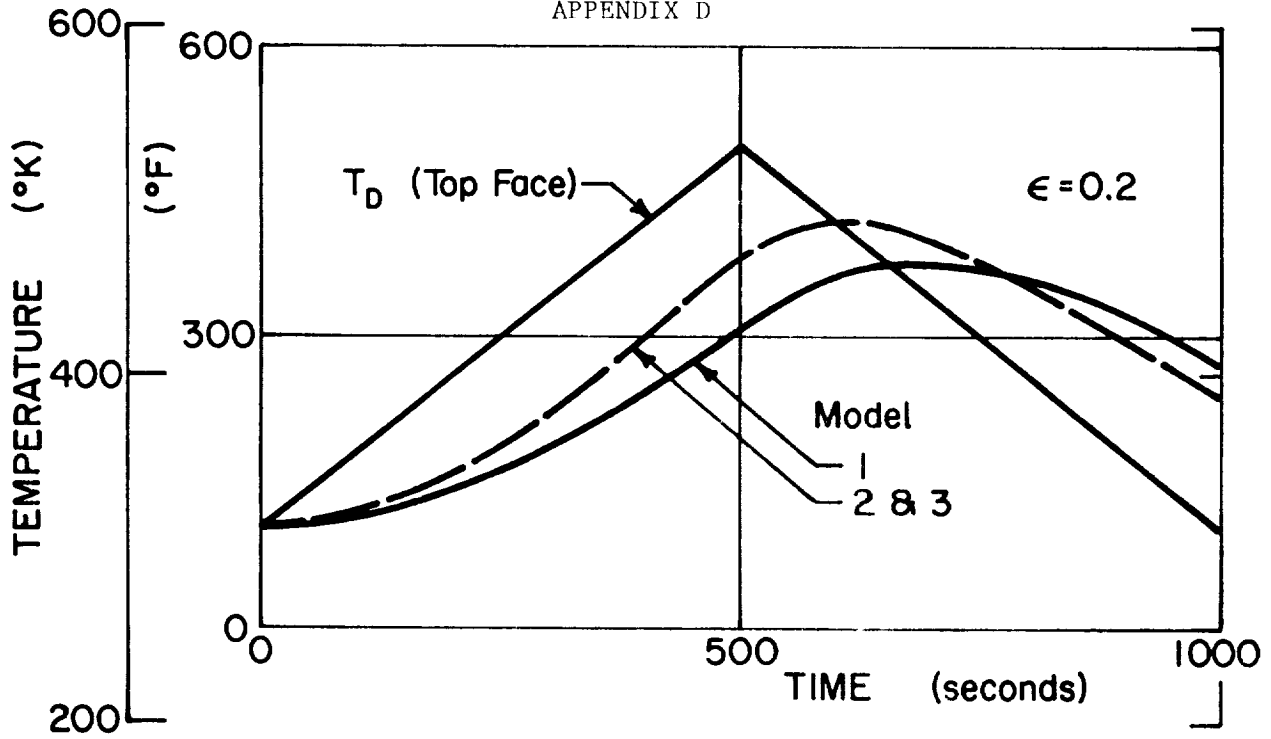


Figure 137.- Heat Transfer through Sandwich Structure, Triangular Pulse

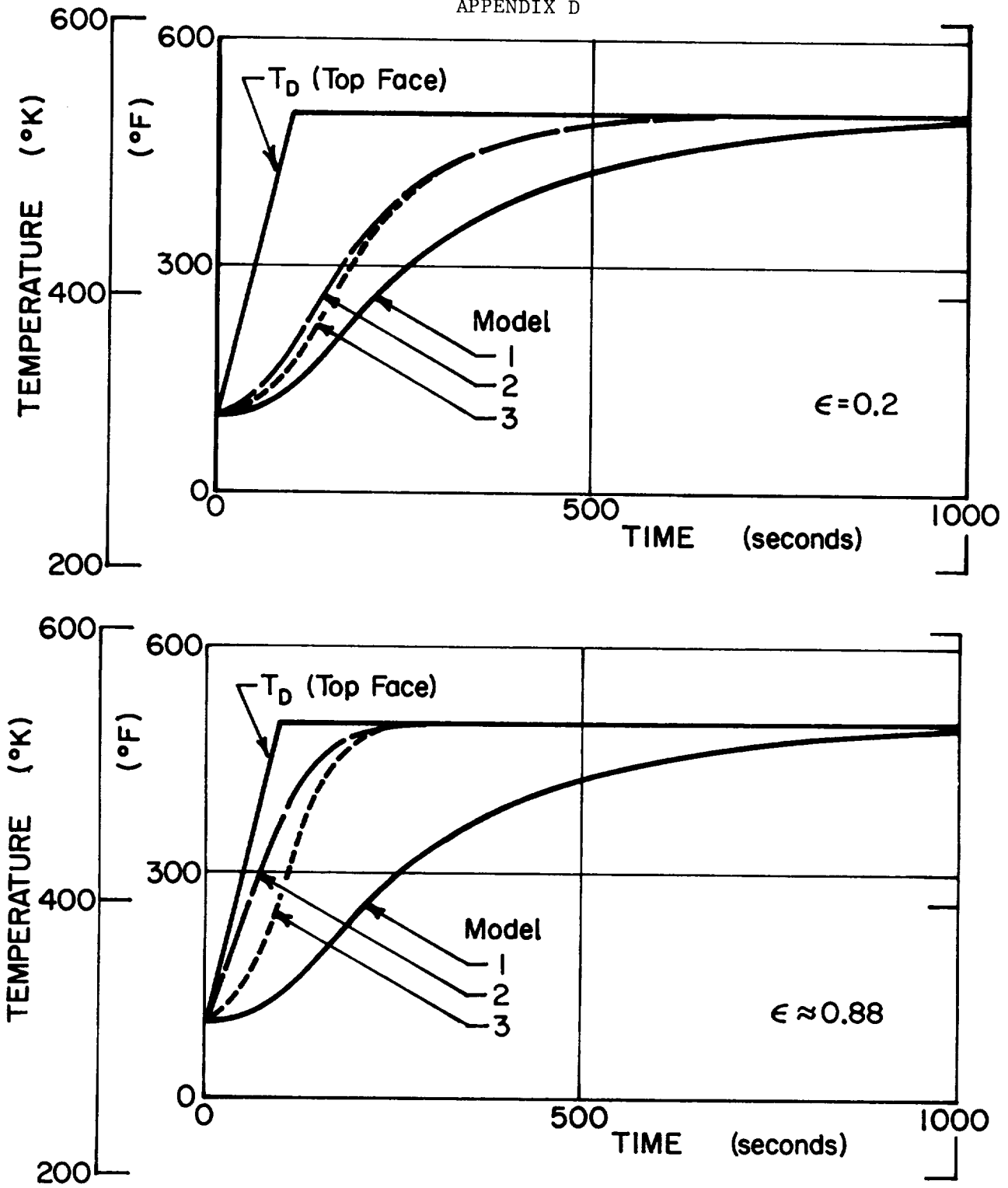


Figure 138.- Heat Transfer through Sandwich Structure, Ramp Pulse

## APPENDIX D

### B. Direct Attach Subpanel Primary Structure Interface

Attaching a TPS subpanel directly to the primary structure, rather than on standoff supports, presents a problem in defining the mode of heat transfer across the interface. Heat transfer will consist of both conductive and radiative modes of heat transfer, depending on the amount of contact between the faying surfaces. To evaluate this problem, a model was analyzed that considered the following percentages of conductive and/or radiative heat transfer:

Conduction, %	Radiation, %
0.00	100.00
0.01	99.99
0.10	99.90
1.0	99.0
50.0	50.0
100.0	0.0

Results of the analysis for high (0.9) emissivity interface surfaces are shown in figure 139. Subpanel and primary structure temperatures are essentially the same when 1% or more of the area is transferring heat by conduction. This is due to the high conductivity of the aluminum compared to the conductivity of the ablator material.

Figure 140 shows results for the same model with low (0.2) emissivity interface surfaces. If conductive heat transfer is considered, the temperatures are identical to those for the high emissivity surfaces. However, 100% radiation results in a much higher peak temperature in the subpanel.

Figure 140 also shows results for the same model with the addition of a 0.127-cm (0.050 in.) layer of foam insulation between the subpanel and primary structure. Heat transfer through the insulation assumed conduction between the insulation and two metallic elements. Although the insulated model shows an approximate 11°K (20°F) decrease in peak structure temperature from the 100% conduction case, a real application of this method would probably show a smaller decrease in peak structure temperature due to conduction through the fasteners and an increase in conductivity in the insulation due to compaction of the material. Considering the increase in weight, due to the insulation, the small decrease in the peak primary structure temperature does not warrant using this approach.

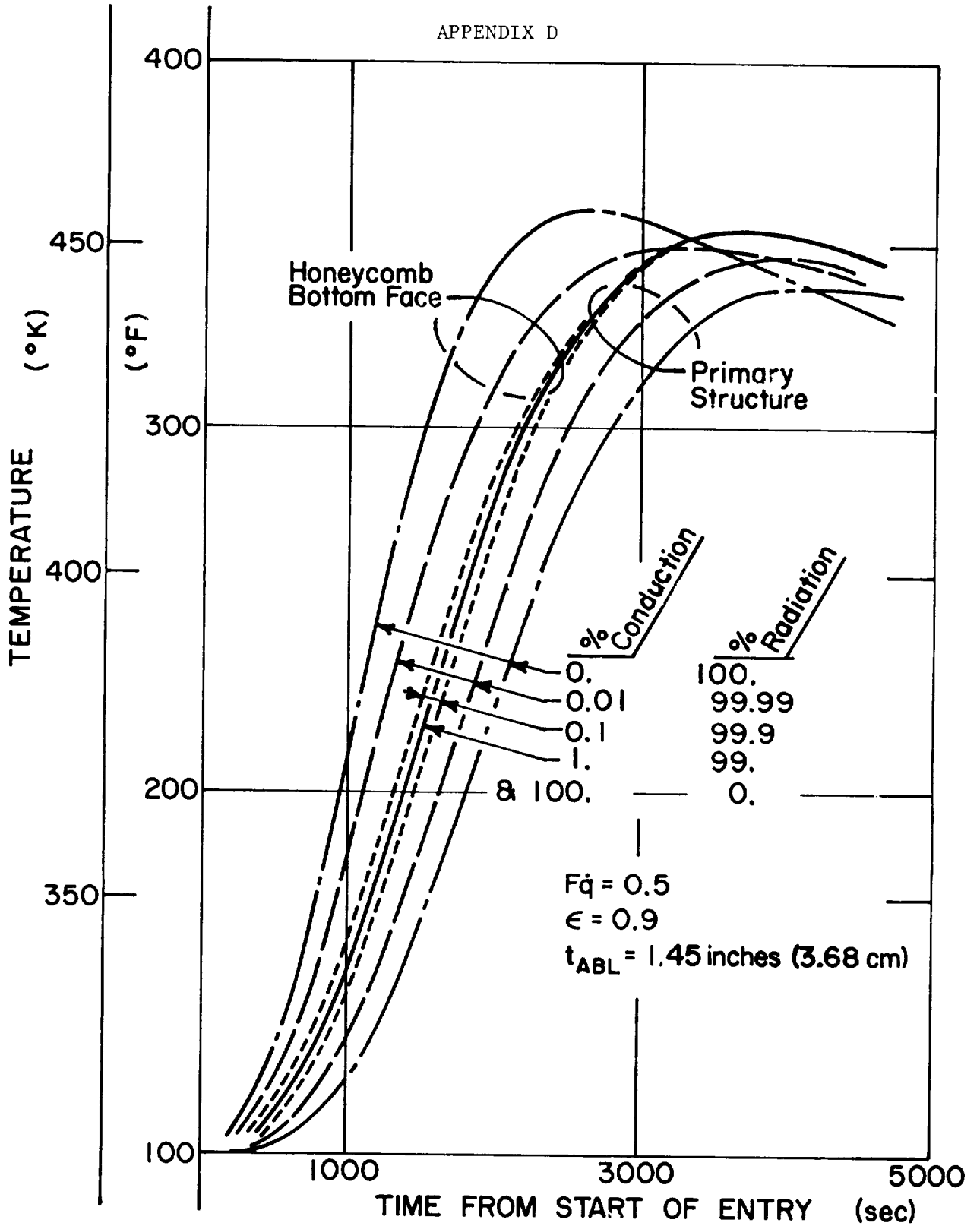


Figure 139.- Heat Transfer across Subpanel, Primary Structure Interface,  $\epsilon = 0.9$

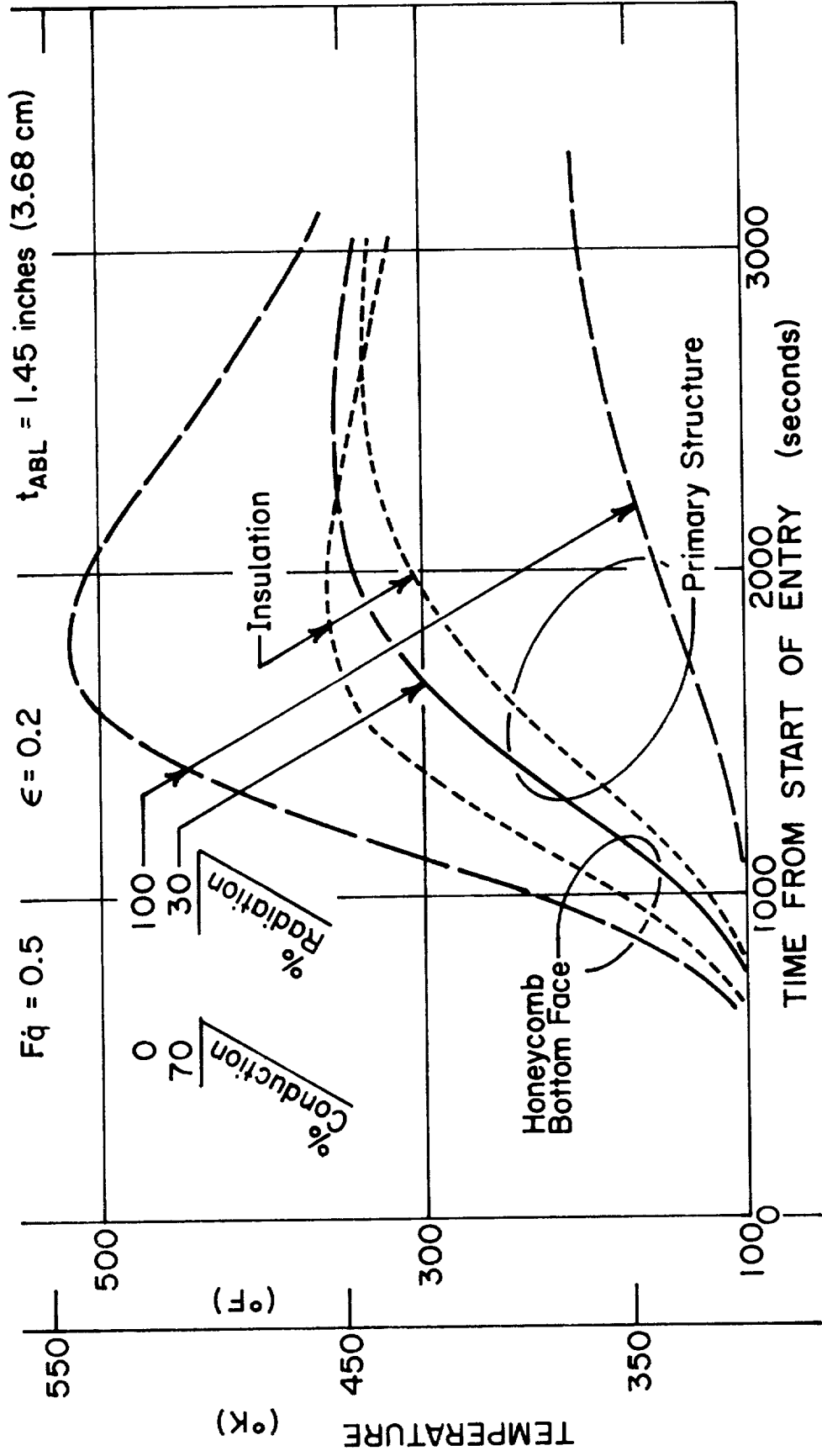


Figure 140.- Heat Transfer across Subpanel, Primary Structure Interface,  $\epsilon = 0.2$

## APPENDIX D

This analysis was conducted on relatively small [2.54x2.54 cm (1x1 in.)] two-dimensional models. A larger, three-dimensional model [12.7x12.7 cm (5x5 in.)] was also analyzed to simulate a large direct attach panel with fasteners on 25.4-cm (10 in.) centers. Heat transfer was by radiation except at one corner where the fastener provided a conduction path. The results, shown in figure 141 for a 6.4 cm<sup>2</sup> (1 in.<sup>2</sup>) conduction path (much larger than a real fastener), indicate that although the area of the conduction path was greater than the previously mentioned 1%, the temperature profiles in areas far from the conduction path are more like the 100% radiation case than the 100% conduction case. This is due to the increase in conduction length to the far corners as compared to the method of analysis for the small models.

Conclusions reached from these studies and their impact on subsequent analyses are:

- 1) Temperature distributions assuming intimate contact and 100% conduction across the interface will be used for sizing of ablator materials. Although the fasteners alone do not provide sufficient conduction paths to give results equivalent to the 100% conduction case, the small percentage of area of each square inch of panel necessary to be in intimate contact with the primary structure to give the 100% conduction results cannot be ignored.
- 2) Temperature distributions assuming 100% radiation across the interface will be used for subpanel design and to evaluate differential expansion between the panels and primary structure.
- 3) Interface surfaces should be treated to provide a high (0.9) emissivity. Treatment of surfaces in this manner would keep the temperature difference between subpanel and primary structure to a minimum and keep the subpanel peak temperatures as low as possible, should insufficient conduction paths exist.

### C. Thermal Control Coating (Entry Initial Temperatures)

A surface coating will be required on the SLA-561 ablative material for prelaunch environmental protection against water, fuel spills, etc. Since significant solar heating during the orbital phase of flight can occur, a thermal control coating was investigated to provide both the prelaunch protection and  $\alpha/\epsilon$  control during orbit.

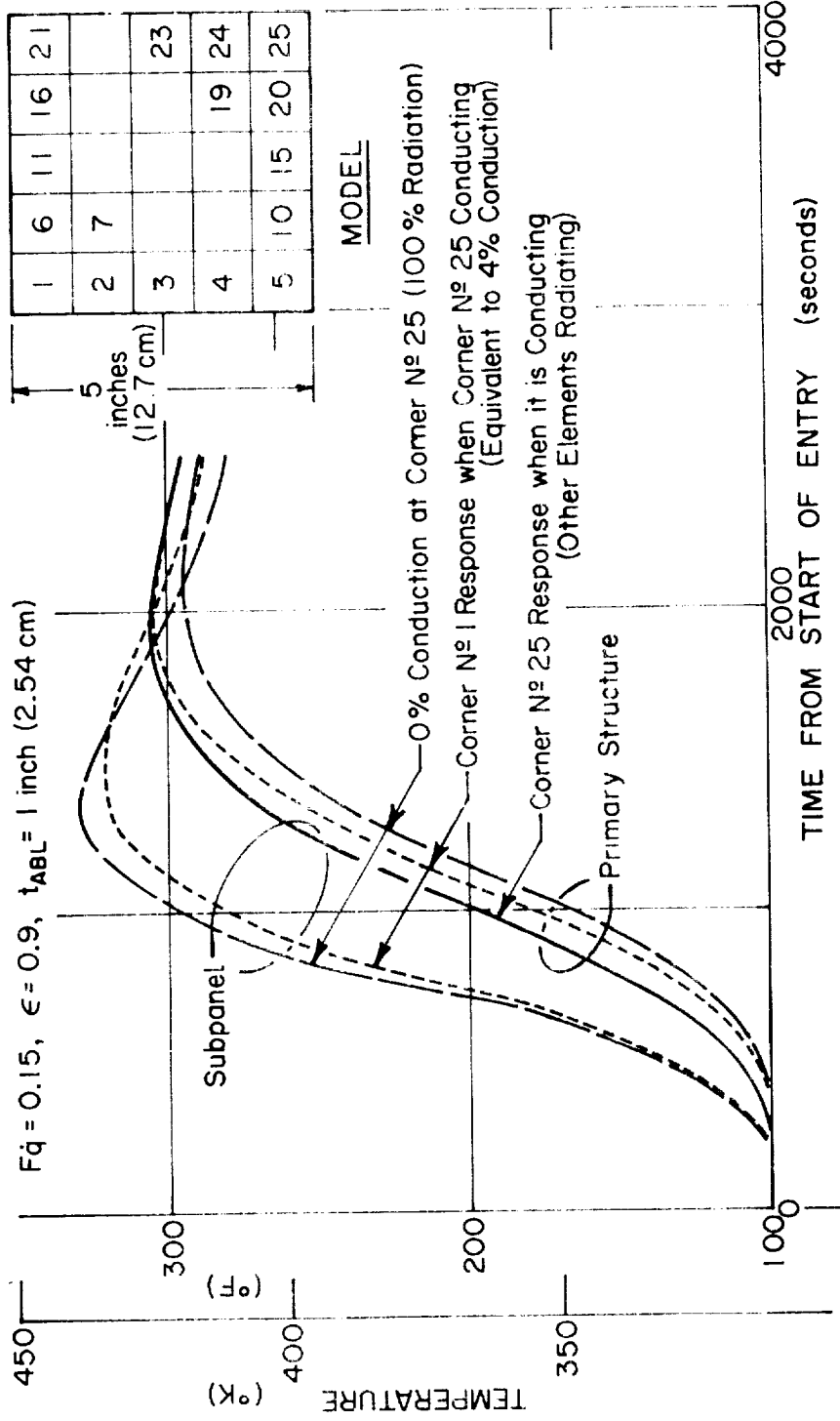


Figure 141. - Heat Transfer across Subpanel, Primary Structure Interface (Fastener Conduction Included)

## APPENDIX D

The thermal control coating considered was DC93-044, which is now used on the Titan III vehicles. The coating exhibits an  $\alpha/\epsilon$  characteristic of 0.23 to 0.31. Initial analysis assumed 0.127-cm (0.050 in.) coating on 3.8-cm (1.5 in.) SLA-561 ablator bonded directly to an adiabatic 0.259-cm (0.102 in.) aluminum structure. The model was analyzed for 100% and 400% of reference point ascent heating and subsequently exposed to the orbital solar flux for approximately 1 hour.

The criteria for the coating DC93-044 to survive ascent conditions was taken to be a 589°K (600°F) peak temperature at the SLA-561 ablator-DC93-044 interface so that the SLA-561 would not degrade appreciably beneath the coating. The coating thickness requirement to meet the above criteria versus local heating conditions ( $F\dot{q}$ ) for the nominal south ascent trajectory is shown in figure 142. Although the figure indicates areas where no coating is required, these areas will still have to be coated with some minimum thickness for prelaunch environmental protection from water absorption, fuel spills, etc. (For this sizing procedure, it was assumed that the  $F\dot{q}$  ( $\dot{q}/\dot{q}_{ref}$ ) distribution is equivalent to the  $Q/Q_{ref}$  distribution for ascent.)

Results, shown in figures 143 and 144, illustrate that, without thermal control coating, ablator surface temperatures at the start of entry would be approximately 400°K (260°F) and structure temperatures would be 344°K (160°F). With the coating, temperatures throughout the ablator and structure are approximately 311°K (100°F) to 316°K (100°F). This reduction in temperature for start of entry represents a considerable savings in ablator weight since TPS sizing is significantly affected by initial temperature.

This analysis assumes the existence of the thermal control coating after exposure to the ascent heating pulse and is therefore restricted to relatively low heating areas. Analyses of the nose cap and leading edge areas show that a relatively thin, 127 cm (0.05 in.), thermal control coating will be removed during ascent. No thermal control protection would be provided during orbit. Analyses showed that the DC93-044 coating in these areas would have to be very thick, approximately 2.03 cm (0.8 in.), (fig. 145) to keep the ablator temperatures beneath the coating low enough, 589°K (600°F), to preclude ablation and loss of the coating. If the coating is stripped off during ascent, an  $\alpha/\epsilon = 1.0$  surface will be exposed to solar flux and temperature responses shown in figure 146 could be expected. The model analyzed considered the surface receiving full solar flux, radiating to infinity, 0°K (-460°F), and radiating off the backface to a 311°K (100°F) heat sink.

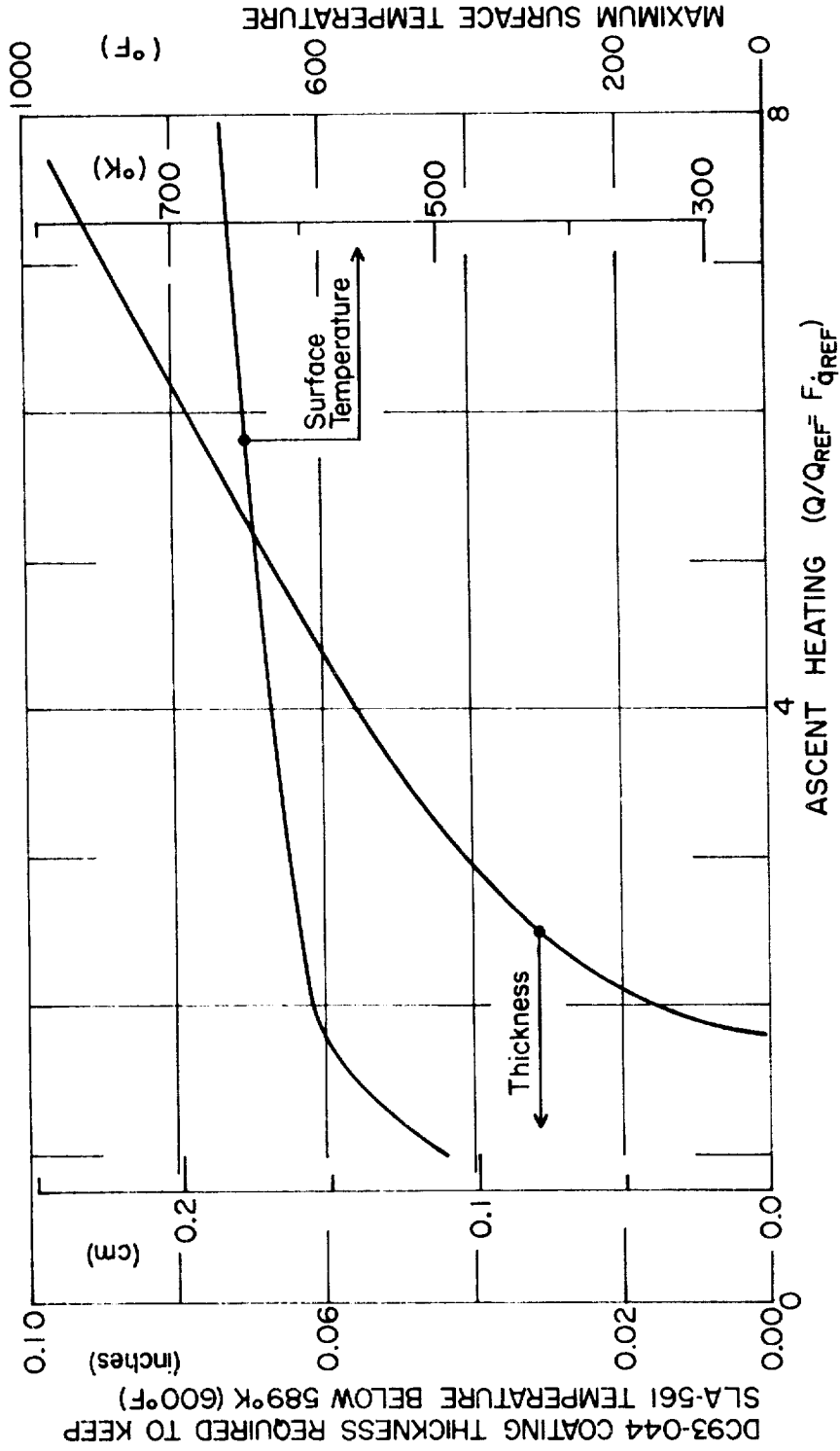


Figure 142.- Coating Requirements in Ascent Areas

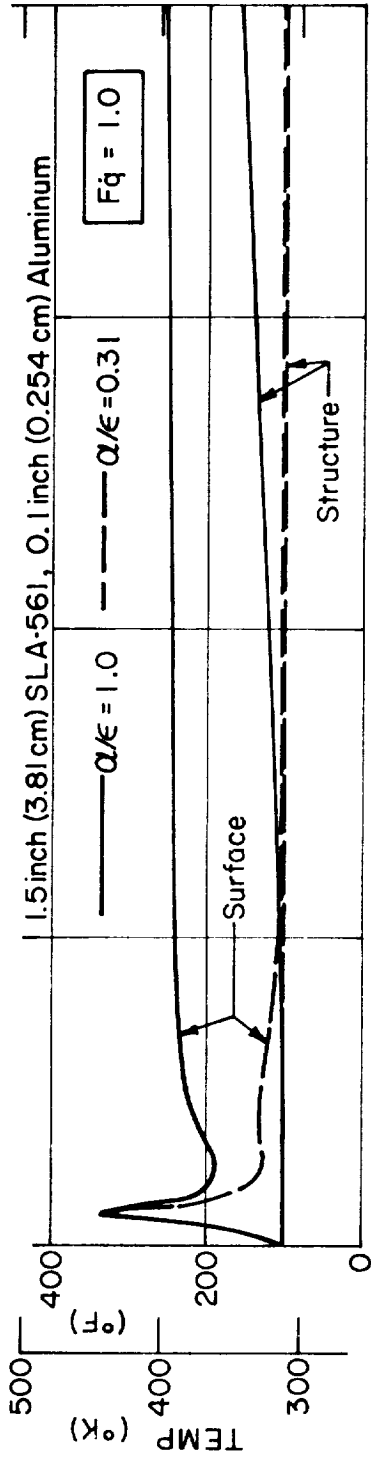


Figure 143.- Ascent and Orbit Heating Surface and Structural Temperatures,  $F\dot{q} = 1.0$

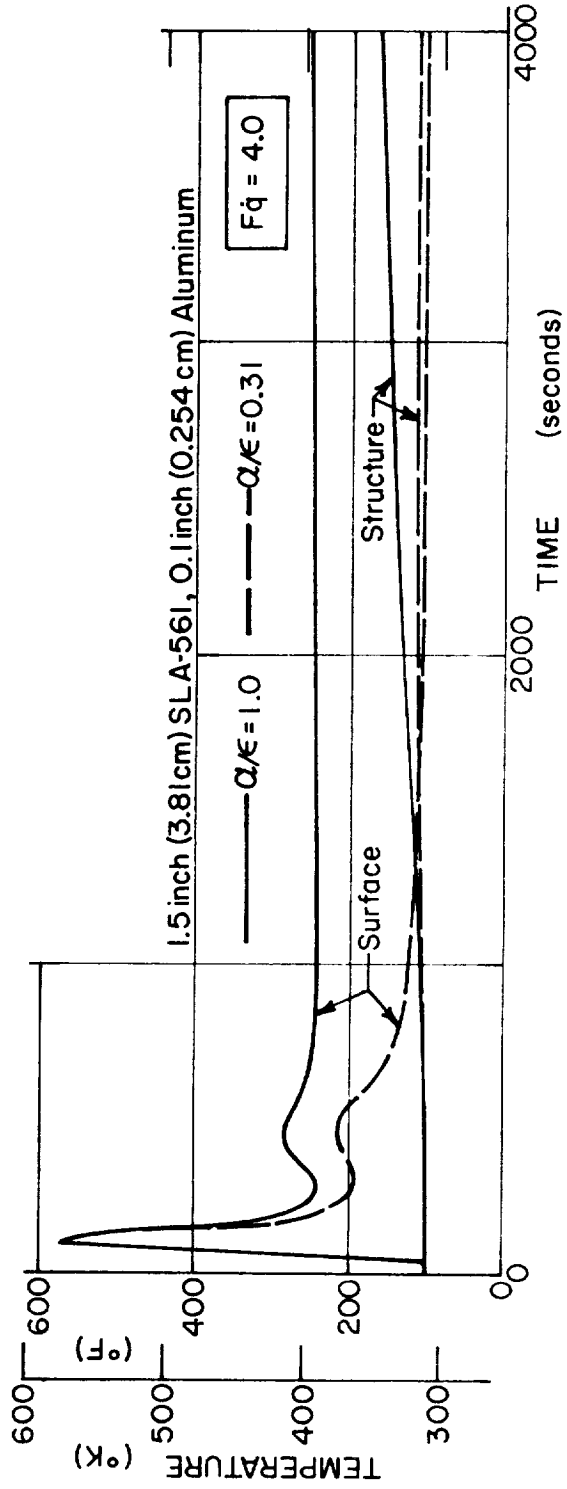


Figure 144.- Ascent and Orbit Heating Surface and Structural Temperatures,  $F\dot{q} = 4.0$

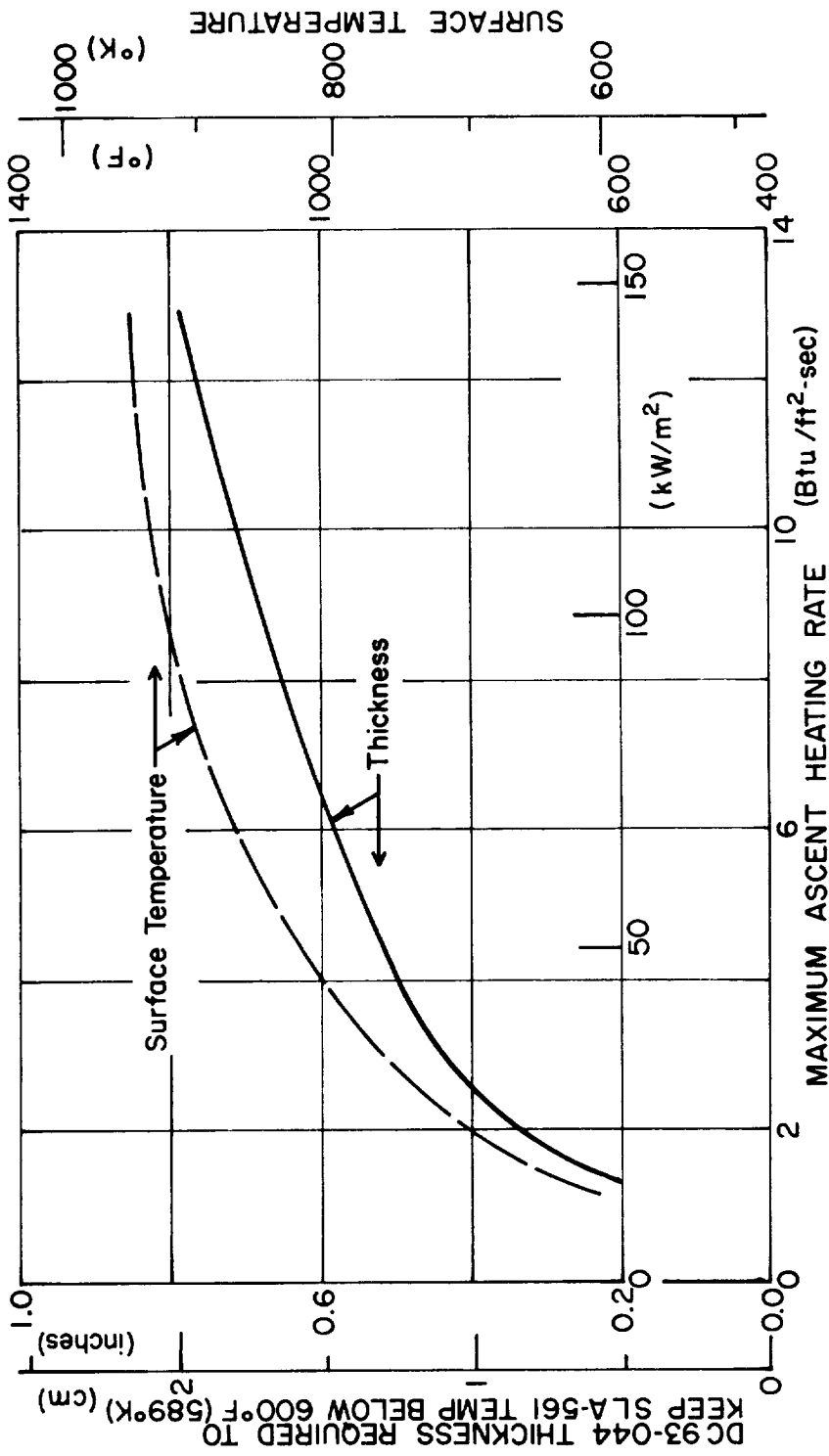


Figure 145.- Thermal Control Coating Requirements in Nose Cap and Leading Edge Areas

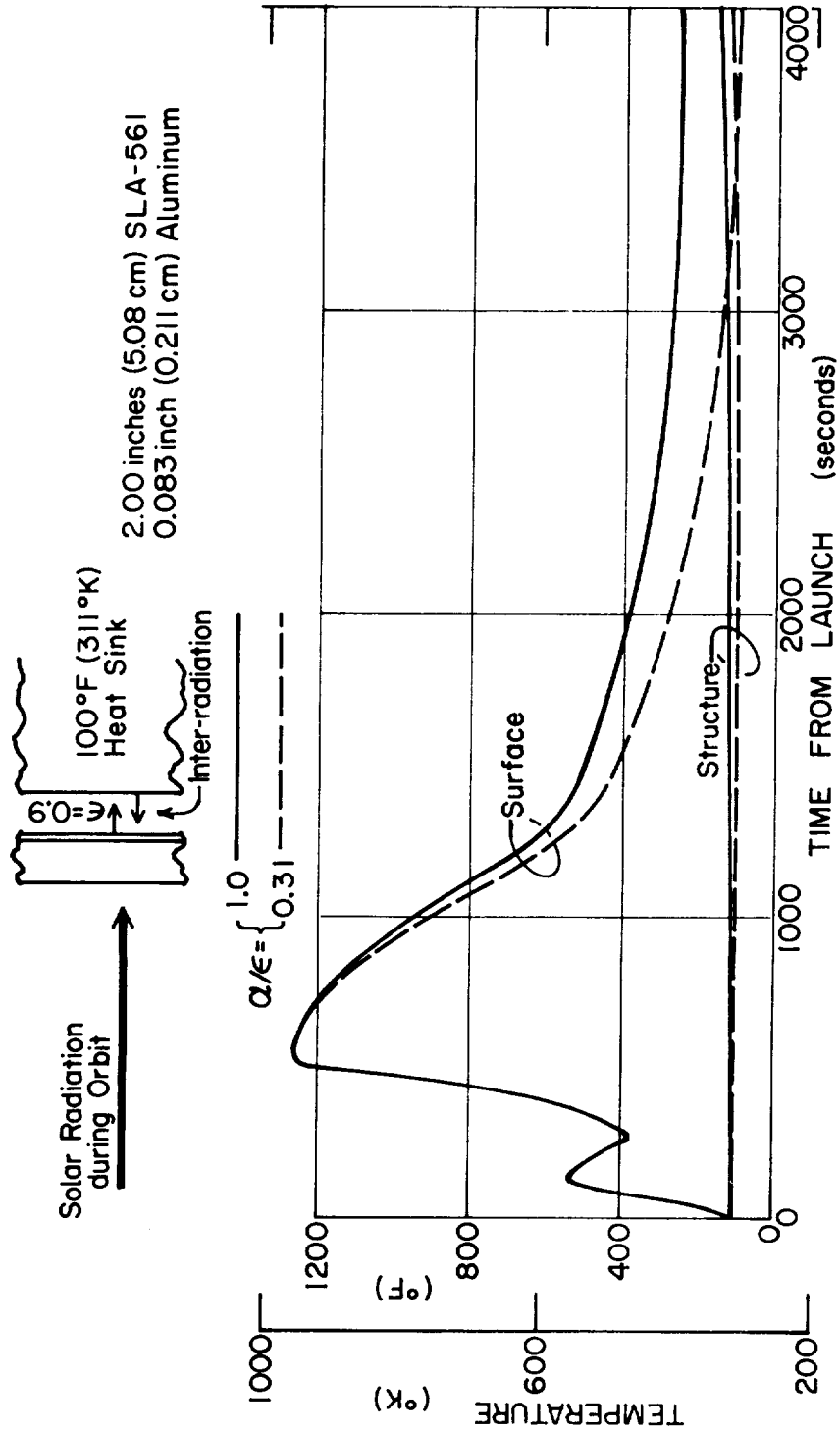


Figure 146.- Nose Stagnation Point Ascent and Orbit Heating Surface and Structural Temperatures

## APPENDIX D

The figure indicates that, for a once-around case, an  $\alpha/\epsilon = 1.0$  material will have a surface temperature of approximately 400°K (260°F) and a backface temperature of approximately 339°K (150°F). An  $\alpha/\epsilon = 1.0$  material exhibited a surface temperature of 399°K (258°F) and a backface temperature of 326°K (128°F). The  $\alpha/\epsilon = 0.31$  material reached a uniform temperature of approximately 311°K (100°F).

A similar model, considering only an adiabatic backface, was also analyzed through ascent and full solar flux orbit conditions. The  $\alpha/\epsilon = 1.0$  material showed a backface temperature of 366°K (200°F) after one orbit and 400°K (260°F) at equilibrium. The  $\alpha/\epsilon = 0.31$  material had a predicted backface temperature of 337°K (147°F) after one orbit and approximately 311°K (100°F) at equilibrium.

Since increasing the backface temperature for start of entry or applying a very thick thermal control coating both represent weight penalties, an estimation of weight differences was made for three possible cases at start of entry:

- 1) Use a minimal [0.127 cm, (0.050 in.)] coating for pre-launch protection, allow the coating to burn off during ascent, start entry with the skin at 366°K (200°F), and allow for greater ablator thicknesses;
- 2) Use a minimal coating as a Case 1, and start entry at 339°K (150°F);
- 3) Use sufficient coating to meet the 589°K (600°F) interface criterion and start entry with skin at 311°K (100°F).

Figure 147 shows results of these tradeoff calculations for Cases 1 and 2 normalized to Case 3. The figure indicates that the coating represents a weight penalty in the nose cap area due to its high density and thickness requirement. The points where Case 3 becomes the lowest weight design are where ascent conditions have decreased so that less than approximately 0.254 cm (0.10 in.) coating is required.

Conclusions reached from these studies are:

- 1) Thermal control coating thickness of 0.127 cm (0.050 in.) will be established by prelaunch environmental protection requirements;
- 2) Entry initial temperatures of 311°K (100°F) will be used in low heating areas where coating is not removed by ascent heating;
- 3) Thermal analyses will include ascent-orbit-entry heating environments in areas where the 0.127-cm (0.05 in.) DC93-044 coating is removed during ascent.

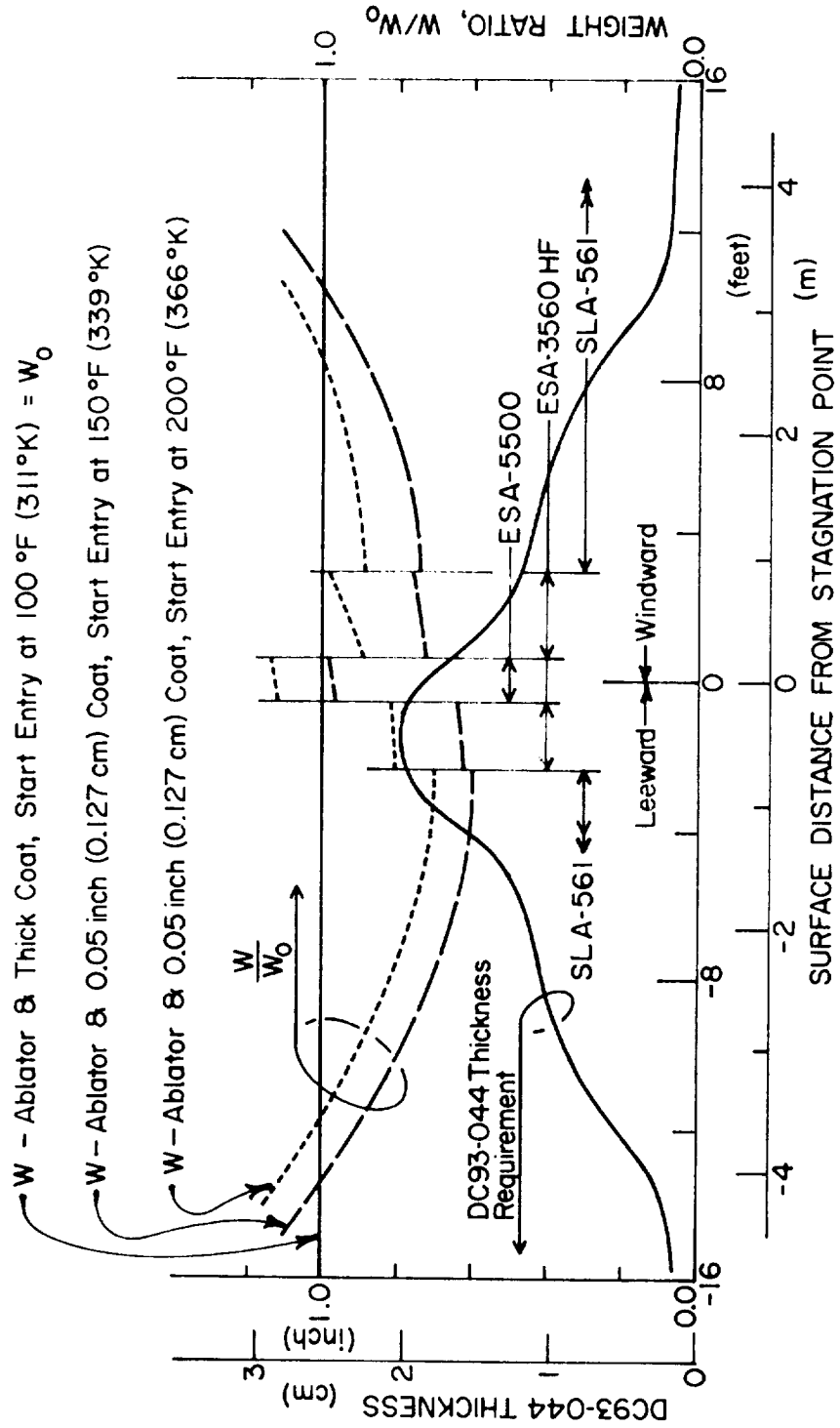


Figure 147.- Weight of TPS in Nose Cap Area

## APPENDIX D

### D. Backup Structure Heat Capacity

A simplifying approach to developing design curves for the direct attach subpanels was used in this study. The approach is based on the backup structure heat capacity, which is

$$\text{Heat Capacity} = (\rho t)C_p + \rho C_p t + \rho C_p t^2$$

where:  $t$  = thickness, cm (in.)

$\rho$  = density, gm/cm<sup>3</sup> (lb/in.<sup>3</sup>)

$C_p$  = specific heat J/kg-°K (Btu/lb-°F)

Several different direct attach subpanel configurations were analyzed for a particular point. The SLA-561 ablator thickness requirements, based on a 450°K (350°F) peak primary structure temperature, were plotted against the heat capacity of the backup structure. Figure 148 shows results of this approach for the reference point  $Q/Q_{ref} = F\dot{q} = 1.0 \times SF$  and illustrates that design curves may be generated with essentially a two point curve. Curves of this type resulted in considerable computational time savings in optimizing subpanel sizes and in generating thickness design curves. Good estimates of ablator requirements can be made for changes in subpanel thicknesses without running through the entire sizing procedure for each variation.

The critical assumptions in this heat capacity approach are the 100% conduction mode of heat transfer from the subpanel to the primary structure and that the conductivity of the subpanel material is relatively large compared to that of the SLA-561.

Estimates of ablator requirements for standoff panels cannot be made from these curves and similar curves are not available for standoff panels. The additional variables of insulation/no insulation and various allowable temperatures for the subpanels (various materials) preclude a simplifying approach such as this. Each standoff panel configuration requires individual analysis.

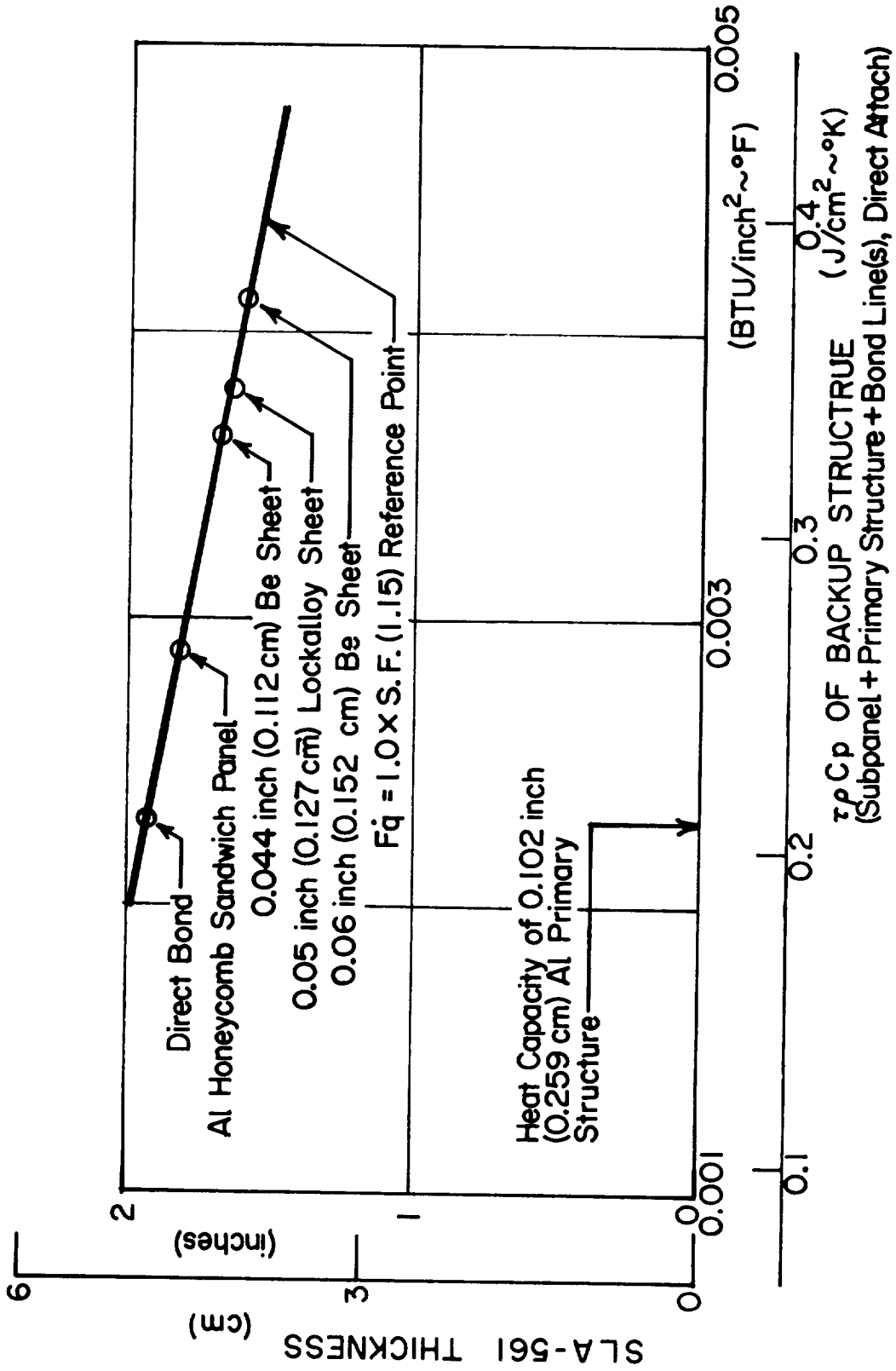


Figure 148.- Backup Structure Heat Capacity vs Ablator Requirement

## APPENDIX E

### VERIFICATION TESTING

#### A. Open-Gap Panel

1. Test plan.- The primary objective of this test was to determine the feasibility of a self-closing gap concept using the ablative materials of the Space Shuttle.

Secondary objectives were to evaluate the stud-bolt concept, which permits subpanel plate motion relative to the supporting structure, and the local temperature distribution in the ablator in the region of the counterbore for the stud bolt.

Approach: One composite panel was tested. The composite panel consisted of two subpanels and a primary structure plate (fig. 149). Each subpanel was composed of a 55.88x55.88x4.39 cm (22x22x1.73 in.) ablator bonded to a similar sized 0.102-cm (0.040 in.) thick aluminum sheet. The subpanels were mounted mechanically on a stiffened 0.254-cm (0.100 in.) thick aluminum sheet, which simulated the primary structure.

The gap between the two subpanels was sized to evaluate the concept of a self-closing gap sealing when exposed to thermal loads.

Thermal loading was applied with radiant heat lamps. Measurement of gap deformation was made electrically by impingement of protruding pins onto a plate conductor. Heat transfer to the primary structure plate was monitored with thermocouples. Deformations in the aluminum subpanel plate due to constraint from the stud bolt and thermal expansion were monitored with strain gages.

Additional thermocouples were used to monitor heat transfer in a subplate bolt-down cavity and to monitor heat transfer to the aluminum support channel.

SLA-561 ablator was used in this test program. These tests were intended to permit correlation with analyses and projection to similar induced Shuttle conditions and other locations on the Orbiter.

APPENDIX E

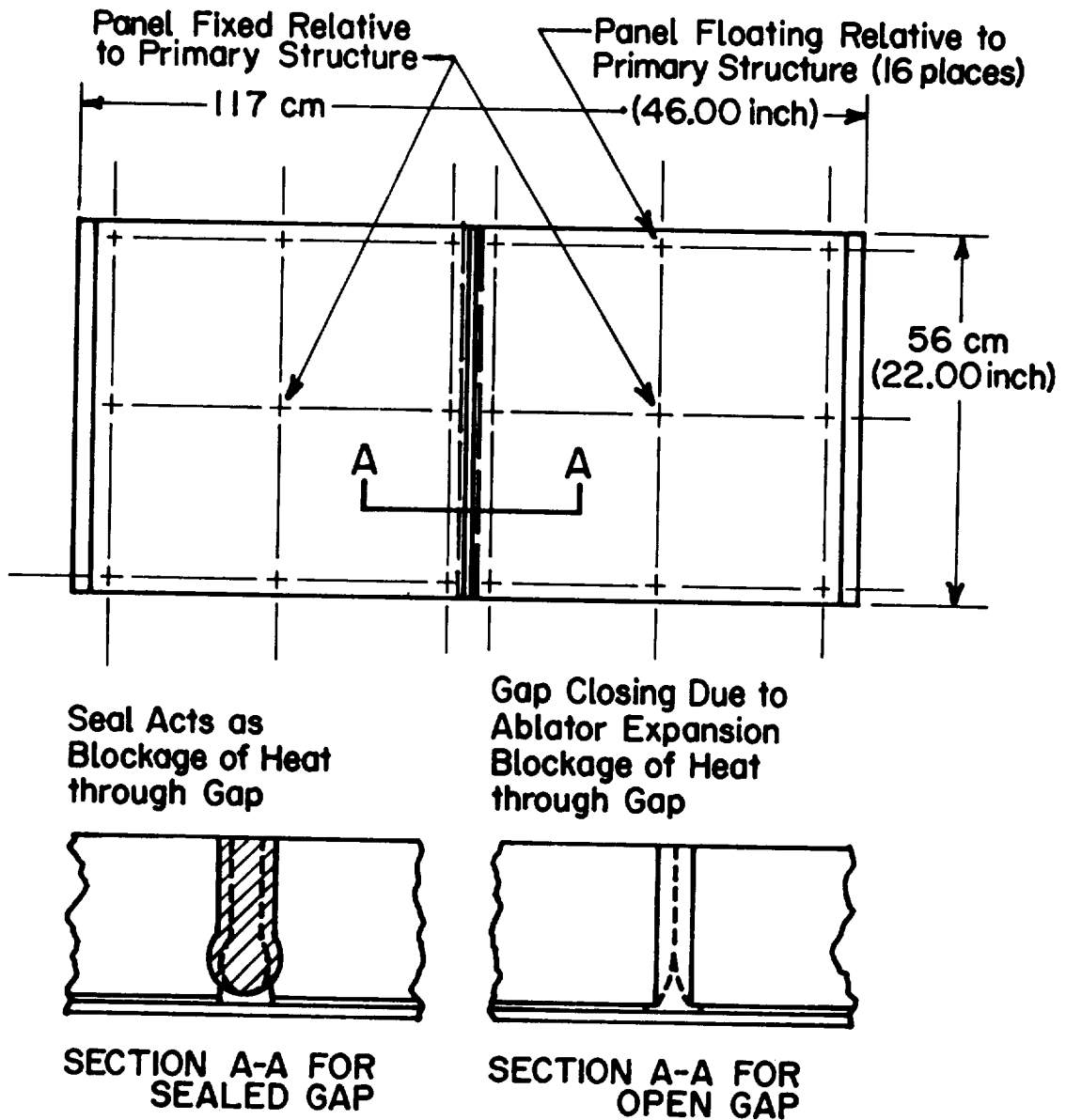


Figure 149.- Test Panel

## APPENDIX E

Test facility: The test facility used was the Structures Laboratory at the Denver Division of Martin Marietta.

Material and specimens: The SLA-561 test specimen is a composite elastomeric-type material supported in a honeycomb structure. The nominal density of the material is  $240 \text{ kg/m}^3$  ( $15 \text{ lb/ft}^3$ ). Details of the test panel construction are shown in figure 88.

Instrumentation: Instrumentation details are shown in figure 88. The subpanels contained the following instrumentation:

- 1) Eight strain gages;
- 2) 28 thermocouples;
- 3) 16 gap-measurement pins and four electrically conducting plates.

One subpanel was instrumented with an additional two thermocouples--one in a bolt-down cavity and the other close to the cavity.

Each primary structure aluminum plate was instrumented with nine thermocouples with maximum temperature capability of  $589^\circ\text{K}$  ( $600^\circ\text{F}$ ).

One aluminum channel of the composite panel was instrumented with two thermocouples.

The strain gage data were used together with the thermocouple data to monitor any restraining effect of the "floating" attachments that would adversely affect the gap deformations. The thermocouples on the rear primary panel surface determined the temperature variation between the ablator protected area and the gap area.

Deformations at the gap were monitored with the electrically conducting pins and conductor plates. The redundant set of measurements permitted the determination of any asymmetry in the panel deformations.

Test: Before the composite panel was tested, calibration tests were performed to verify the uniformity of heating across the area covered by the test panels.

APPENDIX E

One composite test panel was installed in the test fixture. Ambient temperature was noted. Power was applied to the quartz-lamp bank to give the desired thermal loading (fig. 91) at the outer surface of the ablator. Sixty-two measurements were recorded continuously throughout the test. These were:

- 1) Power input to the quartz-lamp bank;
- 2) 41 thermocouple measurements;
- 3) Eight strain gage measurements;
- 4) 12 gap impingement measurements.

2. Test results.- Temperature data at various points of the open-gap test panel are presented in figures 150 through 161. The thermocouple locations are shown in figure 88. If no data are given for a particular thermocouple, this indicates that the thermocouple was inoperative during the test.

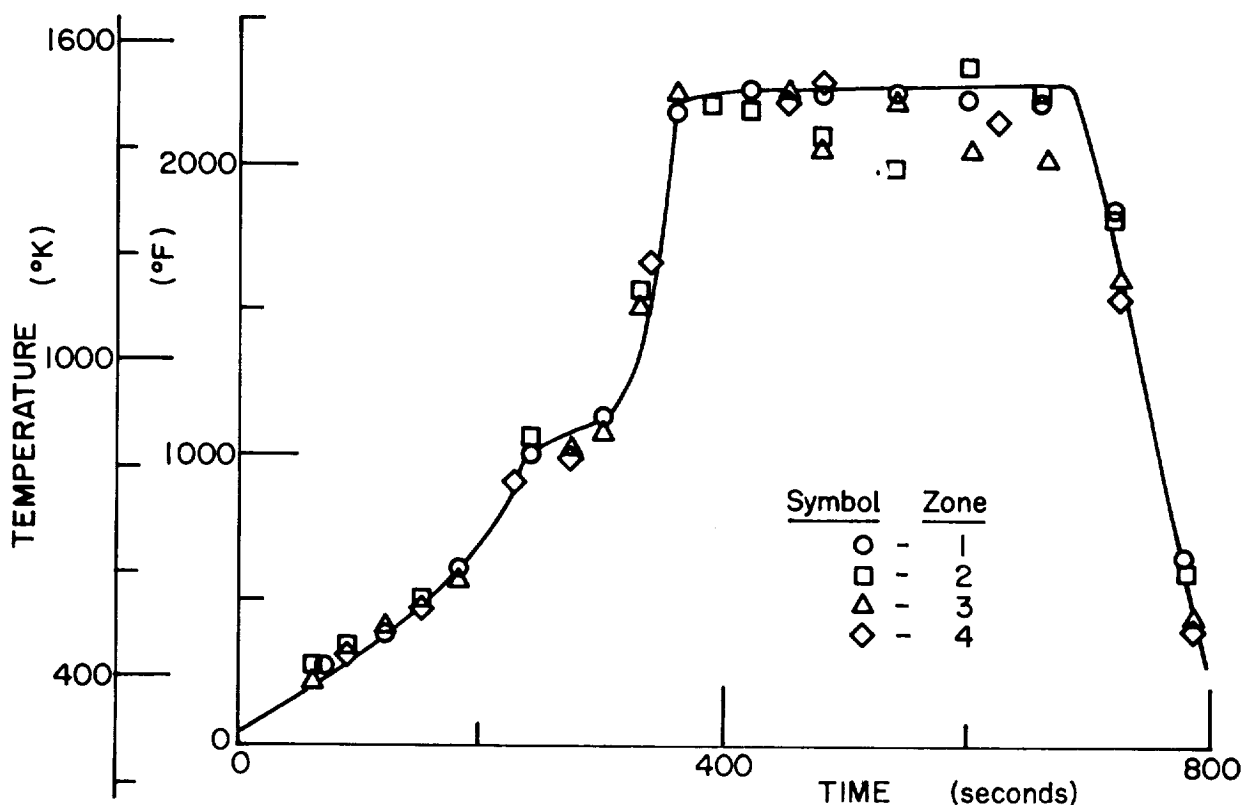


Figure 150.- Surface Thermocouple Measurements

APPENDIX E

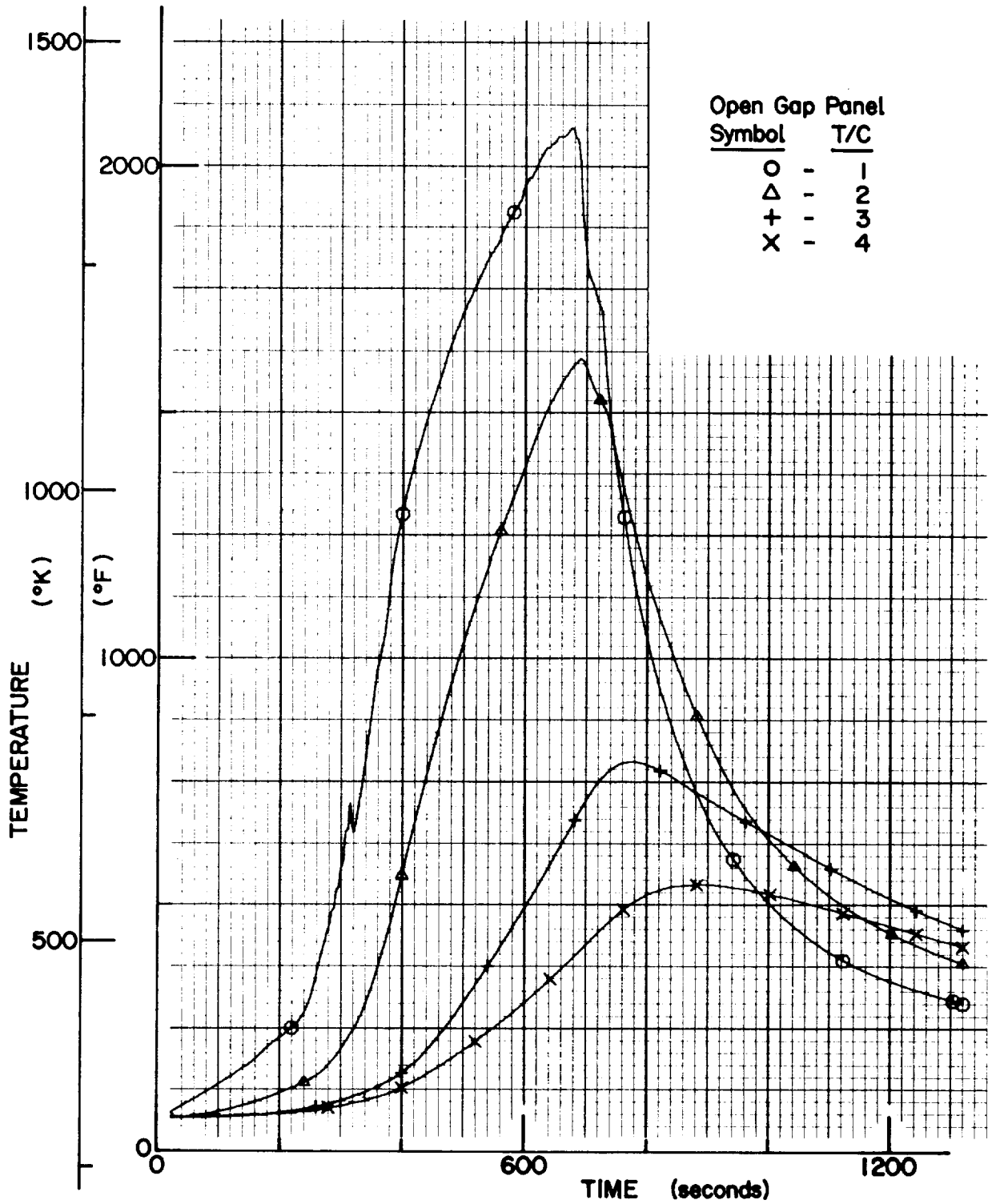


Figure 151.- Thermocouple Measurements (T/C 1, 2, 3, and 4)

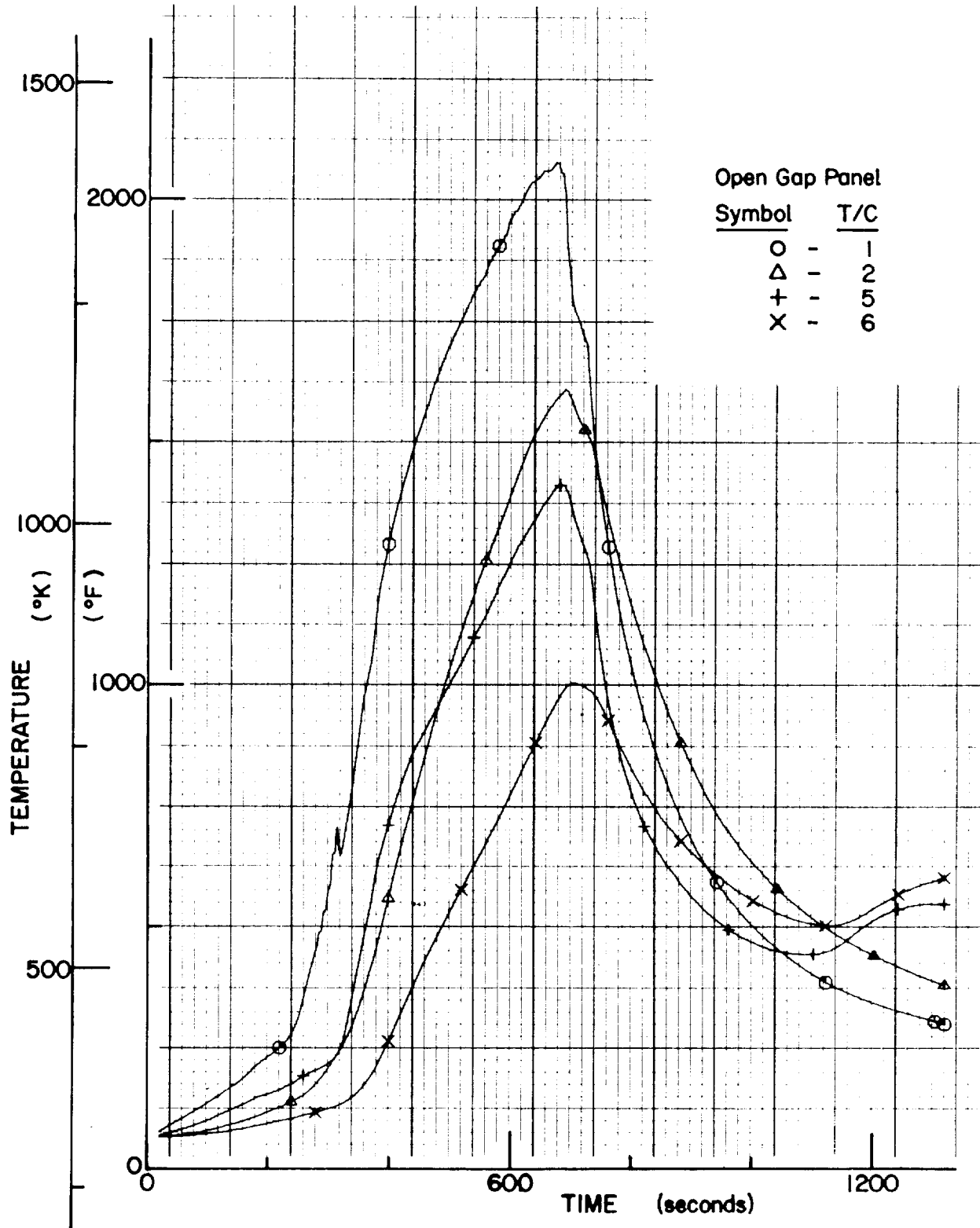


Figure 152.- Thermocouple Measurements (T/C 1, 2, 5, and 6)

APPENDIX E

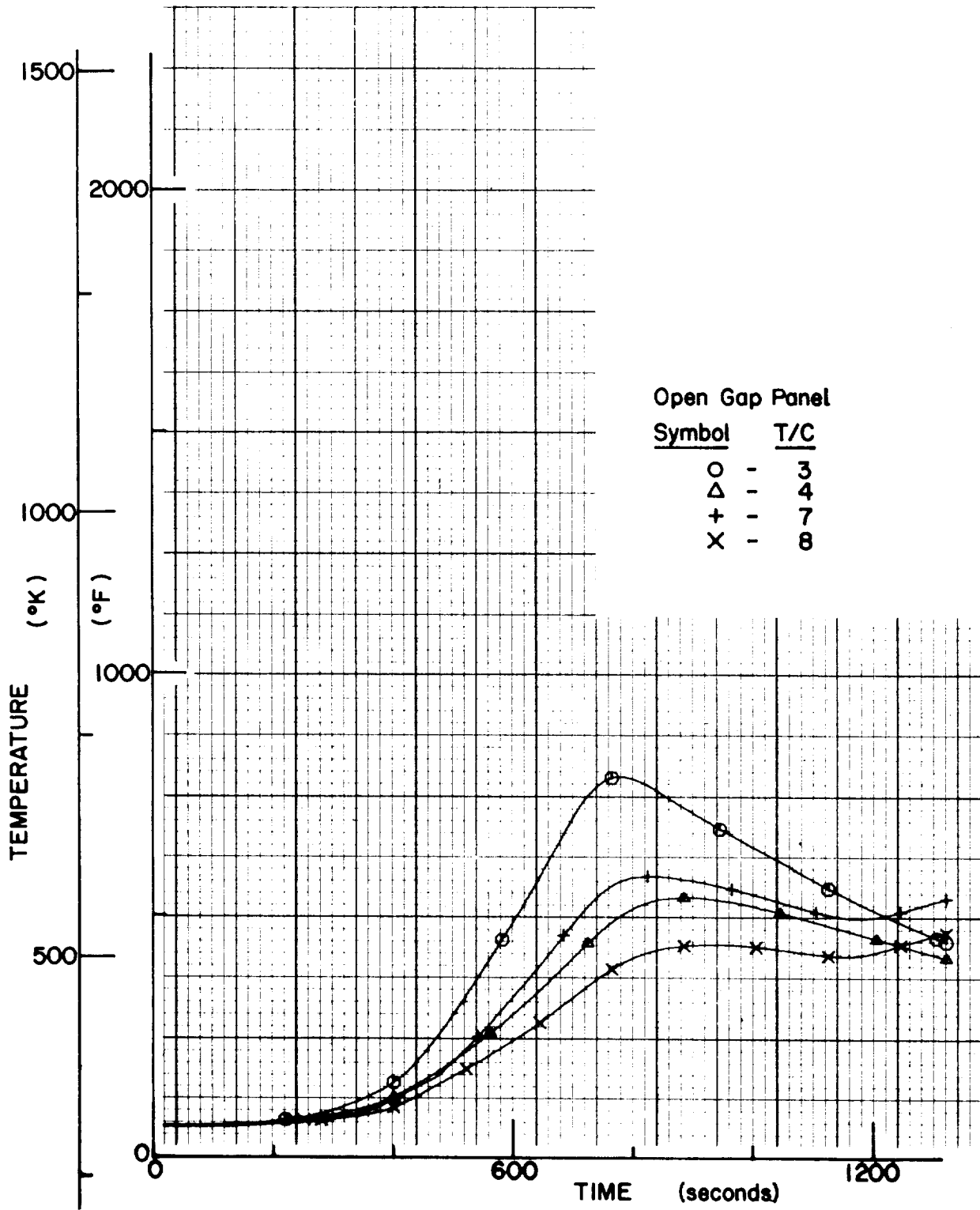


Figure 153.- Thermocouple Measurements (T/C 3, 4, 7, and 8)

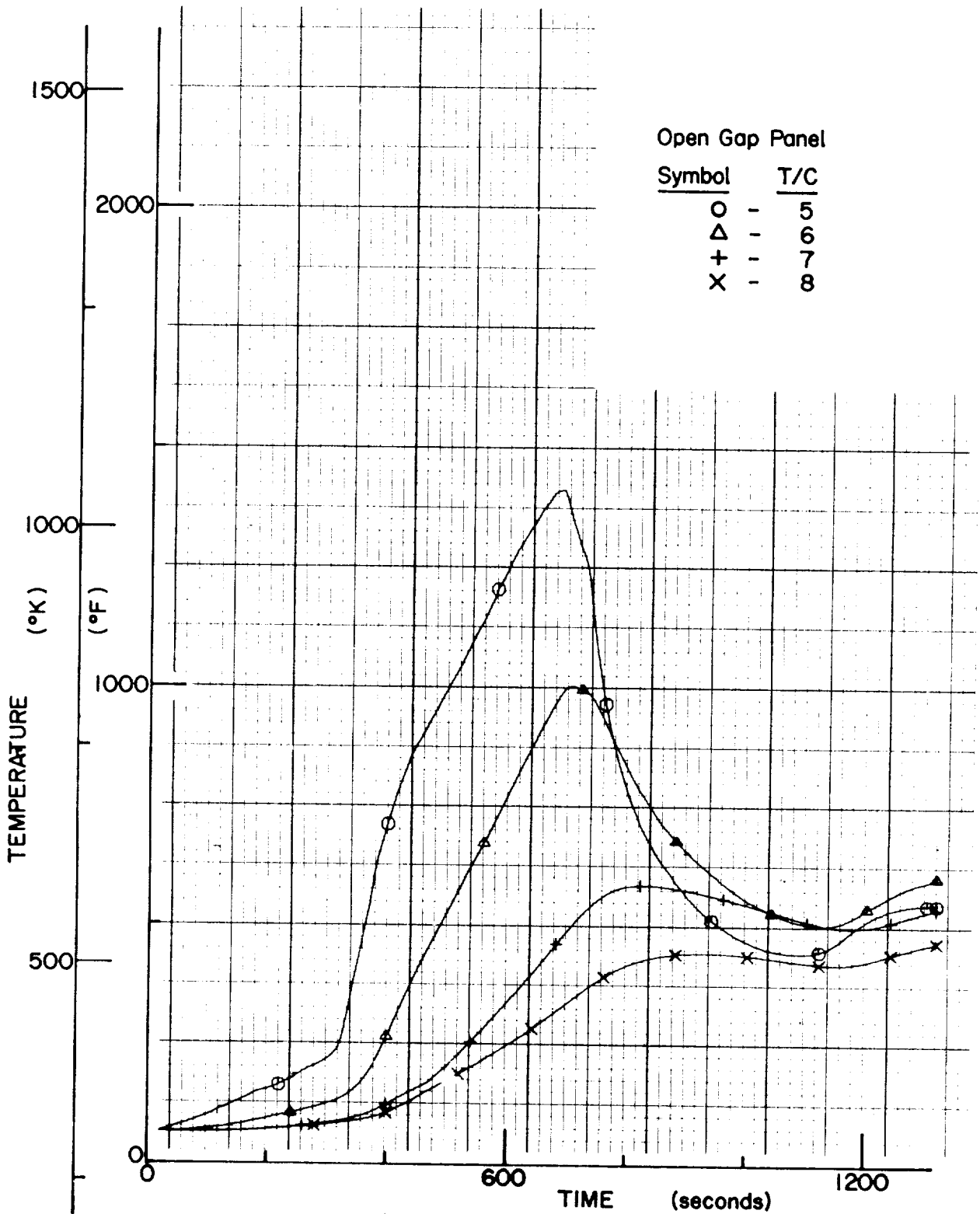


Figure 154.- Thermocouple Measurements (T/C 5, 6, 7, and 8)

APPENDIX E

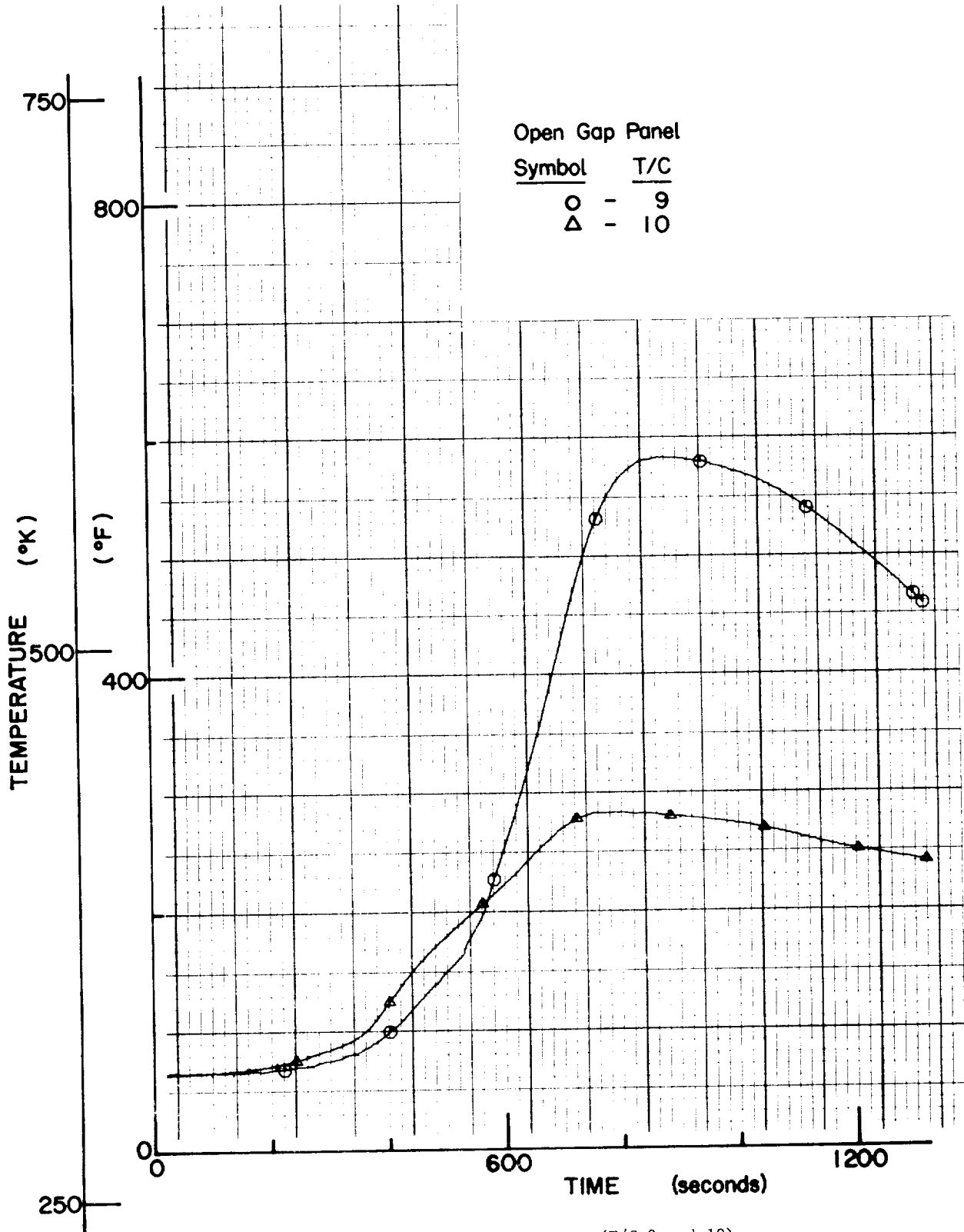


Figure 155.- Thermocouple Measurements (T/C 9 and 10)

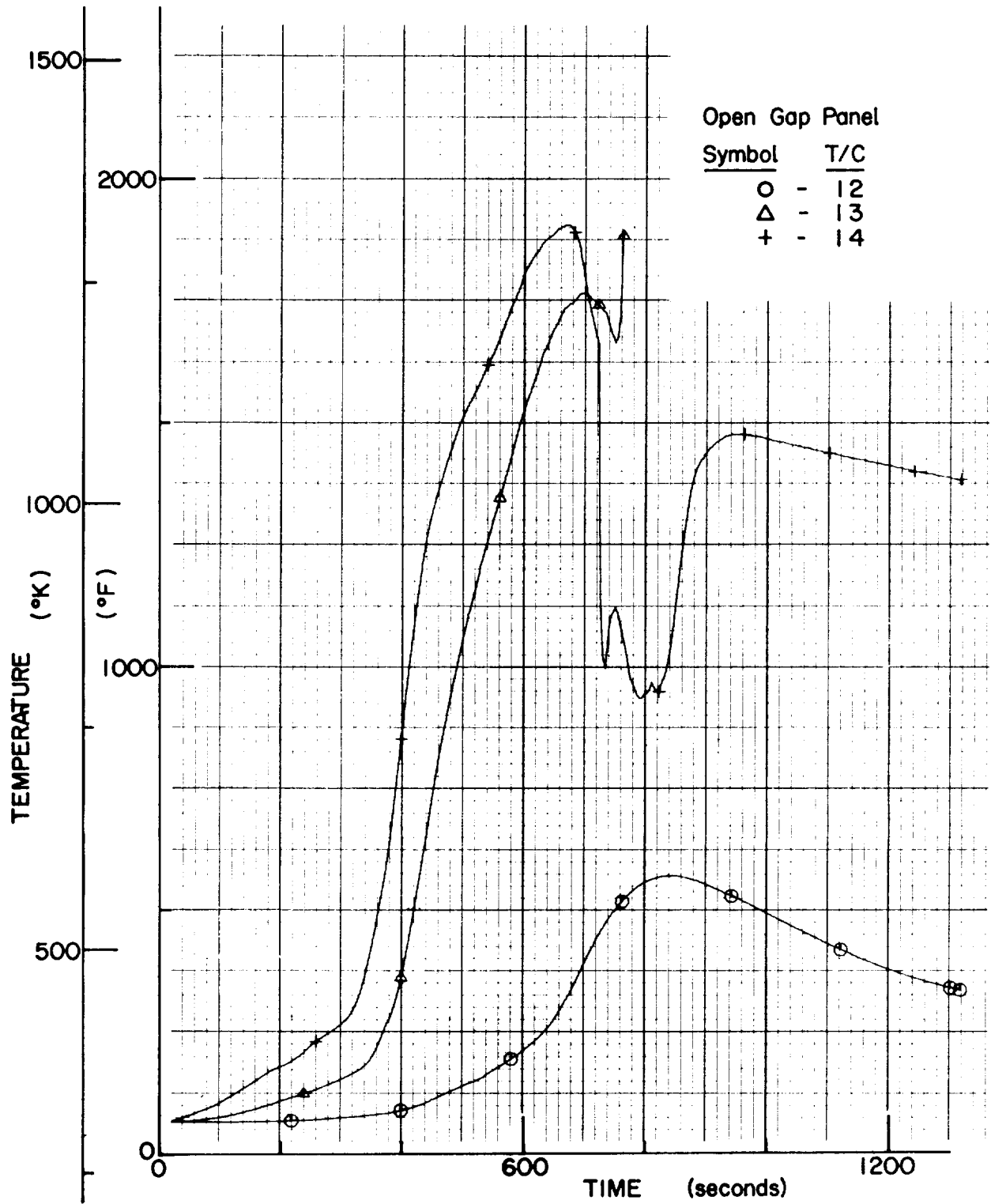


Figure 156.- Thermocouple Measurements (T/C 12, 13, and 14)

APPENDIX E

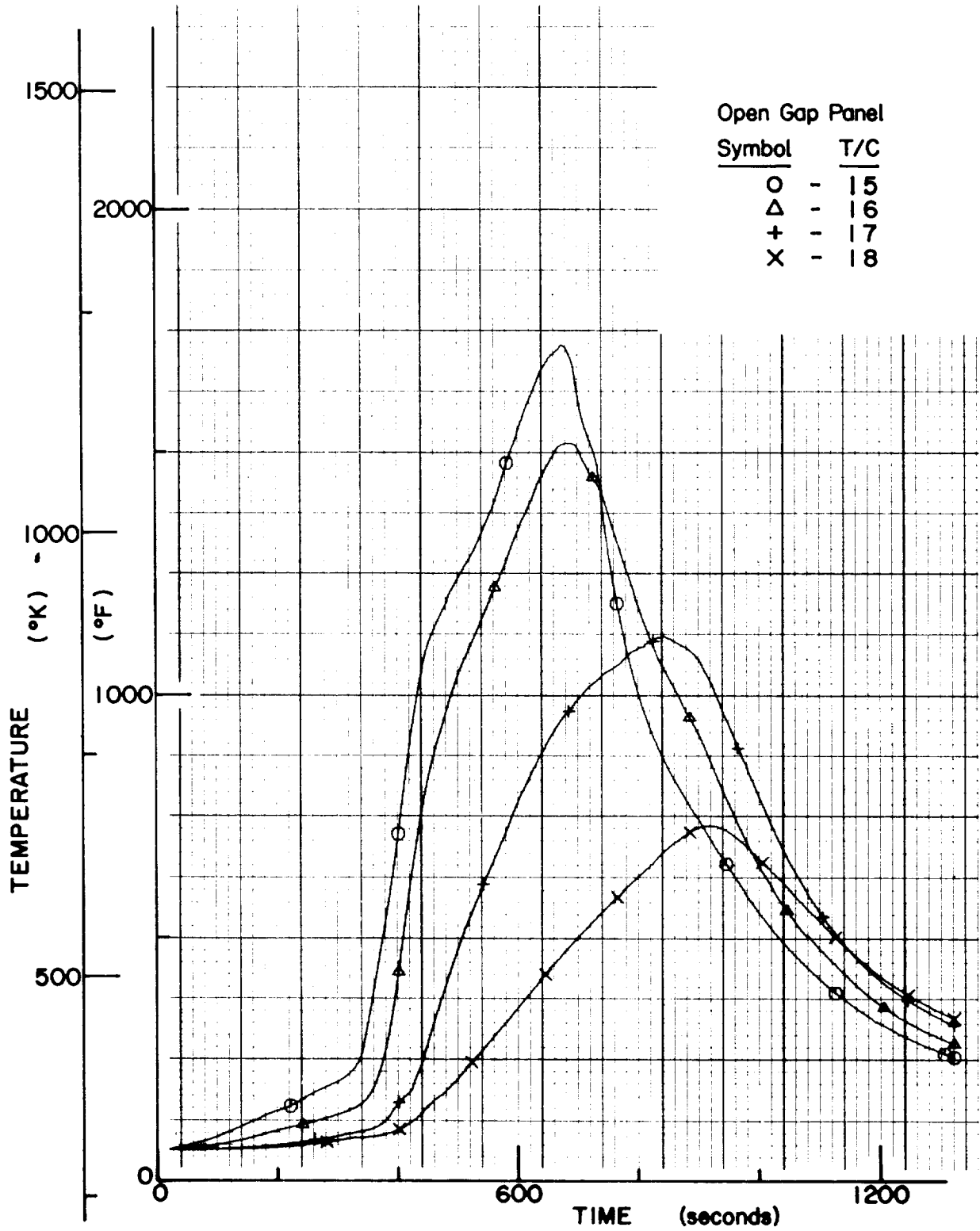


Figure 157.- Thermocouple Measurements (T/C 15, 16, 17, and 18)

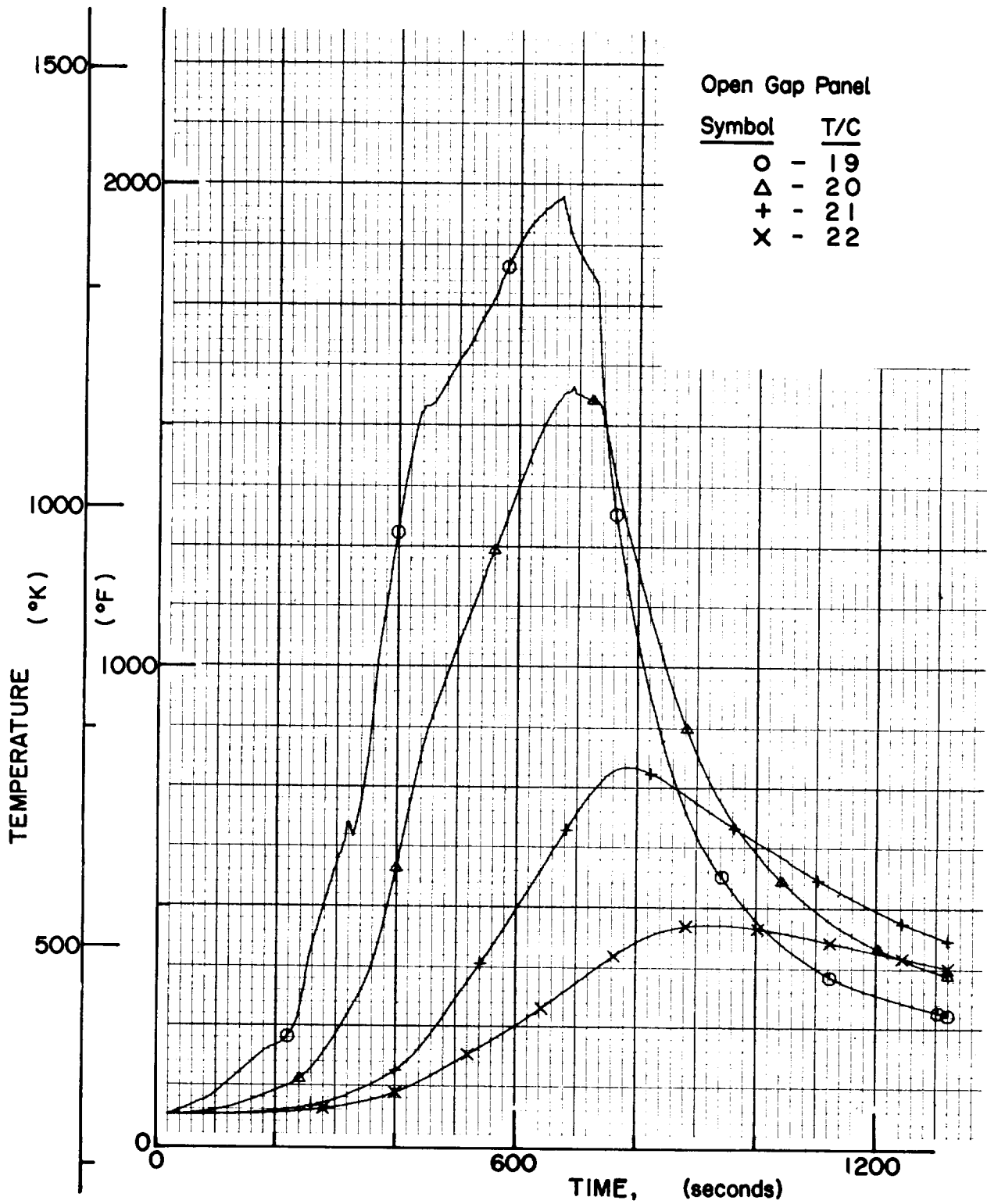


Figure 158.- Thermocouple Measurements (T/C 19, 20, 21, and 22)

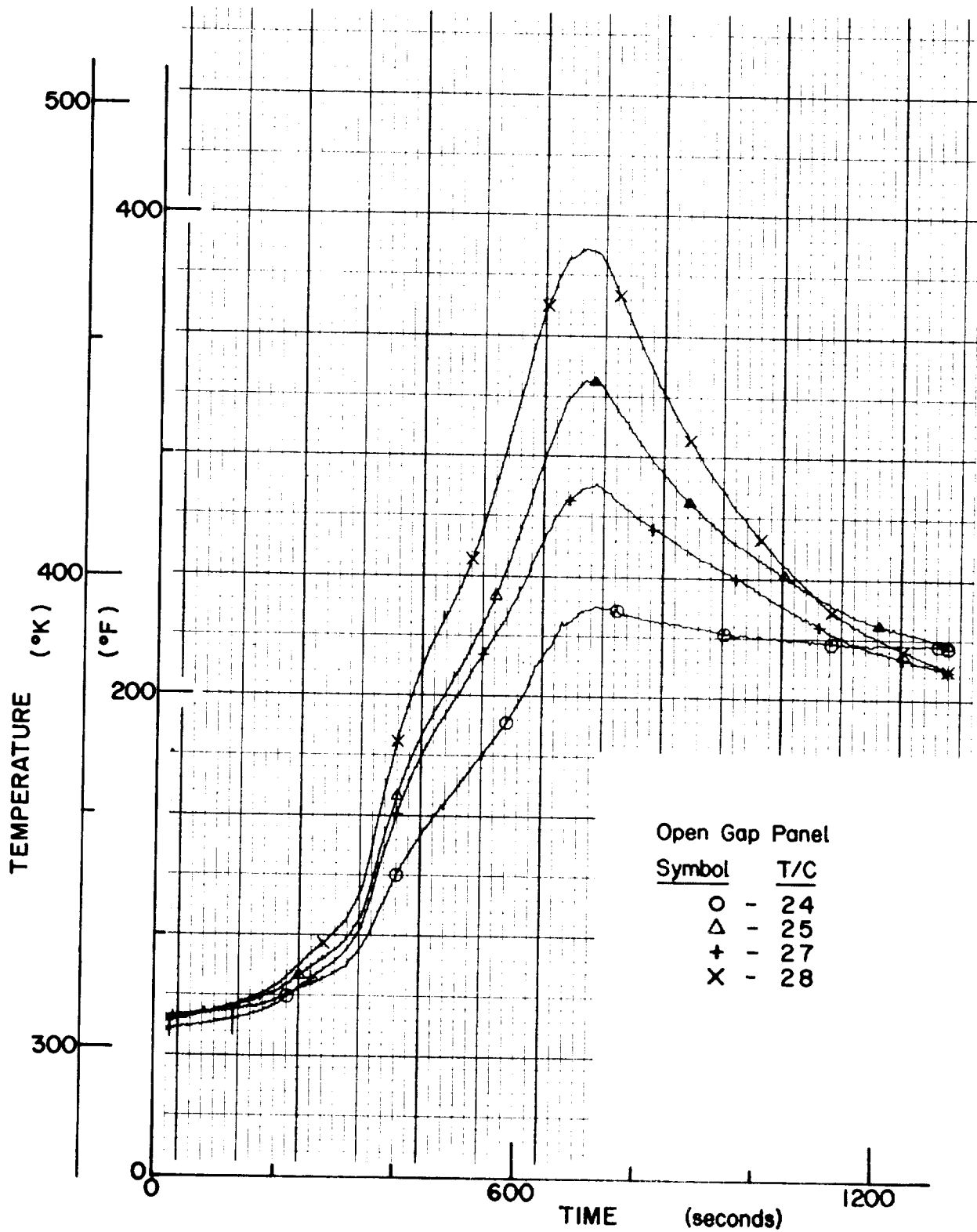


Figure 159.- Thermocouple Measurements (T/C 24, 25, 27, and 28)

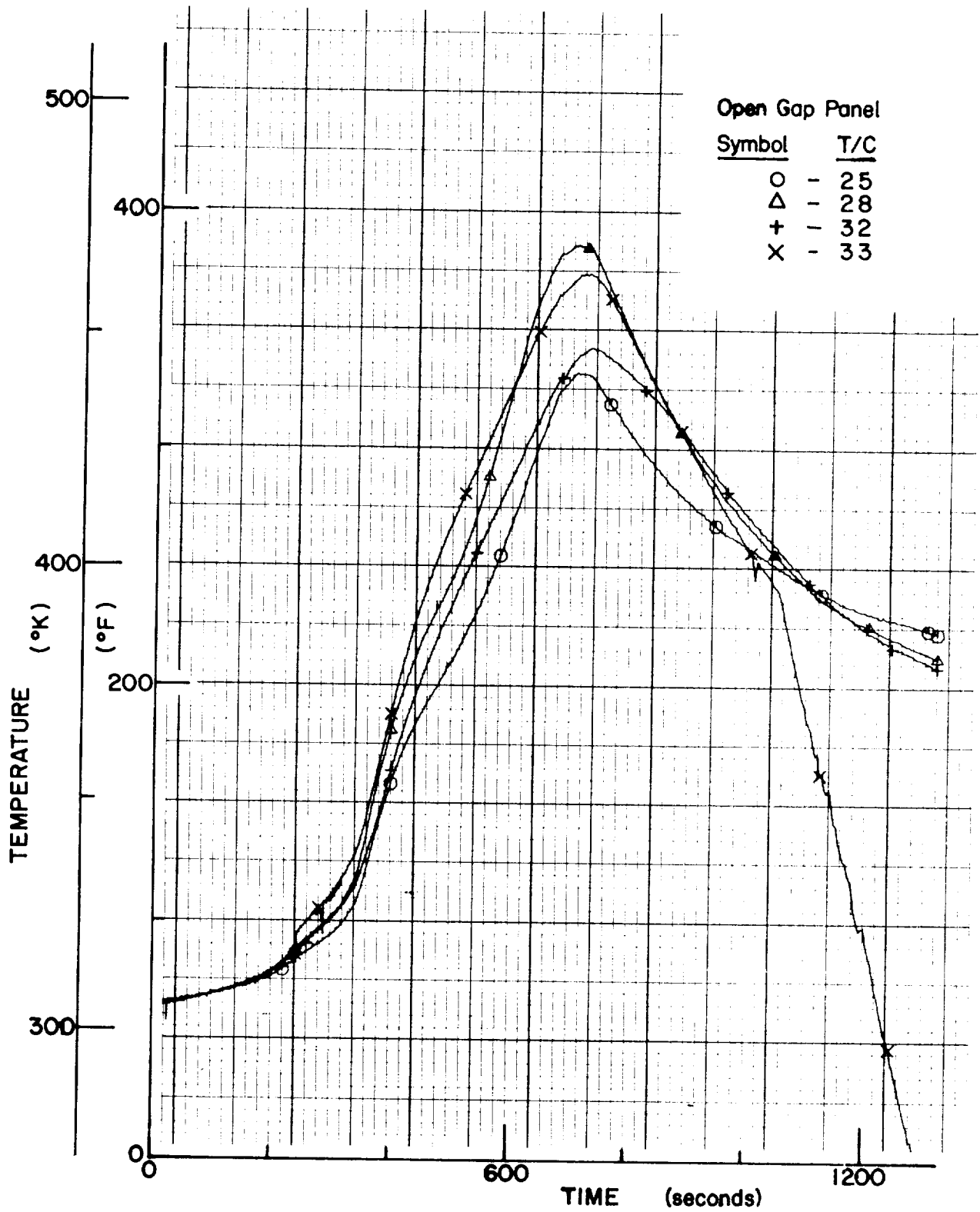


Figure 160.- Thermocouple Measurements (T/C 25, 28, 32, and 33)

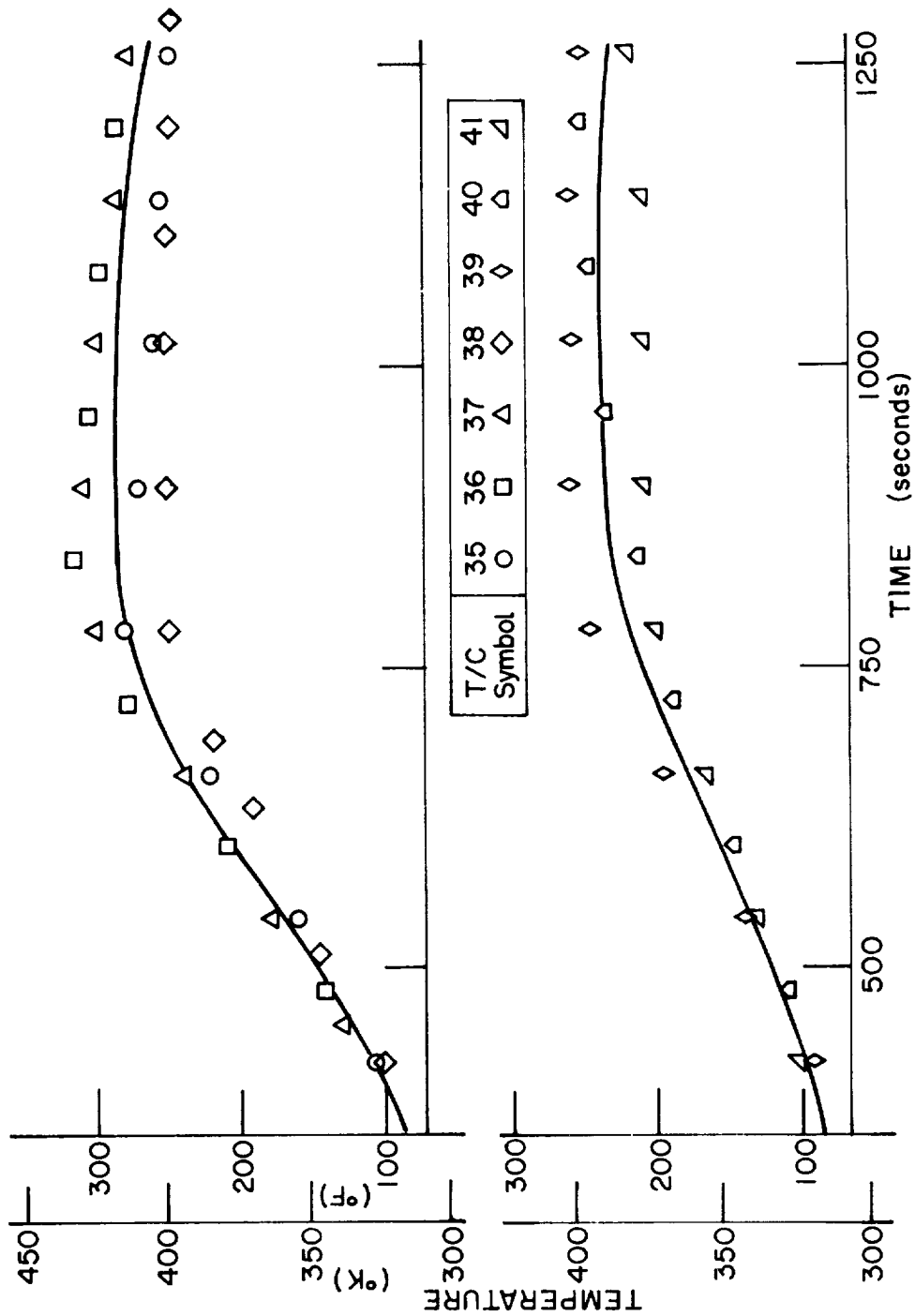


Figure 161.- Thermocouple Measurements (T/C 35 through 41)

## B. Sealed-Gap Panel

1. Test plan.-

Objectives: The primary objective of this test was to determine the feasibility of a resilient material sealed-gap concept using ablative materials of the Space Shuttle.

Secondary objectives were to evaluate the stud-bolt concept that permits subpanel plate motion relative to the supporting structure and the local temperature distribution in the ablator in the region of the counterbore for the stud bolt.

Approach: SLA-561 ablator, used in this test program, had been proposed for use in the acreage areas of the Shuttle.

One composite panel was tested. The composite panel consisted of two subpanels and a primary structure plate (fig. 149). Each subpanel was composed of a 55.88x55.88x4.39-cm (22x22x173 in.) ablator bonded to a similar sized 0.102-cm (0.040 in.) thick aluminum sheet. The subpanels were mounted mechanically on a stiffened 0.254-cm (0.100 in.) thick aluminum sheet, which simulates the primary structure.

Two tests of the panel were made:

- 1) Ascent heating simulation to a maximum surface temperature of 533°K (500°F);
- 2) Descent heating simulation to a maximum surface temperature of 1533°K (2300°F).

Thermal loadings were applied with quartz lamps. Thermocouples were used to monitor the following data: heat transfer in a subplate stud-bolt counterbore; temperature distribution through the ablator thickness; and heat transfer to the aluminum support channel. Deformations in the aluminum subpanel plate due to thermal expansion and possible constraint from the stud bolts were monitored with strain gages.

These tests were intended to permit correlation with analyses and projection to similar induced Shuttle conditions and other locations on the orbiter.

Test facility: The test facility used was the Structures Laboratory at Martin Marietta's Denver Division.

## APPENDIX E

Material and specimens: SLA-561, used for the test specimen, is a composite elastomeric-type material supported in a honeycomb structure. The nominal density of the material is  $0.24 \text{ gm/cm}^3$  ( $15 \text{ lb/ft}^3$ ). Details of the test panel construction are given in figure 99.

Instrumentation: Instrumentation details are also shown in the figure. Each ablator/aluminum subpanel contained the following instrumentation:

- 1) Four strain gages;
- 2) 13 thermocouples (four through the ablator thickness to monitor the temperature at each of two locations, one near the gap, and one adjacent to each of the four strain gages).

One subpanel of the composite panel was instrumented with an additional two thermocouples--one in a stud-bolt counterbore and the other close to the counterbore.

The primary structure aluminum plate was instrumented with 11 thermocouples with a maximum temperature capability of  $589^\circ\text{K}$  ( $600^\circ\text{F}$ ). One aluminum channel was instrumented with two thermocouples.

The strain gage data were used together with the thermocouple data to monitor any restraining effect of the "floating" attachments that would adversely affect the gap deformations. The thermocouples on the rear primary panel surface permitted determination of the temperature variation between the ablator protected area and the gap area.

Test: Before the composite panel was tested, a calibration test was performed to verify uniformity of heating and integrity of the system. Maximum temperature variation at suitable divergent locations across the area covered by the panel were within  $\pm 3\%$ . The complete descent heating profile (fig. 91) was used to qualify the test system for the test panel.

The composite panel was installed in the test fixture to simulate ascent heating. Power was applied to give the desired thermal loading at the outer surface of the ablator (fig. 101). Twenty measurements were recorded continuously throughout the test--12 thermocouple measurements, and eight strain gage measurements.

When thermal equilibrium with the ambient environment was reached, the panel was removed from the test setup for examination.

The panel was installed in the test fixture to simulate descent heating. Power was applied to give the desired thermal loading at the outer surface of the ablator (fig. 91). Forty-nine measurements were recorded throughout the test--41 thermocouple measurements, and eight strain gage measurements. The panel was then removed from the test setup for examination.

2. Test results.-- Temperature data at various points of the sealed-gap test panel are presented in figures 162 through 175. The thermocouple locations are shown in figure 99. If no data are given for a particular thermocouple, this indicates that the thermocouple was inoperative during the test.

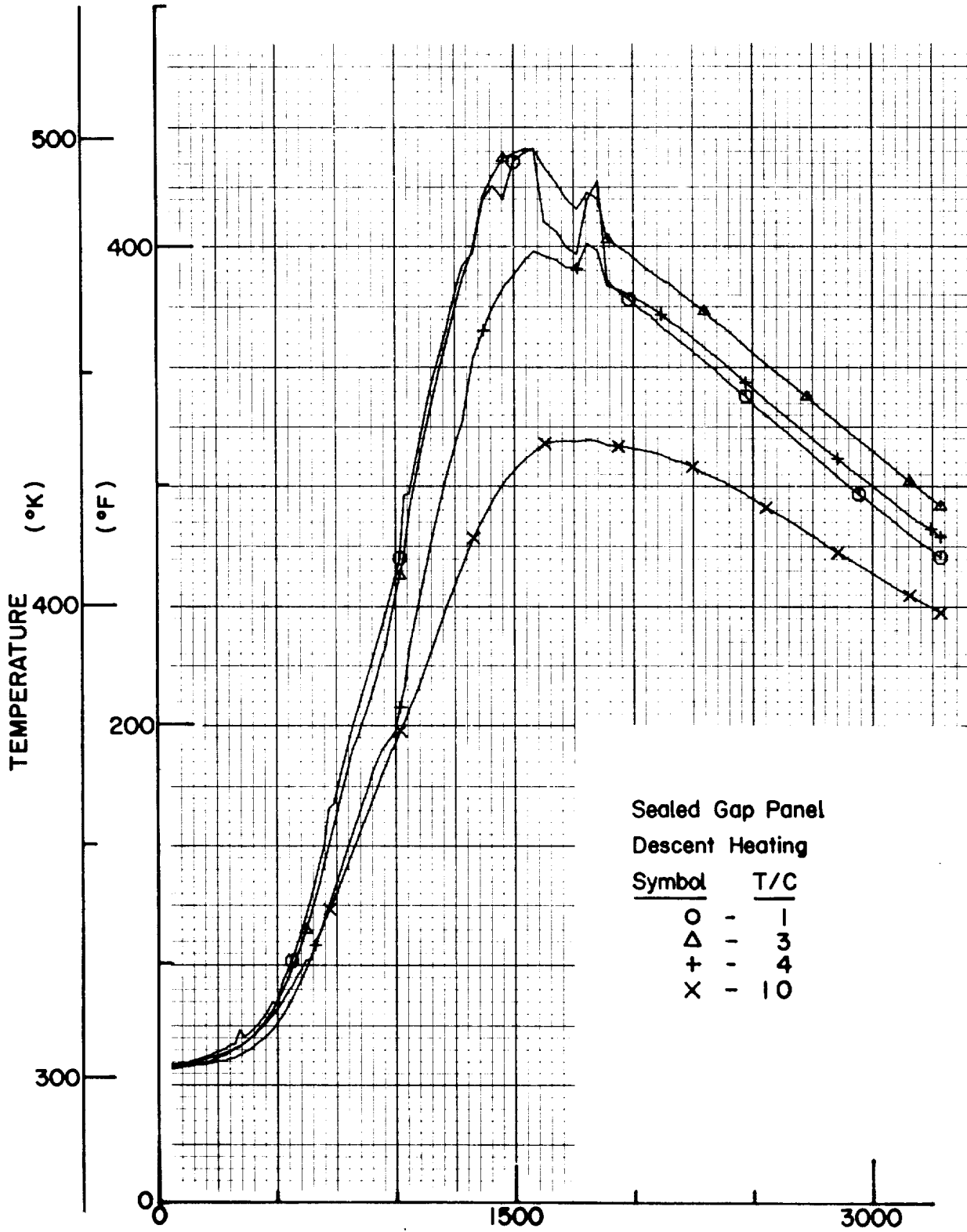


Figure 15 Figure 162.- Thermocouple Measurements (T/C 1, 3, 4, and 10)

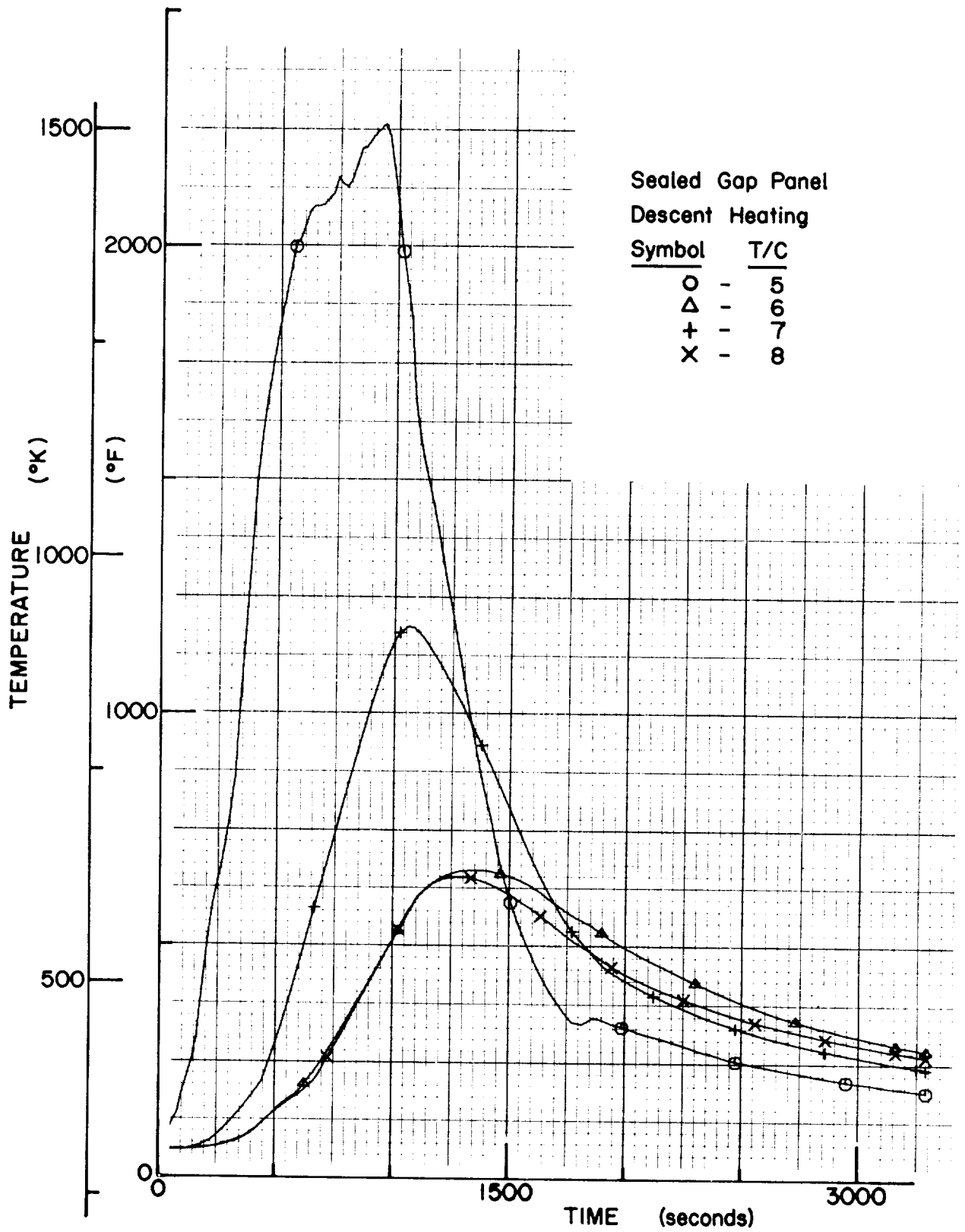


Figure 163.- Thermocouple Measurements (T/C 5, 6, 7, and 8)

APPENDIX E

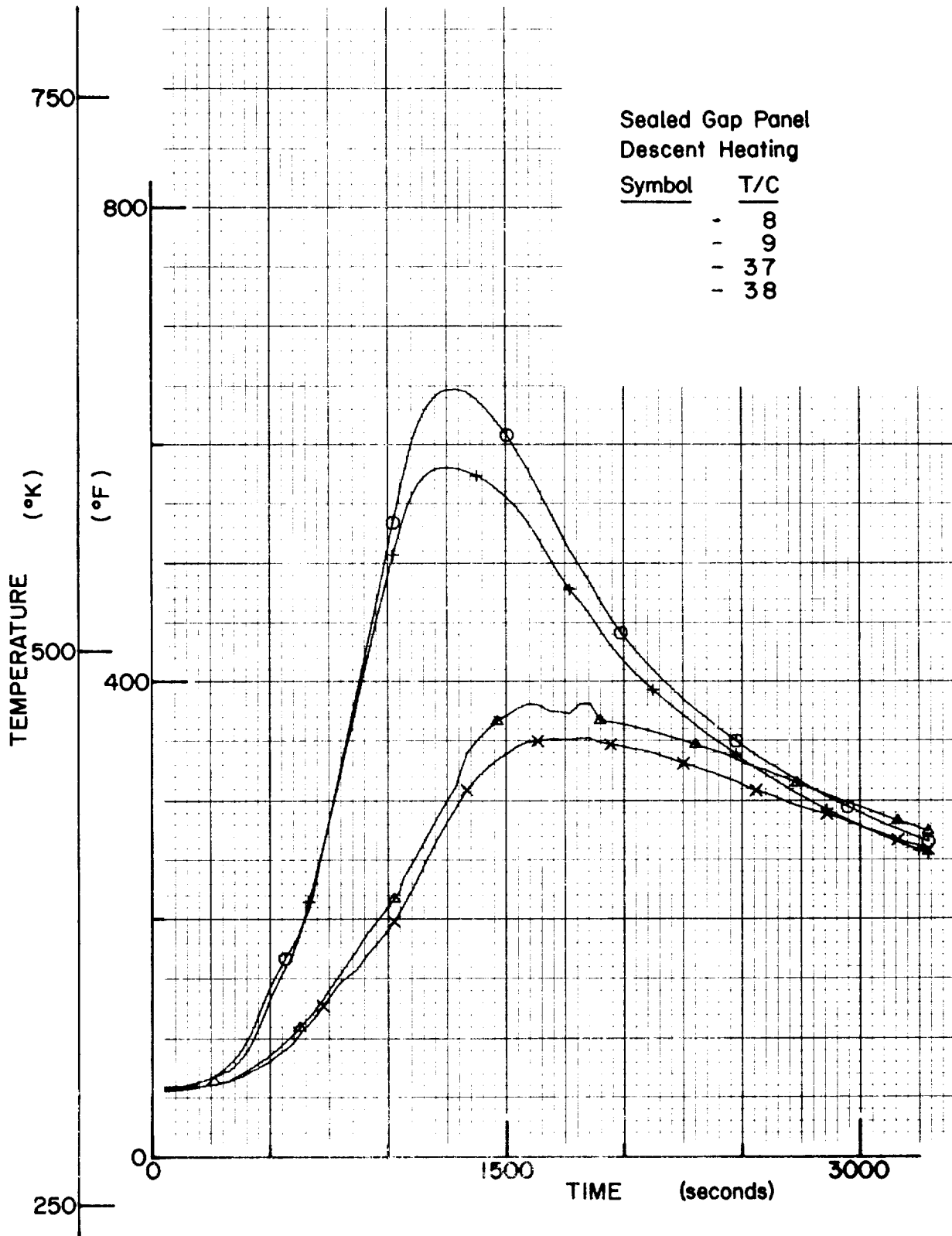


Figure 164.- Thermocouple Measurements (T/C 8, 9, 37, and 38)

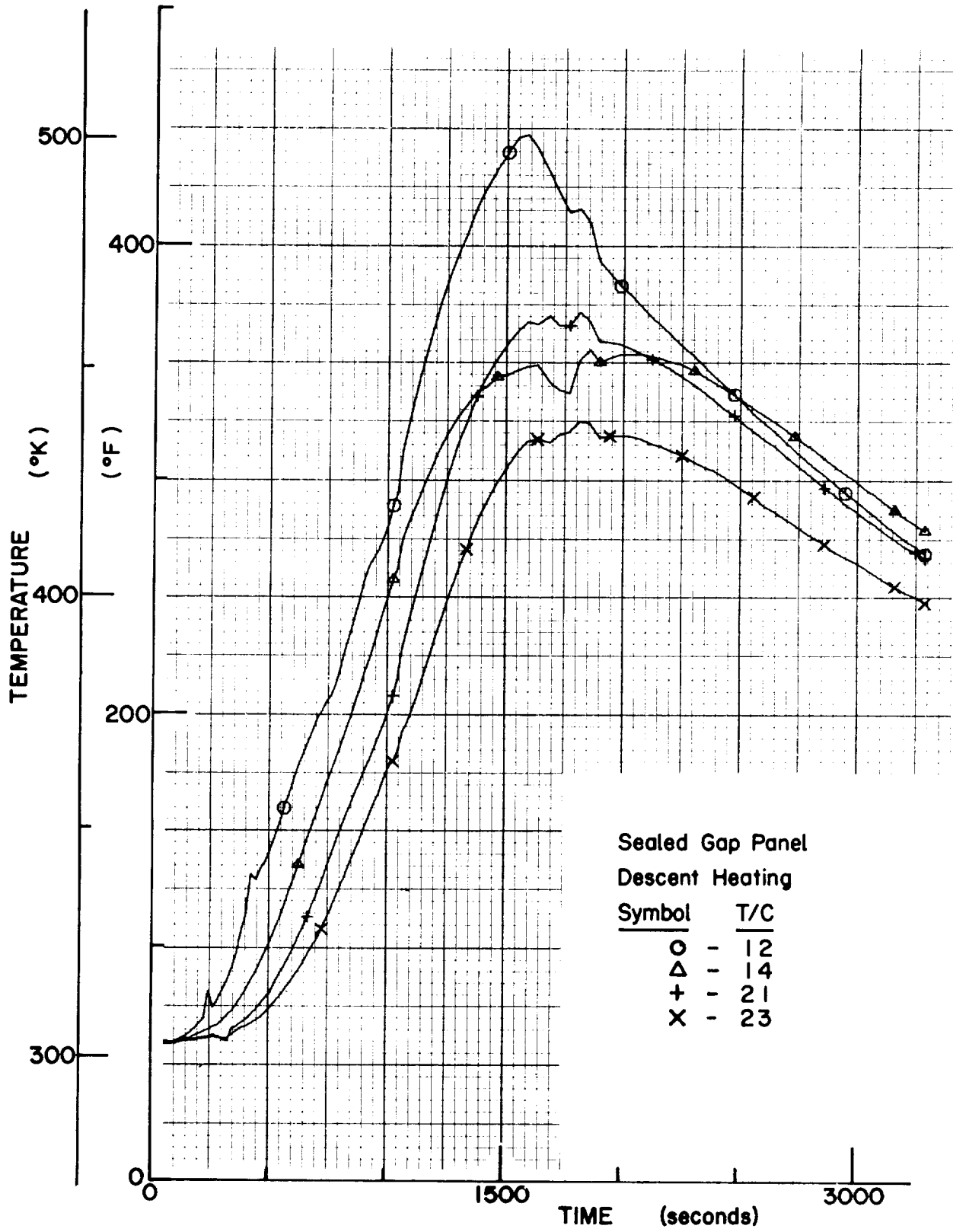


Figure 165.- Thermocouple Measurements (T/C 12, 14, 21, and 23)

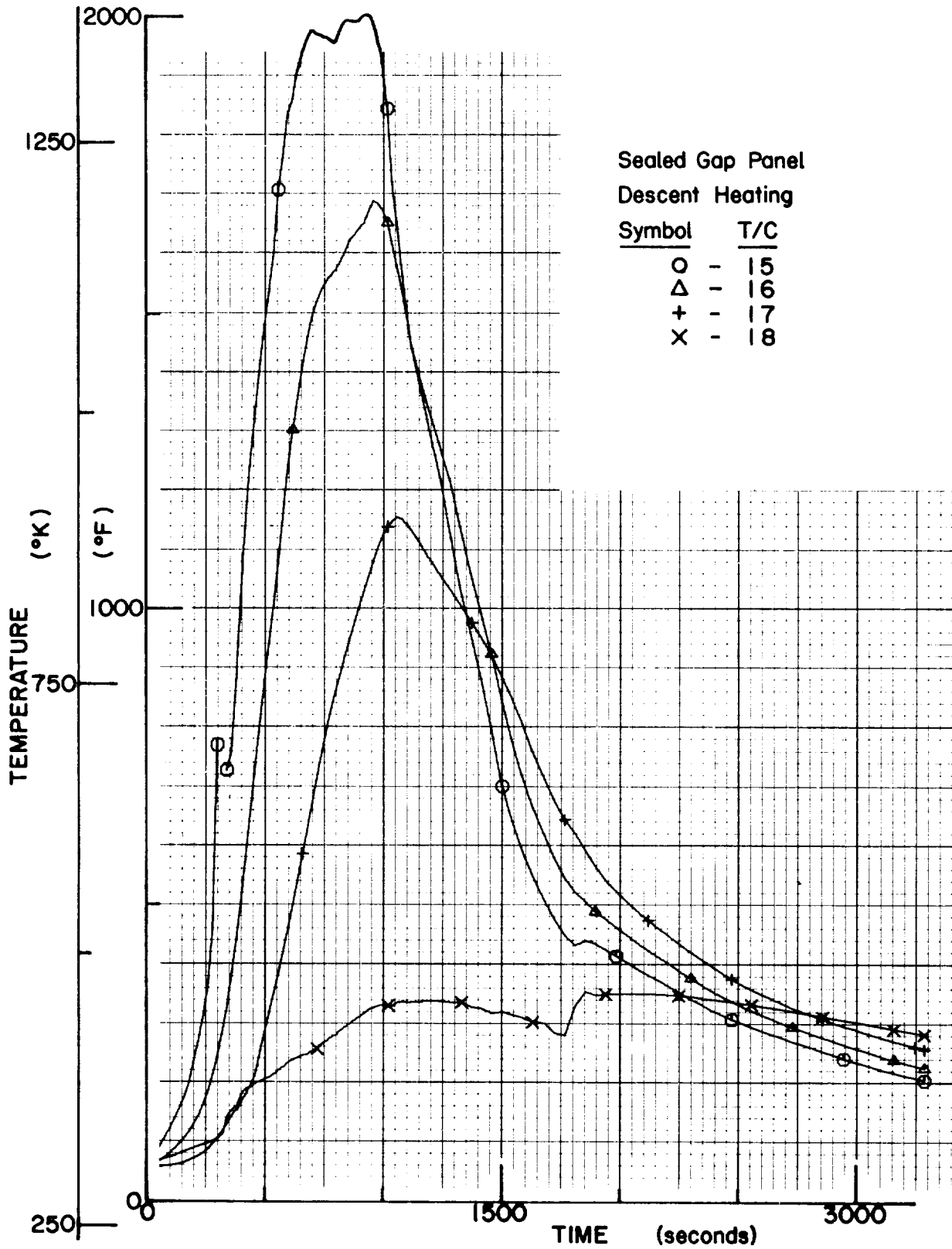


Figure 166.- Thermocouple Measurements (T/C 15, 16, 17, and 18)

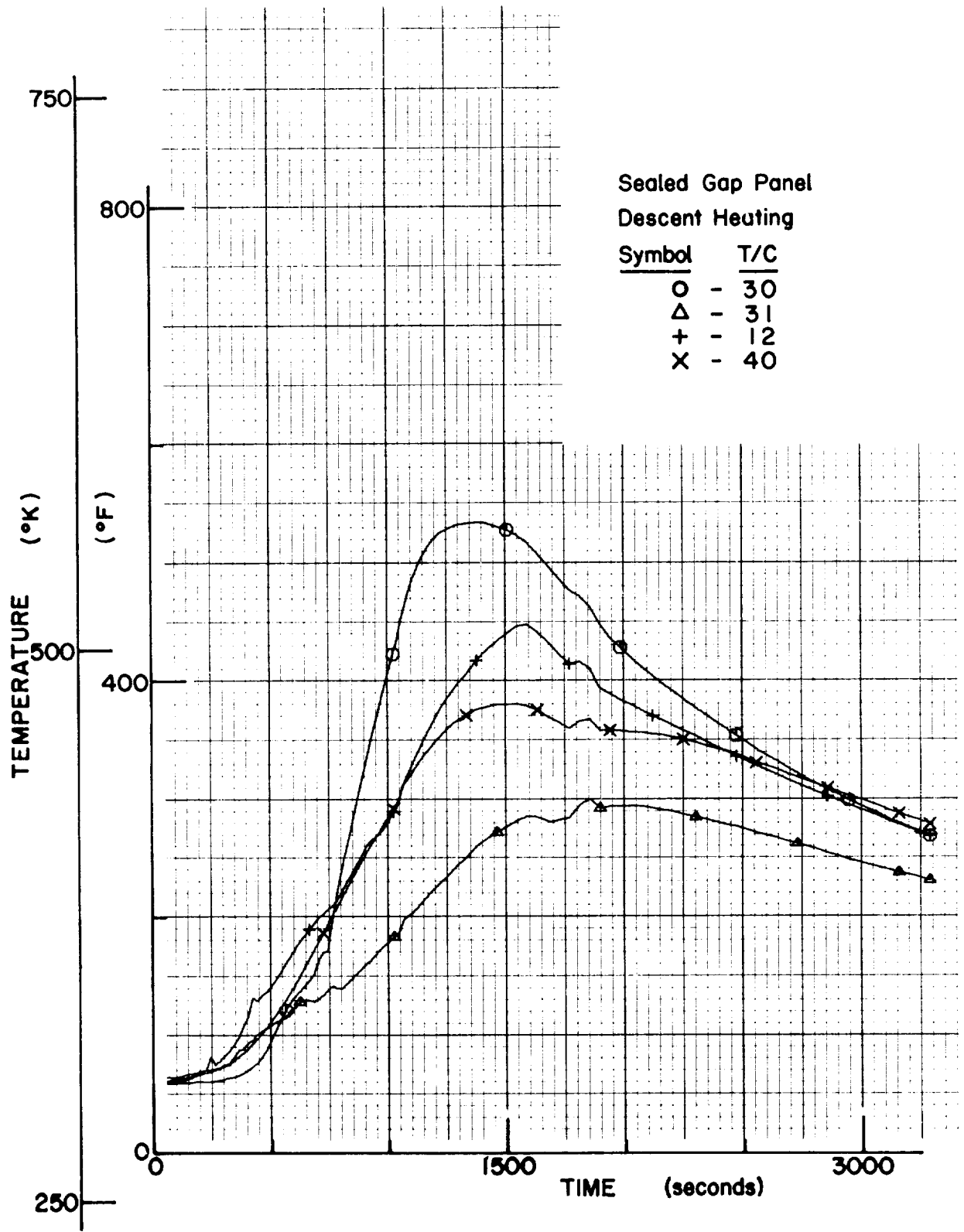


Figure 167.- Thermocouple Measurements (T/C 30, 31, 12, and 40)

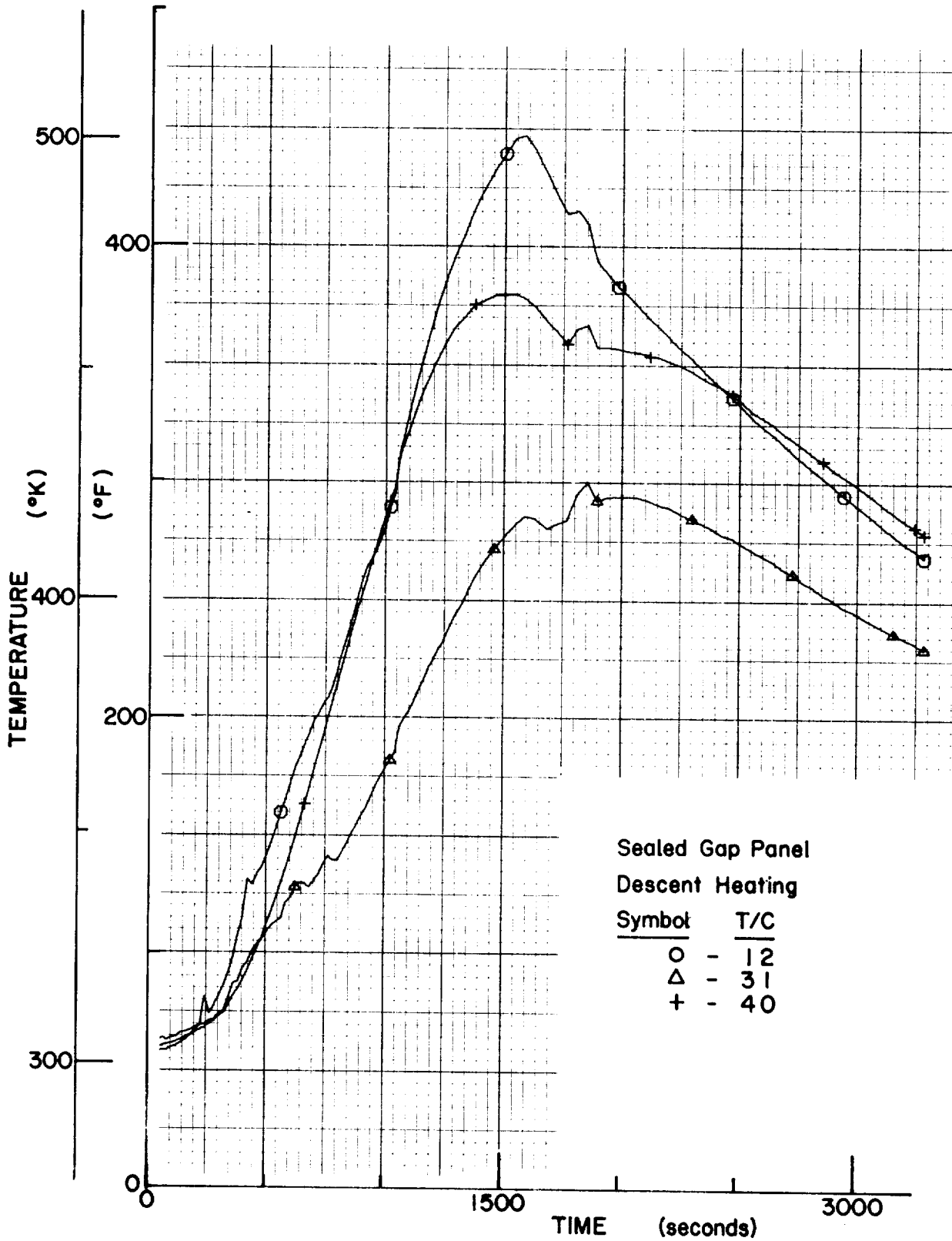


Figure 168.- Thermocouple Measurements (T/C 12, 31, and 40)

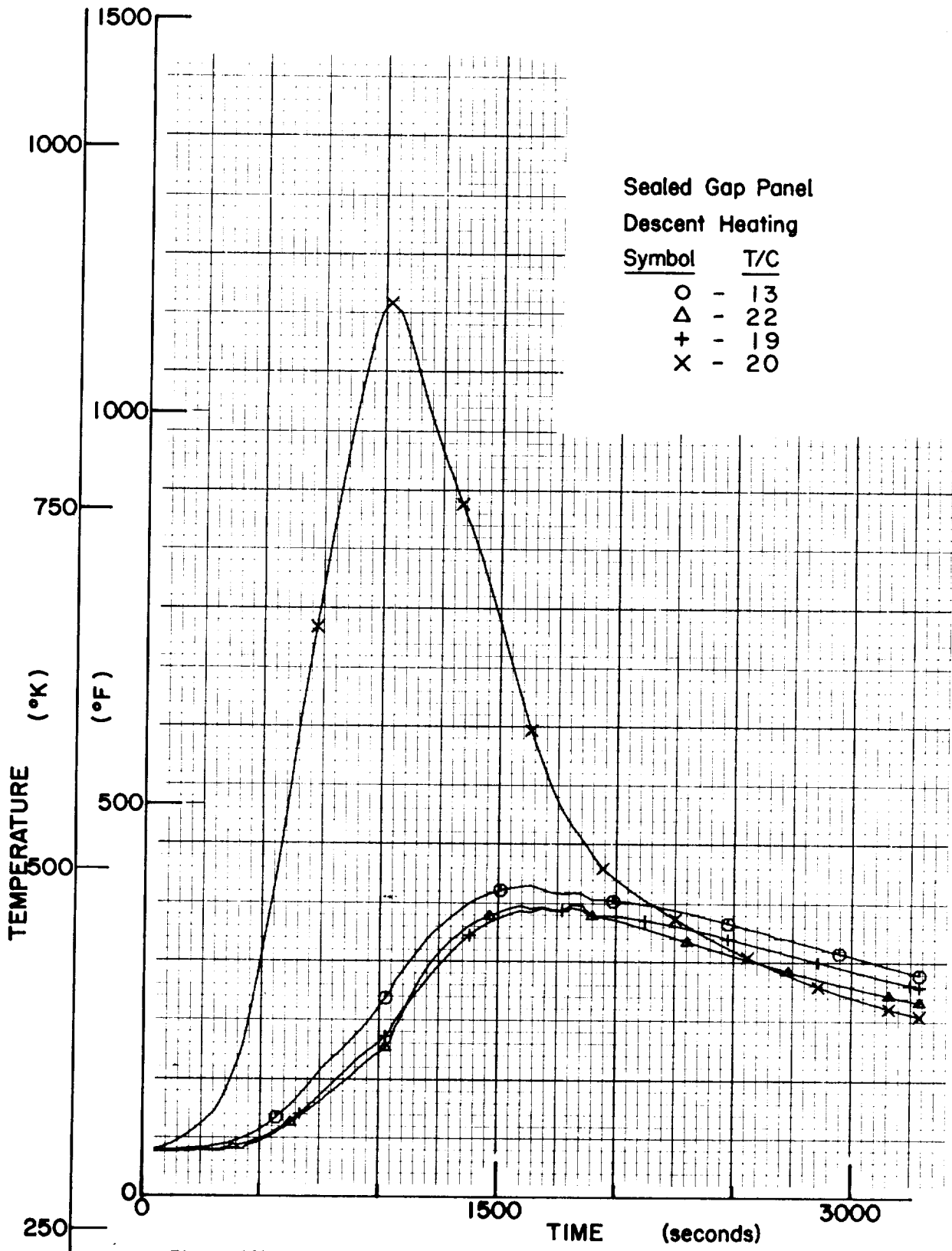


Figure 169.- Thermocouple Measurements (T/C 13, 19, 20, and 22)

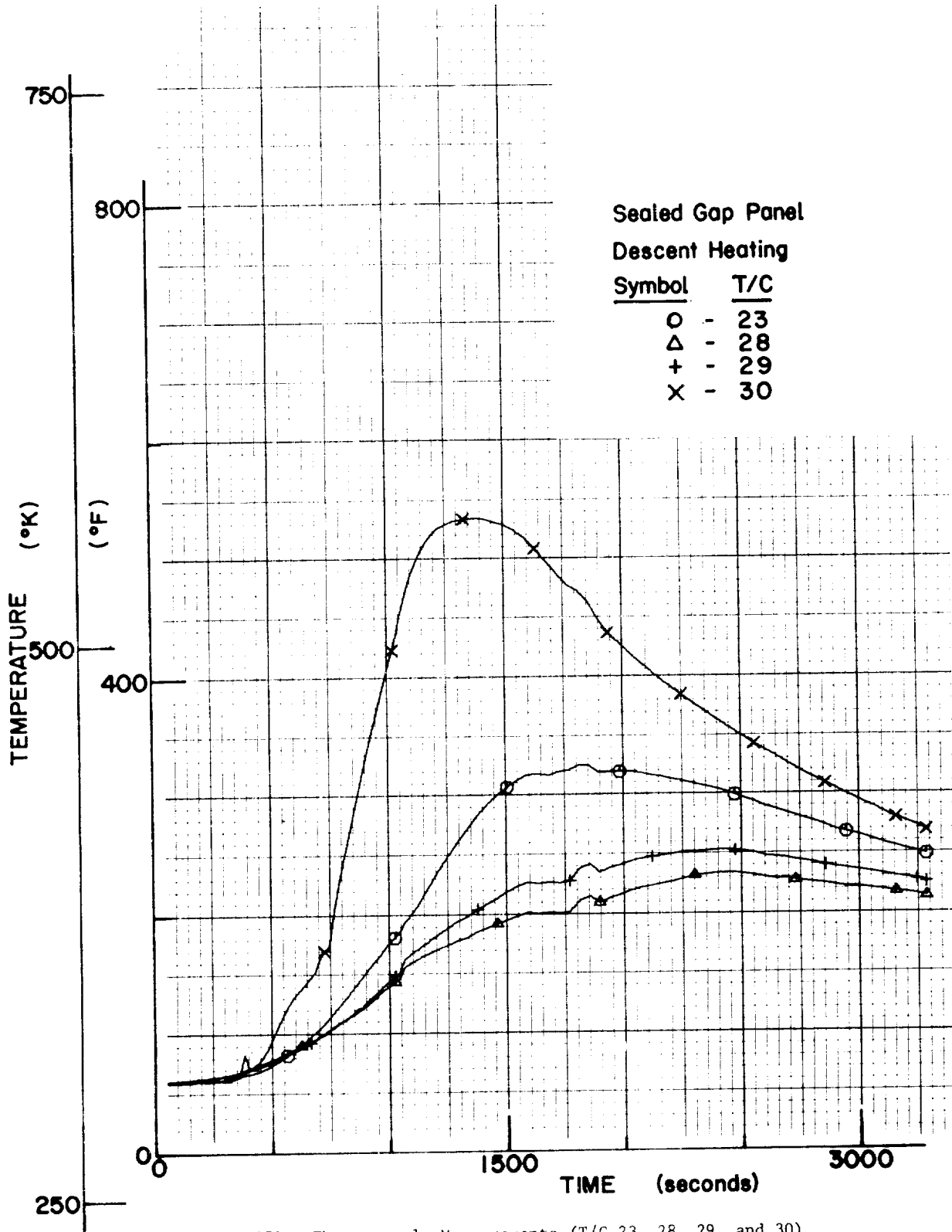


Figure 170.- Thermocouple Measurements (T/C 23, 28, 29, and 30)

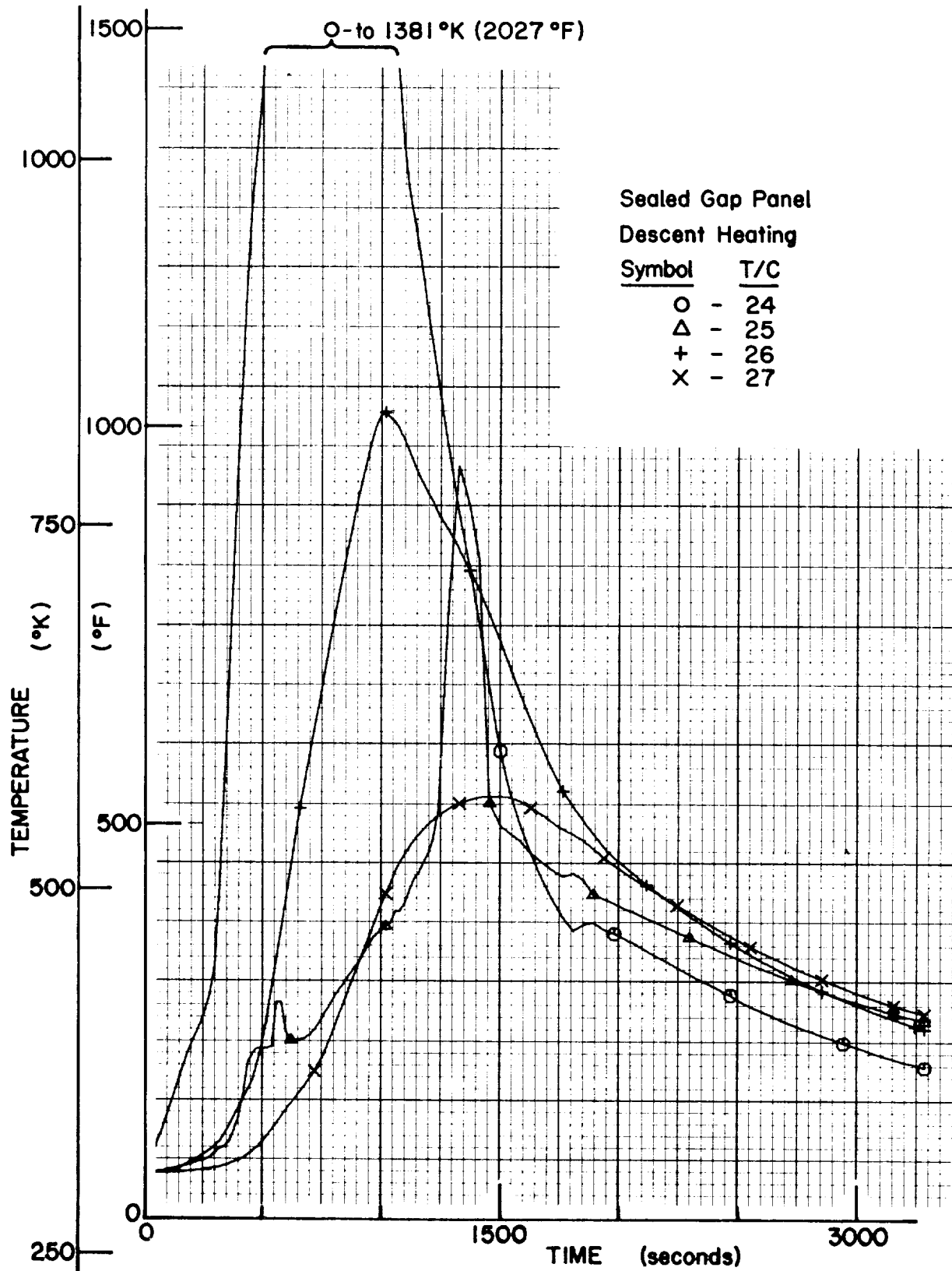


Figure 171.- Thermocouple Measurements (T/C 24, 25, 26, and 27)

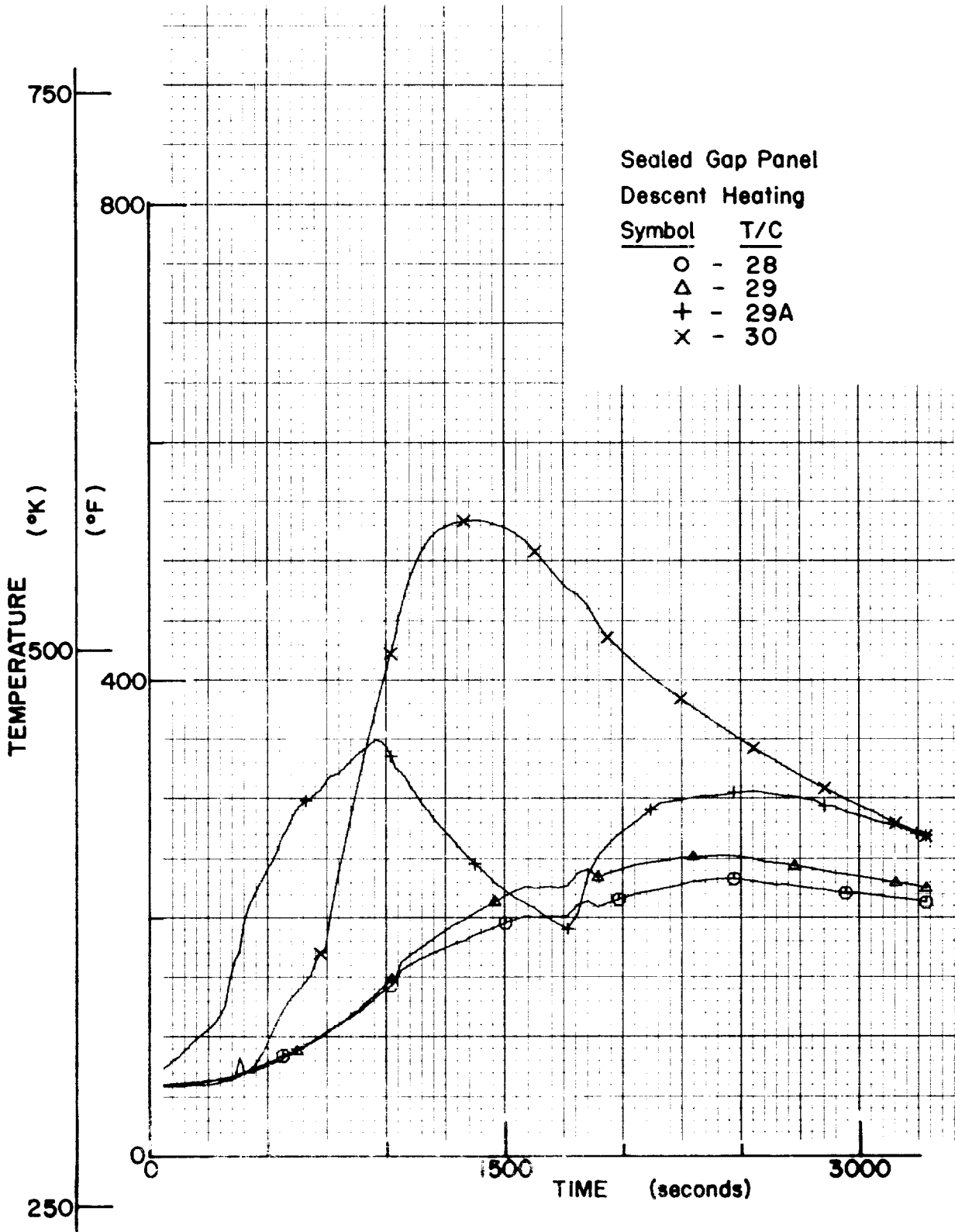


Figure 172.- Thermocouple Measurements (T/C 28, 29, 29A, and 30)

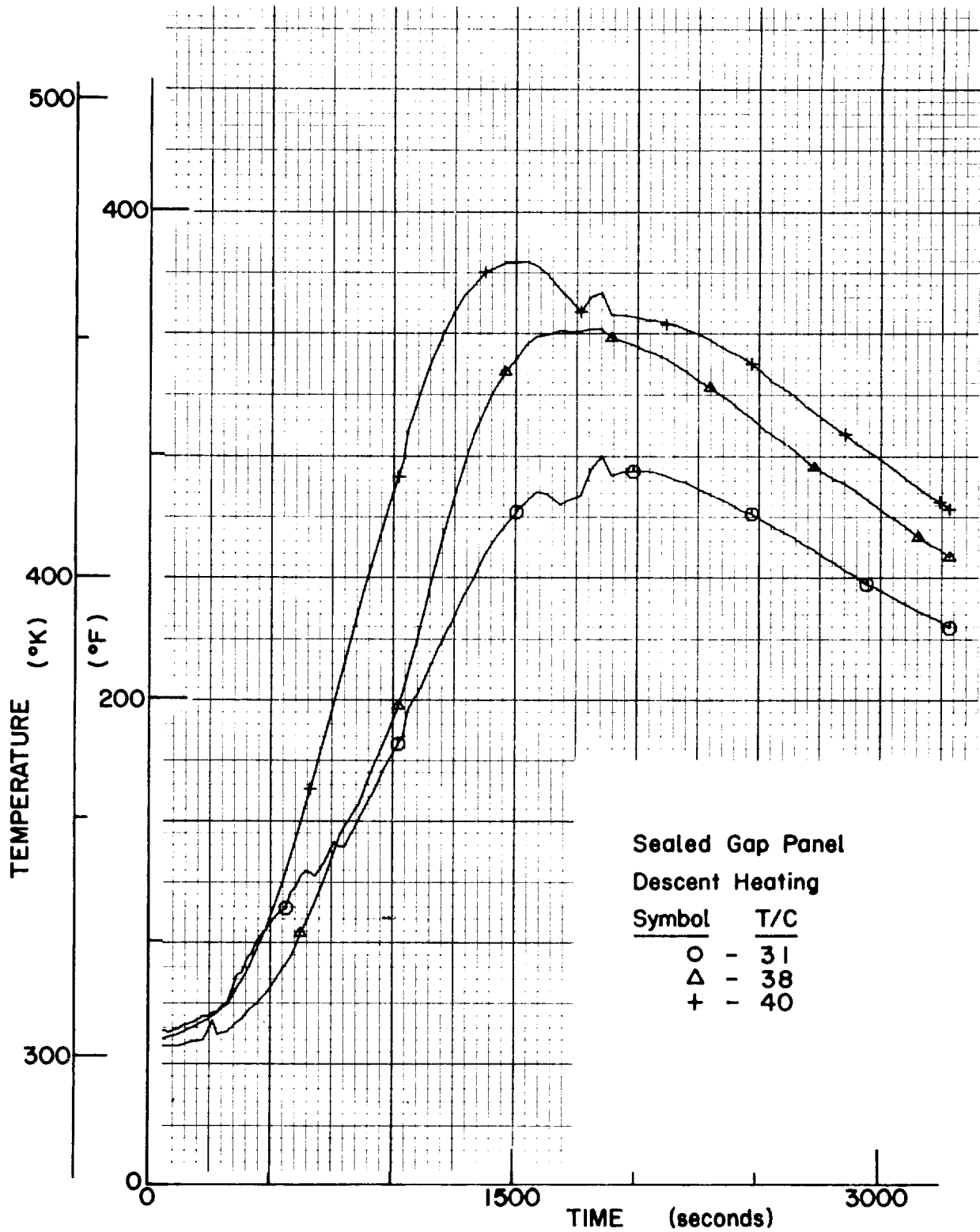


Figure 173.- Thermocouple Measurements (T/C 31, 38, and 40)

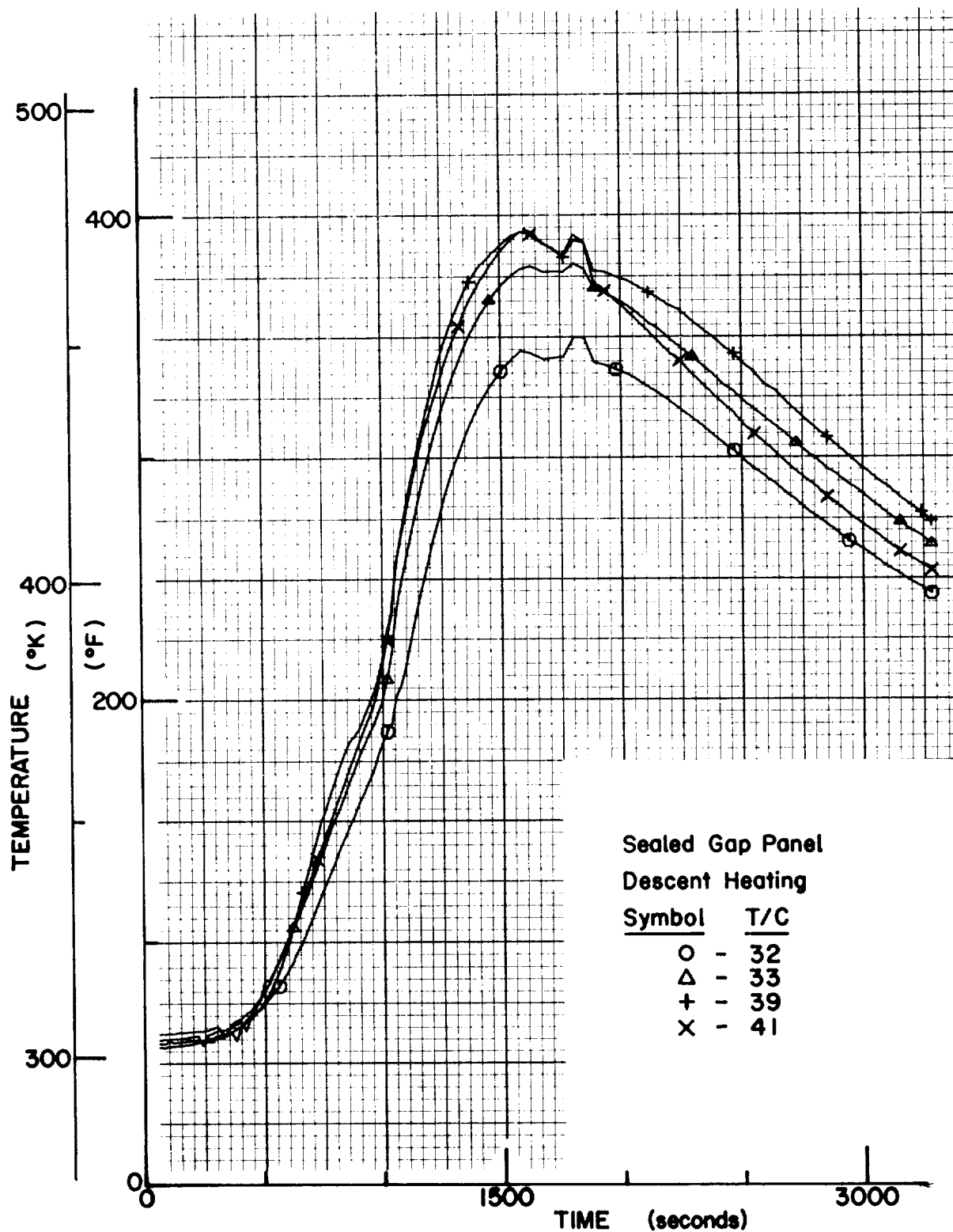


Figure 174.- Thermocouple Measurements (T/C 32, 33, 39, and 41)

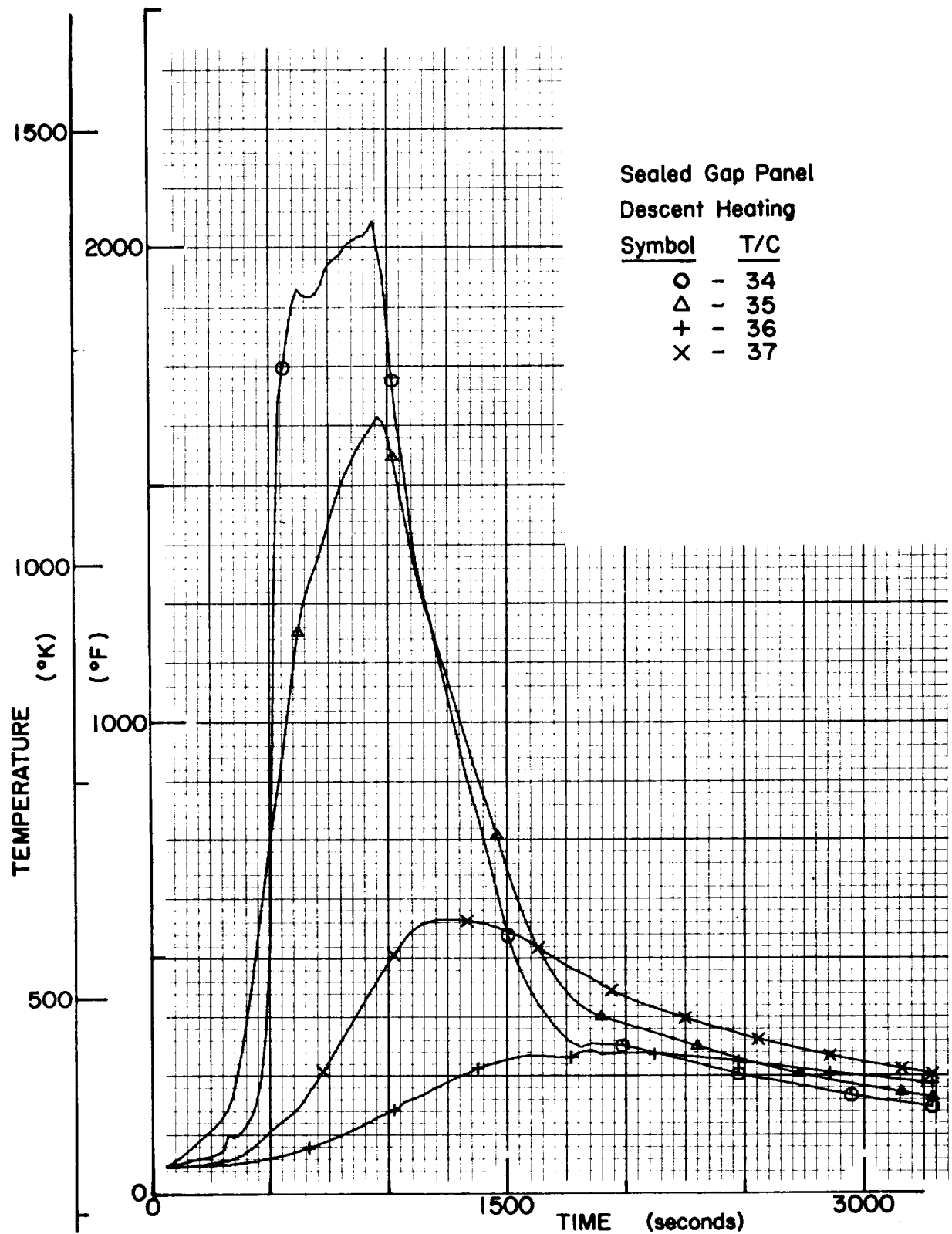


Figure 175.- Thermocouple Measurements (T/C 34, 35, 36, and 37)

## REFERENCES

1. MSFC Shuttle Utilization Planning Office: Preliminary Traffic Model for the Space Shuttle. November 1972.
2. Love, E. S.: Advanced Technology and the Space Shuttle, Tenth Von Karman Lecture. *Astronautics and Aeronautics*, February 1973.
3. Structural Design Criteria Application to the Space Shuttle. NASA SP 8057, January 1971.
4. Metallic Materials and Elements for Aerospace Vehicle Structures. MIL-HDBK-5B. September 1973.
5. Bulletin No. 303-03-PDI, Kawecki Berylco Industries.
6. Structural Sandwich Composites. MIL-HDBK-23A. December 1968.
7. HEXCEL Bulletin TSB-120. August 1971.
8. Dow Corning Bulletin 08-405. April 1969.
9. American Cynamid Co., Corfil 615, Table 1, January 1961, Revised March 1969.
10. LI-1500-Rigid Surface Insulation for Space Shuttle. Design Data Package, LMSC-D 153996, February 1966.
11. Ablation Material Property Book. TN-3770161, NAS1-9000.
12. Miller, C. C.; and Rummel, W. D.: Study of Critical Defects in Ablative Heat Shield Systems for the Space Shuttle, Tasks IV and V. Contract NAS1-10289, MCR-73-184, Martin Marietta Corporation, Denver, Colorado, July 1973.
13. Chandler, H. H.: Investigation of Low Cost Ablative Heat Shield Fabrication for Space Shuttle. NASA CR-112045.
14. Carlson, D. L.: Test Plan for Viking Aeroshell Heat Shield Design Verification. MMC VER-235, August 1972.
15. Terrestrial Environment (Climatic) Criteria Guidelines for Use in Space Vehicle Development. NASA TMX 64589, May 1971.

16. Panel Flutter. NASA SP 8004.
17. Design Criteria for the Prediction and Prevention of Panel Flutter. vol I, AFFDL-TR-67-140, August 1968.
18. Allayaud, D.: Local Surface Pressures on Grumman Space Shuttle Configuration 619. Martin Marietta Memo, 31 October 1972.
19. Meteoroid Criteria. NASA TMX 64627.
20. Roark, R. J.: Formulas for Stress and Strain. McGraw-Hill Book Co., 1938.
21. Timoshenko, S., and Woinowsky-Krieger, S.: Theory of Plates and Shells. McGraw-Hill Book Co., 1959.
22. 478 Ascent Configuration Orbiter Fuselage Bottom Centerline Pressure Distributions. Sem No. MMPS-72-104, MMC/GAC, April 1972.
23. 478 Ascent Configuration Orbiter Fuselage Outer Surface Pressure Distribution. Sem No. MMPS-72-123, MMC/GAC, April 1972.
24. Skylab Vibration, Acoustic and Shock Environment. MSFC IN ASTN AD-70-1, July 1970.
25. Preliminary Vibration, Acoustic and Shock Specification for Components on the Saturn V Vehicle. MSFC IN-P&YE-S-63-2, November 1963.
26. Rehder, J.: Entry Trajectory Optimization Mark I Orbiter Ablative Thermal Protection System. NASA/LRC Symposium, November 1971.
27. Chemical Conversion Coatings on Aluminum and Aluminum Alloys. MIL-C-5541, September 1971.
28. Cornick, D. E., et al.: Post-Program to Optimize Shuttle Trajectories. NASA/LRC Contract NAS1-10811, December 1971.
29. J. Dunavant, et al.: Thermal Panel Report to the Aero-thermodynamic/Configurations Working Group. Heat Transfer Methodology for Space Studies, May 1971.

30. Eckert, E. R. G.: Survey of Boundary Layer Heat Transfer at High Velocities and High Temperatures. WADC Tech Report 59-624, April 1960.
31. Spalding, D. B.; and Chi, S. W.: The Drag of a Compressible Turbulent Boundary Layer on a Smooth Flat Plate with and without Heat Transfer. J. Fluid Mech., vol. 18, part I, January 1964.
32. Hopkins, E. J., et al.: Summary and Correlation of Skin Friction and Heat Transfer Data for a Hypersonic Turbulent Boundary Layer on Simple Shapes. NASA TN D5089, June 1969.
33. Fay, J. A.; and Riddell, F. R.: Stagnation Point Heat Transfer in Dissociated Air. Journal of Aeronautical Science, February 1958.
34. Beckwith, I.E.; and Gallagher, James J.: Local Heat Transfer in Dissociated Air. Journal of Aeronautical Science, February 1958.
35. Lees, L.: Laminar Heat Transfer over Blunt-Nosed Bodies at Hypersonic Flight Speeds, Jet Propulsion, 1956.
36. Deltra, H. W.; and Hidalgo, H.: Generalized Heat Transfer Formulae and Graphs. AVCO Research Report 72, March 1960.
37. Customer Utilization Report, FD-275, Martin Marietta Corporation, Denver, Colorado, June 1971.
38. Groninger, B. V.; and Dressel, M.: Subpanel Design Optimization for Ablator Thermal Protection Systems. September 1971, Revised January 1972.
39. Manual for Structural Stability Analysis of Sandwich Plates and Shells. NASA CR-1457.
40. Astronautic Structures Manual. NASA, December 1970.
41. Customer Utilization Report, PD-225, Martin Marietta Corporation, Denver, Colorado, January 1971.
42. Customer Utilization Report, PD-240-D, Martin Marietta Corporation, Denver, Colorado, November 1972.